Mariappan Rajan
Krishnan Anand
Anil Chuturgoon   *Editors*

Proceedings of the International Conference on Nanomedicine (ICON–2019)

Springer

Springer Proceedings in Materials

Mariappan Rajan · Krishnan Anand ·
Anil Chuturgoon

Editors

Proceedings of the International Conference on Nanomedicine (ICON-2019)

Springer

Editors
Mariappan Rajan
Department of Natural
Products Chemistry
Madurai Kamaraj University
Madurai, India

Krishnan Anand
School of Laboratory Medicine
and Medical Sciences
University of KwaZulu-Natal
Durban, South Africa

Anil Chuturgoon
School of Laboratory Medicine
and Medical Sciences
University of KwaZulu-Natal
Durban, South Africa

Contents

Green Synthesis of Silver Nanoparticles Using *Ledebouria Revoluta* Bulb Extractand Its Biological Activity

R. Aswini, S. Meimozhi, R. Tamilmozhi, M. Kowsalya,
and S. Murugesan[(✉)]

Department of Botany, Periyar University,
Periyar Palkalai Nagar, Salem 636 011, India
drsmbtpu@gmail.com

Abstract. In this present examination explores the viability of silver nanoparticles (AgNPs) green synthesis from bulb extract of *Ledebouria revoluta* as an antitumor specialist utilizing human lung cancer cell line (A549). The AgNPs synthesis was determined by UV-Visible range and it was additionally described by field X-beam diffraction (XRD) and Fourier Transform Infrared Spectroscopy (FTIR) investigation High Resolution Transmission electron microscope (HRTEM) and EDS. The level of dictated by MTT examine. The outcomes demonstrated that green synthesized silver nanoparticles inhibited proliferation of human lung disease cell line A549 with an IC_{50} esteem 72.65 µg/ml. The antimicrobial exercises of silver nanoparticles were checked against gram positive and gram negative strains utilizing in well diffusion technique. The antibacterial chlorophenicol as the positive control was completed. The outcome demonstrated the silver nanoparticles indicated effective movement against bacterial pathogens and cancer growth action.

Keywords: A549 cell line · MTT assay · Gram positive and gram negative bacteria · *Ledebouria revoluta* bulb extract

1 Introduction

Nanotechnology ways to deal with keep the sicknesses in people and regular products have as of late been expanding enormously and select the physiochemical exercises of nanosized metal particles make it fruitful in normal science and medication [1]. The different potential natural uses of nanoparticles have assumed a noteworthy job in the look for ecofriendly procedure of creating nanoparticles utilizing different biomaterials as the traditional synthetic union includes the utilization of dangerous solvents vitality and high weight which might be hurtful to the ecological fields [2]. Nanoparticles combination by restorative plants demonstrates more preferred standpoint they may improve the antibacterial action of silver nanoparticles in light of the fact that the therapeutically vital bioactive particles present stuck the plants may sticky situation on the outside of the nanoparticles and lessen the silver particles to AgNPs [3, 4]. The phytochemicals present in plant removes have been accounted for to make decrease of metal particles nanoparticles and in the long run devastate the utilization of poisonous synthetic

substances high weight temperature vitality and support of microbial societies [5, 6]. This green union of NPs utilizing phytocompounds as bio-reductants is accomplishing a more noteworthy catalyst [7].

Green combination of nanoparticles is a rising part of nanotechnology in which naturally generous materials like plant leaf concentrate, microbes and organisms these utilized for the synthesis [8]. Silver nanoparticles (AgNPs) have pulled in critical enthusiasm among the developing nanoproducts on account of their exceptional properties and expanding use for different applications in nanomedicine [9]. The silver nanoparticles have pulled in with significant enthusiasm because of their broad pertinence in various research fields, for example, science vitality, medication and catalysis. AgNPs were discovered the size extending from 30 to 60 nm. A silver nanoparticle at various focus was assessed for its antibacterial impact, against different pathogens. Hence silver NPs as an antimicrobial operator appear to be contrasted with antimicrobial, also, few reports show synergistic upgrade of action of anti-microbial with AgNPs. Presently the incorporated silver nano particles from natural items have been generally contemplated by different analysts [10].

The *Ledebouria revoluta* Jessop [Syn: Scillaindica (wight) baker or *Scilla hyacinthina* (Roth) J.F. Macbr and Drimiopsisbotryoids baker [syn: Drimiopsiskirkii baker] are Leafaceous species of the family Asparagaceae The Plant List 2013. Traditionally used medicinal plants have recently attracted the attention of pharmaceutical and scientific communities [11]. Cancer is a standout amongst the most life threating ailments in which deregulating expansion of strange cells attacks and upsets encompassing tissues [12]. Cancer is an all out malady in which the cell development is forceful and intrusive and metast ordinarily prompting demise [13]. Today caner is the biggest single reason for death is people and chemoprevention has been a promising anticancer methodologies went for lessening the dismalness and mortality of malignant growth by deferring the procedure of carcinogenesis [14].

The present examination was expected to green combination of silver nanoparticles utilizing bulb extract of *L. revoluta* against cytotoxicity A549 malignant growth cell lines. We have researched the antibacterial movement of integrated nanoparticles fundamental by well dispersion strategies. The impacts of nanoparticles on bacterial development have been additionally broke down by utilizing the base inhibitory fixation strategy.

2   Materials and Methods

2.1   Preparation of Plant Extract

The fresh bulb of *Ledebouria revoluta* gathered from Periyar University grounds. 20 gm of collected fresh bulb was added to 250 ml of refined water and bubbled for 15 min at 60 °C. The prepared aqueous extract was separated through Whatman No. 1 channel paper. The sifted concentrate was put away in cooler at 4 °C.

2.2   Synthesis of AgNPs

For synthesis of AgNPs, 50 ml of the aqueous bulb extract was added to 450 ml of 1 mm silver nitrate (AgNO3) solution. The blend was kept into dim condition at 24 h. The improvements of AgNPs were considered by visual perception of the shading change from light yellow to deep brown color.

2.3   Characterization of AgNPs

2.3.1   UV-Vis Spectroscopy

The synthesized AgNPs was established by sampling the aqueous component behind the reaction and the absorption maxima was scanned by T80 UV-Vis spectrometer at the wavelength of 200–800 nm.

2.3.2   FTIR Spectroscopy

In the FTIR spectrum, the samples were determined using the model of Perklin Elmer spectrum 1FTIR spectroscopy, sample range 500–4000 cm^{-1}.

2.3.3   XRD Analysis

The particle size and nature of the AgNPs were determined using XRD. This was carried out using diffraction meter, brucker, Germany model D8 advance model by 30 kV and 30 mA with Cu ka radians at 2 θ angle.

2.3.4   HRTEM Analysis

HRTEM (Model-Tecnai, G2 20 twin) was utilized to study the surface morphology and size of the integrated nanoparticles. For HR-TEM investigation, the example was set up by dissolving 2 mg of the nanoparticles in 10 ml of methanol by sonication process. Two drops of this arrangement were put on the carbon-copper matrices and were permitted to evaporate the dissolvable.

2.3.5   EDS Analysis

The energy dispersive X-ray spectroscopy was performed by a Bruker EDX spectrometer to determine the elemental composition of the samples.

2.4   Antibacterial Activity

The well diffusion method (Anonymous, 1996) was utilized to show the antibacterial properties. Different concentration of the extract (100 µg/ml) was set up by AgNPs. The test microorganisms were seeded into particular medium by spread plate strategy 10 µl (10 cells/ml) with the 24 h societies of microbes development in supplement stock. After hardening the channel paper wells (5 mm in distance across) impregnated with the concentrates were put on test living being seeded plates. Chloramphenicol (10 µg) utilized as standard for antibacterial test. The antibacterial test plates were hatched at 37 °C for 24 h. The distances across of the restraint zones were estimated in mm.

2.5 Cytotoxicity Activity

2.5.1 Cell Line

The human lung cancer cell line (A549) was obtained from National Centre for Cell Science (NCCS), Pune and grown in Eagles Minimum Essential Medium containing 10% fetal bovine serum (FBS). The cells were maintained at 37 °C, 5% CO2, 95% air and 100% relative humidity. Maintenance cultures were passaged weekly, and the culture medium was changed twice a week.

Cytotoxicity effect of the AgNPs was measured by the MTT assay [17, 18]. The cells were maintained in DMEM medium, added with 10% of bovine serum at 37 °C in humidity field atmosphere with 5% CO2%. The cells were plated in 96 well a flat bottom tissue culture plates at concentration of approximately 1×105 cell s/well and allowed to attach overnight at 37 °C. Then, the cells were incubated by different concentrations of the AgNPs bulb extract of *Ledebouria revoluta* for 48 h. After the incubation, the medium was redundant and 100 µl fresh medium was added with 5 µl of MTT assay (5 mg/ml). After 4 h, the medium added in 100 µl of DMSO to dissolve the Formosan crystals. Then, the absorbance was read at 570 nm in a microliter plate reader. The IC_{50} value was calculated.

2.5.2 Statistical Analysis

All the measurements were carried out in triplets and the results are expressed as mean ± SD using on way analysis (ANOVA) through SPSS software.

3 Results and Discussion

3.1 UV-Vis Spectroscopy

The aqueous of *L. revoluta* with watery arrangement of the nitrate (AgNo3) start to change the shading from yellow to darkish brown shading. It showed the development of AgNPs with decrease of silver particle. The assimilation groups were gotten at 472 nm (Fig. 1). The presence of the dark colored shading was because of excitation of the surface Plasmon vibrations. The arrangement of AgNPs was observed by UV-Visible spectroscopy in the 200–800 nm extend [15]. The result got for UV range for the AgNPs arranged from *P. maderaspatens* is root uncovered the most extreme retention was observed to be at 479 nm.

3.2 FTIR Spectroscopy

The FTIR spectroscopy estimation was concentrated to distinguish the conceivable biomolecules for the development and adjustment of AgNPs. The pinnacles showed up at 3209.55, 2926.01, 1622.13, 1527.62, 1217.08, 1014.56 cm^{-1} (Fig. 2). The solid assimilation tops at 3209.55 cm^{-1} uncovers the nearness of O-H extending liquor and phenol gathering. The pinnacle 2926.01 cm^{-1} maybe allotted to alkenes is clear from C-H extending the pinnacle seemed 1622.13 cm^{-1} was relegated to the extending C = O of gathering amide. The pinnacle acquired at 1527.62 cm^{-1} N-O extending in nitro gathering. The pinnacle got at 1217.08 cm^{-1} shows fragrant C-N. The pinnacle acquired at 1014.56 cm^{-1} compares to C-O extending ether gathering.
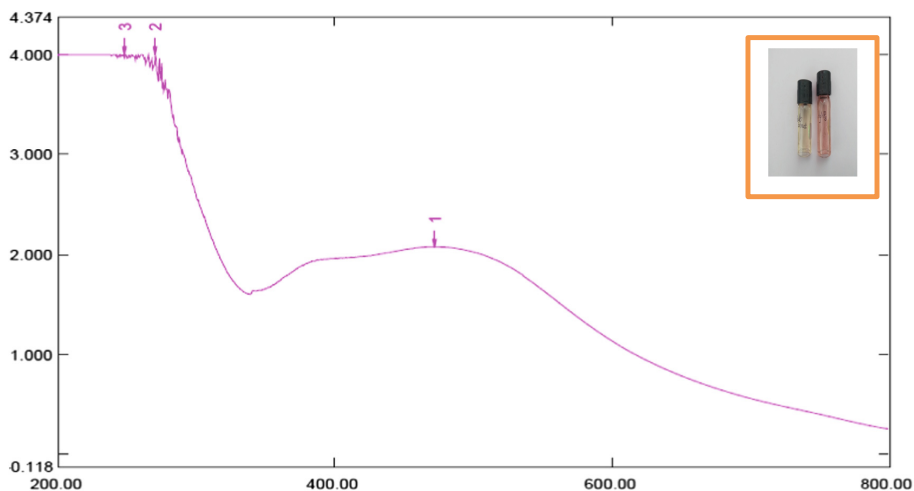
Fig. 1. UV-Vis absorption spectra of silver nanoparticle synthesized extract (AgNPs)
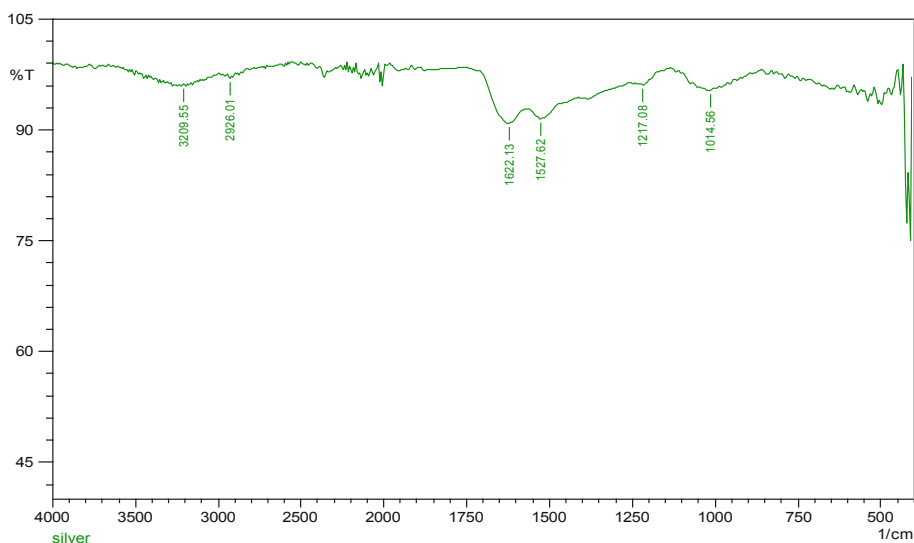
Fig. 2. FT-IR spectrum of silver nanoparticles synthesized by *Ledebouria revoluta* bulb part

3.3 XRD Analysis

The X-ray powder diffraction designs shows distinctive precious stone planes namely (210), (122), (111), (231), (142), (241), (220) and (311) of the nanometals, which relates to the crests with two theta esteems 27.91, 33.45, 46.56, 54.92, 57.32, 64.50, 77.32, same outcome uncovered (Fig. 3). Unidentified crystalline pinnacles (27.89, 32.30, 46.26, 54.79) are likewise clear in numerous works in which the XRD design incorporates the important 20 territory [16].
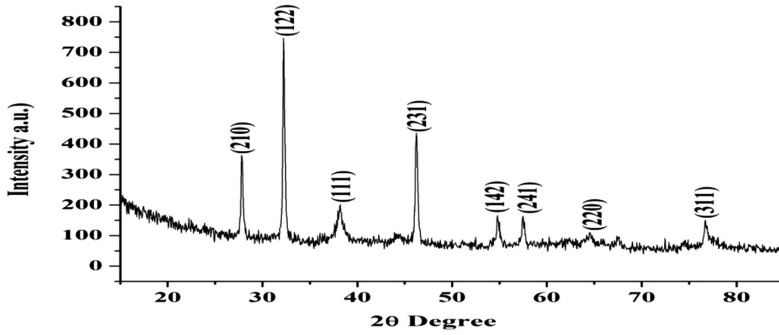
Fig. 3. X-ray diffraction patterns of synthesized AgNPs by *Ledebouria revoluta* bulb part

3.4   HRTEM and EDS

The morphology, measurement and circulation of the integrated nanoparticles were envisioned utilizing high goals transmission electron minuscule investigation. In the investigation dispersive spectroscopy (EDS) of the AgNPs the nearness of essential metal flag was affirmed (Fig. 5). HRTEM picture is the clear that the morphology of silver nanoparticles round shape (Fig. 4).The silver nanoparticles have circular geometry with a normal measurement of 18.05 ± 4.73 nm [17].
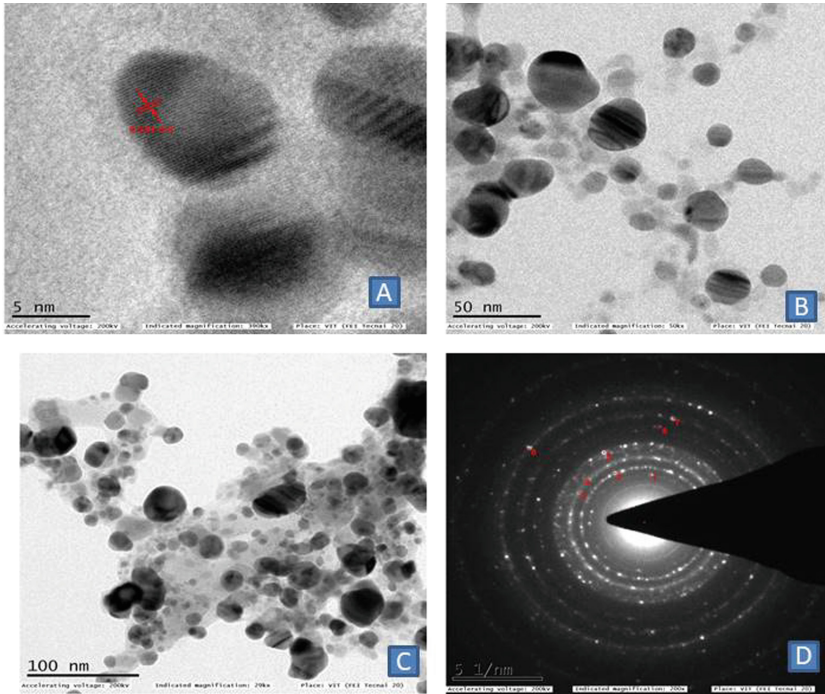
Fig. 4. High resolution transmission electron microscopic images of silver nanoparticles at different magnification. A-C size distribution histogram of TiO_2NPs and (D) SAED pattern.
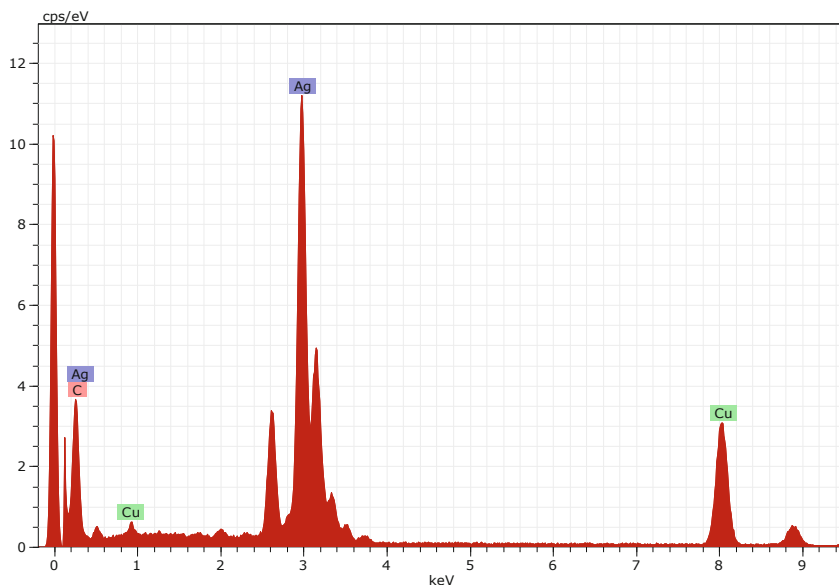
Fig. 5. EDS spectroscopy displays the purity and chemical composition of the AgNPs

3.5   Antibacterial Activity

The antibacterial activity test after effects of AgNo3 against various gram positive and negative microorganism were appeared Tables 1 and 2. Among utilizing three gram negative microbes the high restraint development in *Bacillus cerus* 5.66 ± 2.49 in 25hl (Fig. 6). In gram positive microorganisms the *Salmonella typhi* has been most astounding hindrance as 6 ± 2.44 in 25 μl. He revealed as the comparable outcome that the AgNPs has been great antibacterial movement [18].

Table 1. Gram positive bacterial activity of different concentration of Silver nanoparticles

S. no	Pathogenic bacteria	AgNPs extract Zone of inhibition (mm)				Standard (Chloramphenicol)
		10 μl	15 μl	20 μl	25 μl	
1	*Bacillus cerus*	0.33 ± 0.47	3.33 ± 1.24	3.66 ± 1.69	5.66 ± 2.49	3.66 ± 1.69
2	*Clostridium tetani*	2.33 ± 0.47	3.33 ± 0.94	3.33 ± 1.24	4.33 ± 1.88	3.66 ± 1.69
3	*Mycobacterium tuberculosis*	0.33 ± 0.47	1.66 ± 0.94	3 ± 1.41	4.33 ± 1.24	4.33 ± 2.05

Table 2.   G negative bacterial activity of different concentration of Silver nanoparticles

S. no	Pathogenic bacteria	AgNPs extract Zone of inhibition (mm)				Standard (Chloramphenicol)
		10 μl	15 μl	20 μl	25 μl	
1	Vibrio cholera	1.33 ± 1.24	2 ± 1.63	4 ± 1.4	4 ± 1.69	4.33 ± 0.94
2	Salmonella typhi	0.33 ± 0.47	2.66 ± 0.47	2.33 ± 1.24	6 ± 2.44	4.66 ± 1.24
3	Klebsiella nemoniae	0.66 ± 0.47	0.33 ± 0.47	2.66 ± 0.94	3.33 ± 1.24	5.66 ± 1.24
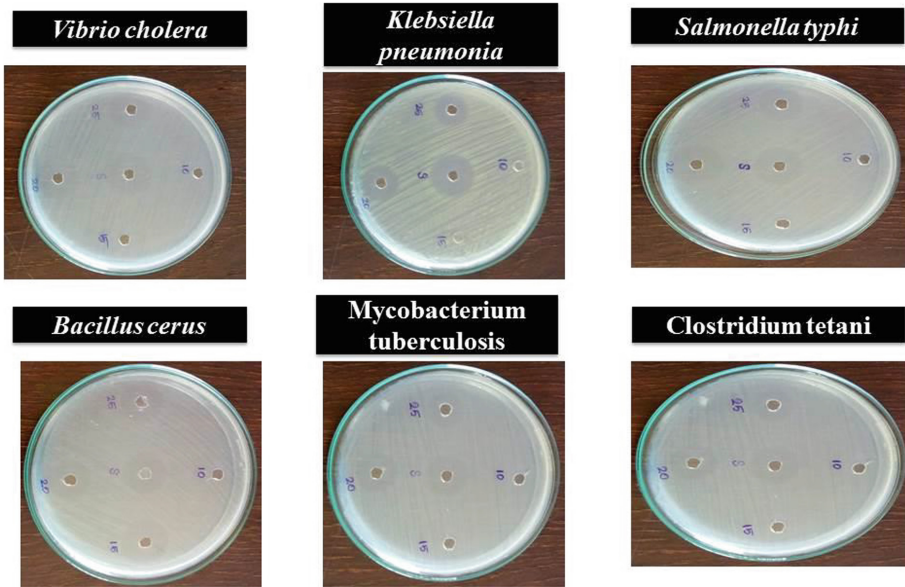
Fig. 6. Zone of inhibition of gram-negative bacterial strains using silver nanoparticles of different concentrations

3.6   Cytotoxicity Analysis of A549 Cell Line

The cytotoxicity of the AgNPs separate was against A549 cell line by MTT measure Fig. 7 demonstrate the cytotoxicity of AgNPs against A549 cell line. The cytotoxicity sway on cell development was inspected at various fixation (6.25, 12.5, 25, 50 and 100 µg) appeared in Table 3. The level of disease cell development restraint was observed to be high with the expanding the centralization of AgNPs the lC$_{50}$ for *L. revoluta* was recorded at 72.65 µg/ml against A549 cells at 100 µg focus (Fig. 7). Detailed the AgNPs remove A549 cell line utilizing *S. aromatium* AgNPS extract [19].

Table 3. AgNPs treated A549 lung cancer cells

Conc	6.25 µg	12.5 µg	25 µg	50 µg	100 µg	Cont
ABS	0.038	0.068	0.141	0.193	0.245	0.425
	0.034	0.065	0.143	0.192	0.247	0.422
	0.033	0.066	0.143	0.192	0.243	0.425
Avg	**0.035**	**0.066333**	**0.142333**	**0.192333**	**0.245**	**0.424**
					IC$_{50}$ value	**72.65 µg/ml**
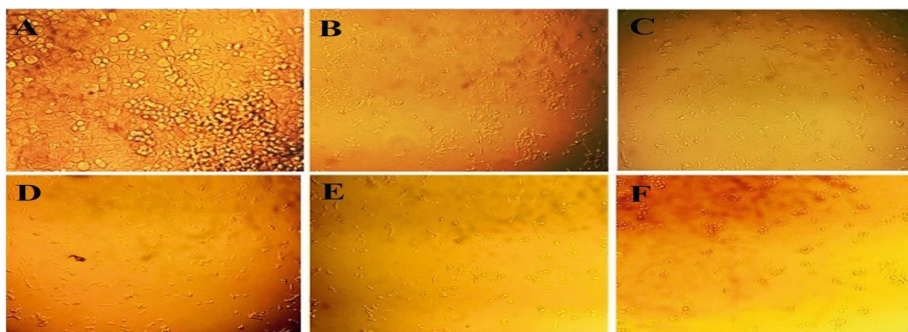
Fig. 7. Morphology of control and AgNPs treated A549 lung cancer cells. A. Control, B. IC_{50} Concentration (6.5 µg/ml), C. IC_{50} Concentration (12.5 µg/ml), D. IC_{50} Concentration (25 µg/ml), E. IC_{50} Concentration (50 µg/ml), F. IC_{50} Concentration (100 µg/ml).

4   Conclusion

Plant extract assisted green synthesis of silver nanoparticles. The synthesized silver nanoparticles were characterized viz., Uv-Vis, XRD, FTIR, TEM and EDS. Their biological significance was proven by efficient in bacterial activity and A549 cell line.

References

1. Jo, Y.K., Kim, B.H., Jung, G.: Antifungal activity of silver ions and nanoparticles on phytopathogenic fungi. Plant Dis. **93**, 1037–1043 (2009)
2. Singaravelu, G., Arokiyamary, J.S., Kumar, V.G., et al.: A novel extracellular synthesis of monodisperse gold nanoparticles using marine algae, Sargassum wightii Greville. Colloids Surf. B **57**(1), 97–101 (2007)
3. Popesucu, M., Velea, A., Lorinczi, A.: Biogenic production of nanoparticles. Dig. J. Nanometer Biostruct. **5**(4), 1035–1040 (2010)
4. Baruwati, B., Polshettiwar, V., Varma, R.S.: Glutathione promoted expeditious green synthesis of silver nanoparticles in water using microwaves. Green Chem. **11**, 926–930 (2009)
5. Jha, A.K., Prasad, K., Kulkarni, A.R.: Plant system: nature's nanofactory. Colloids Surf. B Biointer. **73**, 219–223 (2009)
6. Annamalai, N., Thavasi, R., Vijayalakshmi, S., Balasubramanian, T.: A novel thermostable and halostable carboxymethylcellulase from marine bacterium *Bacillus licheniformis*AUO. World J. Microbial. Biotechnol. **27**, 2111–2115 (2011)
7. Raj, M., Yadav, A.: Plants are potential synthesizer of precious matal nanoaprticles; Prograssand prospects. IET Nanobiotechnol. **7**(3), 117 (2013)
8. Krishnaraj, C., Jagan, E.G., Rajasekar, S., Kalaiselvan, P.T., Mohan, N.: Synthesis of silver nanoparticles using *Acalypha indica* leaf extract and its Antibacterial activity against water borne pathogens. Colloids Surf. B Biointer. **76**, 50–56 (2010)
9. Muleva, E., Ahmed, A.S., Sipamla, A.M., Mtunzi, F.M.: Free radical scavenging and antibacterial activity crude extracts from selected plants of medicinal value used in Zululand. Pak. J. Nutr. **13**(1), 38–42 (2014)

10. Gennari, C., Castoldi, D., Sharon, O.: Natural products with taxol like anti-tumor activity: synthetic approaches to eleutherobin and dictyostain. Pure Appl. Chem. **79**, 173–180 (2007)
11. Guarino, M., Rubino, B., Ballabio, G.: The role of epithelical mesenchymal transition in cancer pathology. Pathology **39**, 305–318 (2007)
12. Kaufman, S.H., Earnshaw, W.C.: Induction of apoptosis by cancer chemotherapy. Exp. Cell Res. **256**, 42–49 (2000)
13. Santhosh, S.B., Ragavenderan, C., Natarajan, D.: Spectral and HRTEM analyses of Annona muricata leaf extract mediated silver nanoparticles and its Larvicidal efficacy against three mosquito vectors Anopheles stephensi, Culex quinquefasciatus, and Aedes aegypti. J. Photochem. Photobiol. B: Biol. 1011–1344 (2015)
14. Kumar, R., Roopan, S.M., Prabhakaran, A., Khanna, V.G., Chakroborty, S.: Agricultural waste Annona squamosalpeel extract, biosynthesis of silver nanoparticles Spectro chim. Acta Part **90**, 173–176 (2012)
15. Francis, S., Joseph, S., Koshy, E.P., Mathew, B.: Synthesis and characterization of multifunctional gold and silver nanoparticles using leaf extract of Naregamia alata and their applications in the catalysis and control of mastitis. New J. Chem. **41**, 14288–14298 (2017)
16. Venugopal, K., Rather, H.A., Rajagopal, K., Shanthi, M.P., Sheriff, K., Llliyas, M., Manikandan, E., Uvarajan, S.: Synthesis of silver nanoparticles (AgNPs) for anticancer activities (MCF 7 breast and A549 lung cell lines) of the crude extract of Syzygium aromaticum. J. Photochem. Photobiol. B: Biol. **167**, 282–289 (2017)
17. Mosmann, T.: Rapid colorimetric assay for cellular growth and survival: application to proliferation and cytotoxicity assays. J. Immunol. Methods **65**, 55–63 (1983)
18. Monks, A., Scudiero, D., Skehan, P., Shoemaker, R., Paull, K., Vistica, D., Hose, C., Langley, J., Cronise, P., Vaigro-Wolff, A., Gray-Goodrich, M., Campbell, H., Mayo, J., Boyd, M.: Feasibility of high flux anticancer drug screen using a diverse panel of cultured human tumour cell lines. J. Nat. Cancer Inst. **83**, 757–766 (1991)

Precision Medicine: A Personalized Treatment from Your Gene

P. K. Balasubramani[1(✉)], K. Preetha[1], and M. Aswanth Harish[2]

[1] Innov4Sight Health Care and Biomedical Systems Private Limited, Bengaluru, KA, India
balasubramanipk@gmail.com

[2] Department of Biotechnology, Sri Venkateswara College of Engineering, Chennai, TN, India

Abstract. Poor healthcare linked to 5 million annual death worldwide. Health is increasingly shaped by ageing populations, urbanization and globalization of unhealthy lifestyles, resulting in a transition in the burden of health care towards non communicable diseases, mental health and injuries. Many of these conditions are chronic, requiring long-term care, with patients commonly suffering from multi-morbidities, all of which adds to escalating health care costs. Precision medicine (PM) is a new approach to health care that matches individual patients with targeted treatments that work best for each them. PM is still in its infancy, but holds so much promise for the healthcare industry which considers genetic variations, environment and lifestyle. There would be global shift in the treatment modalities where people are moving towards pharmacogenomics which takes into consideration of the individual drug response to how body metabolize it helping in catering the patients with minimal Adverse Drug Reaction (ADR). Another field which is showing promise in the healthcare industry is wearable bio-services for better health and disease management. PM has roadblocks to clear before it hits the market clinician acceptability, pharma industry to cater drug to small population, developing diagnostic tests with sufficient sensitivity and specificity and having string regulatory mechanism to ensure clinical validity to the tests.

Keywords: Biomarker · Gene · Genome · Metabolome · Microbiome · Pharmacogenomics · Phenotype · Polymorphism

1 Introduction

Precision medicine (PM) is the emerging disease treatment approach in the last couple of decade moving towards personalization and evidence-based medicine. The tailor made treatment strategy in the future would not only take in to consideration of the genomic variations but also other contributing factors like gender, age, geography, race, family history, immune profile, metabolic profile, microbiome, environment vulnerability and set of circumstances [1]. The benefit of the PM on the patient's perspective is immense establishing personalized health plan and drastically saving the healthcare cost incurred and significantly reducing any adverse reaction from the drug. The approach of treating patients in PM is completely based on the variation in the

genomic read out towards susceptibility for illness and also for the ability of the patient responding to drug metabolism [2]. An personalized approach of this sort would help to cut down to medical cost treating the patient and to provide better care with increased efficacy. Through sequencing of many patient who can be grouped into similar category which in turn would reduce the cost, duration for carrying out clinical trial and early release of the drug to the market [3].

Through omics based approaches (Genomics, Proteomics, Transcriptomics, metabolomics, Epigenomics) data are initially segregated through patient's biopsy and integrated to create a unique molecular profiles corresponding to an individual. Sequenced DNA is reserved in cloud computing Block chain Technology where AI play a vital role by integrating the sequence with large number of reference sequences and seek for polymorphism and Biomarker. These profiles are then challenged with previously defined disease profiles to seek biomarkers, omics signatures or network/pathway signatures that can guide the selection of treatment [4]. Based on those assays and data analysis drug is prescribed, to improve the chance of successful treatment and reduce the probability of side effects. Being an emerging field in healthcare which promises to make treatment modalities cost effective has been well supported by key technologies making it possible for its remarkable rapid growth [5]. The Nano pore based sequencing (fourth generation DNA sequencing technology) are accurate, fast and reliable and the entire genome can be sequenced for less than $1000 with timeline less than a day. High-performance computer systems too have played in key role in analyzing massive genomic data (~ 1.5 GB) which fosters early genome drug discovery. Modern bench top sequencers allow independent researchers run in small laboratories; allowing rapid and efficient sequencing solutions. Many global players are setting up large scale genomic repositories across various countries to analyze genetic polymorphism for various diseases and well the accepted by general population by active a participation in the genomic projects. At clinics the Clinical Decision Support System (CDSS) also been playing key role helping physicians to make quick concrete decision towards the treatment with relevant information. Cloud computing services has been providing the valuable boost by offering cloud based bioinformatics suites and genomic processing services. Machine learning and big data analytics have come handy to see beyond traditional data sets, gives a more specific picture of an individual's health reducing individuals. And newer technologies like Blockchain also functions as a good auditing tool by securing patient genomic data. Mobile apps/wearables are bridging the gap in providing real time follow-up data from the patients.

The new horizons of the Precision medicine have lot of wide potential benefits helping the medical professionals and the patients by preventing, diagnosing, managing and treating a wide range of diseases. The new approaches of PM reduce the adverse side effects of drug by the traditional methods. The drugs can be improvised by designing them specifically to the patients [6]. Hence, time consuming for the trials and treatment is reduced. Moreover, the patients with rare undiagnosed diseases are cured to a certain extent by PM. The respective treatments for those conditions can be predicted. Also, the understanding of the roots of certain diseases can be traced out well. The patients will be provided with individualized patient care. There will be less practice of trial and error prescribing, because patient safety plays a pivotal role. The

efficacy of the treatment modality is improved by targeting the response rate and in the overall survival The Electronic Health records of the patients can be easily accessed by the doctors and patients. PM uses the health care resources wisely by reducing expensive costs and more efficient clinical trials in Research and Development. The informed decisions will be made properly with the help of PM. Due to the better targeted therapies for the patients, the probability of desired outcomes is very high. The onset of any diseases can be traced back.

PM being an emerging field is also presented with unique set of challenges where in interpretation genetic polymorphism/variation remains a challenge across the study population. Any drug in the body is metabolized is determined by multiple set of genes interacting with each other. Analyzing and interpretation of the variation SNPS is time consuming and tedious process. The translation of PM from research to clinical adoption lacks awareness among the patients towards personalized therapies and even many healthcare organizations do not yet have formal plans to use genomics or advanced data for personalized patient care has been huge drawback in translating PM at the clinical level. The regulatory pathway for personalized medicine is still in its infancy as there is no clear roadmap for laboratory-developed tests (LDTs) [7].

2   The Role of Artificial Intelligence in Precision Medicine

The very foundation of precision medicine is strongly supported by various AI based algorithm such as deep learning, natural language processing, and machine learning to deal with the high dimensional data to make clinically viable decisions [8]. Current treatment modalities by physicians across the globe still rely on their experience, judgement, and problem-solving skills while using rudimentary tools and limited resources during treatment. Artificial Intelligence [AI] would assist in analyzing large & complex data set in real-time; wherein support coming from the high end computational power to draw meaningful conclusion supporting the physician community for effective treatment and lowering the risk of adverse drug reaction. The main objective of Precision medicine is based on the grouping of patients based on their disease susceptibility, diagnostic/prognostic information, and treatment response [9]. Complex algorithms, digital health applications and 'Omics'-based tests are the three types of precision medicine to be emerged in clinical practice. The influence of biomarkers, artificial intelligence-based technologies maintain the investment in health care. AI-based technologies will be converting the images to develop algorithms that incorporate scan results into more accurate information. Some of the key benefits to the diseases community is the ability of the AL based deep learning models to achieve higher accuracy of disease risk prediction. It a valuable tool in the detection of cancerous tumor growth from the scanned images in a very period of time interval [10]. Storage if omics data over the cloud and integration of records have tremendously benefited the patients. AI approach towards PM has revolutionized cancer screening and real-time monitoring, and improve the reduction of adverse events and improved patient outcomes. Other areas of application of AI include are drug discovery and gene-editing using CRISPR–Cas9 technology. Recent mobile health markets are flooded with wearables and the internet of things (IoT). Deep learning algorithms have been

shown to make diagnoses at least as well as physicians in cardiology, dermatology, and oncology. The Potential of AI immense where-in back then in 2016 Atomwise able to identify effective drugs for Ebola infectivity in matter of day time [11]. Other specific application of AI in PM include variant calling, interpretation and reporting. In Variant calling the genomic variants coming from the NGS data are analyzed by aligning the read-out sequence with the reference genome. In the process of interpretation any novel variants observed in the read-outs are used a crucial biomarker in the clinical care of the patients and treatment planning. In future the AI can independently analyze the data and draw meaningful conclusion as well disease correlation and actively support the physician community.

3   Global Initiatives

The countries which have initiated precision medicine are United States, United Kingdom, France and Japan. "All of us" a PM initiative started at US in the year 2016. The primary objective is to improve health research and medical breakthroughs, enabling individualized prevention of diseases and its treatment, and care for all the Americans. This goal will be met by nurturing relationships with 1 million participants, developing a large and rich biomedical dataset, and improve the ecosystem of researchers and funders to use and support the system. $130 million was allocated to NIH to develop a cohort-National extensive research contributor group and $70 million was allocated to the National Cancer Institute to lead efforts in cancer genomics as part of PMI for Oncology. In UK, "100,000 Genomes" established in December 2012. The main aim is to benefit the people in health care system of UK. The second goal is to initiate the development of a UK genomics industry by creating the space, potential, and bequest of precision medicine in the United Kingdom. Genomics England will pay £78 million for Illumina to carry out the genetic sequencing, and the company will invest £162 million in the country over the next 4 years. In France "The French plan for genomic medicine" was started in April 2015. The sequencing should be implemented in every clinical practice. The French patients who suffer from rare or common diseases, cancer etc. should be getting easy access to the genomic medicine along with the people who are concerned to the patients by 2025. The second objective is to develop a national genomic sector in which France should be placed among all the leading countries in the field of genomic medicine within next 10 years. The budget is 670 million euro. "Initiative on rare and undiagnosed diseases" is an initiative from Japan started in June 2015 works on the patients who have rare diseases, which was not be diagnosed because of paucity of proficiency and capital. They aim for the better life for those patients and the budget is 6 million USD. "World Economic forum" took precision medicine initiative in March 2017 at San Francisco. This project is aimed at developing protocols that improves the benefits of emerging technologies by minimizing the risks to societies. The project has nine programs; they are Artificial Intelligence and Machine Learning, Blockchain, Future of Drones and Tomorrow's Airspace, Future of Urban and Autonomous Mobility, Internet of Things and Connected Devices, Digital Trade and Cross-Border Data Flows, Environment and the Fourth Industrial Revolution, Future of Production and Precision Medicine [12].

4   Future of Precision Medicine

Future treatment for any disease would take into consideration of complete genome sequence and in-the future would be default test for the patients. The lack of early treatment for most of the hereditary diseases would be addressed in the future by PM [13]. The role played many genetic determinants towards a disease can be ascertained. There has been an ever increase in the interest in the general population to use wearable to monitor health in real time [14]. In precision medicine arena it has been flourished with implantable biosensors. Advances in the fields of electronics and micro fabrication techniques have caused increased interest in the use of implant-able medical devices in precision medicine. These devices have uncanny ability to provide real-time and continuous data points based on the analyte of interest with the need for intervention of the physicians and patients community. Few of the commonly used wearables are insulin pump for Type I diabetes; BioScarf an air filtration device for to reduce the risk of respiratory disorder; Body guardian heart to monitor cardiac arrhythmias etc. [15]. A better antibiotics of choice for treatment for during serious illness like sepsis; medication with fewer drug side effects as PM would eliminate to make any guess work towards the treatment. Drug metabolism is based not only on our genetic makeup; it is also affected by many factors, such as epigenetics, exposure, body size, and age. Pharmacogenomics procedure can improve patient safety, health outcomes, and decrease overall health care costs so that the right drugs will be given to the right patients [16]. This strategy may also provide an opportunity to advance the field of pharmacogenomics by collecting data on genetic testing results and drug effectiveness, including costs of therapy and avoiding adverse events. Specific diagnosis for cancer are already been undertaken only post accessing the gene expression level of the key protein (HER2 in breast cancer). The future of PM towards healthcare looks very promising and would be highly impactful on the patient community [13].

5   Challenges of Precision Medicine

The medical fraternity is been challenging to deliver the best available treatment benefiting the patients but the same advancement in technology like PM is not easy to adapt straightaway replacing the tradition knowledge based medicine [14]. The identification of each disease must be linked to highly specific biomarker to make a strong genetic predisposition in the identification of disease using the modern sequencing platform. Association of biomarker(s) to a disease is daunting task for which genomic sequence across large population has to be sequenced and global key players are playing a major role in setting up large genome project. We still lack robust genomic sequence analytical tools and supplementary tools like that assist in accurate determination of drug stability, bio-distribution and immune response post administration of the drug of interest. The field of precision medicine since being very naive has ever more hurdles to cross [17]. For PM to be outreach solutions for any treatment modality has to have a novel strategy and solution to make in more meaningful and useful to global patient community. The Precision Medicine Initiative is found to raise ethical, social, and legal issues because of its consequences. The sequencing of the several

patients would be an expensive affair and also make a use full interpretation would be a tedious task for the health care initiatives. The data of the patients has to be protected to safe guarded is also can crucial task [18]. Currently there is no standardized format in analyzing the genomic data coming from the various sequencing machines available in the market. A clear-cut data-processing software for diseases marker are still not applied in practical use. The conversion of these basic medical research findings into clinical practice is an obstacle for precision medicine. The public must also play a key role in the due participation to providing biological samples which would be beneficial for the generations to follow. Evaluation of the disease solely through genetic testing parally raised many ethical hurdles and there is also a need to establish specific guidelines [16]. Genomic data analysis has been the key missing link in the chain in the PM approach for curing the patients because of the challenges faced in data acquisition and its meaningful interpretation. A strong support system coming in from the government agency would drastically improve the early stage innovations by sharing the clinical findings.

6 Conclusion

Precision medicine are already been in the limelight being publicly available at a time where patient satisfaction on disease treatment with reduced incidence of adverse effects is considered primed important to ensure better quality of life. With the support coming in the way from sequencing technology platform, data analysis, supercomputing facility, regulatory body. PM is nicely shaping up be the go-to future disease treatment methodology taking over the conventional medicine.

References

1. Kalaitzopoulos, D.: The potential of precision medicine. New Horizons Transl. Med. **3**, 63–65 (2016)
2. Kwon, H., Jung, E.-Y.: The impact of policy on the growth of precision medicine. Healthy Policy Technol. **7**, 347–357 (2018)
3. Islamaj Doğan, R.: Overview of the BioCreative VI precision medicine track: mining protein interactions and mutations for precision medicine. Database (Oxford) (2019). https://doi.org/10.1093/database/bay147
4. Roukos, D.H.: Clinical cancer genome and precision medicine. Ann SurgOncol. **19**(12), 3646–3650 (2012)
5. Rebecca, L.: Cancer Statistics. CA Cancer J. Clin. (2018). https://doi.org/10.3322/caac.21442
6. Mesko, B.: The role of artificial intelligence in precision medicine. Expert Rev. Precis. Med. Drug Dev. **2**(5), 239–241 (2017)
7. Knowles, L.: Paving the road to personalized medicine: recommendations on regulatory, intellectual property and reimbursement challenges. J. Law Biosci. **4**, 453–506 (2017)
8. Awwalu, J., Garba, A.G., Ghazvini, A., Atuah, R.: Artificial intelligence in personalized medicine application of ai algorithms in solving personalized medicine problems. Int. J. Comput. Theory Eng. **7**(6), 439–443 (2015)

9. Williams, A.M., Liu, Y., Regner, K.R., Jotterand, F., Liu, P., Liang, M.: Artificial intelligence, physiological genomics, and precision medicine. Physiol. Genom. **50**(4), 237–243 (2018)

10. Barker, R.W.: Is precision medicine the future of healthcare? Pers. Med. **14**(6), 459–461 (2017)

11. Bartlett, G., Rahimzadeh, V., Longo, C., Orlando, L.A., Dawes, M., Lachaine, J., Bochud, M., Paccaud, F., Bergman, H., Crimi, L., Issa, A.M.: The future of genomic testing in primary care: the changing face of personalized medicine. Pers. Med. **11**, 477–486 (2014)

12. Advancing Disease Modeling in Animal-Based Research in Support of Precision Medicine: Proceedings of a Workshop, National Academies Press (US). https://www.ncbi.nlm.nih.gov/books/NBK507215/#sec_31. Accessed 30 May 2018

13. Chang, L.-C., Colonna, T.E.: Recent updates and challenges on the regulation of precision medicine: the United States in perspective. Regul. Toxicol. Pharmacol. **96**, 41–47 (2018)

14. Conti, R., Veenstra, D.L., Armstrong, K., Lesko, L.J., Grosse, S.D.: Personalized medicine and genomics: challenges and opportunities in assessing effectiveness, cost-effectiveness, and future research priorities. Med. Decis. Making **30**(3), 328–340 (2010)

15. Gray, M., Meehan, J., Ward, C., Langdon, S.P., Kunkler, I.H., Murray, A., Argyle, D.: Implantable biosensors and their contribution to the future of precision medicine. Vet. J. **239**, 21–29 (2018)

16. Malod-Dognin, N., Petschnigg, J., Pržulj, N.: Precision medicine - a promising, yet challenging road lies ahead. Curr. Opin. Syst. Biol. **7**, 1–7 (2018)

17. Korngiebel, D.M., Thummel, K.E., Burke, W.: Implementing precision medicine: the ethical challenges. Trends Pharmacol. Sci. **38**(1), 8–14 (2017)

18. Love-Koh, J., Peel, A., Rejon-Parilla, J.C., Ennis, K., Lovett, R., Manca, A., Taylor, M.: The future of precision medicine: potential impacts for health technology assessment. PharmacoEconomics **36**, 1439–1451 (2018)

Ultrasonic Studies on Molecular Interaction and Their Excess Properties of Ternary Liquid Mixtures of 2-Nitroanisole and 1-Propanol in n-Hexane at Different Temperatures 303, 308 and 313k

J. Edward Jeyakumar[1(✉)], S. Chidambara Vinayagam[1], and J. Senthil Murugan[2]

[1] PG and Research Department of Chemistry, Presidency College, Chennai 600005, Tamil Nadu, India
edwardchemistry@gmail.com
[2] Department of Chemistry, S.I.V.E.T College, Gowrivakkam, Chennai 600073, Tamil Nadu, India

Abstract. The behavior of liquid mixture of 2-Nitroanisole, 1-Propanol and n-Hexane as a function of temperature and composition has been investigated by measuring ultrasonic velocity in conjunction with density and viscosity at 303, 308 and 318 K for frequency 2 MHz using ultrasonic interferro meter. With the help of the measured values ultrasonic velocity (u), viscosity (η) and density (ρ), the acoustical parameters like acoustic impedance, adiabatic compressibility, free length, free volume and internal pressure has been calculated, in order to know the molecular interaction between the component in the ternary liquid mixture and the nature and strength of molecular interaction in the component of the ternary mixture, the actual values of acoustical parameters were computed in to their excess properties. Excess ultrasonic velocity (U^E), excess acoustic impedance (Z^E), excess intermolecular free length (L_f^E) excess adiabatic compressibility (β^E), excess free volume (V_f^E) and excess internal pressure have been calculated for the ternary liquid mixtures containing 2-Nitroanisole, 1-Propanol in n-Hexane at various temperatures 303, 308 & 313 K at fixed frequency 2 MHz, for different concentrations ranges from 0.001 M to 0.01 M and fitted to the Redlich-Kister polynomial equation. The computed excess values were plotted against the concentration of ternary liquid of the mixture at different temperatures 303, 308 & 313 K at a fixed frequency of 2 MHz. A good agreement has been found between the experimental and calculated values of the ultrasonic velocity. The strength and the nature of the interactions between like and unlike molecules have been discussed in terms of dipole-dipole, dipole-induced dipole, induced dipole-induced dipole interaction through hydrogen bonding.
.

Keywords: Acoustical parameters · Complex formation · Dipole-dipole · Excess properties · Interaction · Ternary liquid and ultrasonic studies

1 Introduction

The measurement of ultrasonic speed in liquid mixture enables accurate determination of some useful acoustical parameters and their excess values which are highly sensitive to molecular interactions in their mixtures, the intermolecular forces of liquid in a mixture shows a considerable effects on the physical-chemical properties [1–5]. Ultrasonic measurements are very useful in chemical & food processing; material testing under water ranging and cleaning. These studies are also extensively used in textile industry, leather Industry and pharmaceutical industry.

In recent years, the sound velocity measurements are very useful in the technology of polymers to understand polymer solvent, polymer interactions, structure of polymers. Ultrasonic studies provide a wealth of information about the liquid state. It explains the many of the properties of individual liquids and combination of the liquids. Extensive studies of ultrasonic velocity in liquids, liquid mixtures and their interpretation in the light of molecular structure has gained much importance during the last three decades [6–10].

Ultrasonic velocity and related data of liquid mixtures are found to be the most powerful tool in testing the theories of the liquid state. In addition, ultrasonic velocity data can be utilized to deduce some useful properties of liquid mixtures which are not easily accessible by other means. Ultrasonic velocity is one of the powerful probes for characterizing the physic-chemical properties of liquid mixtures.

Molecular interaction is associated with 1-alkanol hybrids, which are one of the most unique components since the alkanol group is very polar, because it is deeply with other groups that attraction of polar ends. 2-Nitroanisole is an organic compound and yellowish aromatic oil. Since Methoxy group present in 2-Nitroanisole is an ortho and para directing it strongly affects the pi electron cloud of benzene ring which renders the ring more electron rich. Industrial usage of Nitroanisole is immense, it's a reagents, catalyst in organic chemical reaction in manufacturing sectors since the author taken up Nitroanisole is one of the components in the present investigation.

Alcohols are associated organic liquids and are widely used as basic organic compounds for the synthesis of other organic compounds. Branching of the alkyl group attached to the hydroxyl group results in abnormal behaviour of alcohols. In this present study, it reports the excess ultrasonic velocity (U^E), excess acoustic impedance (Z^E), and excess intermolecular free length (L_f^E) for ternary mixture 2-Nitroanisole, 1-Propanol and n-Hexane at various temperatures viz., 303, 308 and 313 K at constant frequency 2 MHz. With the aim of analyzing the disruption of self association in 1-Propanol and the breaking of the dipole-dipole interactions of 2-Nitroanisole along with the interaction between the hydroxyl group of alcohol molecule in n-hexane is a good non polar solvent.

In this present study, ultrasonic velocity, density and viscosity have been measured for the ternary liquid mixtures of 2-Nitroanisole and 1-Propanol in n-Hexane at different temperature, from the measured values the molecular interaction and excess properties have been discussed in terms of possible interactions of the ternary mixtures.

2 Materials and Methods

A Single crystal Ultrasonic pulse echo Interferometer (Model F-81) manufactured by Mittal Enterprises working at 2 MHz was used to measure the sound velocity of a liquid mixture. The ultrasonic velocity had an accuracy ±0.01 m/s. Water at desired temperature is circulated through the outer jacket of the double-walled measuring cell containing the experimental liquid. To determine viscosity of liquid, Ostwald Viscometer is used and a stop watch of accuracy in milli seconds is selected to note the time of flow of the liquid. Specific gravity bottle is employed to determine density of liquid and the weight of the liquid is determined by using single pan electronic balance capable of measuring up to 0.5 mg.

The liquid mixtures of various concentration (0.001–0.010 M) of 1:1 ratio of 2-Nitroanisole,1-Proponal in n-Hexane were prepared by taking AR grade chemicals, which were purified by standard methods, ultrasonic velocity have been measured using an ultrasonic interferometer working at frequency 2 MHz. All precautions were taken to minimize the possible experimental error, the set up was checked for standard liquids

3 Theoretical Aspect

The following acoustical and thermodynamics parameters were calculated:

1. Adiabatic compressibility (β) has been calculated from the ultrasonic velocity (U), and the density (ρ) of the medium using the Newton- Laplace equation [9] as follows:

$$\beta = 1/U^2\rho \tag{1}$$

2. Intermolecular free length (L_f) has been determined as [10] follows:

$$L_f = K_T\beta^{1/2} \tag{2}$$

Where K_T is the temperature – dependent constant known as Jacobson's constant ($K_T = 2.131 \times 10^{-6}$ at 318 K), and β is the adiabatic compressibility.

3. Free volume (V_f) in terms of ultrasonic velocity (U) and the viscosity (η) of liquid [11] is as follows:

$$V_f = (M_{eff}U/k\eta)^{3/2} \tag{3}$$

Where M_{eff} is the effective molecular weight of the mixture ($M_{eff} = \Sigma m_i X_i$, where m_i and X_i are the molecular weight and mole fraction of individual constituents, respectively), k is temperature independent constant which is equal to 4.281×10^9 [12] for all liquids

4. Internal pressure ($\prod_i$) can be calculated using the relation [13] as follows:

$$\prod_I = bRT(k\eta/U)^{1/2}\left(\rho^{2/3}/M_{eff}^{7/6}\right) \tag{4}$$

Where b stands for cubic packing, which is assumed to be 2 for all liquids, k is a dimensionless constant independent of temperature and nature of the liquids, its values is 4.281×10^9. T is the absolute temperature in Kelvin, M_{eff} is the effective molar weight, R is the universal gas constant, η is the viscosity of the solution in Nsm^{-2}, U is the ultrasonic velocity in ms^{-2} and ρ is the density in kgm^{-3} of solution.

5. The Gibbs free energy can be determined using the relation as follows:

$$\Delta G = k_B, T. \ln(k_B.T.\tau/h) \tag{5}$$

Where τ is viscous relaxation time, T is the absolute temperature, k_B is Boltzmann's constant, and h is Planck's constant.

6 Acoustic impedance (Z) is given as follows:

$$Z = U.\rho \tag{6}$$

Where U and ρ are the ultrasonic velocity and density of the mixture, respectively.

3.1   Excess Values

The excess values can be determined by using the general formula;

$$A^E = A_{exp} - A_{ideal} \tag{7}$$

Where $A_{id} = \Sigma A_i X_i$, A_i is any acoustic parameters and X_i mole fraction of the liquid component.

The Excess Free Volume (V^E) is the difference between mean molar volume and the average volume is calculated using the given formula:

$$V^E = V - (V_1X_1 + V_2X_2) \tag{8}$$

Where, V_1 and V_2 are the mean molar volumes of pure liquids 1&2 respectively.

The Excess Adiabatic Compressibility (β_{ad}^E) can be calculated the difference between adiabatic compressibility and the sum of the fractional contributes of the two liquids is given,

$$(\beta_{ad}^E) = (\beta_{ad}) - ((\beta_{ad})X_1 + (\beta_{ad})X_2) \tag{9}$$

Where, $(\beta_{ad})X_1$ and $(\beta_{ad})X_2$ are the individual (β_{ad}) values of pure liquid in the mixtures at constant Temperature.

The excess viscosity (η^E) can be calculated difference between viscosity (η) and the sum of the fraction contribution of the liquids are given by Fort and Moore is:

$$(\eta^E) = (\eta)_{mix} - (\eta)_1 X_1 + (\eta)_2 X_2) \tag{10}$$

Where, $(\eta)_{mix}$, $(\eta)_1$ and $(\eta)_2$ are the individual viscosity values of pure liquid in the mixture and viscosity of mixture.

The Excess Mean Free Length (L_f^E) at concentration is the difference between mean free length and sum of the fraction contribution of the two liquid are given by:

$$\left(L_f^E\right) = L_f mix - (L_{f1} X_1 + L_{f2} X_2) \tag{11}$$

Where L_{fmix}, L_{f1} and L_{f2} are the individual mean free length values of pure liquid in the ternary mixtures and mean free length of mixture.

Specific Acoustic Impedance (Z) is also calculated using the below relation:

$$Z = \rho U \tag{12}$$

Excess Acoustic Impedance (Z^E) is difference between the ideal acoustic impedance and acoustic impedance of the pure components i.e.

$$\left(Z^E\right) = Z_{real} - Z_{ideal} \tag{13}$$

Finally, the Excess Velocity (U^E) is difference between the ideal velocity and velocity of the pure components.

$$U^E = U_{real} - U_{ideal} \tag{14}$$

4   Results and Discussion

The present investigation involves the application of ultrasonic velocity measurement to determine the type of molecular interaction in n-Hexane solution containing 2-Nitroanisole and 1-Propanol at various temperature. Ultrasonic velocity measurement coupled with density and viscosity determination has been used in the calculation of certain acoustical parameters. A study of excess value is used to determine more information about the type of interaction.

The comparison of density, viscosity and velocity of pure substance of the ternary liquid mixture of 2-Nitroanisole, 1-Propanol and n-Hexane at 303, 308, 313 K with the literature values are given in Table 1, given values has been used in determination of excess properties of the present ternary mixtures.

The experimentally measured values of ultrasonic velocity, density and viscosity for the ternary liquid mixture (2-Nitroanisole + 1-Propano + n-Hexane) at 303 K, 308 K and 313 K are tabulated in Table 2. The calculated excess values of ternary mixture, excess acoustic impedance, excess ultrasonic velocity, excess free volume,

excess internal pressure, excess adiabatic compressibility and excess free length are depicted in Tables 4 and 5 respectively.

From Table 2, by the obtained value of ultrasonic velocity, its observed that it is increased with concentration with respect to temperature, whereas density and viscosity found to decrease with increasing concentration of the ternary mixture, however ultrasonic velocity, density and viscosity decreases in all cases as temperature is increased, the same is plotted and presented in Figs. 1, 2 and 3 (Figs. 4, 5, 6, 7, 8 and 9).

The nature and the strength of molecular interaction in the mixtures were explained based on the variation of ultrasonic velocity and related acoustical parameters with the change in composition of the component of the pure liquids. In the present study, a linear variation in ultrasonic velocity has been noticed, a linear variation in terms of increase with change in composition of the ternary liquid mixture indicates absence of complex formation which is observed from variation of velocity from Table 2. Increasing velocity results in a decrease in adiabatic compressibility, free length and free volume and increase in internal pressure which is observed in present liquid mixture from Table 3. The observation indicates the closer packing of molecules inside the shield.

In order to show the molecular interaction between the component molecules of the ternary liquid mixtures of 2-Nitroanisole, 1-Propanol in n-Hexane, it is of interest to discuss the molecular interaction of ternary liquid mixtures in terms of excess values of acoustic parameters rather than its actual acoustic values.

The idea about the linearity of the system as association, dissociation (or) other type of interaction [11] can be seen from Tables 4 and 5 that the excess adiabatic compressibility is negative over the entire range of the system, Sridevi et al. [11] suggested that negative excess adiabatic compressibility has been due to close packed molecules, with the positive excess value due to weaker interaction between unlike molecules the similar idea were also discussed by Islam and Quadri [12].

The variation in excess parameters of the liquid mixture is used to explain the structure making or breaking properties of the liquid mixtures, during the study the existence of weak, strong complex formation and strength of molecular interaction in the liquid mixture through ultrasonic is discussed. The presence of dispersive force makes a positive contribution to the excess values.

The negative contribution to excess adiabatic compressibility (β_{ad}^E) shown in Table 4, excess free length (L_f^E) presented in Table 4, and excess ultrasonic velocity (U^E) seen in Table 4 and the positive contribution to excess acoustic impedance (Z^E), excess internal pressure (π_i^E) observed in Table 5 respectively indicates the presence strong interaction in the present ternary liquid mixtures. The magnitude and sign of excess adiabatic compressibility (β_{ad}^E) can be used to study the structure making/breaking properties of the liquid mixtures, if more than one type of interaction is present between the interacting components. The negative contribution of excess acoustic compressibility can be attributed to structure making effect in the present investigation.

Nitroanisole is relatively a complex molecule, and its non-ideality in all probability may be due to the polarity arising out of C-N and N-O bonds. As per as nitro group is concerned, it rotates freely along the C-N axis which is likely to give more flexibility to the interaction arising due to highly polar N-O bonds.

n-Hexane belongs to alkane of six carbon atom (hydrocarbon), its highly inert towards an electrophile or nucleophile at ordinary temperature, its being a non-polar solvent is not expected to be involved any strong interaction with the other component present in the liquid mixture.

The Table 4 shows, that the negative excess values of U^E (ultrasonic velocity) its presence of dispersion interaction in the ternary liquid mixture. The negative value of U^E due to the interaction of π electron cloud of benzene ring with delocalised π electron cloud over nitrogen and oxygen atom of the $-NO_2$ group. The negative value of excess free length which is present in Table 4, predicts its existence of strong interaction in the ternary liquid mixture due to charge transfer, dipole-induced dipole, dipole-dipole interactions, interstitial accommodation and orientation ordering. The excess adiabatic compressibility is negative in the present ternary liquid mixture at different temperatures as shows in Table 4, Fort and Moore found that the negative excess adiabatic compressibility indicates that the greater interaction between the components of the mixtures. The negative excess values of excess adiabatic compressibility which indicates the closely packed molecules in the mixtures due to their shape and size of the molecules.

Excess adiabatic compressibility shows the negative values in the present study which indicates the formation of strong charge transfer complexes. Normally dispersive force makes a positive excess values and dipole-dipole, dipole-induced dipole, charge transfer interaction and hydrogen bonding between unlike components makes negative contribution. In the present study, (2-Nitroanisole + 1-Propanol in n-Hexane) excess adiabatic compressibility and excess free length makes negative contribution shows the presence of dipole-dipole and hydrogen bonding between 2-Nitroanisole, 1-Propanol in n-Hexane at 303, 308 and 313 K, the presence of $-NO_2$ group at ortho position decreases the interaction between the components in the liquid mixture, it is confirmed by positive excess values of internal pressure presents in Table 5.

The positive values of excess free volumes are influenced by (i) the specific interaction between the component molecules and weak physical forces like dipole – dipole (or) dipole – induced dipole interaction (or) Wander waal's forces (ii) the dispersive forces, streric hindrance of component molecules, unfavorable geometric fitting and electrostatic repulsion.

The former effect leads to contraction of volume and the latter effect leads to expansion of volume. In the present study the positive value of excess free volume may be interpreted as the expansion of volume. The positive value of excess free volume favorable for the latter effect which is account for the weaker molecular interactions.

The values of excess internal pressure shown in Table 5 is positive in the present ternary system, the positive value of excess internal pressure indicates the existence of weak interaction in the liquid system.

Table 1. Comparison of observed value and literature in velocity, density and viscosity of pure liquid in the ternary liquid mixture of 2-Nitroanisole, 1-Propanol and n-Hexane at 303, 308 and 313K.

Name of component in the ternary mixtures		Velocity (ms^{-1})			Density Kg/m^3			Viscosity $\times 10^{-04}$ Nsm^{-2}		
		Temperature (K)			Temperature (K)			Temperature (K)		
		303	308	313	303	308	313	303	308	313
n-Hexane	Observed	1065.1	1054.5	1034.6	0.651	0.648	0.646	0.326	0.315	0.302
	Literature	1058.30 [14]			0.65 [19]			0.296 [20]		
1-Propanol	Observed	1182.5	1180.8	1162.0	0.801	0.798	0.796	1.658	1.516	1.498
	Literature	1198.5 [15]		1189.1 [16]	0.795 [17]		0.787 [18]	1.73 [17]		1.381 [18]
2-Nitroanisole	Observed	1499.8	1491.3	1469.1	1.151	1.1321	1.111	3.525	3.396	3.282
	Literature	–	–	–	–	–	–	–	–	–

Table 2. Velocity, density and viscosity of 2-nitroanisole and 1-propanol in n-hexane at 303 K, 308 K and 313 K.

Con. $\times 10^{-03}$ M	Velocity (ms^{-1})			Density Kg/m^3			Viscosity Nsm$^{-2} \times 10^{-04}$		
	Temperature (K)			Temperature (K)			Temperature (K)		
	303	308	313	303	308	313	303	308	313
1	1072.9	1056.3	1007.0	801.0	802.0	796.0	4.7	5.3	5.1
2	1074.8	1058.0	1009.8	801.0	802.0	790.0	4.6	5.0	4.7
3	1076.9	1060.3	1012.4	801.0	802.0	796.0	4.7	5.0	4.7
4	1077.1	1062.5	1014.3	801.0	802.0	796.0	4.7	5.1	4.8
5	1078.8	1065.5	1017.1	813.0	808.0	796.0	4.9	5.2	4.8
6	1079.0	1067.0	1021.1	813.0	808.0	802.0	4.9	5.2	5.0
7	1080.6	1068.0	1022.6	814.0	808.0	790.0	4.9	5.2	5.0
8	1081.7	1068.1	1023.0	814.0	808.0	790.0	4.9	5.3	5.0
9	1082.5	1069.0	1026.1	814.0	808.0	802.0	4.9	5.3	5.1
10	1083.7	1070.4	1028.7	815.0	809.0	796.0	4.9	5.4	5.1
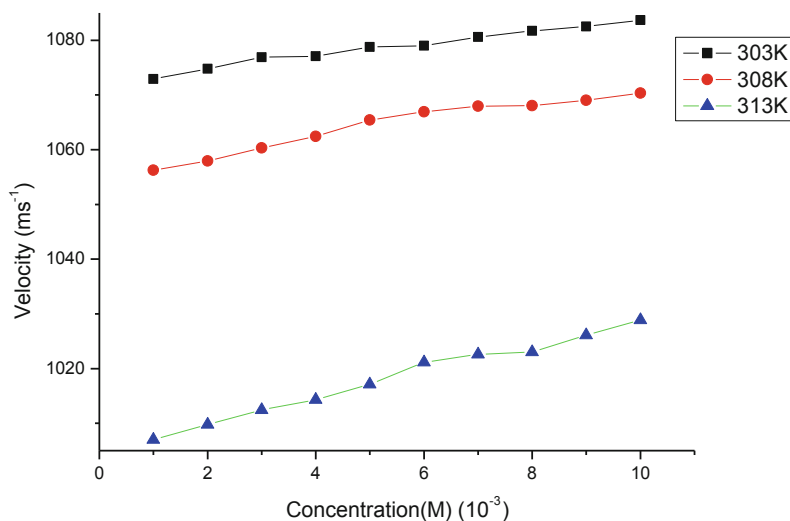
Fig. 1. Plot of velocity vs concentration.
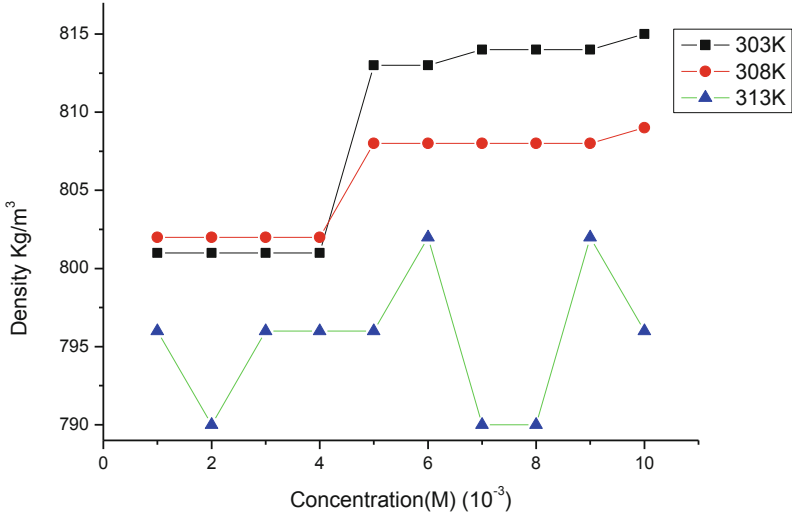
Fig. 2. Plot of density vs concentration.
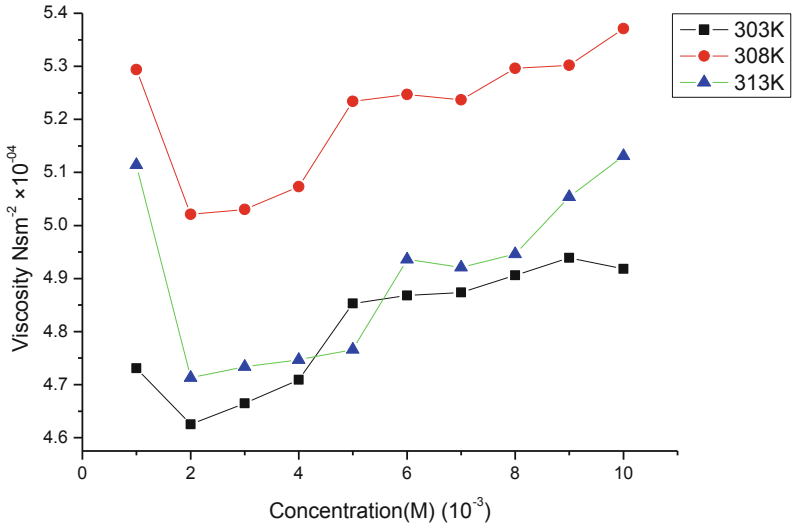
Fig. 3. Plot of viscosity vs concentration.

Table 3. Adiabatic compressibility (β), Acoustic impedance (Z), Free length (L_f), Free volume (V_f) and Internal pressure (Π_i) of 2-Nitroanisole, 1-Propanol and n-Hexane at 303 K, 308 K and 313 K.

Con. 10^{-03} M	(β) × 10^{-09} kg^{-1} ms^2			(Z) × 10^{05} Kgm^{-2}s^{-1}			(L_f)pm × 10^{-11}			(V_f) × 10^{-07} m^3			(Π_i) × 10^{08} atm		
	Tem (K)			Tem (K)			Tem (K)			Tem (K)			Tem (K)		
	303	308	313	303	308	313	303	308	313	303	308	313	303	308	313
1	1.1	1.1	1.2	8.6	8.4	8.0	6.5	6.7	7.0	4.0	3.3	3.2	2.7	3.0	3.0
2	1.1	1.1	1.2	8.6	8.4	8.0	6.5	6.6	6.9	3.1	3.0	3.0	3.4	3.5	3.5
3	1.1	1.1	1.2	8.6	8.5	8.0	6.5	6.6	6.9	3.1	3.0	3.0	3.4	3.5	3.5
4	1.1	1.1	1.2	8.6	8.5	8.0	6.5	6.6	6.9	3.0	3.0	3.0	3.4	3.5	3.5
5	1.1	1.1	1.2	8.7	8.6	8.1	6.4	6.6	6.9	2.9	3.0	3.0	3.5	3.6	3.5
6	1.1	1.1	1.2	8.7	8.6	8.1	6.4	6.5	6.8	2.9	2.5	3.0	3.5	3.6	3.5
7	1.1	1.1	1.2	8.8	8.6	8.1	6.4	6.5	6.8	2.9	2.5	2.6	3.5	3.6	3.5
8	1.1	1.1	1.2	8.8	8.6	8.2	6.4	6.5	6.8	2.9	2.5	2.6	3.5	3.6	3.5
9	1.1	1.1	1.2	8.8	8.6	8.2	6.4	6.5	6.8	2.9	2.5	2.5	3.5	3.6	3.6
10	1.0	1.1	1.2	8.8	8.7	8.2	6.4	6.5	6.8	2.9	2.5	2.5	3.5	3.7	3.7

Table 4. Excess adiabatic compressibility (β^E), excess free length (L_f) and Excess ultrasonic velocity (U^E) of 2-Nitroanisole and 1-Propanol in n-Hexane at different temperature 303 K,308 K and 313 K.

Con. × 10⁻³ M	Excess adiabatic compressibility × 10⁻¹⁰ kg⁻¹ ms² Temperature (K)			Excess free length × 10⁻¹⁰ m Temperature (K)			Excess ultrasonic velocity (m/s) Temperature (K)		
	303	308	313	303	308	313	303	308	313
1	−3.38	−3.47	−3.02	−6.96	−7.1	−7.22	−33.75	−31.17	−60.46
2	−4.97	−5.10	−4.83	−7.19	−7.33	−7.46	−60.14	−59.95	−88.14
3	−6.57	−6.93	−6.55	−7.40	−7.53	−7.66	−84.29	−85.83	−113.72
4	−8.33	−8.83	−8.54	−7.59	−7.71	−7.85	−108.52	−110.01	−138.10
5	−10.50	−10.93	−10.75	−7.76	−7.87	−8.02	−129.65	−131.53	−159.79
6	−12.70	−13.17	−13.21	−7.92	−8.02	−8.18	−150.71	−152.95	−178.72
7	−15.29	−15.70	−15.78	−8.06	−8.16	−8.31	−169.08	−173.41	−198.72
8	−18.11	−18.68	−18.81	−8.18	−8.28	−8.44	−186.72	−193.50	−218.49
9	−21.35	−21.97	−22.58	−8.30	−8.39	−8.56	−211.51	−234.37	−234.37
10	−25.19	−25.79	−26.60	−8.41	−8.50	−8.67	−228.07	−249.51	−249.51
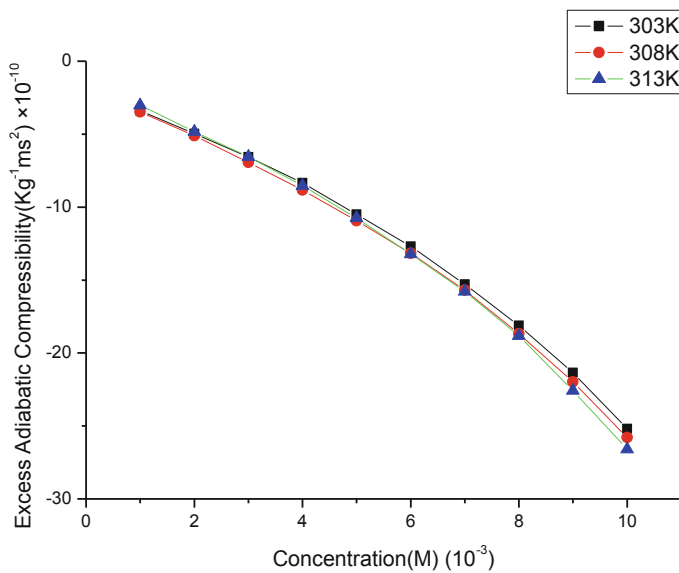
Fig. 4. Plot of excess adiabatic compressibility vs concentration
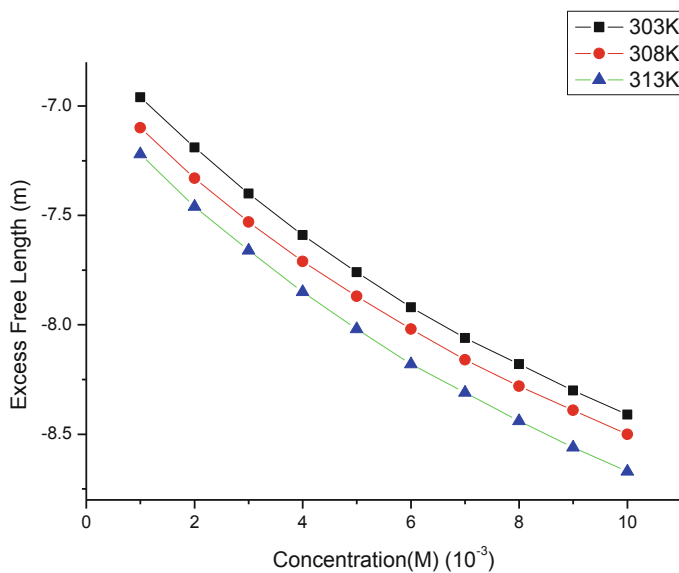
Fig. 5. Plot of excess free length vs concentration.
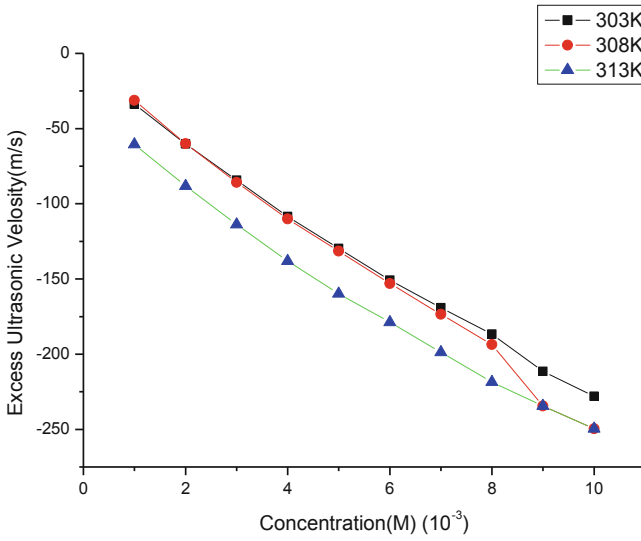
Fig. 6. Plot of excess ultrasonic velocity vs concentration

Table 5. Excess free volume (V_f^E), Excess internal pressure (π_i^E) and Excess Acoustic Impedance of 2-Nitroanisole and 1-Propanol in n-Hexane at different temperature 303 K, 308 K and 313 K.

Excess free volume $\times$ 10^{-07} m^3				Excess Internal Pressure $\times$ 10^{+08} Nm^{-2}			Excess acoustic impedance $\times$ 10^{05}Kgs^{-1}		
Con. $\times$ 10^{-3} M	Temperature (K)			Temperature (K)			Temperature (K)		
	303	308	313	303	308	313	303	308	313
1	13.3	6.4	5.7	1.2	1.4	1.4	1.6	1.5	1.3
2	10.6	6.4	7.0	1.4	1.6	1.6	1.7	1.7	1.4
3	9.9	6.0	6.6	1.3	1.5	1.5	1.7	1.7	1.4
4	9.6	5.9	6.7	1.3	1.4	1.4	1.8	1.8	1.5
5	8.4	4.8	6.6	1.2	1.4	1.3	2.0	1.9	1.6
6	7.9	4.4	5.1	1.2	1.3	1.3	2.0	2.0	1.7
7	8.5	5.1	5.8	1.1	1.2	1.2	2.1	2.0	1.7
8	8.6	5.0	6.2	1.0	1.2	1.1	2.2	2.0	1.7
9	7.6	4.3	4.5	0.9	1.1	1.1	2.2	2.1	1.8
10	7.8	3.8	4.1	0.9	1.1	1.0	2.2	2.3	1.8

Fig. 7. Plot of excess free volume vs concentration.

Fig. 8. Plot of excess internal pressure vs concentration.
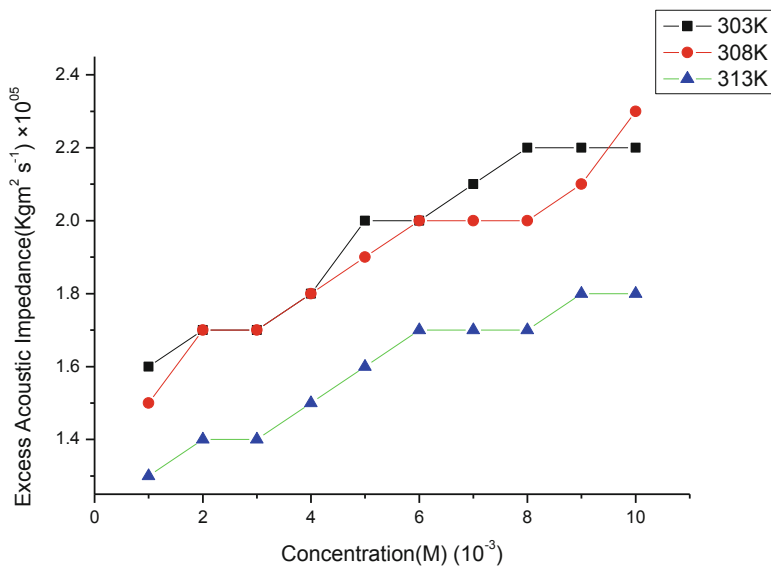
Fig. 9. Plot of excess acoustic impedance vs concentration.

5   Conclusion

On the basis of experimental values of ultrasonic velocity, density and viscosity the excess values for the ternary liquid mixture can be calculated, it is concluded that there is exist dipole-dipole and dispersion interaction are observed, the interaction decreases with increases of temperature. The increase in temperature due to ther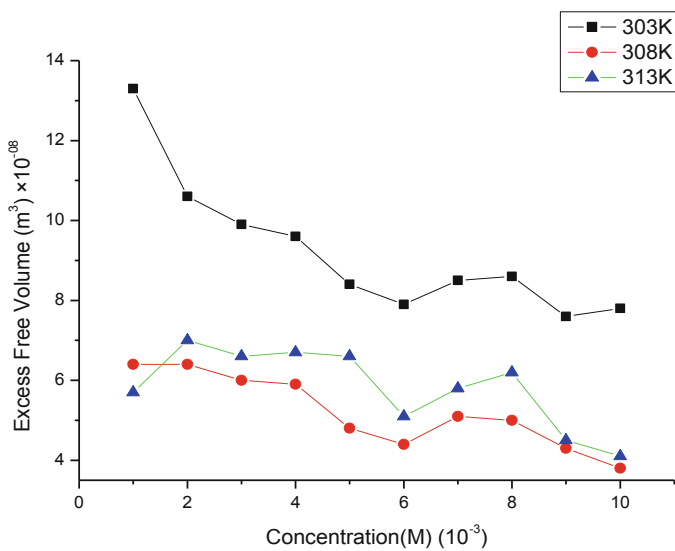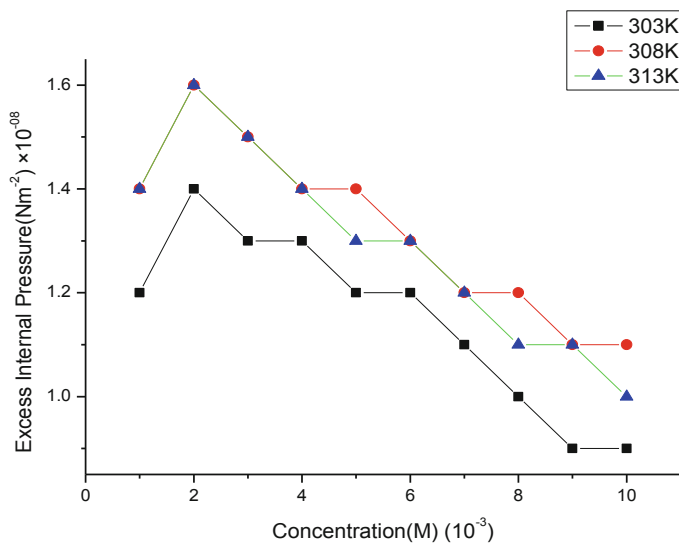mal agitation, resulting in a decrease in ultrasonic velocity. An increase in viscosity with increase in concentration suggests that molecular interactions are increasing in thickness of the liquid mixture and molecular size and shape of the elements that play an equally important role. The adiabatic compressibility suggests that interaction between unlike molecules that have the minimum declarations. In the present study, (2-Nitroanisole + 1-Propanol in n-Hexane) excess adiabatic compressibility and excess free length makes negative contribution shows the presence of dipole – dipole and hydrogen bonding between 2-Nitroanisole, 1-Propanol in n-Hexane at 303, 308 and 313 K. Negative excess ultrasonic velocity confirms the dispersive type of interaction and the interaction becomes strong at 303 K by the high positive value of excess acoustic impedance.

References

1. Gulwade, D.P., Narwade, M.L., Wadodkar, K.N.: Ultrasonic behaviour and study of molecular interactions of substituted azole in N,N dimethylformarnide at different temperatures and concentrations. Indian J. Chem. **43A**, 2102 (2004)
2. Galka, J., Suaki, L., Tomczy, K.P.: Ultrasonic velocity and compressibility of fused bismuth + bismuth halide solutions. J. Chem. Thermodyn. **9**, 673 (1997)

3. Kannappan, V., Jaya Santhi, R.: Ultrasonic study of induced dipole-dipole interactions in binary liquid mixtures. Indian J. Pure Appl. Phys. **43**, 750 (2005)

4. Bolotnikov, M.F., Neruchev, Y.A., Melikhov, Y.F., Verveyko, V.N., Verveyko, M.V.: Temperature dependence of the speed of sound, densities, and isentropic compressibilities of hexane + hexadecane in the range of 293.15 to 373.15 K. J. Chem. Eng. Data **50**, 1095 (2005)

5. Valles, C., Mainar, A.M., Santafe, J., Dominguez, M.: Excess enthalpy, density, speed of sound, and viscosity for 2-methyltetrahydrofuran +1-butanol at 283.15, 298.15, and 313.15 K. J. Chem. Eng. Data **51**, 1105 (2006)

6. Amalendupal, Guru Charandas: Acetonitrile + 1-Hexanol. J. Pure Appl. Ultrason. **21**(1), 9 (1999)

7. Nikkam, P.S., Jdhav, M.C., Hasan, M.: Molecular-interactions in mixtures of dimethylsulfoxide with some alkanols - an ultrasonic study. Acustica **83**, 86 (1997)

8. Syal, V.K., Chauhan, M.S., Chandra, B.K., Chauhan, S.: J. Pure Appl. Ultrason. **18**, 104 (1996)

9. Nikkam, P.S., Pathak, R.B., Hasan, M.: J. Pure Appl. Ultrason. **18**, 19 (1996)

10. Patel, L.A.T.: J. Chem. Eng. Data **40**, 194 (1995)

11. Sridevi, U., Samatha, K., Sarma, A.V.: Excess thermodymamic properties in binary liquids. J. pure Appl. Ultrason. **26**, 1–11 (2004)

12. Islam, M.R., Quadri: Ultrasonic velocity and viscosity of binary liquid mixtures. Thermo. Chim. Acta **115**, 335 (1987)

13. Rajendran, V., Marikani, A.: Investigation of thermodynamic properties of amine-alcohol mixtures at 303.15 K. Acoust. Lett. **18**, 90–94 (1994)

14. Kannappan, V., Kothai, S.: Indian J. Pure Appl. Phys **40**, 17–23 (2004)

15. Thirumaran, S., Murugan, R., Prakash, N.: Acoustic studies of intermolecular interactions in binary liquid mixtures. J. Chem. Res. **2**(1), 53–61 (2010)

16. Trivedi, C.M., Rana V.A, Ultrasonic studies of molecular interaction in the mixtures of Pyridine with 1-Propanol at different temperature. In: International Symposium on Ultrasonics (IJSR), no. 1, pp. 22–24 (2015)

17. Dikio, E.D., Nelana, S.M., Isabirye, D.A., Ebenso, E.E.: Density dynamic viscosity and derived properties of binary mixtures of methanol, ethanol, n-propanol, n-butanol with pyridine at T = (293.15, 303.15, 308.15, and 323.15) K. Int. J. Electrochem. Sci. **7**, 11101–11122 (2012)

18. Liu, J., Zhu, C., Ma, Y.: Densities and viscosities of binary solutions of Benzene-1,3-diol + water, ethanol, propan-1-ol, Butane-1-ol, at T (293.15–333.15) K. J. Chem. Eng. Data. **56**, 2095–2099 (2012)

19. Riddick, J.A., Bunger, W.B., Sakano, T.: Organic Solvents. Techniques of Chemistry, vol. 1, 4th edn. Wiley, New York (1986)

20. TRC: Thermodynamics tables: hydrocarbons thermodynamic research centre: the Texas. A & M University System, College Station, Texas (1989)

Thermal and Physical Properties of Some Deep Eutectic Solvents

P. G. Ramesh[1] and D. Ilangeswaran[2](✉)

[1] Department of Chemistry, Swami Dayananda College of Arts and Science,
Manjakkudi, Tiruvarur, Tamilnadu, India
pgrjan2011@gmail.com

[2] Department of Chemistry, Rajah Serfoji Govt. College (Autonomous),
Thanjavur, Tamilnadu, India
dhailangeswaran@gmail.com

Abstract. Deep eutectic solvent is abbreviated as DES. Deep Eutectic Solvents are types of environmentally green solvents. As a new type of solvents, DES has an extremely large number of applications. Even though the problems associated with conventional volatile organic solvents are well studied, the usage of green and bio-renewable solvents still remains a never-ending challenge. DES have been studied in a variety of applications, different process and metal-catalyzed organic reactions. In recent years, low melting mixtures consisting of carbo-hydrates, urea, and inorganic salts have been introduced as new alternative sustainable solvents for organic transformations. In the present work, amino acid Glycine was added to Citric acid and Malonic acid and Tartaric acid was added to Ethylene glycol to form binary deep eutectic solvents. The physical properties such as conductivity, density, viscosity and pH were measured and analyzed as function of temperature in the range of 300–350 K. The thermal properties such as thermal decomposition temperature, molar heat capacity and glass transition temperature were measured for these deep eutectic solvents. These DESs were characterized by FTIR spectra to evaluate the formation of hydrogen bond.

Keywords: Deep eutectic solvent · Citric acid · Malonic acid · Tartaric acid · Glycine · FT-IR

1 Introduction

In recent days green chemistry plays a predominant role in electrodeposition, electropolishing, electroplating of metals, drug solubilization, solvents for various enzyme-based bio-transformations, biocatalytic process, bio-diesel purification, dearomatization of liquid fuels etc., [1–8]. The physical properties like density, viscosity, conductivity, surface tension and refractive index of the similar groups being capable of interacting with each other forming a hydrogen bond. One can easily find it as a result of electrostatic interaction.

2 Experimental

2.1 Materials

The chemicals Glycine, Citric acid, Malonic acid, Tartaric acid and Ethylene glycol, used in this study were analytical reagent (A.R) grade, purchased from Merck and used as received for the preparation of the DESs.

2.2 Preparation of DESs

Three kinds of deep eutectic solvents Citric acid (CA) with Glycine (GLY), Malonic acid (MA) with Glycine (GLY) and Ethylene glycol (EG) with Tartaric acid (TA) were prepared by taking in the mole ratio of 1:1 by evaporation methods [9]. In this method the pair of substances as mentioned above with 1:1 mole ratio was dissolved in excess of water to a clear solution and then subjected to the evaporation of excess water by gentle heating at 100 °C until solution with constant weight is obtained. The resultant liquids were cooled to room temperature and then kept in a dessicator containing anhydrous Calcium chloride for a fortnight. As there was no turbidity seen during this observation period, the DESs were examined for their thermal and physical properties. The FTIR spectra of these DESs were also obtained to ascertain the H bonded interactions during the formation of DESs.

2.3 Characterization of DES

The conductivities of the DESs were measured using Systronics conductivity meter 304 at room temperature. The densities of the DESs were measured at room temperature using a standard Pycno meter. The viscosities of the DESs were measured using digital rotational viscometer of LABMAN WENSAR make model LMDV 60 by following standard procedure at room temperature. The pH of these three DESs were measured using digital pH meter of ELICO make model no LI120 using the combined electrode CL-51B. The variation of conductivity, density and pH with temperature were also measured for these three DESs. The physical properties, conductivity and pH were correlated as a function of temperature. The FTIR spectra of the DESs were obtained using a PerkinElmer spectrophotometer to analyze the H-bonded interactions.

The thermal decomposition temperatures of citric acid-glycine, malonic acid-glycine and ethylene glycol-tartaric acid DESs were determined using a thermogravimetric analyzer (Perklin-Elmer/Pyris). The samples were placed in a crucible under nitrogen atmosphere (flow rate 20 ml. min^{-1}) and heated at the temperature range from 30 °C to 500 °C with the heating rate of 10 °C min^{-1}. The accuracy of temperature is ±1 °C.

3 Results and Discussion

The physical, thermal and FTIR spectral properties of citric acid-glycine, malonic acid-glycine and ethylene glycol-tartaric acid DESs were discussed as following.

3.1   Conductivity

The electrical conductivities of these DESs citric acid-glycine, malonic acid-glycine and ethylene glycol-tartaric acid were found to be 5.8, 1.3 and 21 ms cm^{-1} at room temperature [8, 10]. The variation of conductivities as a function of temperatures were given in Fig. 1. The conductivity greatly increases with temperature for the DES of ethylene glycol-tartaric acid (EG-TA). But the conductivities of citric acid-glycine (CA-GLY) and malonic acid-glycine (MA-GLY) were slightly increased with temperature.
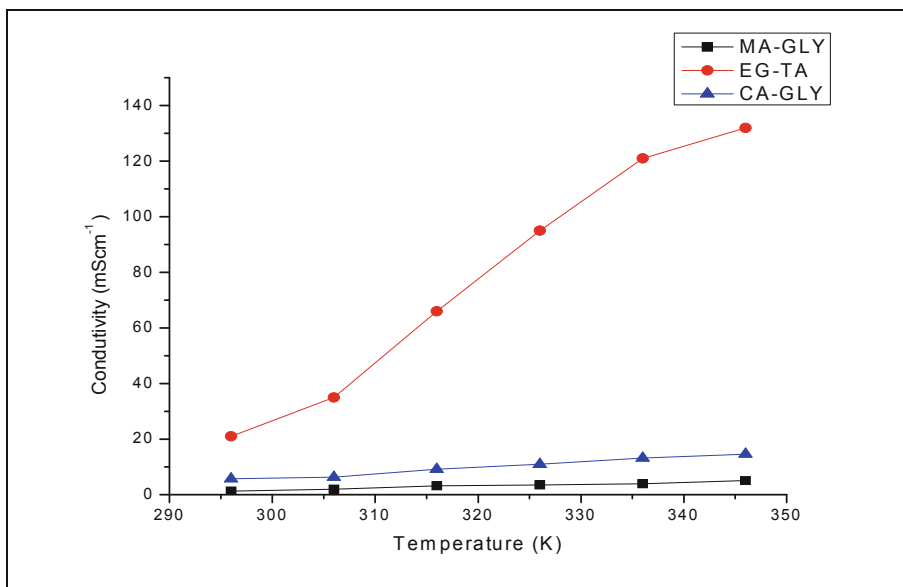
Fig. 1.   Conductivities for DESs as a Function of Temperature.

3.2   Density

Density is an important characteristic of any liquid and in the mass transfer calculations density is a most important factor. The densities of citric acid-glycine, malonic acid-glycine and ethylene glycol-tartaric acid were found to be 1.512, 1.361 and 1.278 g. cm^{-3} respectively at 303 K.

3.3   Viscosity

In hydrodynamic processes, the viscosity is a key factor behind all applications of ionic liquids [11]. The transport phenomena in pure, molten salts and ionic solids are more in the aqueous solutions. The viscosity of citric acid-glycine DES was found to be 1501.5 mPa. s at 300 K. The malonic acid-glycine DES showed the viscosity of 7443.6 mPa. s at 299 K whereas the viscosity of ethylene glycol-tartaric acid DES was measured as 5562.2 mPa. s at 300 K.

3.4 The PH

The pH is an important physical property and it has essential impact on chemical reactions. The pH is important for the applications of DES in catalysis, biochemical reactions, or in dissolution of metals [12–15]. The pH values of citric acid-glycine, malonic acid-glycine and ethylene glycol-tartaric acid DESs were measured to be 2.92, 2.43 and 0.97 at the temperature of 297 K. The variation of pH as a function of temperature was mentioned in Fig. 2. The pH in malonic acid-glycine and ethylene glycol-tartaric acid were slightly increased with increasing temperature. The DES citric acid-glycine showed decrease in pH with increasing temperature. The pH values of DES based on all DESs appeared to be stable within the temperature range 300 K to 350 K.
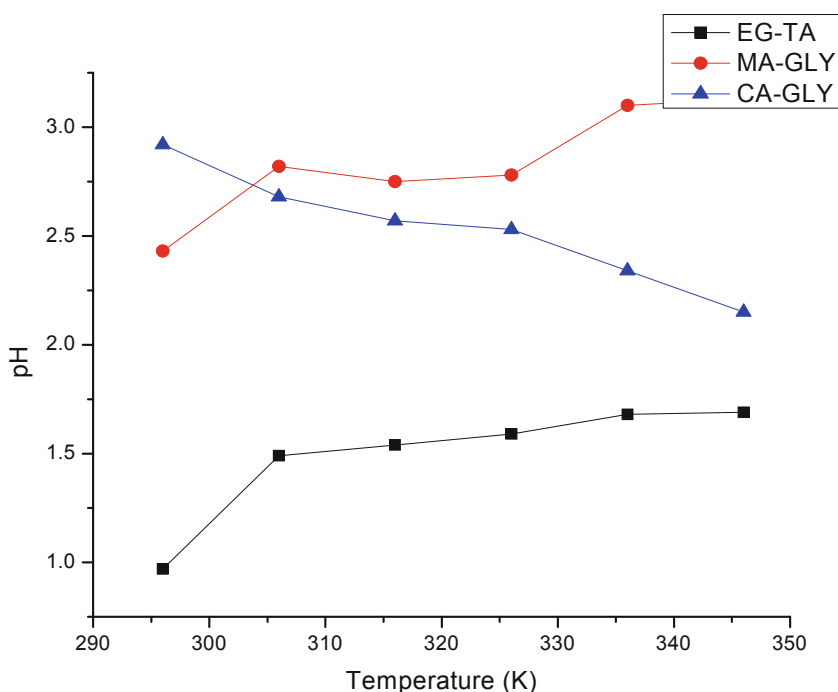
Fig. 2. pH values for all DESs as a function of temperature T.

3.5 Thermal Decomposition Temperature

The variation in the thermal decomposition with temperatures of these DESs were measured and the variation of weight of DESs with increase in temperature were showed in Fig. 3 [16]. The glycine based deep eutectic solvents CA-GLY and MA-GLY were found to be stable up to 130 °C while the DES of EG-TA was found to be stable till about 300 °C.
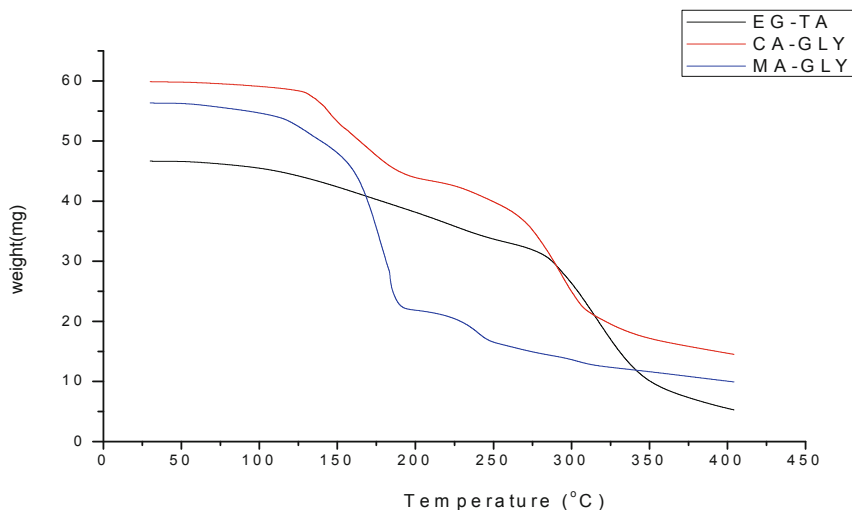
Fig. 3. The thermal decomposition temperatures of all DESs.

3.6   FTIR Spectrum of Citric Acid-Glycine

The Fourier transformation infrared spectrum of DES of citric acid-glycine is shown in Fig. 4. In the FTIR spectrum of DES of citric acid-glycine, there seems to be a broad peak at 3000–3486.05 cm^{-1}. Generally, the O-H stretching of carboxylic acids are observed at 3400 cm^{-1}. The N-H stretching due to either primary or secondary amines are expected at 3300 to 3500 cm^{-1}. Here the broad peak at 3000–3486.05 cm^{-1} due to the hydrogen bond formation [17] of these groups of citric acid and glycine. The CO stretching of carboxylic acid of citric acid and glycine are observed around 1736.79 cm^{-1}. The CH$_2$ deformations of citric acid and glycine were noticed at 1430.86 cm^{-1}. The peak at 1632.14 cm^{-1} was due to the out C = N stretching of Glycine. The medium peak at 995.61 cm^{-1} was due to C – N stretching of L-Lysine.
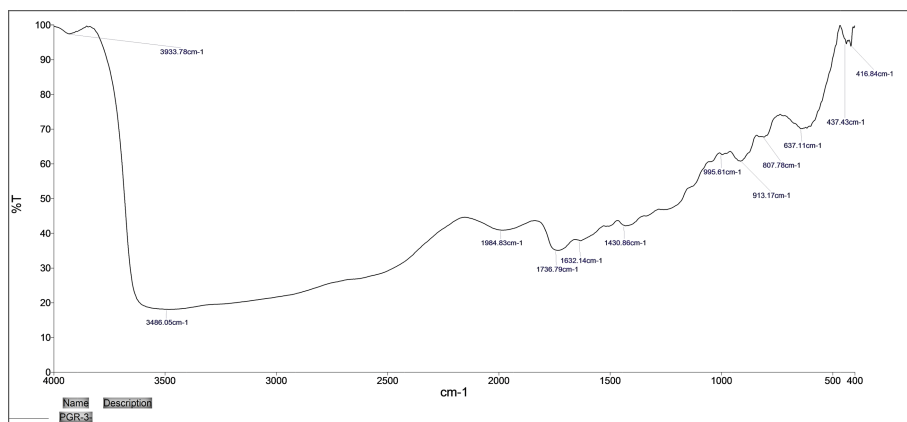
Fig. 4. FTIR spectrum of DES of citric acid-glycine.

3.7   FTIR Spectrum of Malonic Acid-Glycine

The Fourier transformation infrared spectrum of DES of malonic acid-glycine is shown in Fig. 5. In the FTIR spectrum of DES of malonic acid-glycine there seems to be a broad peak at 3000–3448.19 cm^{-1}. Here the broad peak at 3000–3448.19 cm^{-1} due to the hydrogen bond formation of these groups of malonic acid and glycine. The C = O stretching of carboxylic acid of malonic glycine are observed around 1732.51 cm^{-1}. The CH$_2$ deformations of malonic acid and glycine were noticed at 1414.45. cm^{-1}. The peak at 1631.81 cm^{-1} was due to the out C = N stretching of glycine. The medium peak at 1119.26 cm^{-1} was due to C – N stretching of glycine.
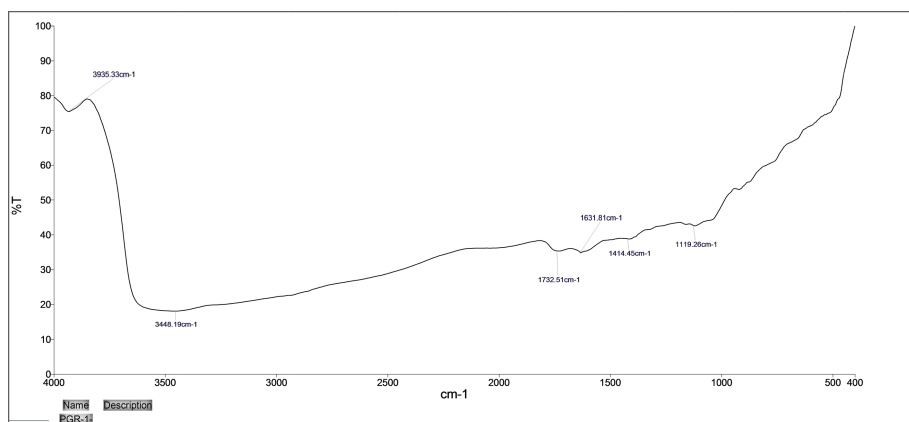
Fig. 5.   FTIR spectrum of DES of malonic acid-glycine.

3.8   FTIR Spectrum of Ethylene Glycol-Tartaric Acid

The Fourier transformation infrared spectrum of DES of tartaric acid-Ethylene glycol is shown in Fig. 6. In the FTIR spectrum of DES of ethylene glycol-tartaric acid, there seems to be a broad peak at 3000–3495.93 cm^{-1}. Here the broad peak at 3000–3495.93 cm^{-1} due to the hydrogen bond formation of these groups of tartaric acid and ethylene glycol. The C = O stretching of carboxylic acid of tartaric acid was observed around 1751.95 cm^{-1}. The CH$_2$ deformations of ethylene glycol-tartaric acid were noticed at 1453.51 cm^{-1}.
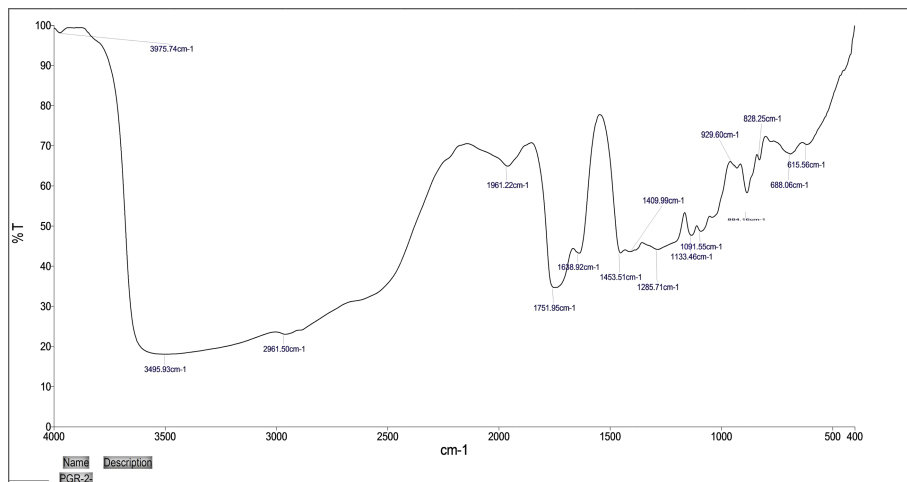
Fig. 6. FT-IR spectrum of Tartaric acid-ethylene glycol.

4   Conclusions

In this work three different deep eutectic solvents (DES) citric acid-glycine, malonic acid-glycine and ethylene glycol-tartaric acid in the 1:1 mole ratio containing minimum amount of water were prepared. They were existed as a clear liquid at room temperature for more than fifteen days. Their physical properties such as conductivity, density, viscosity, pH and the thermal decomposition temperatures were measured for these DESs. The FT-IR Spectra of these DESs were obtained and the spectral data were analyzed to know the H bonded interaction in the formation of DESs. The broad peak observed in the region of 3000 to 3400 cm^{-1} for all three DESs were provided enough evidences for the formation of hydrogen bonds.

References

1. Abbott, A.P., Capper, G., McKenzie, K.J., Ryder, K.S.: Voltammetric and impedance studies of the 316 stainless steel in a choline chloride based ionic liquid. Electrochim. Acta **51**, 4420–4425 (2006)
2. Abbott, A.P., Mckenzie, K.J.: Application of ionic liquids to the electrodeposition of metals. Phys. Chem. **8**, 4265–4279 (2006)
3. Morrison, H.G., Sun, C., Neervannan, S.: Characterization of thermal behaviour of deep eutectic solvents and their potential as drug solubilization vechicles. Int. J. Pharm. **378**, 136–139 (2009)

4. Gutierrz, M.C., Ferrer, M.L., Mateo, R., del Monte, F.: Freeze drying of aqueous solutions of deep eutectic solvents: a suitable approach to deep eutectic suspensions of self-assembled structures. Lamgmuir **25**, 5509–5515 (2009)
5. Abedin, S.Z.E., Endress, F.: Ionic liquids the link to high temperature molten salts. Acc. Chem. Res. **40**, 1106–1113 (2007)
6. Abbott, A.P., Harris, R.C., Ryder, K.S., Agostino, D., Gladden, L.F., Mantle, M.D.: Glycerol eutectics as sustainable solvent systems. Green Chem. **13**, 82–90 (2011)
7. Gano, Z.S., Mijali, F.S., Al-Wahaibi, T., Al-Wahaibi, Y., Al-Wahabi, Y., AlNasef, L.M.: Solubility of thiophene and dibenzothiophene in anhydrous $FeCl_3$- and $ZnCl_2$-based deep eutectic solvents. Ind. Eng. Chem. Res. **53**, 6815–6823 (2014)
8. Zhang, Q., De Olivera Vigier, K., Royer, S., Jerome, F.: Deep Eutectic solvents: syntheses, properties, and applications. Chem. Soc. Rev. **41**, 7108–7146 (2012)
9. Dai, Y.T., van Spronsen, J., Witkamp, G.J., Verpoorte, R., Choi, Y.H.: Natural deep eutectic solvents as new potential media for green technology. Anal. Chim. Acta **766**, 61–68 (2013)
10. Chemat, F., Anjum, H., Shariff, A.M., Kumar, P., Murugesan, T.: J. Mol. Liq. **216**, 301–308 (2016)
11. Popescu, A.M., Donath, C., Constantin, V.: Bul. Chem. Commun. **46**(3), 452–457 (2014)
12. Wasserscheid, P., Welton, T. (eds.): Ionic Liquids in Synthesis. Wiley-VCH, Weinheim (2003)
13. Jibril, B.Y., Mijali, F.S., Naser, J., Gano, Z.: New tetrapropylammonium bromide-based deep eutectic solvents: synthesis and characterizations. J. Mol. Liq. **199**, 462–469 (2014)
14. Harris, R.C.: Physical properties of alcohol based Deep Eutectic solvents. Ph.D. thesis, Department of Chemistry, University of Leicester (2008)
15. Skulcova, A., Russ, A., Jablonsky, M., Sima, J.: pH of solvents Biosources **13**(3), 5042–5051. http://bioresources.com
16. Hayan, A., Mijali, F.S., AINashef, I.M., Al-Wahabi, Y.M.: J. Mol. Liq. **178**, 137–141 (2013)
17. Ramesh, P.G., Ilangeswaran, D.: Int. J. Adv. Sci. Res. Manage., Special Issue 4, 100–104 (2019). ICAMA-18, http://www.ijasrm.com

Apoptotic Activity in Cervical Cancer HeLa Cell Lines Treated with Chitosan Nanoconjugated Drug Doxorubicin – as Nanocarrier for Drug Delivery

M. R. Kamala Priya[(✉)] and Priya R. Iyer

Post Graduate and Research Department of Biotechnology, Women's Christian College, College Road, Chennai 600006, Tamilnadu, India
kamalipriya23@gmail.com

Abstract. Nanocarriers play an indispensible role in drug delivery mechanisms thereby increasing the efficiency and overall activity of the specified drug in the given dosage. Chitosan is a well known biocompatible molecule that is exploited for various *in vivo* applications. In this current study, a biocompatible nanocarrier is developed as a conjugate using chitosan nanoparticles for the drug Doxorubicin. A nanoparticle is synthesized using the green extract of a medicinal plant. Upon successful synthesis, a chitosan conjugate is prepared along with the drug and synthesized nanoparticles. The synthesis of gold nanomaterials using *Catharanthus roseus* (**Nithyakalyani**) is successfully carried out. The initial confirmation of the nanoconjugate is from UV visible spectrophotometric analysis, which showed the characteristic peak for nanoparticles. SEM & HRSEM analysis revealed the size and shape of the nanocojugate. The Zeta potential is measured to check the stability of the nanoconjugate. The *in vitro* cytotoxicity is carried out in VERO cell lines and anti cancer study in cervical cancer HeLa cell lines. Further, the gene expression of one of the apoptotic molecule, Caspase was screened. The nanocarrier showed anti cancer activity in treated cervical cancer HeLa cell lines and as well as commendable non toxicity in treated normal vero cell lines. On this positive note, this nanocarrier study could be further expanded.

Keywords: Nanocarriers · Chitosan · Doxorubicin · Gold nanoparticles · Cytotoxicity · Vero cell lines · Anti cancer activity · Cervical cancer · HeLa cell lines

1 Introduction

Plants and Herbs are important sources of various phytochemicals. In cancer cells, those Polyphenolic compounds that are present in the plants, function in different dimensions, like induction of apoptosis, growth arrest, inhibition of DNA synthesis and modulation of signal transduction pathways. It has been previously demonstrated in other studies that phytochemicals have anti-oxidative, anti-inflammatory and anticancer activities. The use of phytochemicals for the treatment of cancer may enhance the efficacy of chemotherapy, lowering toxicity to normal cells. Therefore, phytochemicals

in combination with CDDP may reduce the side effects caused by CDDP treatment alone (Koraneekit *et al.* 2018).

Chitosan is a product of chitin, which is a natural polysaccharide possessing tremendous properties that could be exploited for various diversified applications. It can act as a substitute for synthetic compounds. The functional group of Chitosan consists of glucosamine and *N*-acetyl glucosamine units, that makes Chitosan an unique polycationic, chelating and film forming agent. Additionally Chitosan is biocompatible, biodegradable non-toxic, nonantigenic and has strong adsorption properties (Hettiarachchi *et al.* 2011).

Hence a medicinal plant with anti cancer activity was chosen for the nanoparticle synthesis and this nanoparticle along with Chitosan and drug Doxorubicin was combined in the presence of STPP to form a Nanocarrier. This nanocarrier was screened for *in vitro* anti cancer activity in Cervical cancer HeLa cell lines. Further, the induction of apoptosis in the cancer cells was confirmed through gene expression studies with one of the apoptotic marker, Caspase. Caspase plays a pivotal role by activation of Caspase cascade which ultimately leads to apoptotic cell death in cancerous cells.
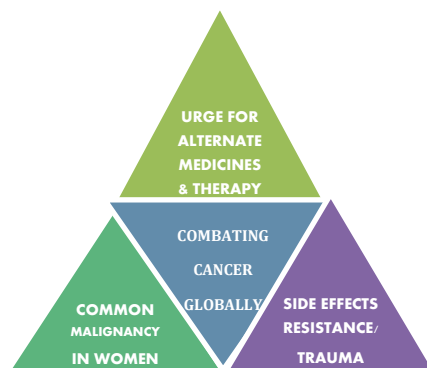
2   Materials and Methods

2.1   Synthesis of Chitosan Nanoconjugated Drug

Collection of the Plant Material

The flowers of the plant *Catharanthus roseus* was collected from the campus of Women's Christian College, Chennai. The flowers were crushed and boiled for about 5–10 min in double distilled water. Then the filterate was collected and stored at 4 °C and used for further synthesis (Priya and Iyer 2014a).

Preparation of the Stock Solution - Chloroauric Acid

Chloroaurate or Chloroauric acid was the precursor used for the synthesis of gold nanoparticles. It was procured from Loba Chem and used as such without further purification. The required molar concentration of $AuCl_4^-$ was prepared and this chloroauric acid was stored as stock solution for further experiments (Priya and Iyer 2014c).

Preparation of Chitosan Solution

Chitosan was procured from Loba chem and used without further purification. About 2 mg/ml chitosan solution was prepared upon addition of few drops of glacial acetic acid. The chitosan was allowed to completely dissolve to form a colloidal suspension. An aqueous solution of STPP(sodium tri poly phosphate) (1 mg/ml) was prepared which was added to aid the process of Chitosan-nanoparticles-drug nanocnjugate formation.

Chitosan AuNp's Drug - Nanocarrier Synthesis

Chitosan is a well known biocompatible molecule that is exploited for various *in vivo* applications. A biocompatible nanocarrier is developed as a conjugate using chitosan and gold nanoparticles with the anti cancer drug Doxorubicin. Equal volumes of synthesized gold nanoparticle and chitosan solution was mixed. To this 1 ml of the drug solution was added and homogenized for 30 min at 400 rpm with drop wise addition of STPP. The prepared chitosan nanoconjugate was further characterized and studied for anti cancer activity (Priya and Iyer 2015a; Panyam and Labhasetwar 2003).

2.2 Characterization of Nanoparticles Using UV Visible Spectrophotometer

The sample was diluted in 1:30 ml dilution with double distilled water and characterized for the formation of nanoparticles. The UV visible spectrum corresponding to the Chitosan gold nanoparticles were recorded using a Systronic smart DBS 2303 UV Visible spectrophotometer operating in the wavelength between 500 to 700 nm (Mukunthan et al. 2011).

2.3 Zeta Potential

The stability of the nanoparticles synthesized is elucidated on analysis of Zeta potential. It is the measure of the charged species present at the nanoparticle surface that prevents from aggregation and enusring highly stable nanoformulations. The more the positive or the more the negative, the Zeta measure possess the strongest stability.

2.4 SEM & HRSEM Analysis (Scanning Electron and High Resolution Scanning Electron Microscope)

For the sample preparation, about 10 μl of the synthesized nanoparticles was placed on the aluminum foil and allowed to air dry. Then the Scanning Electron Micrographs and High Resolution Scanning Electron Micrograph of the samples was carried out using a Hitachi S-3400N, Variable Pressure Scanning Electron Microscope (VP-SEM) equipped with Horiba EMAX detector, Japan, at NCNSNT, University of Madras and SAIF (Sophisticated Analytical Instrumentation Facility), IIT Madras, Adyar (Priya and Iyer 2015b).

2.5 Phytochemical Analysis the Green Extracts of the Plants Tested

The green extract of *Catharanthus roseus,* was analysed for the presence of different phytochemicals such as terpenoids, flavonoids, saponins, tannins, phenols, Coumarins, Triterpenoids and the results were recorded. These phytochemicals act as the reducing and stabilizing agents, for the plant mediated synthesis of nanoparticles (Priya and Iyer 2019).

2.6   *In Vitro* Cytotoxicity and Anti Cancer Activity of the Gold Nanoparticles

Procedure

The vero cell lines were used to check cytotoxicity and HeLa cell lines were used to check anti cancer activity of the synthesized nanoconjugate. Both the cell lines used were from Translational Research Platform for Veterinary Biologicals (TRPVB) TANUVAS, Chennai. About 1×10^5 cells (10,000 total cells) were added into each well of 96 well plate and incubated overnight. To this different concentration of gold nanoconjugate was added. The treated cells were incubated for 24 h at 37 °C in the CO_2 incubator. About 10 µl of 5 mg/ml of MTT was added to each well. The cells were incubated for about 3 h for the formation of formazan crystals. About 100 µl of DMSO was added to dissolve the formazan crystals and incubated for about 1–2 h. Then the absorbance was read at 540 nm with a reference filter of 620 nm. Percentage of cell viability was calculated. Formula for cell inhibition = (O.D of treated cells/O.D of control) $\times$ 100. Formula to check cell viability = (100 – cell inhibition) (Priya and Iyer 2014b).

2.7   Apoptotic Gene Expression - Western Blotting

Doxorubicin is a standard drug used to treat various types of cancer. In order to enhance its activity and to increase its bioavailability in a sustained release manner, the drug was conjugated with the synthesized nanoparticles & Chitosan. The nanoconjugate induced cell death over the treated cervical cancer cells. In the process of cell death, the caspase cascade had been activated. The gene expression was checked in line with one of the caspases, Caspase 12. Caspase 12 polyclonal antibody and HRP labeled secondary antibody were procured from Cusabio, USA. The HeLa cell lines were treated with the nanoconjugate for about 24 h in 6 well plates. After treatment, the wells were scraped and centrifuged to pellet down the cells. The collected whole cell protein was lysed using RIPA buffer. The protein concentration was quantified using Bradford's method. The protein sample was prepared and loaded in SDS-PAGE apparatus and subjected to electrophoresis. The gel was removed and blotted over PVDF membrane. Then the membrane was blocked using 1% skimmed milk for about 2 h. After blocking, the membrane was washed and primary antibody was incubated for overnight at 4 °C. The next day, primary antibody was removed and the blot was washed. Then, secondary antibody was added and incubated for about 4 h. After the incubation, the blot was developed with DAB and the positive bands were observed (Li et al. 2008).

3   Results and Discussion

3.1   Synthesis of Chitosan Nanoconjugated Drug

Chitosan Nanocarrier Synthesis

The nanoparticles were synthesized using the flower extract of the medicinal plant, *Catharanthus roseus* on reduction with Chloroauric acid. The synthesized nanoparticles were in deep wine red colour. A chitosan nanoconjugate was prepared along with doxorubicin upon STPP.

Similar results has been reported for chitosan loaded insulin drug by Bhumkar *et al.* 2007
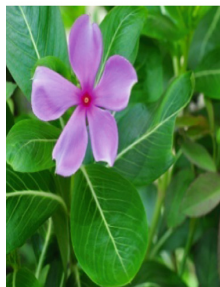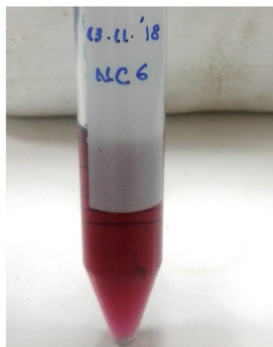
| Flowers of *C.roseus* | Gold Nanoparticles | Chitosan-Dox-Nanoconjugate |
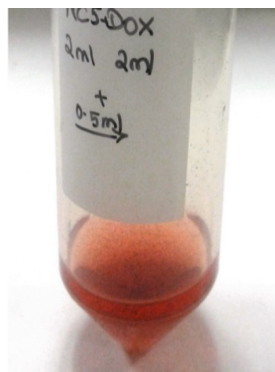
3.2   Characterization – UV-Visible Spectrometer Analysis

The UV absorption peak corresponds to the wavelength at which the optical absorption spectra of metal nanoparticles are dominated by surface plasmon resonance (SPR), which shifts to longer wavelength with increasing particle size. The preliminary confirmation of the nanoconjugate is from UV visible spectrophotometer, which showed
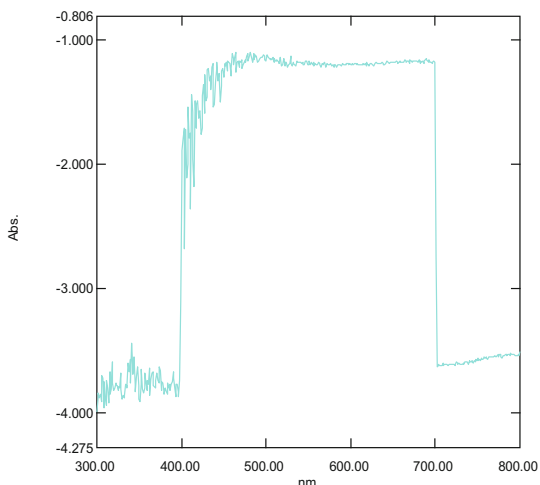
the characteristic peak for nanoparticles.
   Similar results has been stated for nanoparticles synthesis by Song *et al.* 2009.

3.3   Zeta Potential Analysis

The stability of the nanoconjugate synthesized was elucidated on analysis of Zeta potential. It is the measure of the charged species present at the nanoparticle surface that

prevents from aggregation and enusring highly stable nanoformulations. The more the positive or the more the negative, the Zeta measure possess the strongest stability. The zeta potential measurement also gives projection over the stability of the synthesized colloidal suspensions. In general, when the zeta potential value is about >30 mV, there are less chances for agglomeration of the particles due to the electrostatic forces between
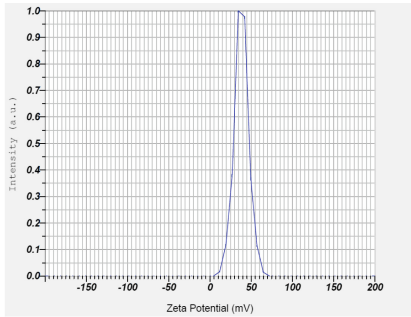
– **Zeta Potential (Mean) : 41.3 mV**

– **Zeta Potential (Mean) : 38.2 mV**

– **Zeta Potential (Mean) : 34.9 mV**

the particles (Bhumkar *et al.* 2007).

The results were in concordance with similar reports by Bhumkar *et al.* 2007.
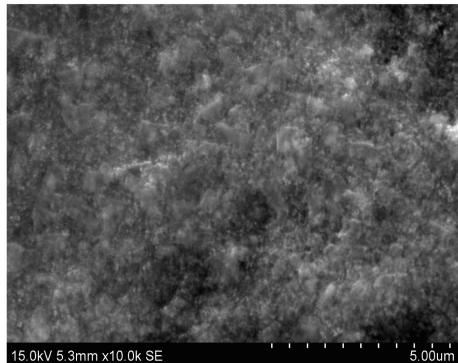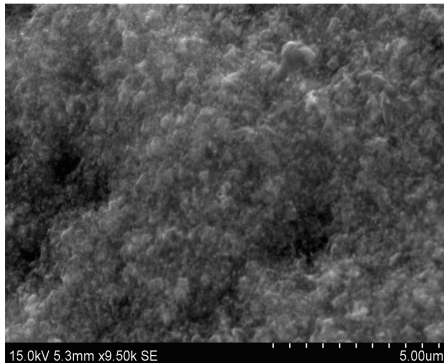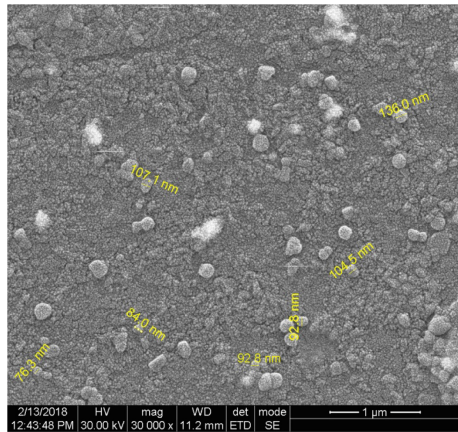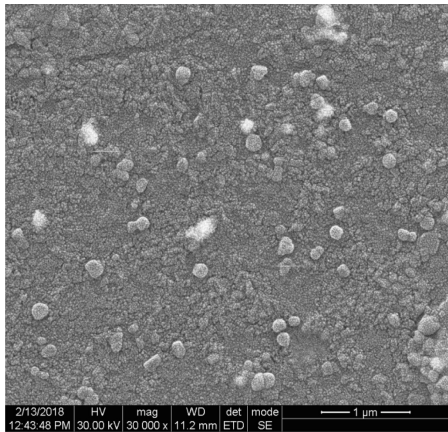
3.4   SEM & HRSEM–Scanning Electron Microscope and High Resolution Scanning Electron Microscope Images

From the SEM & HRSEM analysis, the nanoconjugate synthesized was spherical in morphology and monodispersed. The size of the nanoconjugate was ranging between 70 nm–120 nm. The morphology and dimensions of the nanoparticles is proportionally related to its efficiency. The spherical nanoparticles can accommodate various drugs within the molecule thereby serving as excellent platforms for targeted drug delivery. On this context, the synthesized spherical nanoparticles can be of great utility in drug delivery approaches.

The significance on the size of the nanoparticles has been similarly reported by Sahoo et al. (2002).

3.5   *In Vitro* Cytotoxicity in Vero Cell Lines
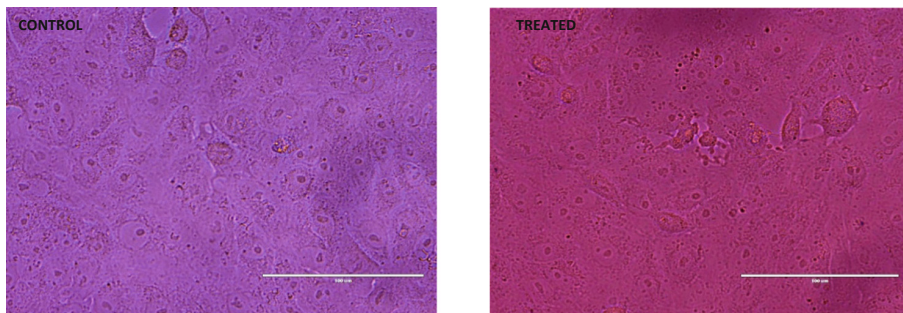
Fig. 1. Control-untreated vero cell lines, Treated- cell lines after 24 h drug treatment
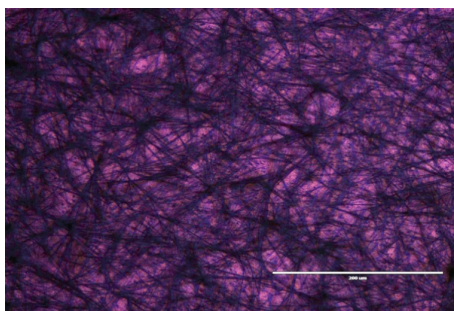
The results of the *in vitro* cytotoxicity showed that the Nanoconjugate tested has higher cell viability at all the tested concentrations. Hence the synthesized nanoconjugate is non-toxic over the treated cells.

Fig. 2. Formazan crystals formed after incubation with MTT

(See Figs. 1, 2, 3)
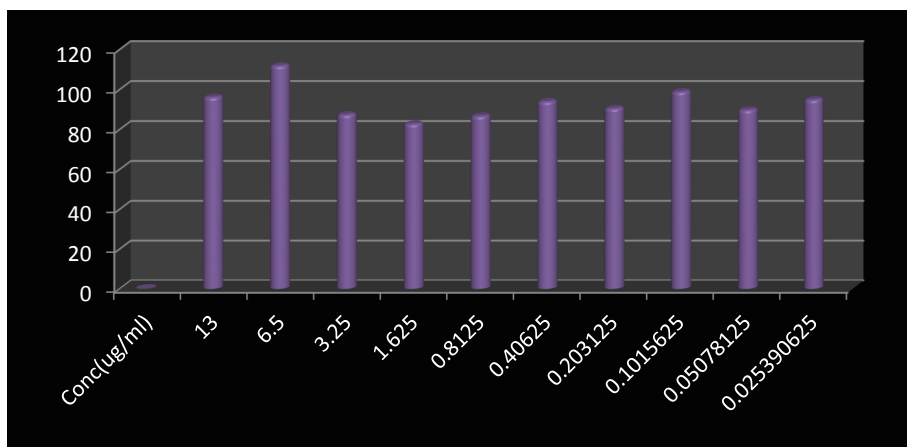
Fig. 3. % of cell viability at different tested concentrations of the nanoconjugate

Similar reports on *in vitro* cytotoxicity assay has been reported by Vijayaku-mar and Ganesan (2012)
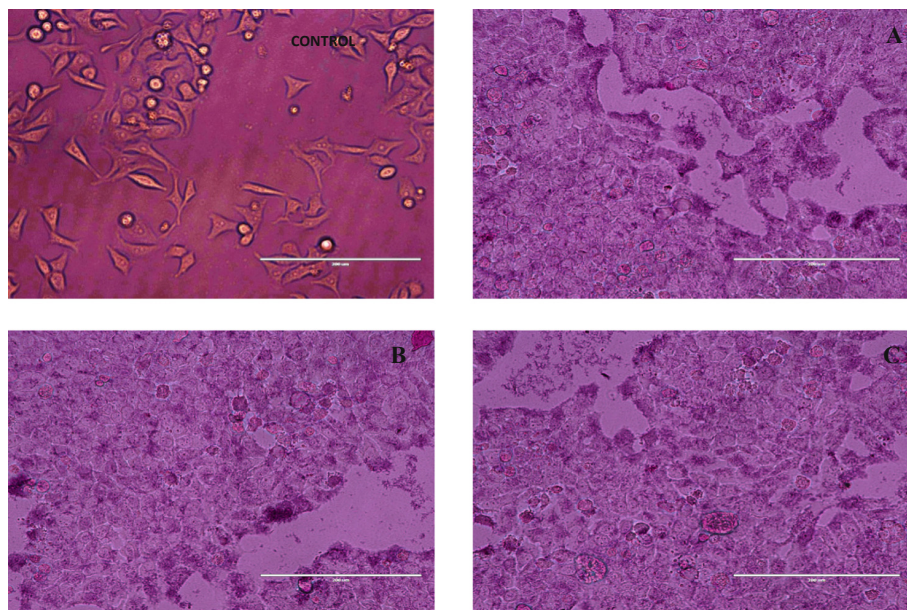
Fig. 4. Control, A, B, C-cells treated with the nanoconjugate at various concentrations. From the images, it could be seen that the treated cells showing degrees of cells undergoing cell death compared to the control cells.

3.6 *In Vitro* Anti Cancer Activity in Cervical Cancer Hela Cell Lines
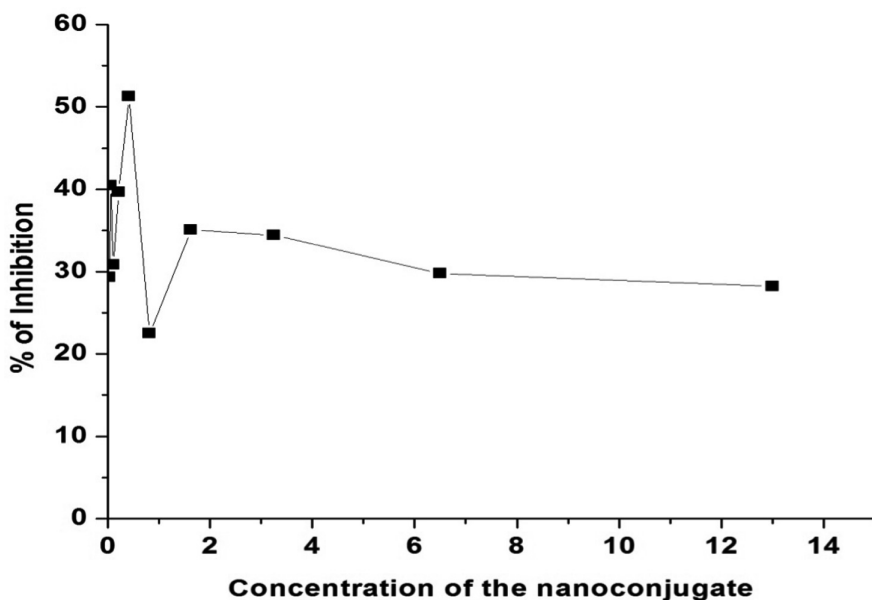
Fig. 5. IC50 of the nanoconjugate against cervical cancer HeLa cells lines

From the figures, comparing between the control cells and treated cells there was significant difference noted in the morphology which implied that the cells were undergoing apoptosis (Fig. 4).

Similar study involving anti cancer activity of copper oxide nanoparticles against HeLa cell lines has been reported by Nagajyothi *et al.* 2017 (Fig. 5).

The results of the anticancer activity on the cervical cancer HeLa cell lines showed that the drug loaded nanocarrier had well anti proliferative activity against cancer cells. And proved to be efficient in most of the concentrations tested and the IC 50 was around 16.13 µg/ml.

The results showed an IC50 at much lesser concentration in comparison to the studies reported by Fatemeh *et al.* 2014.

3.7   Protein Expression – Western Blotting

Caspase Activity in Nanocarrier Treated Cancer Cells

Caspase cascade plays an important role in Apoptosis Pathway. From the western blot, the positive band at 39 KDa for Caspase 12 showed that the cells have undergone apoptosis; thereby the caspase cascade has been activated and induced the cancer cells to apoptotic cell death.

Similar studies has been reported by Lu *et al*. 2017.
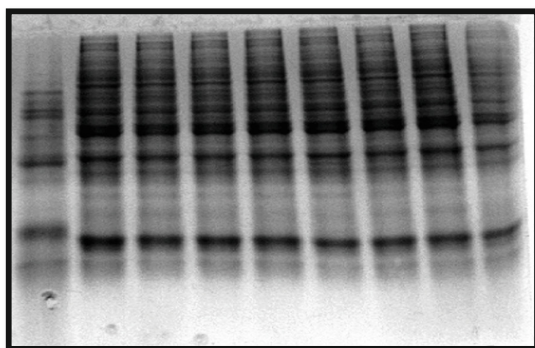
CBB stained SDS-PAGE showing different protein bands

Casp 12

Positive western blot detected for
Caspase 12 at 39 kDa

4 Summary

In this study, the biosynthesis of nanoparticles was successfully carried out using a medicinal plant extract, *Catharanthus roseus*. Further this nanoparticle was conjugated with Chitosan and Doxorubicin as formed as a nanoconjugate. This nanoconjugate was analysed under UV Visible spectrophotometer for the confirmation of the nanoconjugate formation. The size and morphology was imaged under SEM & HRSEM, which revealed the synthesized nanoconjugate was spherical in shape and size was ranging between 70–120 nm. The nanoconjugate was visibly clear colloidal suspension and the Zeta potential measures ensured that the nanoformulations were stable that was in concordance with the observed stability. The *in vitro* cytotoxicity in vero cell lines showed high survival percentage of the cells in almost all the tested concentrations, thereby emphasizing on the non-toxic effect of the synthesized nanoconjugate over normal cells. The results of the anti cancer activity on the cervical cancer HeLa cell lines proved that the nanoconjgate has well anti proliferative effect over the tested carcinoma cells. And the IC 50 of the nanoconjugate was 16.13 µg/ml. Further, the apoptotic expression was checked for Caspase 12 protein, which gave the positive band detection in Western blotting.

5 Conclusion

Nanoparticles based targeted drug delivery is gaining prominence due to its several advantages like enhanced drug activity, sustained drug release and prolonged drug efficiency. And the nanoparticles synthesized using green extracts have benefits over the chemical synthesized materials. Biosynthesis reduces the cost of production to a large extent. Based upon these, biosynthesis of nanoparticle was carried out using a medicinal plant extract and drug conjugate has been formulated. The in vitro studies showed that the nanoconjugate were non toxic to the normal cells and as well had well

anti proliferative effect over the cancer cells. Further, drug related parameters will confirm on sustained drug release of the nanoconjugate. The nanoconjugate can serve as an efficient material to carry various drugs and biomolecules for systemic delivery.

Conflict of Interests. We wish to confirm that there are no known conflicts of interest associated with this publication and there has been no significant financial support for this work that could have influenced its outcome.

References

Koraneekit, A., et al.: Synergistic effects of cisplatin-caffeic acid induces apoptosis in human cervical cancer cells via the mitochondrial pathways. Oncol. Lett. **15**, 7397–7402 (2018)

Hettiarachchi, M.A., Wickramarachchi, P.A.S.R.: Synthesis of chitosan stabilized silver nanoparticles using gamma ray irradiation and characterization. J. Sci. Univ. Kelaniya **6**, 65–75 (2011)

Priya, M.R.K., Iyer, P.R.: Extracellular rapid biosynthesis of gold nanoparticles using various green extracts of plants. Int. J. Mol. Biol. Biochem. **2**, 33–40 (2014a)

Priya, M.R.K., Iyer, P.R.: Anticancer studies of the synthesized gold nanoparticles against MCF 7 breast cancer cell lines. Appl. Nanosci. **5**, 443–448 (2014b)

Priya, M.R.K., Iyer, P.R.: Studies on the various parameters underlying the Synthesis of nanoparticles and the *in-vitro* stability of nanoparticles. Front. Biotechnol. 1–4 (2014c)

Priya, M.R.K., Iyer, P.R.: Applications of the green synthesized gold nanoparticles-antimicrobial activity, water purification system and drug delivery system. Symbiosis 1–4 (2015a)

Priya, M.R.K., Iyer, P.R.: Comparitive study on the characterisation of gold nanoparticles synthesized using various plant extracts. Int. J. Phytother. **5**, 17–21 (2015b)

Priya, M.R.K., Iyer, P.R.: Anti-cancer study in hela cell lines of phytosynthesized gold nanocompounds using A*ndrographis paniculata* (nilavembu) - characterisation, optimization, phytochemical analysis & anti microbial study. Indian J. Appl. Res. **9**, 24–27 (2019)

Lu, Z., et al.: Experimental study on the apoptosis of cervical cancer Hela cells induced by juglone through c-Jun N-terminal kinase/c-Jun pathway. Asian Pac. J. Trop. Med. **10**, 1–4 (2017)

Li, J., et al.: Aqueous extract of Solanum nigrum inhibit growth of cervical carcinoma (U14) via modulating immune response of tumor bearing mice and inducing apoptosis of tumor cells. Fitoterapia **79**, 548–556 (2008)

Mukunthan, K.S., et al.: Catharanthus roseus: a natural source for the synthesis of silver nanoparticles. Asian Pac. J. Trop. Biomed. **1**(4), 270–274 (2011)

Song, J.Y., et al.: Biological synthesis of gold nanoparticles using Magnolia kobus and Diopyros kaki leaf extracts. Process Biochem. **44**, 1133–1138 (2009)

Bhumkar, D.R., et al.: Chitosan reduced gold nanoparticles as novel carriers for transmucosal delivery of insulin. Pharmac. Res. **24**(8), 1415–1426 (2007)

Panyam, J., Labhasetwar, V.: Biodegradable nanoparticles for drug and gene delivery to cells and tissue. Adv. Drug Deliv. Rev. **55**, 329–347 (2003)

Nagajyothi, P.C., et al.: Green synthesis: In-vitro anticancer activity of copper oxide nanoparticles against human cervical carcinoma cells. Arab. J. Chem. **10**, 215–225 (2017)

Tabatabaei Mirakabad, F.S., et al.: A Comparison between the cytotoxic effects of pure curcumin and curcumin-loaded PLGA-PEG nanoparticles on the MCF-7 human breast cancer cell line. Artif. Cells Nanomed. Biotechnol. **44**, 1–8 (2014)

Sahoo, S.K., et al.: Residual polyvinyl alcohol associated with poly D L lactide coglycolide nanoparticles affects their physical properties and cellular uptake. J. Control. Release **82**, 105–114 (2002)

One Step Synthesis of Reduced and *Moringa oleifera* Treated Graphene Oxide: Characterization and Antibacterial Studies

R. Kanish Siddarth[1], M. Manopriya[1], G. Swathi[1],
G. Vijayvenkataraman[2], and K. R. Aranganayagam[3(✉)]

[1] Department of Biotechnology, Kumaraguru College of Technology,
Coimbatore 641049, Tamilnadu, India
[2] Department of Textile Technology, Kumaraguru College of Technology,
Coimbatore 641049, Tamilnadu, India
[3] Department of Chemistry, Kumaraguru College of Technology,
Coimbatore 641049, Tamilnadu, India
aranganayagam@gmail.com

Abstract. Reduced graphene oxide (rGO) was synthesised by the direct one-step synthesis using modified Hummers method. Synthesized rGO was treated with *Moringa oleifera* plant extract (MO-rGO). The synthesized rGO and MO-rGO were characterised using Fourier Transform Infrared (FTIR), Raman spectroscopy, X-ray Diffraction (XRD), Scanning Electron Microscope (SEM) and High Resolution Transmission Electron Microscope (HRTEM) along with Energy Dispersive X-ray Spectroscopic analyses (EDS). The formation of rGO and MO-rGO were studied using XRD. The presence of functional groups and structural behaviour was studied using FTIR and Raman spectroscopic studies. It is observed that the functional groups are incorporated in the synthesized samples and found to be the formation of rGO. The morphology and elemental compositions of the synthesized rGO's were studied using SEM, HRTEM and EDS, respectively. In order to understand the bacterial activity of synthesized rGO's were tested against *E. Coli* and *S. Aureus*. The synthesized rGO's shows the better efficiency than graphite.

Keywords: Reduced graphene oxide (rGO) · XRD · *Moringa oleifera* · Raman spectroscopy · Direct synthesis

1 Introduction

Graphene is a 2D monolayer structure which is hexagonally arranged sp2 bonded carbon atom [1]. It is the only carbon form in which each atom is in exposure for bonding [2]. The British chemist, B.C. Brodie discovered a highly oxidised form of graphite known as "graphon" that is graphene oxide [3]. Huge specific surface area conjugated aromatic ring structure, good dispersion characteristics in water and excellent stability are some notable characteristics of Graphene oxide (GO) [4]. The synthesis of graphene and graphene oxide has been a benchmark achievement due it its application in various fields. It is known for its unique chemical, electrical, optical and

mechanical properties. Several procedures are prevailing for the production of graphene products like chemical vapour deposition, mechanical or ultrasonic exfoliation, microwave irradiation, solvothermal reduction and chemical reduction of graphene oxide (GO) [5]. The reduction of graphene to graphene oxide can be done in many methods but wet reduction method is preferred as it is commercially feasible. The other methods are expensive and bulk production is not possible. The wet reduction method uses reducing agents like hydrazine, sodium borohydride, dimethylhydrazine, hydroquinone etc. It is used to prevent irreversible stacking of the reduced graphene oxide during reduction process. These reducing agents are toxic and have detrimental effects on human body if it's used in application on biological processes. The association of hazardous chemical reducing agents in the reduction step is a major disadvantage and ongoing efforts are there to find alternative methods [6]. Thus, we are in the need to develop a non-toxic and eco-friendly method due to its extensive application, its thermal stability, high intrinsic mobility, electrical conductivity and high specific surface area. *Moringa oleifera* commonly known as drumstick plant is native to India. It grows in tropical and sub-tropical areas which are known for its high nutritive values. Each part of this plant has high medical values. The leaves are rich in minerals, essential phyto chemicals and vitamins. It is used as potential antioxidants, phytochemicals, anti-diabetic, anti-cancer and anti-inflammatory agent [7].

In this paper, attempts were made to synthesis of reduce graphene oxide in one step and it was achieved by making alterations in methodology. Further, it was treated with *Moringa oleifera* leaves extract rich in calcium. Physicochemical characterisation of as-synthesised reduced graphene oxide and treated graphene oxide were studied using XRD, FTIR spectroscopy, Raman spectroscopy, SEM, HR-TEM and EDS and the results were compared. Further, the antibacterial activities of synthesised samples were also discussed.

2 Materials and Methods

All the chemicals were used for this study are Analar grade and used as such. Solvents were purified under standard procedures.

2.1 Synthesis of reduced Graphene Oxide (rGO)

Graphene oxide and reduced graphene oxide sheets were prepared by using Modified Hummers method from graphite [8]. Graphite (6 g) and Sodium nitrate (NaNO$_3$, 2 g) were mixed with 100 ml of conc. sulphuric acid (H$_2$SO$_4$, 95%). The mixture was stirred vigorously for about 2 h in an ice bath. 12 g of potassium permanganate (KMnO$_4$) was slowly added to the above mixture with vigorous stirring and the temperature is maintained below 20 °C. The stirring was continued for about 4 h until and brown pasty mixture was formed while 100 ml of doubly distilled water was slowly added and stirred for an additional 45 min. The action temperature was rapidly increased to 98 °C and 50 ml of 30% H$_2$O$_2$ was added when the colour changed from dark purple to brilliant yellowish brown. Then the mixture was heated on a hot plate until the total volume was reduced to less than 60 ml. The product was washed with

5% HCl and deionised water and filtered using Whatman 4 filter paper. The resultant product was centrifuged at 15000 rpm and the product was collected and labled.

2.2 Extract Preparation of *Moringa oleifera*

The leaves of *Moringa oleifera* was collected and washed several times with distilled water. The fresh leaves were crushed and grinded using a mortar and pestle. The crushed leaves were mixed with ethanol and heated gently for about 90 m with constant stirring. The heated plant extract was filtered using Whatmann 1 filter paper. The collected filtrate was used to prepare rGO composite.

2.3 Preparation of *Moringa oleifera* Treated rGO Composite

The prepared rGO (Sect. 2.1) was added to the *Moringa oleifera* leaves extract (80:20 ratio) and the mixture was stirred for about 12 h at RT. The reaction mixture was centrifuged and the product was collected and tested.

2.4 Antibacterial Activity

The antibacterial testing was performed against human pathogenic Gram –ve (*E. Coli*) and Gram +ve (*S. Aureus*) by agar well diffusion method. Sample discs are soaked overnight in sample solution, 100 µg and standard Ciprofloxacin was used against these bacteria, 10 µg, are placed with the help of sterile forceps. Then Petri dishes are refrigerated at 4 °C or at room temperature for 1 h for diffusion. The dishes are also incubated at 37 °C for 24 h. Observe the zone of inhibition produced by different samples.

2.5 Characterisation Techniques

X-ray diffraction studies were carried out in the range of 20 to 80 degree using Shimadzu 6100 X-ray diffractometer with CuKα. FTIR was recorded in the range of 400 to 4000 cm^{-1} using BRUKER Optik GmbH. SEM micrographs were captured from JEOL, Japan. HRTEM were recorded using JEOL JEM 2100 high resolution scanning electron microscope.

3   Results and Discussion

3.1 FTIR Analysis

FTIR spectra of graphite, reduced graphene oxide (rGO) and *Moringa oleifera* treated rGO (MO-rGO) are shown in the Fig. 1. From the FTIR spectra, the broad peak around 3428 cm^{-1} was observed in graphite sample due to the extensive oxidation and absorption of water molecule and it was accounted for O-H stretching vibration. The medium broad peak was observed at 2998 and 2815 cm^{-1} may be attributed to asymmetric and symmetric stretching vibration of C-H groups in the samples. The presence of C = C and C = O vibration was observed at 1714 cm^{-1}. Notably, the peak

intensity is weak in graphite and strong in rGO and MO-rGO, confirms the formation of rGO and the plant extract were played a role in terms of surface functionalization results the formation rGO and MO-rGO from graphite. Also, epoxy C-O-C vibrations were observed at 1560 cm^{-1}. It is not found in pure graphite sample, shows the oxidation processes done in the sample. The bending vibration of epoxy C-OH was observed at 1270 cm^{-1} and the peak intensity was increased after the reaction and treatment with MO. The intensity of the peaks in rGO and MO-rGO is much higher than the graphite peaks. These results indicate that rGO is obtained by reduction of graphite and it has undergone a reaction with *Moringa oleifera* extract.
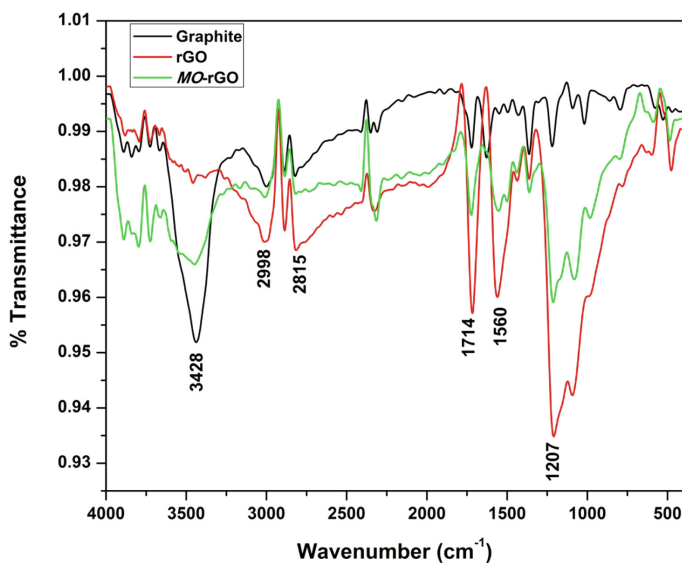
Fig. 1. FTIR spectrum

3.2 Raman Spectroscopic Studies

Raman spectroscopic analysis has been carried ooout to understand the structural behaviour and the quality of the synthesised rGO and MO-rGO samples. It is observed from Fig. 2, for graphite sample a strong peak at 1568 cm^{-1} (G band) and small two peaks at 1358 (1D band), 2709 cm^{-1} (2D band) are attributed to the first order scattering and second order resonant process, respectively. In rGO, strong two bands are observed at 1358 cm^{-1} (D) and 1599 cm^{-1} (G) due to the strong oxidation and high thermal process [9]. The intensity ratio of the D and G bands in rGO is increased than graphite. This relative intensity ratio (I_D/I_G) increased from 0.20 to 1.007 due to the elimination of defects in the synthesized rGO [10].
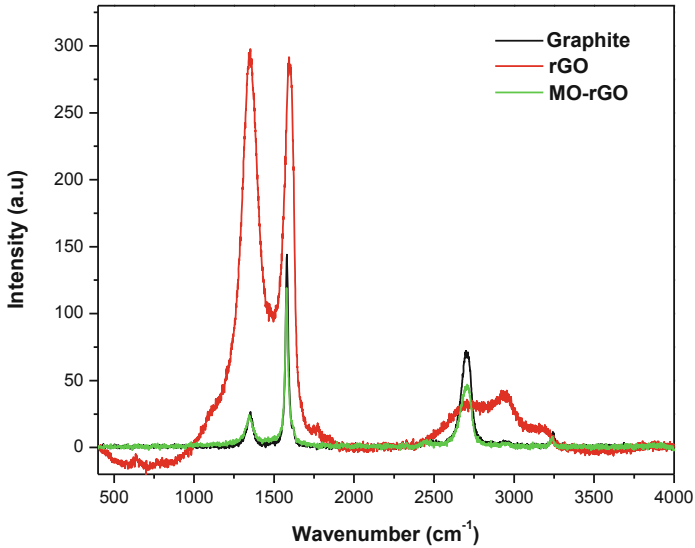
Fig. 2. Raman spectra of synthesised samples

3.3   XRD Analysis

In order to understand the phase structure of synthesised materials, XRD analysis was performed and showed in Fig. 3. XRD pattern of pure graphite peaks are indexed with the support of JCPDS card no. 41-1487. XRD result reveals that the sharp peak is observed at $2\theta = 26.3226$ which is attributed to (002) plane of graphite with the d spacing of 0.38 nm. Notably during the oxidation process, the graphene oxide peak (around $2\theta = 10.52$) is not appeared, instead a broad peak in the range of 24.3034 with d-spacing of 0.36 nm was observed. This may be due to the formation of residual oxygen functionalities in rGO sheets [6, 11]. It is suggested that peak broadening in the rGO and the difference in the d spacing values (0.01 nm) may attributed to formations of layers/sheets. Also, the proposed reaction scheme is help to synthesis directly rGO. The layer to layer distance increases significantly for rGO compared to graphite due to the presence of residual O_2 and H [12].
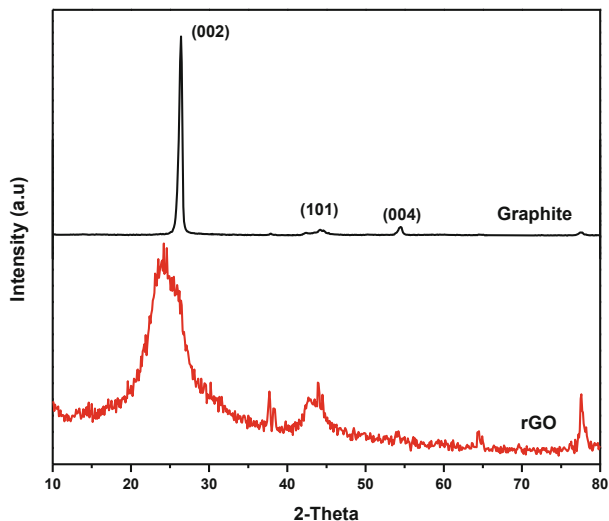
Fig. 3. XRD pattern of graphite and rGO

3.4 Morphological Analysis

The morphology of graphite, rGO and MO-rGO were analysed using SEM, HRTEM and the elemental compositions were recorded using enrgy dispersive X-ray spectroscopic technique (EDS) are depicted in Figs. 4 and 5. From the Fig. 4(a–c), SEM images of rGO and MO-rGO shows layers of sheets stacked over one another and are aggregated to some extent. The treated rGO's SEM image shows partial formation of rod structure which are again aggregated to some degree. Evidently, more number of wrinkles and foldings indicate greater reduction rate. HRTEM micrograph (Fig. 4d–f) clearly shows the smooth layers of graphite stacked each other without any wrinkles and folding. Transparent portion of images are represented as single layer and the dark portion of images are due to the folding/multiple sheets. Whereas, in rGO shows some lattice fringes of graphene and there are wrinkles and folds which conforms the formation of reduced Graphene oxide. In MO-rGO, the wrinkles and folds have decreased when its compared with graphite and rGO. This confirms the interaction and chemical modifications occurred between the leaf extract and reduced Graphene oxide. Also, the corresponding SAED pattern (inset of Fig. 4d–f) shows the clear distribution of electrons in the crystallographic structure of Graphite, reduced Graphene oxide and *Moringa oleifera* treated reduced Graphene oxide.
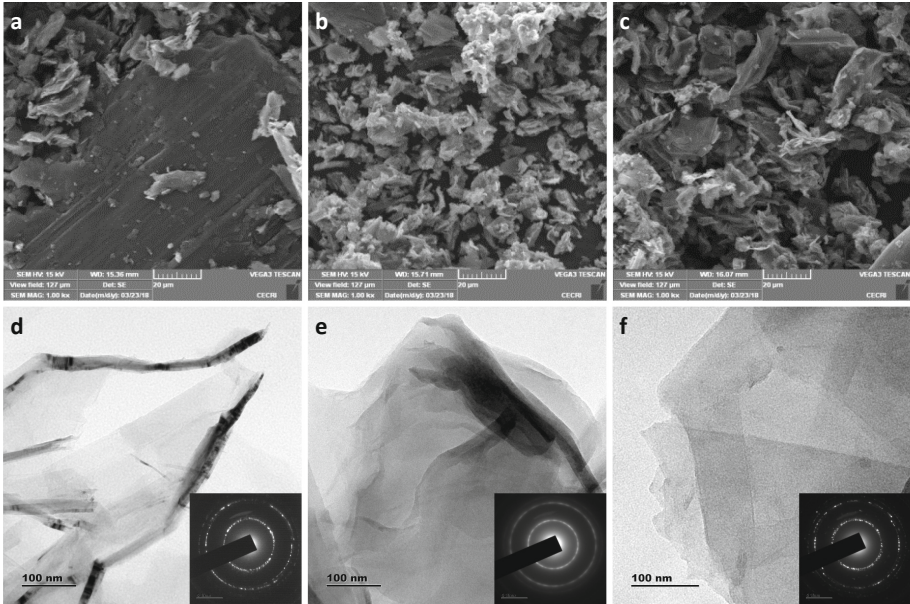
Fig. 4. SEM Images of (a) Graphite, (b) rGO (c) MO-rGO; HRTEM images (d) Graphite, (e) rGO (f) MO-rGO

The EDS spectrum for graphite, rGO and MO-rGO is listed in Table 1 and illustrated in Fig. 5. The constituents of graphite and rGO are carbon and the related signals are found to be high in graphite for about 98.50% when compared to rGO. Whereas, MO-rGO, calcium signals was observed. This may be due to the calcium mineral in the leaves extract is highly influenced the structure of rGO.
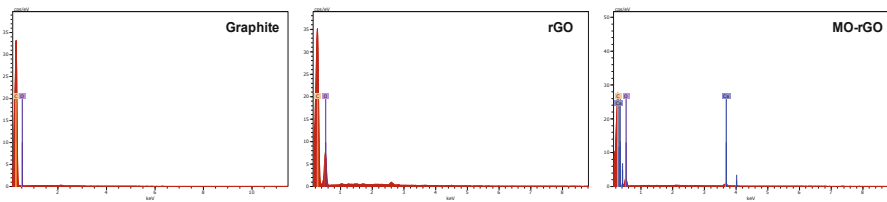
Fig. 5. EDS spectrum of samples

Table 1. EDS and anti bacterial studies data

Samples	EDS DATA			Biological Studies	
	Atomic wt%			ZOI (mm)	
	C	O	Ca	*E.Coli*	*S. Aureus*
Graphite	98.50	1.50	–	6 (18)	3 (14)
rGO	74.38	25.62	–	9 (18)	7 (14)
MO-rGO	84.47	14.95	0.58	12 (18)	9 (14)

3.5 Antibacterial Studies

Antibacterial studies were carried out against the human pathogenic Bacteria E.Coli and S. Aureus. The zones of inhibition (ZOI) are listed in the Table 1, Ciprofloxacin was used as a standard and the respective ZOI are given in bracket. The experimental ZOI of the synthesised rGO and MO-rGO showed the better results than graphite. This may be due to the active functional groups on the surface of graphene.

4 Conclusion

One step direct reduced graphene oxide (rGO) was synthesised by using improved and modified Hummers method. *Moringa oleifera* plant extract was used to treat the synthesised rGO (MO-rGO). The synthesised rGO and MO-rGO were characterised. XRD studies clearly show the formation of rGO with well defined bragg peaks. The results of FTIR and Raman spectra confirm the presence of oxygen functionalities in the synthesised samples and the interaction of plant extract towards the structural behaviour was studied. The layered rGO sheets with modifications were seen in the samples shows that the formation of rGOs from graphite. It is also coincides with the EDS analysis. Enhancement in the bacterial activity of synthesised rGO's against E. Coli and S. Aureus was observed. The proposed methodology for the synthesis of rGO can be used for bulk production.

References

1. Chu, H.J., Lee, C.Y., Tai, N.H.: Green reduction of graphene oxide by Hibiscussabdariffa L. To fabricate flexible graphene electrode. Carbon **80**, 725–733 (2014)
2. Agharkar, M., Kochrekar, S., Hidouri, S., Azeez, M.A.: Trends in green reduction of graphene oxides, issues and challenges: a review. Mater. Res. Bull. **59**, 323–328 (2014)
3. De Silva, K.K.H., Huang, H.H., Joshi, R.K., Yoshimura, M.: Chemical reduction of graphene oxide using green reductants. Carbon **119**, 190–199 (2017)
4. Chowdhury, S., Balasubramanian, R.: Recent advances in the use of graphene-family nanoadsorbents for removal of toxic pollutants from wastewater. Adv. Coll. Interface. Sci. **204**, 35–56 (2014)
5. Hou, D., Liu, Q., Cheng, H., Li, K., Wang, D., Zhang, H.: Chrysanthemum extract assisted green reduction of graphene oxide. Mater. Chem. Phys. **183**, 76–82 (2016)
6. Upadhyay, R.K., Soin, N., Bhattacharya, G., Saha, S., Barman, A., Roy, S.S.: Grape extract assisted green synthesis of reduced graphene oxide for water treatment application. Mater. Lett. **160**, 355–358 (2015)
7. Gopalakrishnan, L., Doriya, K., Kumar, D.S.: Moringaoleifera: a review on nutritive importance and its medicinal application. Food Sci. Hum. Wellness **5**(2), 49–56 (2016)
8. Marcano, D.C., Kosynkin, D.V., Berlin, J.M., Sinitskii, A., Sun, Z., Slesarev, A., Alemany, L.B., Lu, W., Tour, J.M.: Improved synthesis of graphene oxide. ACS Nano **4**(8), 4806–4814 (2010)
9. Kudin, K.N., Ozbas, B., Schniepp, H.C., Prud'Homme, R.K., Aksay, I.A., Car, R.: Raman spectra of graphite oxide and functionalized graphene sheets. Nano Lett. **8**(1), 36–41 (2008)

10. Abdolhosseinzadeh, S., Asgharzadeh, H., Kim, H.S.: Fast and fully-scalable synthesis of reduced graphene oxide. Sci. Rep. **5**, 10160 (2015)
11. Yu, H., Zhang, B., Bulin, C., Li, R., Xing, R.: High-efficient synthesis of graphene oxide based on improved hummers method. Sci. Rep. **6**, 36143 (2016)
12. Husnah, M., Fakhri, H.A., Rohman, F., Aimon, A.H., Iskandar, F.: A modified Marcano method for improving electrical properties of reduced graphene oxide (rGO). Mater. Res. Express **4**(6), 064001 (2017)

Encapsulation of Amphotericin B into Quercetin Based Silver Nanoparticles: Preparation, Characterization and Preliminary Investigation of Antiparasitic Activity

Anukragah Sundar[1], Sankarganesh Arunachalam[1], Sridhar Jayavel[2], and Lakshmanan Muthulakshmi[1,3(✉)]

[1] Department of Biotechnology, Kalasalingam Academy of Research and Education, Krishnankoil 626 126, Tamil Nadu, India
mthlakshmi27@gmail.com
[2] Department of Biotechnology, Madurai Kamaraj University, Madurai 625021, Tamil Nadu, India
[3] Department of Materials Science, Madurai Kamaraj University, Madurai 625021, Tamil Nadu, India

Abstract. *Terminalia catappa* is a medicinal plant, belongs to the *Combretaceae* family, enriched with potential bioactive compounds and exhibits broad-spectrum of pharmacological activity. The leaves possess antihepatic, antibacterial, antiparasitic and anti-inflammatory properties. It contains Quercertin, Punicalagin and Punicalin as major compounds having strong antioxidant activities and being traditionally used to treat many diseases. Amphotericin B (AmB) is a macrolide polyene antifungal drug used to treat the life threatening fungal and parasitic diseases. We prepared nanoformulated drug by using silver nanparticles (AgNPs) and (AmphotericinB) AmB. The prepared nanoformulations were characterized by UV and FTIR. Interactions between AmB with AgNPs are confirmed by their morphological characteristics obtained from SEM images. Antifungal activity of the prepared nanoformulation was tested against the plant fungal pathogen *Verticillium dahlia,* which has confirmed its potential antifungal property. Interestingly, anti-promastigote activity of the nanoformualtion (500-1.9 μg/ml) was identified against *L. donovani* parasites. Preliminary investigation on the results has suggested that these nanoformulation exhibits potent antifungal and antiparasitic activities compared with the standard AmB.

Keywords: *Terminalia catappa* · Silver nano particles · Amphotericin B

1 Introduction

Plant is a good source for identification of novel drugs. The commercially available drugs cause side effects and poor clinical strength leads to number of severe complications. In order to combat all these problems, commercially available synthetic drugs are replaced and focused to develop a new kind of traditional drugs from natural sources [1]. Novel strategies are followed to improve the efficacy of drugs by adopting

techniques like nanoformulations. Combinations of drugs from natural sources with nanoparticles are promising strategy against parasites. The leaf extracts of *Ixora coccinea* has been shown to possess anti-leishmanial activity against the promastigotes of *L. Donovani* [2]. The root extract of *Perovskia abrotanoides* showed good level of anti-leishmanial activities [3]. The anti-leishmanial activities of *Aloe Vera* leaf and *Tamarix aphylla* bark extracts are reported [4]. New kind of nanoformulation was prepared from *Terminalia catappa* and evaluated against parasites in this study. The leaves of *T. catappa* contain several flavonoids (such as Kaempferol or Quercetin) and Tannins (such as Punicalin, Punicalagin or Tercatin) [5]. The leaves possess antioxidant, anti-cancer, antidiarrheic, antihepatatoxic, antifungal and antiparasitic properties. Due to the presence of diverse secondary metabolites, the formulations from *T. catappa* leaves are used to treat liver diseases [6].

The metal nanoparticles are having an increased surface to volume ratio and ability to bind easily with sulfur and phosphorus containing groups which enhances the anti-leishmanial activities [7]. Number of reports highlighted the applications of AgNPs in treating parasitic infections. For considering increased total surface area and slow release of ions, it easily protects the wound from parasitic and bacterial infections. AmB is a potent polyene antifungal drug, it binds with ergosterol of fungal cell membrane and induces the membrane damage and ion leakage leads to fungal cell death [8]. The continuous administration of AmB causes serious renal toxicity. Hence, we need to look for the alternative strategy to avoid the toxic effects of AmB without compromising on the antiparasitic activity. The scope of this study is to prepare nanoformualtion from quercetin based biogenic AgNP in combination with AmB drug. The antifungal activity of nanoformulation was tested against *Verticillium dahlia*. The preliminary anti-promastigote activity of nanoformualtion was tested against *L. donovani*.

2 Materials and Methods

2.1 Materials

The required materials Amphotericin B drug and silver nitrate were purchased from Sigma Aldrich, India. Nanoparticle synthesis and nanoformualtion of drugs carried out with Milli-Q water (Millipore).

2.2 Preparation of AmB-AgNP Nanoformulations

20 ml of leaf extract was mixed with 80 ml of (5 mM) silver nitrate added with 0.2 µg AmB and kept in a shaking incubator for 48 h at room temperature. The sample was collected at different time intervals for analysis of AmB-AgNP entrapments by UV/VIS spectrophotometry. Aggregated AmB-AgNP nanoformulation was centrifuged at 10,000 rpm at 4 °C for 15 min and the pellet was collected for further studies.

2.3 Characterization of AmB-AgNP Nanoformualtion

2.3.1 UV/Visible Spectrum Analysis

The drug encapsulation efficiency of nanoformualtion was analyzed by UV/Visible spectrometer (UV-mini, Shimadzu, Japan) and the wavelength recorded in the range of 200–600 nm.

2.3.2 FTIR Analysis

The interaction between the nanoformualtion was analyzed with SHIMADZU FT-IR spectrometer in the range of 400 to 4000 cm^{-1} by KBr pellet method.

2.3.3 Scanning Electron Microscopic Observation of AmB-AgNP Nanoformualtion

The surface morphology of encapsulated AmB-AgNP nanoformualtion was analyzed with Zeiss 018 SEM at an accelerating voltage of 300 kV.

2.3.4 Antifungal Activity of AmB-AgNPs Nanoformulation

The antifungal activity of AmB-AgNP nanoformulation was determined by the disc diffusion method. The overnight grown *Verticillium dahlia* was inoculated in to the Potato Dextrose Agar (PDA) plates and the sterile discs having a diameter of 2 mm were impregnated with 30 μl of sample and were placed on the surface of PDA plates. The plates were then incubated at 22 °C for 48 h to observe the antifungal activity by the zone of inhibition (mm) produced by the samples and the results were compared with control.

2.3.5 *In Vitro* Cytotoxicity of AmB-AgNP Nanoformulation Against *L. Donovani* (Dd8 Strain) *Parasites* by MTT Assay

The 1×10^6 cells/100 μl/well of *Leishmania donovani* (Dd8 strain) parasite were plated in 96-well plate and further treated with the different concentrations (500-1.9 μg/ml) of AmB formulated AgNPs. The plate was kept in a B.O.D. incubator for 48–72 h at 26 °C. After the incubation period the plate was centrifuged at 3500 rpm for 10 min at room temperature. The supernatant was discarded and 50 μl of MTT solution (0.5 mg/ml) was added to each well kept in a dark condition for 4–5 h at 37 °C. The formazan crystals were dissolved by adding 100 μl of DMSO and absorbance was measured at 570–690 nm after 10–15 min.

3 Results and Discussion

3.1 UV/VIS Analysis

The Surface Plasmon Resonance (SPR) of AmB-AgNPs were detected from the range of 400–500 nm. *T. cattappa* leaf extract was found to reduce the silver nitrate solution and the strong peak was observed at 428 nm (Fig. 1a). The sharp peak indicates the formation of AgNPs. In the case of AmB entrapped AgNPs (Fig. 1b) the λ$_{max}$ was observed at 428 nm. The AgNP peaks are slightly shifted and the broadened SPR peak

were noted at 339 nm, 369 nm and 421 nm (Fig. 1b) this peak was compared with standard drug AmB. The maximum absorbances (λmax) of AmB were noted at 384 nm and 406 nm [9].
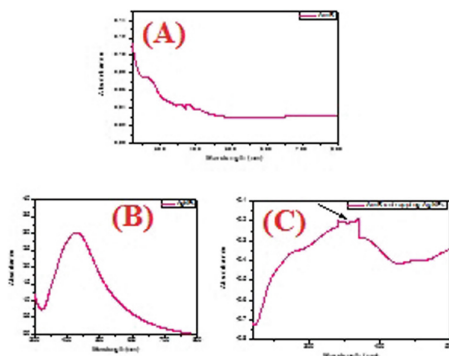
Fig. 1. UV/Vis Spectroscopic analysis of (A) AmB (B) AgNP (C) AmB-AgNP

3.2   Morphological Analysis of AmB-AgNP

The morphology of AmB-AgNPs and interactions are confirmed with scanning electron microscopic images. The micrographs (see Fig. 2a), shows that the control drug–AmB (35.00KX 200 nm). The image (see Fig. 2b), confirmed the reduction and formation of spherical shape of nanoparticles within the range of 23–100 nm (60.00 KX, 100 nm) by using the *T.cattappa* leaf extract. The micrograph (see Fig. 2c) shows the nanoformulated AmB - AgNP (35.00 KX 300 nm) indicates the well interactions of AgNP and the Amphotericin B drug. The efficiency of encapsulated AmB into AgNPs are well observed in (see Figs. 2b and 3c). The image reveals that the entrapment of AmB on the surface of AgNP and the established porosity was observed. This porosity is due to the amorphous nature of the prepared nanoformulation, which proved that the drug loaded nanoparticles are good source for sustained drug delivery systems, with their sizes in nano range required for its parental chemotherapy [10].

3.3   FTIR Analysis

An FTIR spectrum reveals the reduction of AgNP by the presence of *T. cattappa* leaf extract compounds quercetin and other functional compounds. These compounds are responsible for the reduction and generation of AgNPs (see Fig. 3b). The observed intense peak of AmB-AgNP interactions were compared with control (AmB). The observed results of FTIR bands showed at graph (a) the peaks 1784 cm^{-1} and 1188 cm^{-1} represents the presence of C-O and C–O bonds and the peak at 1041 cm^{-1} confirms the C–OH bond present in the AmB. The graph (b) indicates the generated
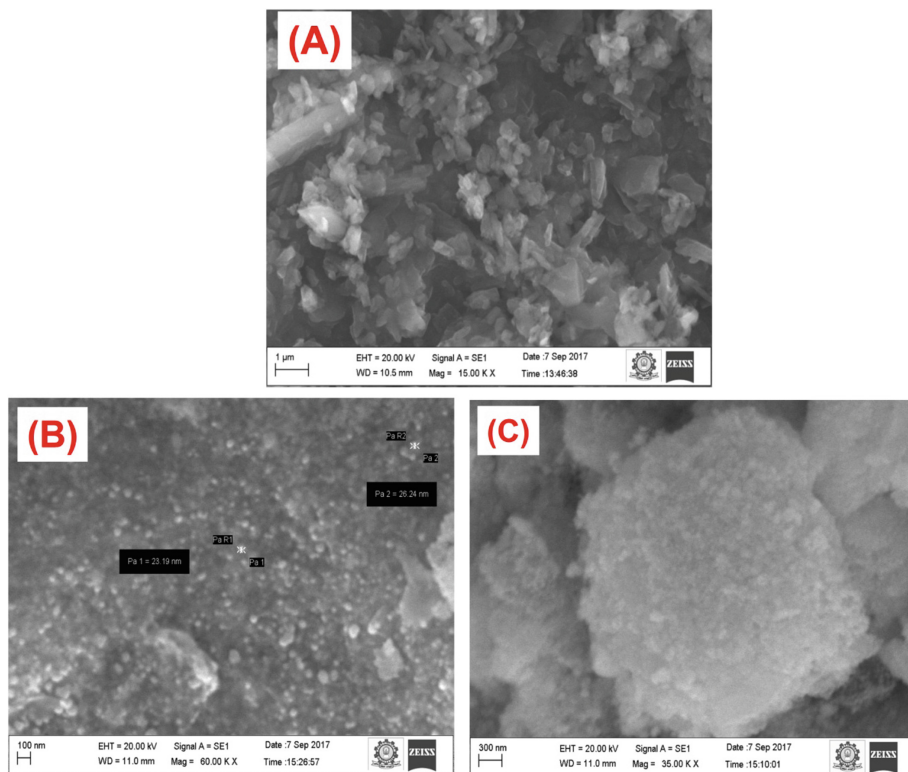
Fig. 2. SEM images of (a) AmB (b) AgNP (c) AmB-AgNP

AgNP in the FTIR Spectrum of absorption band at 2881 cm^{-1}, 2823 cm^{-1}, 1718 cm^{-1}, 1323 cm^{-1}, 1066 cm^{-1}. The drug loaded silver nanoparticles exhibit peaks at 3836 cm^{-1}, 3662 cm^{-1}, 2881 cm^{-1}, 2360 cm^{-1}, 666 cm^{-1}, 1489 cm^{-1}, 1323 cm^{-1}, 1172 cm^{-1}, 1066 cm^{-1} and 1010 cm^{-1} which were observed respectively in graph (c). Above results, slightly confirmed the presence of functional compounds in the nanoformualted AmB-AgNP [11].

3.4 Antifungal Activity of AmB-AgNP Nanoformualtion Against *Verticillium Dahliae*

Figure 4 depicts the zone of clearance of the prepared AmB-AgNP nanoformuation compared with same amount of standard drug AmB with biogenic AgNPs. The observed results indicates the inhibition of fungal growth by the drug AmB (2 mm) but the enhanced biogenic activity was noted in AmB loaded AgNPs. Silver ions are widely applied in combination with drugs to enhance the biological activity. Based on the observed results nanoconjugated drugs are suitable antifungal agents. The AmB-AgNP nanoformulation were released into the mitochondrial membrane and bind with
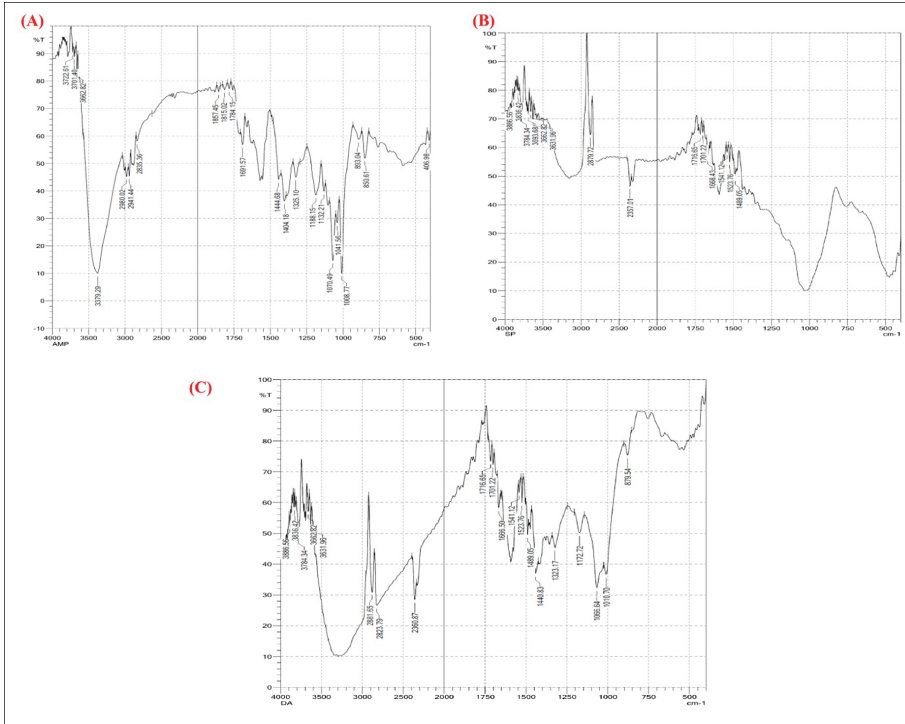
Fig. 3. FTIR analysis of (a) AmB (b) AgNP (c) AmB-AgNP

the parasitic enzymes and proteins inside the membrane and make a complex and looking forward to damage the parasites and the infection rate of parasites were reduced because of AmB-AgNP interactions [12].

3.5 Efficacy of Nanoformulation (AgNPs with AmB Drug) on *L. Donovani* Promastigote by MTT Assay

The AmB-AgNP nanoformulation (500-1.9 μg/ml) anti-leishmanial efficacy was analyzed against promastigote and the maximum cell death was noted below 3 μg/ml of nanoformulation. The complete cell death was noted at highest concentration of AmB-AgNP nanoformulation. Preliminary investigation of the antiparasitic efficacy of AmB-AgNP nanoformulation was evaluated against *L. donovani* parasites by MTT assay (Fig. 5).
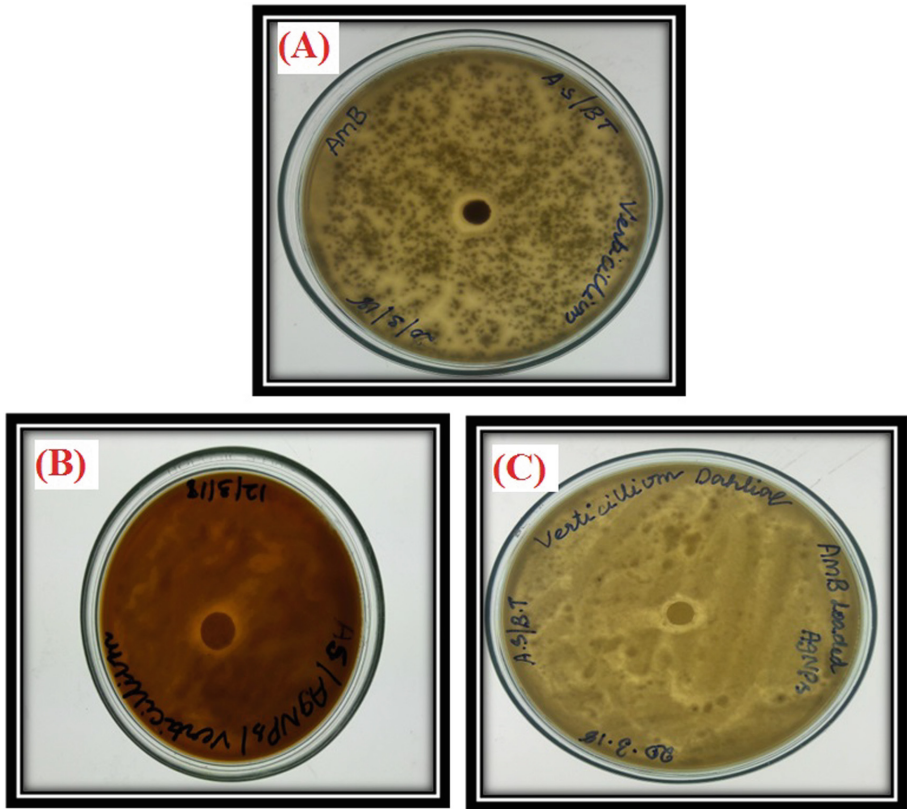
Fig. 4. Antifungal activity of (a) AmB (b) AgNP (c)AmB-AgNP
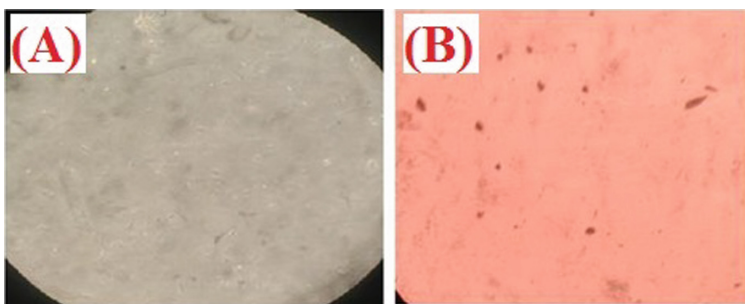
Fig. 5. Antiparasitic activity of (a) *L. donovani* (b) *L. donovani* were exposed to AmB-AgNP nanoformulation black colour dots indicates the promastigotes death.

4 Conclusion

Presence of diverse bioactive metabolites in the medicinal plants makes them as suitable choice for treating many diseases. Presence of Quercertin, Kaempferol and other secondary metabolites in *T. cattapa* leafs has triggered us to evaluate their antiparasitic activity along with nanoformulations. Preliminary investigation on antiparasitic activity of AmB-AgNPs nanoformulation was carried out by MTT assay. Further, the antiparasitic activity of the biologically synthesized AgNP from *T. catappa* is compared with AmB-AgNP nanoformulation through UV, FTIR and SEM analysis. The antifungal activity of AmB-AgNP was reported from this study against *Verticillium dahlia*. Overall, our investigation implies that traditional antibiotic AmB along with AgNPs synthesized with *T. catappa* plant extract might be applied as potent antifungal and antiparasitic agent.

References

1. Ullah, N., Nadhman, A., Siddiq, S., Mehwish, S., Islam, A., Jafri, L., Hamayun, M.: Plants as antileishmanial agents: current scenario. Phytother. Res. **30**(12), 1905–1925 (2016)
2. Naskar, M., Bhattacharya, S., Biswas, M.: Antileishmanial effect of Ixora coccinea leaf extracts on the in vitro growth of Leishmania donovani promastigotes. J. Adv. Pharm. Educ. Res. **3**(4), 471–474 (2013)
3. Jaafari, M.R., Hooshmand, S., Samiei, A., Hossainzadeh, H.: Evaluation of leishmanicidal effect of perovskia abrotanoides karel. Root extract by in vitro leishmanicidal assay using promastigotes of Leishmania major. Pharmacology Online **1**, 299–303 (2007)
4. Iqbal, H., et al.: Comparative efficacy of *Aloe vera* and *Tamarix aphylla* against cutaneous leishmaniasis. Int. J. Basic Med. Sci. Pharm. **2**(2), 42–45 (2012)
5. Venkatalakshmi, P., Vb, V.: Identification of flavonoids in different parts of *Terminalia catappa L.* Using LC- ESI-MS/MS and investigation of their anticancer effect in EAC cell line model. J. Pharmac. Sci. Res. **8**(4), 176–183 (2016)
6. Tang, X.H., Gao, L., Gao, J., Fan, Y.M., Xu, L.Z., Zhao, X.N., Xu, Q.: Mechanisms of hepatoprotection of *Terminalia catappa L.* extract on D-galactosamine-induced liver damage. Am. J. Chin. Med. **32**(4), 509–519 (2004)
7. Allahverdiyev, A.M., Abamor, E.S., Bagirova, M., Ustundag, C.B., Kaya, C., Kaya, F., Rafailovich, M.: Antileishmanial effect of silver nanoparticles and their enhanced antiparasitic activity under ultraviolet light. Int. J. Nanomed. **6**, 2705–2714 (2011)
8. Zia, Q., Khan, A.A., Swaleha, Z., Owais, M.: Self-assembled Amphotericin B-loaded polyglutamic acid nanoparticles: preparation, characterization and *in vitro* potential against *Candida albicans*. Int. J. Nanomed. **10**, 1769–1790 (2015)
9. Ahmad, A., Wei, Y., Syed, F., Khan, S., Khan, G.M., Tahir, K., Yuan, Q.: Isatistinctoria mediated synthesis of amphotericin B-bound silver nanoparticles with enhanced photo induced antileishmanial activity: a novel green approach. J. Photochem. Photobiol. B **161**, 17–24 (2016)
10. Prajapati, V.K., Awasthi, K., Gautam, S., Yadav, T.P., Rai, M., Srivastava, O.N., Sundar, S.: Targeted killing of *Leishmania donovani in vivo* and *in vitro* with Amphotericin B attached to functionalized carbon nanotubes. J. Antimicrob. Chemother. **66**(4), 874–879 (2011)

11. Vaghela, R., Kulkarni, P.K., Osmani, R.A.M., Varma, V.N.S.K., Bhosale, R.R., Raizaday, A., Hani, U.: Design, development and evaluation of mannosylated oral Amphotericin B nanoparticles for anti-leishmanial therapy: oral kinetics and macrophage uptake studies. J. Drug Deliv. Sci. Technol. **43**, 283–294 (2018)
12. Ahmad, A., Wei, Y., Syed, F., Tahir, K., Taj, R., Khan, A.U., Hameed, M.U., Yuan, Q.: Amphotericin B-conjugated biogenic silver nanoparticles as an innovative strategy for fungal infections. Microb. Pathogen. **99**, 271–282 (2016)
13. Ahmad, A., Syed, F., Shah, A., Khan, Z., Tahi, K., Ullah Khana, A., Yuan, Q.: Silver and gold nanoparticles from Sargentodoxa cuneata: synthesis, characterization and antileishmanial activity. RSC Adv. **5**, 73793–73806 (2015)

Dual Delivery of Antibiotic and Antiresorptive Drugs by Hydroxyapatite-Chitosan Composite Nanocarrier for the Treatment of Osteomyelitis

S. Ram Prasad[1,2], A. Jayakrishnan[1], and T. S. Sampath Kumar[2(✉)]

[1] Biomaterials Laboratory, Department of Biotechnology,
Bhupat and Jyoti Mehta School of Biosciences,
Indian Institute of Technology Madras, Chennai, India
jayakrishnanl953@gmail.com

[2] Medical Materials Laboratory, Department of Metallurgical
and Materials Engineering, Indian Institute of Technology Madras,
Chennai 600 036, Tamil Nadu, India
tssk@iitm.ac.in

Abstract. Development of new bone-filling materials using hydroxyapatite (HA)-polymer composites are of much interest due to their similarity with bone minerals, as well as their osteoconductive, mechanical properties. It has been extensively used as a carrier for delivery of small molecules, growth factors and for tissue engineering and orthopedic applications. An attempt has been made to develop hydroxyapatite (HA)-chitosan (CH) nanocarrier for dual and sustained delivery of sodium alendronate (SA) (antiresorptive) and gentamicin (GEN) (antibiotic) for the treatment of osteomyelitis. HA were synthesized by wet chemical method and loaded with SA. CH was coated onto the drug loaded nanoparticles (NPs) with coating efficiency of 15%. GEN was physically adsorbed onto the CH coated SA loaded HA NPs. The drug content of SA and GEN was found to be 84% and 75% respectively. *In vitro* drug release studies reveled that there was sustained release of both GEN (87%) and SA (70%) for a period of 10 days. Sustained release of both the molecules from drug loaded NPs showed potent activity against Staphylococcus aureus (*S. aureus*) and Escherichia coli (*E. coli*) in concentration dependent manner. Simultaneous delivery of antibiotic and antiresorptive drugs using bioresorbable nanocarrier will enhance the treatment efficiency of osteomyelitis by inhibiting the bacterial infection in addition to bone formation.

Keywords: Hydroxyapatite · Osteomyelitis · Gentamicin ·
Sodium alendronate · Chitosan

1 Introduction

Osteomyelitis is an infection/inflammation of bone and soft tissue damage caused by infectious microorganisms such as gram positive (Staphylococcus aureus), gram-negative (Salmonella, Pseudomonas aeruginosa), strains of mycobacterium and fungi [1–3]. Standard treatment procedure for osteomyelitis involves surgical debridement,

removal of abscess and necrotic tissues, removal of implant and systemic administration of antibiotics followed by reconstruction of defective area by allograft, auto graft or implantation of artificial materials [4].

Oral and systemic antibiotic therapy is a traditional method for treating chronic osteomyelitis. High dose, systemic toxicity and expensive hospitalization are the major drawbacks in the conventional treatment regimen [3–5]. To overcome the limitations, past decades clinicians moved to local delivery of antibiotics to the target area. Local delivery of antibiotics using biodegradable and non-biodegradable carriers extensively studied for the treatment of bone infections particularly for osteomyelitis [3, 4]. Synthetic bone grafts substitute such as Simplex® P, Osteoset P®, Collatamp®, Stimulan® etc., are commercially available in market [3]. Although a variant products are available, complete elimination of bacteria and bone formation in the defective site is major concern in the existing treatments. Delivery of antibiotics locally has unique advantages compare to the systemic/oral route such as higher antibiotic concentration at the infection site, less dose and reduced toxicity [6–10]. Among them carrier-based implantable delivery systems are more preferred due to the advantage of sustained release of antibiotics for prolonged period and short hospital stay with less cost leads to improvement in patient compliance [11]. Polymethylmethacrylate (PMMA) beads containing antibiotics was clinically approved and current gold standard treatment after surgical debridement. Even though antibiotic loaded PMMA beads are clinically used, orthopedic clinicians looking for different material due to its limitations such as instability of drugs molecules, poor antibiotic elution, immunogenicity, non-biodegradable nature and subsequent removal of beads after release of antibiotics [3, 4].

To overcome the limitations of non-biodegradable systems, collagen, lactic acid polymers and calcium phosphate-based ceramics were studied for delivery of antibiotics from biodegradable carriers [4]. Calcium phosphate based carrier such as hydroxyapatite (HA) is much focused due to chemical similarity of bone constituents, biocompatibility, mechanical strength, high osteogenic properties, excellent carrier for drug loading and delivering the drugs in sustained manner through diffusion-controlled release kinetics [7, 12, 13]. Antibiotics such as arbekacin, cefoperazone, cefuroxime, ciprofloxacin, gentamicin and vancomycin loaded HA blocks, composites, scaffolds, nanoparticles (NPs) and cements were extensively studied for the treatment of osteomyelitis [4].

Drug resistance, recurrence of infection and treatment failures are the major drawbacks in the local antibiotic therapy. To improve the flaws in the existing treatment protocol, recently combinational delivery of two or more drugs are focused in the implantable local drug delivery systems. Dual delivery of antibiotics and antibiotics with growth factors were studied using polymeric, ceramic based micro and nano carriers [14–18].

Huang et al. [14] developed calcium phosphate cement containing two drugs, icariin and vancomycin for local delivery which showed drug release in sustained fashion and improved treatment outcomes. Hsu et al. [15] fabricated PLGA core (vancomycin & ceftazidime) and rhBMP-2 shell nanofibers by electrospinning coaxial technique and *in vitro* drug release studies showed sustained release of antibiotics (13 days) and protein for more than 30 days.

Co delivery of vancomycin and rifampin loaded 3D printed calcium phosphate scaffolds were studied in osteomyelitis mouse model has shown significant

improvement in the treatment [16]. In our earlier studies single and combinational delivery of antibiotics and anti-inflammatory drugs were studied for management of bone infections by calcium deficient hydroxyapatite nanocarrier [17, 18]. Recently, bone resorptive drug bisphosphonates were studied for the prevention of osteolysis and aseptic loosening in joint replacement surgery. Ozturk et al. fabricated vancomycin and alendronate impregnated bone grafts for controlling osteolysis in osteomyelitis [19]. Effect of alendronate with antibiotics in the combinational therapy using hydroxyapatite nanoparticles (HA NPs) based carrier systems has not been explored for the treatment of bone infections to the best of available literature.

Our aim of the study is to develop of synthetic bone substitute material which deliver antibiotics as well bone resorptive drug from ceramic polymeric nanocarrier in sustained fashion for the treatment of osteomyelitis. HA, ceramic carrier was chosen due to high osteogenic and bone resorptive nature. Chitosan (CH), a natural polysaccharides and biocompatible polymer has demonstrated as wide spectrum of antimicrobial activity against gram positive and gram-negative organisms and extensively studied for bone tissue engineering [3, 14] Sodium alendronate (SA), a bisphosphonate molecule has shown improved the early bone formation and inhibit bone resorption. Currently, a class of bisphosphonates were used in the treatment of bone tissue repair and bone disorders on combination with HA due to high affinity in bone mineral components [19, 20]. Gentamicin sulphate (GEN) is an aminoglycoside a broad-spectrum antibiotic mainly used in the several bone infections particularly in osteomyelitis [21–23]. SA were loaded onto the HA NPs and CH was coated onto the NPs. GEN was loaded onto the CH coated SA HA NPs and explored for the combinational delivery for the treatment of osteomyelitis.

2   Materials and Methods

2.1   Synthesis of SA Loaded HA NPs

HA NPs were synthesized by wet chemical precipitation which was previously reported with some modifications [24]. Sodium alendronate (SA) were loaded onto the HA NPs by physical adsorption. Briefly, 100 mg of SA were dissolved in phosphate buffered saline (PBS, pH 7.4) and 100 mg of HA NPs were incubated at room temperature for 24 h. After incubation, the solution was centrifuged at 10000 rpm and the pellet was separated. The percentage loading of SA was calculated by estimating the supernatant concentration using Ferric chloride in 2M perchloric acid by UV Visible spectroscopy at λmax 291 nm [25]. The resultant NPs are designated as SA-HA NPs.

2.2   Chitosan Coating on HA NPs and SA-HA NPs

Chitosan (5%) solution was prepared by 2% acetic acid solution. 50 mg of HA NPs or SA-HA NPs were added to the solution, sonicated for 10 min and coated using Rotospin (Tarsons, Mumbai, India) at 50 rpm for 24 h. After 24 h, the solution was centrifuged at 10000 rpm and the supernatant was separated. The residual pellet was

lyophilized and weight gain was measured. The experiment was performed in triplicate. These NPs are designated as CH-SA-HA NPs.

2.3 GEN Loaded CH-SA-HA NPs

The CH-SA-HA NPs (50 mg) were added to 1 mL of 5% GEN in PBS, pH 7.4 and incubated at 4 °C for 24 h. After 24 h incubation, the mixture was centrifuged at 12000 rpm and supernatant was separated. Remaining pellet was collected and lyophilized. The amount of GEN loaded in the nanoparticles was calculated by measuring the drug concentration in the supernatant by ninhydrin-colorimetric assay which was reported by Dorati et al. [26]. Briefly, 0.2% w/v ninhydrin was prepared freshly in PBS pH 7.4 and samples were mixed with ninhydrin solution and heated at 95 °C for 15 min. Then samples were cooled in ice bath for 10 min and absorbance was measured by using UV Visible spectrophotometer at 400 nm. The amount of GEN and SA was calculated by using the following formula

$$\text{Percentage of drug loaded}$$
$$= \frac{\text{Initial concentration of drug added to NPs} - \text{Final concentration of drug in the supernatant}}{\text{Initial concentration of drug added to NPs}} \times 100$$

2.4 *In Vitro* Drug Release Studies

GEN-CH-SA-HA NPs (5 mg) were added to 10 mL of PBS in a 25 mL glass bottles and incubated at 37 °C in a constant temperature bath. At regular time intervals 1 mL of sample was withdrawn and replaced with fresh buffer. The percentage drug release was calculated by measuring absorbance at 291 nm (SA) and 400 nm (GEN) in UV-visible spectrophotometer. Drug release studies were also carried out using SA-HA NPs (uncoated) and CH Coated SA HA NPs for comparison.

2.5 Antibacterial Activity Studies

2.5.1 Broth Microdilution Assay

Microdilution assay [27, 28] was adopted to determine the MIC (minimum inhibitory concentration) of GEN-CH-SA HA NPs and free gentamicin. *Staphylococcus aureus* (ATCC29213) (S. aureus) and Escherichia coli (B L21) (*E. coli)* were used as target strain. The bacterial culture was grown in LB broth at 37 °C and 180 rpm for 12 h. Briefly, 100 μL of overnight grown bacterial cell suspension (10^6–10^7 CFU/mL) of the respective target strain were seeded in sterile 96 well micro titer plate.

Indirect contact method was established for determine the MIC of the test samples. Briefly, different concentration of NPs (2 mg, 5 mg and 10 mg) were accurately weighed and UV sterilized for overnight then incubated in 1 mL of LB broth in orbital shaker at 37 °C for 24 h. Further the samples were filtered using 0.2 mm syringe filter. Different concentration of (500, 250, 125, 62.5, 31.25, 15.62, 7.81, 3.90 and 1.95 μg/mL) of extracted sample 100μL were added into the wells seeded with target

strain and incubated at 37 °C for 24 h. After incubation the samples were analyzed by microplate reader at 600 nm and MIC was calculated using the formula

$$MIC = OD \text{ of Sample}/OD \text{ of Control} * 100$$

2.5.2 Agar Diffusion Assay

Agar disk diffusion method is official standard method to test the susceptibility of antimicrobial compounds which is approved by Clinical and Laboratory Standard Institute (CLSI). Sensitivity of the bacterial strain against the test samples was determined by measuring the inhibition zone formed by diffused antimicrobial agents from the wells into the surrounding medium [27, 28].

Same procedure as mentioned in the Sect. 2.5.1 was followed for culturing two bacterial strains such as *S. aureus* and *E. coli*. From the subculture, 100 μL of respective bacterial suspension was spread on the LB Agar plates and 5 mm pore was created in the plates. The test samples 10 μL, 20 μL, 30 μL were (Extracted from 2 mg, 5 mg and 10 mg of NPs in 1 mL LB Broth) added into the wells and free gentamicin was used as positive control. Further, the agar plates were incubated at 37 °C for 24 h and diameter of zone inhibition was measured.

3   Results and Discussion

Treatment of bone infections and implant associated infections with antibiotics and reconstruction of the defect area is challenging task in clinical aspects and bone tissue engineering. In this study, an attempt has been made to develop the biodegradable and bioresorbable ceramic (HA)-polymer (CH) hybrid nanocarrier to deliver antiresorptive drug (SA) and antibiotic (GEN) for the treatment of osteomyelitis. HA NPs were synthesized by wet precipitation technique and CH was coated onto the NPs. The drug loaded HA-CH nanocarrier were extensively characterized by different techniques and effect of antimicrobial activity were examined in two bacterial strains.

3.1   Characterization of NPs

The synthesized HA NPs, SA-HA NPs, CH-SA-HA NPs and GEN-SA HA NPs were characterized by FTIR spectroscopy. HA shows prominent peaks at 3571 (structural OH), 3433 cm^{-1} (adsorbed water), 1089 cm^{-1} (HPO$_4^{2-}$), 1041 cm^{-1} (PO$_4^{3-}$ bending), 631 cm^{-1} (structural OH$^-$), and 601 cm^{-1} and 566 cm^{-1} (PO$_4^{3-}$ bending) (Fig. 1A). SA-HA NPs showed broad peak between 2700 to 3600 cm^{-1} (OH and NH stretch), 1632 cm^{-1} (NH bending), 1544 cm^{-1} (alendronate PO$_4^{3-}$ bending), 1401 cm^{-1} (C-H bending), 1190 cm^{-1} (Alendronate P = O Str), 1044 cm^{-1} (PO$_4^{3-}$ bending) with addition to HA absorption peaks (Fig. 1B). Additional peaks at 1637 cm^{-1}, 1191 cm^{-1} confirms the presence of SA onto the HA NPs (Fig. 1B). CH-SA-HA NPs showed peak at 1124 cm^{-1} (corresponds to C-O-H, C-O-C, CH$_2$-C-O of chitosan) and all other peaks of alendronate and HA was observed (Fig. 1C). IR peaks of CH- coated samples were compared with the Negrea et al. [29] reported the detailed analysis of infra-red

absorption peaks of chitosan. The spectrum of the GEN-CH-SA-HA NPs showed characteristic peaks of HA, SA and CH in addition to the peaks of GEN 1676 cm^{-1} (C = O stretch) and 1629 cm^{-1} (C-O Str), 1285 (C-N alkyl Str) thus confirming the presence of GENon the NPs (Fig. 1D). On comparing the FTIR spectra of HA NPs with SA HA NPs, CH-SA HA NPs and CH-GEN-CH-SA-HA NPs broad peak in the range of 2700 cm^{-1} to 3400 cm^{-1} confirms the OH and NH stretching with corresponds to CH, SA and GEN (Fig. 1).
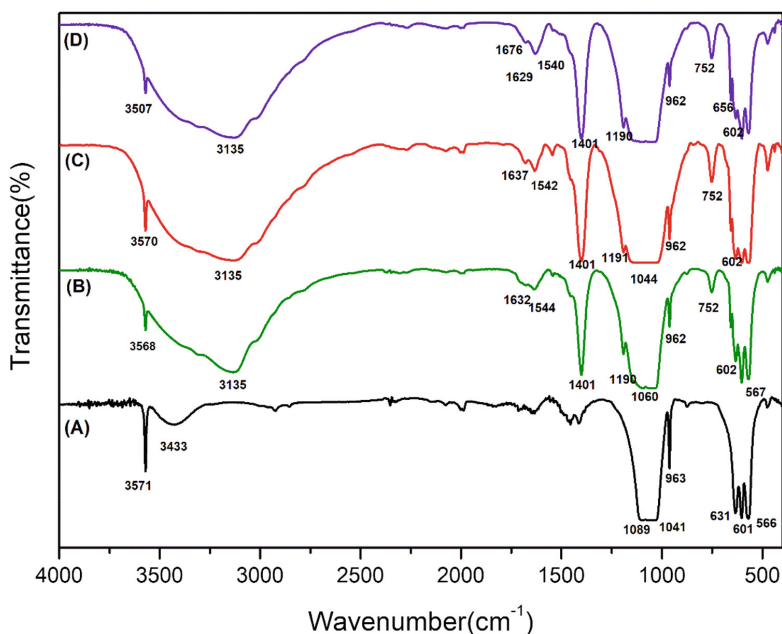
Fig. 1. FTIR spectrum of HA NPs (A), SA-HA NPs (B), CH-SA-HA NPs (C) and GEN-CH-SA-HA NPs (D).

HA NPs and drug loaded NPs were characterized by XRD to determine the phase purity and crystallinity. The XRD spectrum of HA (Fig. 2A) was compared with standard JCPDS (09432) and found be similar to stoichiometric HA. The broad peak at plane 211 (Fig. 2A) indicate the HA NPs were in the range of nano-size and further the crystal size was calculated by using Scherrer formula t = Kλ/BCos θ, where t is average crystal size (nm), K is shape factor, λ is X-ray wavelength (λ = 1.5405 Å for Cu Kα radiation), B is full width half maximum and θ is Bragg's diffraction angle. The synthesized HA crystal size was found to be 32 nm and results showed that synthesized samples were highly crystalline nature and phase pure. The SA loaded HA NPs shows an additional peak at 45 (2θ) near to the plane 400 and small peak at 31 (2θ) corresponds to the SA (Fig. 2B). May be due to binding and strong affinity of phosphate groups (SA) to the calcium sites of the HA, there is no more prominent additional peaks were seen in the samples. Due to the chitosan coating and presence of GEN onto the samples a small hump like peak was observed in the range of 15 (2θ) to 25 (2θ)

(Fig. 2C and D). Surface morphology of the NPs were characterized by TEM and diffused layer of polymer was clearly seen and exhibited two distinct layers of HA core and chitosan shell (Fig. 3).
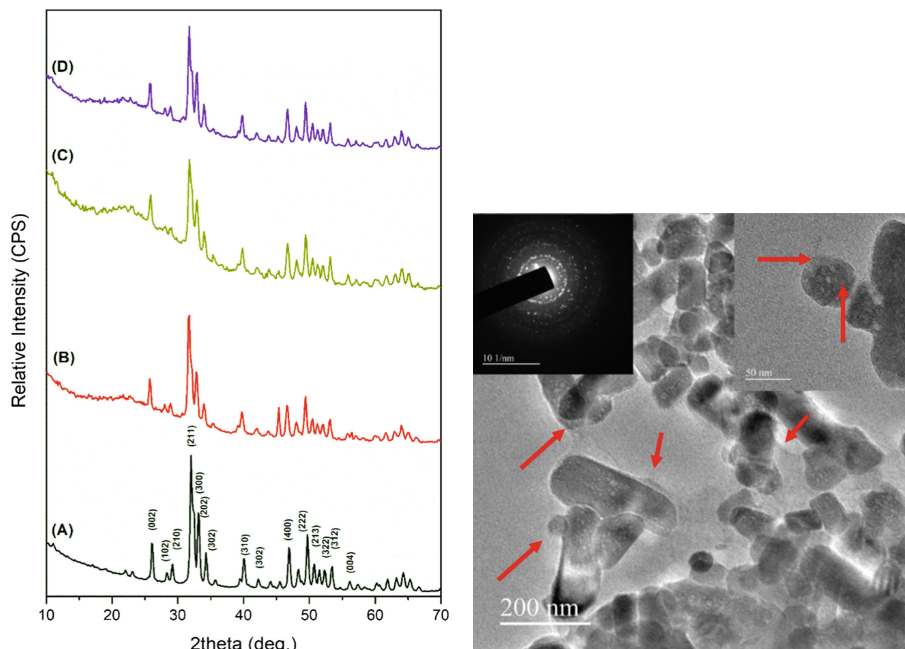
Fig. 2. XRD spectrum of HA NPs (A), SA-HA NPs (B), CH-SA-HA NPs (C) and GEN-CH-SA-HA NPs (D)

Fig. 3. Morphology of GEN-CH-SA-HA NPs by TEM

The amount of polymer content and thermal stability of NPs were determined by TGA. HA NPs was thermally stable with 1.16% weight loss upto 700 °C which may be due to moisture evaporation (Fig. 4A). SA HA NPs showed three stage degradation at 176.55 °C (2.18%), 329.26 °C (4.67%) and 570.05 °C (7.80%) due to sodium alendronate (Fig. 4B). Albu et al. [30] reported three stage degradation for alendronate, weight loss up to 130 °C due to moisture, ammonia loss in the range of 220 to 280 °C and above that due to the complex degradation and pyrolysis to sodium pyrophosphate. These results are in line with our SA loaded samples. CH-SA HA NPs showed four stage degradation at 73.48 °C (1.41%) due to moisture and 174.22 °C (3.01%), 329.28 °C (6.25%) and 540.70 (8.08%) due to the polymer and alendronate degradation (Fig. 4C). CH coated samples showed degradation at 70 to 100 °C (moisture) and maximum degradation at 330 °C, which corroborated with Neto et al. [31] and Tirkistani et al. [32]. In case of GEN loaded CH-SA HA NPs three stage degradation was observed, loss of water at 101.21 °C (1.15%) followed by degradation at 227.95 °C (2.31%) to 564.50 °C (11.76%) due to polymer and drug molecules

(Fig. 4D). Steady state weight loss was observed in the range of 100 to 230 °C may be due to degradation of GEN which was reported as GEN loss in the range of 150 to 200 °C by Mosselhy et al. [28]. From the TGA results, polymer coated efficacy on the NPs was found to be in the range of 8 to 12% (Fig. 4).
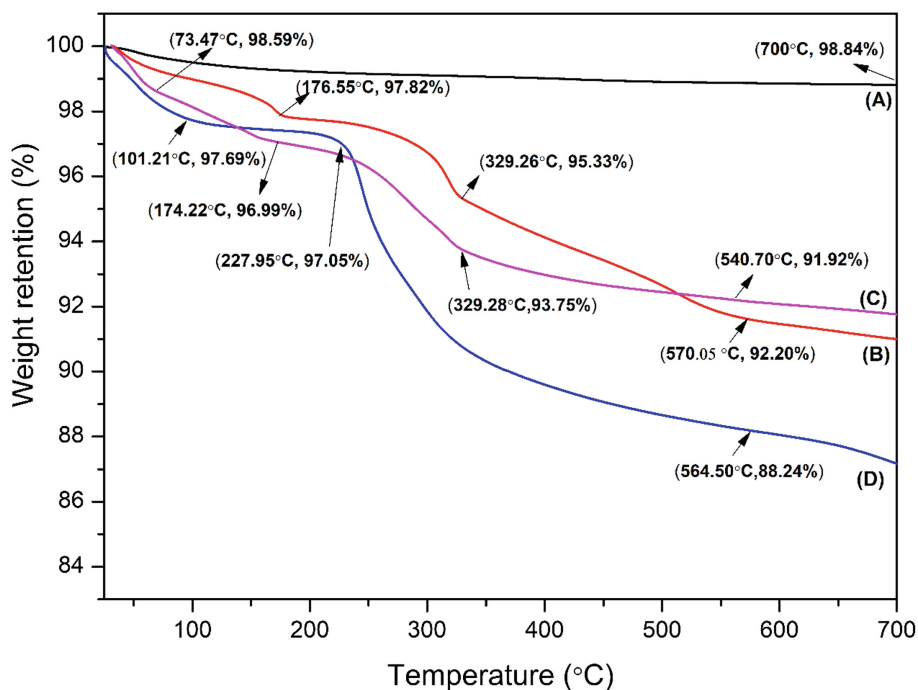
Fig. 4. TGA spectra of HA NPs (A), SA-HA NPs (B), CH-SA-HA NPs (C), GEN-CH-SA-HA NPs (D).

3.2   Coating Efficiency in HA NPs

The percentage coating efficiency of CH-SA-HA NPs were determined by weight percentage analysis. Briefly, 5% polymer solution was added in pre-weighed Eppendorf tubes and 50 mg of CH-SA-HA NPs was added. After coating and lyophilization, the coating efficiency of NPs was calculated by weight difference between the before and after coated samples. The optimized coating efficiency was found to be $15.93 \pm 2.21\%$. Coating efficiency was given in Table 1.

3.3   Drug Loading Efficiency in HA NPs

After 24 h incubation of drug molecules in the PBS pH 7.4, the maximum amount of SA loaded onto the HA NPs was found to be $84.35 \pm 1.35\%$. GEN loading on the chitosan coated SA-HA NPs were found to be $74.82 \pm 1.5\%$. The drug content in the

product (GEN-CH-SA HA NPs) was found to 0.8 mg (GEN) and 0.4 mg (SA) per mg of NPs respectively.

3.4   *In Vitro* Drug Release

In vitro drug release profile showed initial burst release followed by sustained release for 10 days. Initial stage at the end of 24 h, NPs showed burst release around 30% (GEN) and 20% (SA) respectively. The maximum drug release from the NPs was found to be 86% (GEN) and 71% (SA) (Fig. 5). Simultaneous release of both SA and GEN was observed in GEN-CH-SA-HA NPs. *In vitro* drug release studies were also performed for uncoated SA HA NPs for comparison with the chitosan coated SA-HA NPs.

SA release was retarded around 10 to 15% may be due to coating of polymer onto the NPs. On comparing drug release profile of CH coated and uncoated samples, significant difference was observed on CH coated samples which showed maximum release around 60% and in case of uncoated samples showed 80% (Fig. 5B). Both showed initial burst release around 20 to 35%, Sustained release of SA from the HA (uncoated samples) may be due to binding of alendronate (phosphate groups) in the HA NPs. The difference in the release profile of coated and uncoated samples showedless than $\sim$20% may be due to the aggregation and polymer coating onto the NPs.

3.5   Antibacterial Studies

Antibacterial activity of the NPs was examined using S. aureus and E. coli by micro broth dilution technique and agar diffusion assay. MIC of free gentamicin was found to be 2 μg/mL (S. aureus) and 4 μg/mL (E. coli). Concentration dependent bacterial growth inhibition was found in both gram negative and positive strain. MIC of extracted NPs in S. aureus was 63 μg/mL (2 mg NPs), 8 μg/mL (5 mg NPs) and 2 μg/mL (10 mg NPs) and for E. coli was 125 μg/mL (2 mg NPs), 15 μg/mL (5 mg NPs) and 4 μg/mL (10 mg NPs). Extracted NPs samples were tested in the plates and the diameter of inhibition zone was measured for both strains (Figs. 6 and 7). Zone of inhibition diameter were shown in Tables 2 and 3.

For antibacterial studies, leachate method was performed to extract the GEN from the NPs. At 24 h extraction 30% of GEN was released from different concentration of NPs (2, 5 and 10 mg). The drug release data and MIC of free GEN and extracted GEN form NPs were compared and correlated. Mossehly et al. [28] emphasized the importance of correlating *in vitro* drug release data with the antibacterial activity results to check the sub-inhibitory concentration of released drug from the NPs to overcome the drug resistance. Previously Perni et al. [33] reported that resistance of drug not only depends on the low concentration drug molecules but also the interaction of the bacterial cells with the NPs. In our studies, GEN drug release studies showed that 280 μg/mL was released within 24 h and maximum release of 350 μg/mL for 10 days.

All the extracted samples showed potent activity against both gram positive and negative strains. Drug loaded NPs (10 mg) has shown (2 μg/mL) equal activity assimilar to the GEN. MIC of the drug loaded NPs samples showed higher MIC values compared with the free GEN which may be due to the structural activity relationship, configuration and binding of molecules to the NPs as observed in our earlier studies

[17]. In the zone of inhibition studies, diameter of zone was increased with respect to the increase in concentration of drug molecules (Figs. 6 and 7).
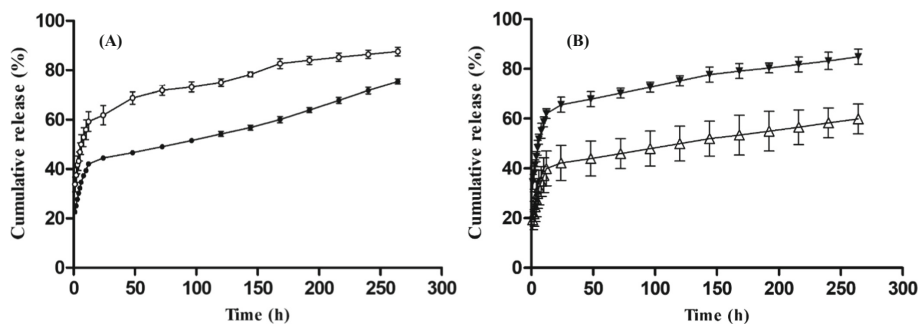
Fig. 5. *In vitro* drug release profile of GEN (o) and SA (●) from GEN-CH-SA-HA NPs (A). *In vitro* drug release profile of SA released from CH SA-HA NPs (Δ) and uncoated SA-HA NPs (▼) (B).

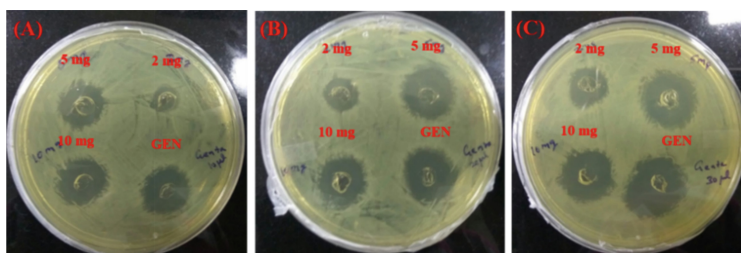**Fig. 6.** Zone of Inhibition against S. aureus for extracted NPs with free GEN. 10 µg/mL (A), 20 µg/mL (B) and 30 µg/mL (C)
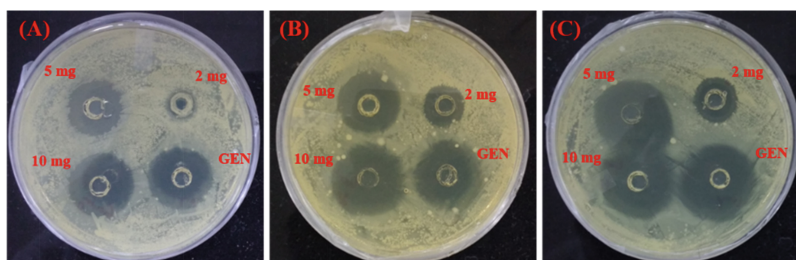

Fig. 7. Zone of inhibition against E. coli for extracted NPs with free GEN. 10 µg/mL (A), 20 µg/mL (B) and 30 µg/mL (C)

Table 1. Coating efficiency of chitosan on SA HA NPs

Batch	Initial weight SA HA NPs: Chitosan (mg)	Final weight after coating and lyophilization (mg)	Coating efficiency (%)
I	50: 50	56.8	13.6
II		58.1	16.2
III		59.0	18.0

Table 2. Diameter of zone of inhibition against S. aureus

GEN-CH-SA-HA NPs (extracted)	Zone of inhibition diameter in mm		
	10 μL	20 μL	30 μL
2 mg NPs	11 ± 1.4	13 ± 1	17 ± 2.2
5 mg NPs	15 ± 1	17 ± 2.1	17 ± 2.2
10 mg NPs	16 ± 2.8	21 ± 1.4	23 ± 1.4
Free Gentamicin	19 ± 1.4	23 ± 1.4	26 ± 1.4

Table 3. Diameter of zone of inhibition against E. coli

GEN-CH-SA-HA NPs (extracted)	Zone of inhibition diameter in mm		
	10 μL	20 μL	30 μL
2 mg NPs	9.5 ± 2.1	13 ± 1	16 ± 2.8
5 mg NPs	19 ± 1.4	18 ± 3.5	24 ± 1.4
10 mg NPs	22 ± 2.1	23 ± 1.4	23 ± 2.8
Free Gentamicin	23 ± 2.2	24 ± 1.4	27 ± 1.4

4   Conclusions

HA based ceramic polymer hybrid nanocarrier was formulated and characterized. This nanoparticulate carrier was explored for the dual delivery of antibiotic (GEN) and antiresorptive (SA) drugs. CH was coated onto the HA NPs previously loaded with SA. Slow and retarded release of SA was observed in coated samples. Layer of polymer around the NPs showed core shell structure and confirmed by TEM. *In vitro* drug release studies showed initial burst release followed by sustained release over a period of time for all the samples. Drug release curve of dual drug loaded samples showed simultaneous release of GEN and SA. Antibacterial studies revealed that the concentration dependent inhibition was observed and potent activity against the organisms. Thedual drug nanocarrier system consists of HA core with antiresorptive drug and polymeric (CH) shell loaded with antibiotic drug will be a capable bone defect filling material in the treatment of bone infections and orthopedic applications.

Conflict of Interest. The authors declare no conflict of interest.

References

1. Lima, A.L.L., Oliveira, P.R., Carvalho, V.C., Cimerman, S., Savio, E., Sosa, A., López, A., Rodriguez Taveras, C.J., Ferreira Starling, C.E., Kiffer, C., Dos Santos, E.L.B., Molinedo Pérez, L.E., Coura Filho, G.B., Del Sel, H., Pezzarossi Zelaya, H.E., Marinho, I., LopesRocha, J.L., Matheus Guimarães, J.A., Mello Sampaio, J.L., Amim Zabeu, J.L., Melo, L.H., Abagge, M., Costa Salles, M.J., Ferreira, M.S., De Rezende, M.R., Rodrigues, M.B., Lech, O., Dos Reis, P.R., Ramon-Pardo, P., Guarniero, R., Junior, W.R: Recommendations for the treatment of osteomyelitis. Braz. J. Infect. Dis. **18**, 526–534 (2014)
2. Walter, G., Kemmerer, M., Kappler, C., Hoffmann, R.: Treatment algorithms for chronic osteomyelitis. Dtsch. Arztebl. Int. **109**, 257–264 (2012)
3. Dorati, R., DeTrizio, A., Modena, T., Conti, B., Benazzo, F., Gastaldi, G., Genta, I.: Biodegradable scaffolds for bone regeneration combined with drug-delivery systems in osteomyelitis therapy. Pharmaceuticals **10**, 96 (2017). https://doi.org/10.3390/ph10040096
4. Nandi, S.K., Mukherjee, P., Roy, S., Kundu, B., De, D.K., Basu, D.: Local antibiotic delivery systems for the treatment of osteomyelitis - a review. Mater. Sci. Eng., C **29**, 2478–2485 (2009)
5. Kumar, G.S., Govindan, R., Girija, E.K.: In situ synthesis, characterization and in vitro studies of ciprofloxacin loaded hydroxyapatite nanoparticles for the treatment of osteomyelitis. J. Mater. Chem. B. **2**, 5052–5060 (2014)
6. Itokazu, M., Ohno, T., Tanemori, T., Wada, E., Kato, N., Watanabe, K.: Antibiotic-loaded hydroxyapatite blocks in the treatment of experimental osteomyelitis in rats. J. Med. Microbiol. **46**, 779–783 (1997)
7. Yamashita, Y., Uchida, A., Yamakawa, T., Shinto, Y., Araki, N., Kato, K.: Treatment of chronic osteomyelitis using calcium hydroxyapatite ceramic implants impregnated with antibiotic. Int. Orthop. **22**, 247–251 (1998)
8. Zalavras, C.G., Patzakis, M.J., Holtom, P.: Local antibiotic therapy in the treatment of open fractures and osteomyelitis. Clin. Orthop. Relat. Res. **427**, 86–93 (2004)
9. Qiu, X.S., Zheng, X., Shi, H.F., Zhu, Y.C., Guo, X., Mao, H.J., Xu, G.Y., Chen, Y.X.: Antibiotic-impregnated cement spacer as definitive management for osteomyelitis. BMC Musculoskelet. Disord. **16**, 254 (2015)
10. Gomes, D., Pereira, M., Bettencourt, A.F.: Osteomyelitis: an overview of antimicrobial therapy. Braz. J. Pharm. Sci. **49**, 13–27 (2013)
11. Saito, T., Takeuchi, R., Hirakawa, K., Nagata, N., Yoshida, T., Koshino, T., Okuda, K., Takema, M., Hori, T.: Slow-releasing potential of vancomycin-loaded porous hydroxyapatite blocks implanted into MRSA osteomyelitis. J. Biomed. Mater. Res. **63**, 245–251 (2002)
12. Yang, L., Sheldon, B.W., Webster, T.J.: Nanophase ceramics for improved drug delivery: current opportunities and challenges. Am. Ceram. Soc. Bull. **89**, 24–32 (2010)
13. Sadat-Shojai, M., Khorasani, M.T., Dinpanah-Khoshdargi, E., Jamshidi, A.: Synthesis methods for nanosized hydroxyapatite with diverse structures. Acta Biomater. **9**, 7591–7621 (2013)

14. Huang, J.G., Pang, L., Chen, Z.R., Tan, X.P.: Dual-delivery of vancomycin and icariin from an injectable calcium phosphate cement-release system for controlling infection and improving bone healing. Mol. Med. Rep. **8**, 1221–1227 (2013)

15. Hsu, Y.H., Lin, C.T., Yu, Y.H., Chou, Y.C., Liu, S.J., Chan, E.C.: Dual delivery of active antibactericidal agents and bone morphogenetic protein at sustainable high concentrations using biodegradable sheath-core-structured drug-eluting nanofibers. Int. J. Nanomed. **11**, 3927–3937 (2016)

16. Inzana, J.A., Trombetta, R.P., Schwarz, E.M., Kates, S.L., Awad, H.A.: 3D printed bioceramics for dual antibiotic delivery to treat implant-associated bone infection. Eur. Cells Mater. **30**, 232–247 (2015)

17. Madhumathi, K., Kumar, T.S.S.: Regenerative potential and anti-bacterial activity of tetracycline loaded apatitic nanocarriers for the treatment of periodontitis. Biomed. Mater. **9**, 035002 (2014)

18. Kalidoss, M., Kumar, S.T., Doble, M.: Combinatorial delivery of antibiotic and anti-inflammatory drugs using calcium deficient hydroxyapatite nanocarriers for the management of bone infections. Biomater. Tissue Technol **1**, 1–5 (2017)

19. Ozturk, A.M., Tabak, A.Y., Aktekin, C.N., Altay, M., Erdemli, E., Karahuseyinoglu, S., Korkusuz, F.: Alendronate enhances antibiotic-impregnated bone grafts in the treatment of osteomyelitis. Int. Orthop. **32**, 821–827 (2008)

20. Li, D., Zhu, Y., Liang, Z.: Alendronate functionalized mesoporous hydroxyapatite nanoparticles for drug delivery. Mater. Res. Bull. **48**, 2201–2204 (2013)

21. Iwakura, T., Lee, S.Y., Niikura, T., Miwa, M., Sakai, Y., Nishida, K., Kuroda, R., Kurosaka, M.: Gentamycin-impregnated calcium phosphate cement for calcaneal osteomyelitis: a case report. J. Ortho. Surg. **22**, 437–439 (2014)

22. Xie, Z., Cui, X., Zhao, C., Huang, W., Wang, J., Zhang, C.: Gentamicin-loaded borate bioactive glass eradicates osteomyelitis due to Escherichia coli in a rabbit model. Antimicrob. Agents Chemother. **57**, 3293–3298 (2013)

23. Knaepler, H.: Local application of gentamicin-containing collagen implant in the prophylaxis and treatment of surgical site infection in orthopaedic surgery. Int. J. Surg. **10**, S15–S20 (2012)

24. Zhang, Y., Lu, J.: A simple method to tailor spherical nanocrystal hydroxyapatite at low temperature. J. Nanopart. Res. **9**, 589–594 (2007)

25. Kuljanin, J., Jankovicá, I.J., Nedeljkovicá, J.N., Prstojević, D., Prstojević, P., Marinković, V., Marinković, M.: Spectrophotometric determination of alendronate in pharmaceutical formulations via complex formation with Fe(III) ions. J. Pharm. Biomed. Anal. **28**, 1215–1220 (2002)

26. Dorati, R., DeTrizio, A., Genta, I., Grisoli, P., Merelli, A., Tomasi, C., Conti, B.: An experimental design approach to the preparation of pegylated polylactide-co-glicolide gentamicin loaded microparticles for local antibiotic delivery. Mater. Sci. Eng. C **58**, 909–917 (2016)

27. Clinical and Laboratory Standards Institute (CLSI): Methods for dilution antimicrobial susceptibility tests for bacteria that grow aerobically, Approved standard-ninth edition, M07-A9, pp. 1–68, CLSI, Wayne, PA, USA (2012)

28. Mosselhy, D.A., Ge, Y., Gasik, M., Nordström, K., Natri, O., Hannula, S.P.: Silica-gentamicin nanohybrids: synthesis and antimicrobial action. Materials (Basel) **9**, 170 (2016). https://doi.org/10.3390/ma9030170

29. Negrea, P., Caunii, A., Sarac, I., Butnariu, M.: The study of infrared spectrum of chitin and chitosan extract as potential sources of biomass. Dig. J. Nanomater Biostruct. **10**, 1129–1138 (2015)

30. Albu, P., Doca, S.C., Anghel, A., Vlase, G., Vlase, T.: Thermal behavior of sodium alendronate. J. Therm. Anal. Calorim. **127**, 571–576 (2017)
31. Neto, C.G.T., Giacometti, J.A., Job, A.E., Ferreira, F.C., Fonseca, J.L.C., Pereira, M.R.: Thermal analysis of chitosan-based networks. Carbohydr. Polym. **62**, 97–103 (2005)
32. Tirkistani, F.A.A.: Thermal analysis of some chitosan Schiff bases. Polym. Degrad. Stabil. **60**, 67–70 (1998)
33. Perni, S., Prokopovich, P.: Continuous release of gentamicin from gold nanocarriers. RSC Adv. **4**, 51904–51910 (2014). https://doi.org/10.1039/C4RA10023A

The Impact of Gold Nanoparticles with Low Energy Irradiation Treatment on Temperature Induction and Cell Viability of Breast Cancer Cell

R. Sowmiya[1], Tanakorn Osotchan[2,3], and Dakrong Pissuwan[3,4(✉)]

[1] Department of Nano Science and Technology, K. S. Rangasamy College of Technology, Tiruchengode, TN, India

[2] Department of Physics, Faculty of Science, Mahidol University, Bangkok, Thailand

[3] Materials Science and Engineering Program, Faculty of Science, Mahidol University, Bangkok, Thailand
`dakrong.pis@mahidol.ac.th`

[4] Nanobiotechnology and Nano Biomaterial Research (N-BMR) Laboratory, School of Materials Science and Innovation, Faculty of Science, Mahidol University, Bangkok, Thailand

Abstract. The photothermal therapy (PTT) has attracted the cancer treatment because it is non-invasive and relatively safe technique. The gold nanoparticles (AuNPs) have been a great source of interest due to its novel characteristics which make them suitable for the promising applications such as the photothermal therapy, drug delivery, nanomedicine, photonics, biochemical sensors and imaging. AuNPs were prepared via a citrate reduction method. The characterization techniques such as UV-vis spectroscopy and transmission electron microscope (TEM) were used to characterize AuNPs. The spherical shape of the AuNPs with the size of 35 ± 5 nm was identified under TEM. The Michigan Cancer Foundation-7 (MCF-7) human breast cancer cells were used as a model cell for cell viability investigation after treatment. The AuNPs at concentrations 0.1 μg/ml and 0.5 μg/ml were applied into MCF-7 cells and then the cells were exposed to a light emitting diode (LED). It found that MCF-7 cells treated with 0.1 μg/ml AuNPs and then exposed to a LED for 5 min had a reduction of cell viability when compared with the control or cells treated with the same condition without LED exposure. But, when cells were treated with a higher concentration of AuNPs and then LED irradiation, the cell viability was dropped when compared with cells treated with AuNPs without LED irradiation. It is important to note here that when MCF-7 cells were treated with AuNPs alone without irradiation, the cell viability was slightly enhanced when compared with non-treated cells. Nevertheless, the future studies could be made on the treatment of the AuNPs with LED for extended time period which could possibly make them an effective agent to destroy cancer cell.

Keywords: Gold nanoparticles · MCF-7 breast cancer cell · Light Emitting Diode (LED)

1   Introduction

Nanotechnology has risen throughout the world because they have been considered revolutionary in many fields. Metallic nanoparticles are new generation materials being widely investigated for biomedical and therapeutic applications. Among the metallic nanoparticles, AuNPs are quite attractive in because they can be easily synthesized to desirable sizes. Furthermore, their surface can be easily modified for various functionalities such as proteins and other molecular species without altering the biological activity of the conjugated species [1]. Generally, AuNPs have advantages over other metal nanoparticles due to their biocompatibility and non-cytotoxicity on healthy cells [2]. AuNPs can accumulate in the tumour cells and show optical scattering. Therefore, these can act as a probe for microscopic study of cancer cells and can be used in chemotherapy and diagnosis [3].

Globally, cancer as an invasive and malignant disease is considered to be a second leading cause of mortality. Breast cancer is a leading cause of cancer-related death in women. The development of the effective breast cancer treatment is of great importance and will greatly improve survivorship. Current cancer therapies, such as surgical excision, chemotherapy, radiation therapy, or even combination therapy, have some limitations such as surgery that could result in hurt or injury in the adjacent healthy critical tissues and also exhibits violent side effects [4, 5]. To overcome these limitations, PTT utilizing external light-induced hyperthermia to ablate malignant tissues while avoiding damage to healthy tissues has recently attracted considerable attention for promising clinical applications due to its simplicity, high selectivity non-invasiveness, safety and remote-controllable properties [6]. Effective PTT depends on heat generation upon exposure of tumor cells to near-infrared radiation (NIR). The combination of PTT with AuNPs can enhance absorb light energy, which causes electron excitation and subsequent non-radiative relaxation leading to gain kinetic energy. This can result in heat generation in the medium surrounding AuNPs, which later can destroy target cells [7]. On the other hand, the development of AuNPs for biomedical applications especially in bioimaging applications has also received much attention [8].

The previous studies have shown the conversion of the absorbed light to heat energy through three main photo-physical processes. The first and second processes allow for the formation of a hot metallic lattice in the metal NPs, and the last one allows for a cooling off, which means heat dissipation from the NPs to the surrounding environment. Accordingly, the dissipated energy will heat up the cancerous cells around the AuNPs causing cell destruction. However, such energy conversion and dissipation occur when the frequency of the incident light is overlapped with the SPR absorption band [9]. From the previous report, the use of AuNPs to kill breast cancer cells via photothermal therapy was achieved [10].

The scope of the present investigation here is to delineate the simple, non-invasive method suitable for the photo thermal therapy in *invitro* by using spherical shape AuNPs in combination with a low energy irradiation (a LED; wavelength ∼638 nm) for MCF-7 breast cancer cell destruction. We were interested to use the low energy irradiation because we would like to seek for the possibility of using less energy for

killing target cancer through PPT. The AuNPs prepared by citrate reduction method, were characterized by TEM and UV-vis spectroscopy techniques. In order to investigate cancer destruction of AuNPs with a LED irradiation, cytotoxicity studies was performed. MCF-7 cells (model breast cancer cells) treated with 0.1 µg/ml AuNPs and illuminated to LED exhibited the reduction of cell viability comparing to the control cells (no treatment). In support of these results, we prove that AuNPs with a LED irradiation are able to destroy MCF-7 cells. The overall view of study is shown in Fig. 1.
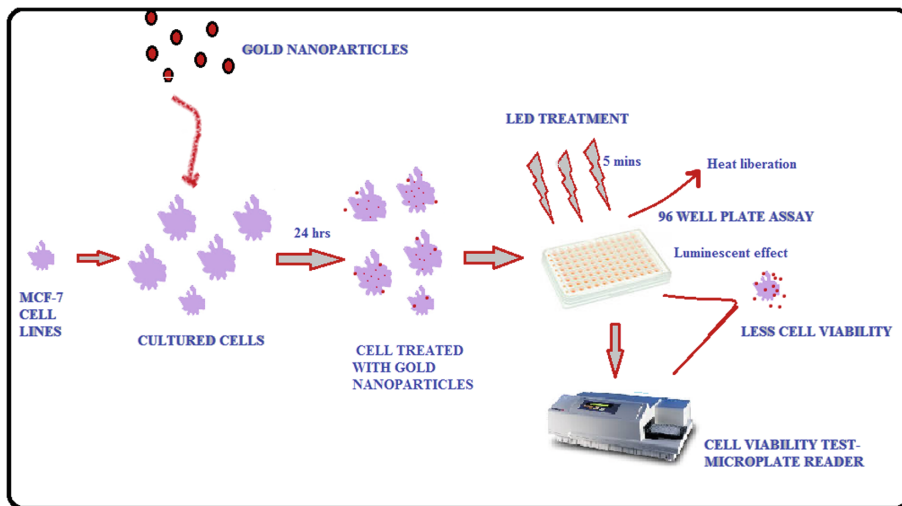
Fig. 1. Schematic representation of irradiation effect on breast cancer cells with AuNPs

2   Experimental

2.1   Materials and Reagent

The chloroauric acid (HAuCl$_2$) 2% was purchased from Clin tech., tri-sodium citrate (Na$_3$C$_6$H$_5$O$_7$.2H$_2$O) was purchased from Sigma-Aldrich. The reagents were of analytical grade. The cell line of Michigan Cancer Foundation-7 (MCF-7 breast cancer cell) was purchased from the Riken cell bank.

2.2   Synthesis of AuNPs

The AuNPs were synthesized by a citrate reduction method using tri-sodium citrate as reductant. The gold solution was prepared by addition of 5 ml of gold solution (Clin Tech) in milli-Q(MQ) water and mixed well using vortex. The tri-sodium citrate solution was made by addition of 0.101 g tri-sodium citrate in MQ water. The gold solution was heated under the boiling point of 95 °C and stirred at a rate of 5.5 rpm. Once the temperature reached to 95 °C, tri-sodium citrate solution was poured directly

to the boiling gold solution along with heating and vigorous stirring. The colour change from yellow to reddish wine was observed. Ultimately, AuNPs were finally obtained.

2.3 Cell Culture Procedure

The MCF-7 breast cancer cells were cultured in media DMEM & MEM, supplemented with 5% of FBS and 1% of antibiotic. The cultured dishes were incubated in a CO_2 incubator at 37 °C plus a 5% CO_2. The cultured cells are shown in the Fig. 2.
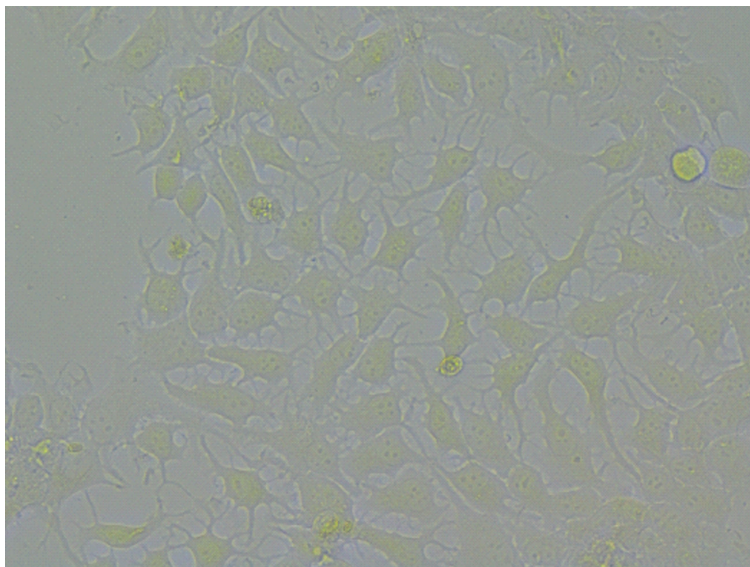
Fig. 2. The image of MCF-7 human breast cancer cell observed under an optical light microscope.

2.4 *In-Vitro* Cell Cytotoxicity Study After Treating with AuNPs and a LED Irradiation

MCF-7 cells at a concentration of 1×10^4 cells/well were added in the 96 well plate. The cells were incubated overnight in the CO_2 incubator at 37 °C. Three different treatments, non-treated cells (control), cells treated with 0.1 µg/ml and 0.5 µg/ml AuNPs, were prepared. After the incubation of cells for 3 h, cells were irradiated with a LED for 5 min (with an output power $\sim$2.3 mW). Following this, cells were further incubated for 48 h and then measured their cell viability using CellTiter-Glo® luminescent cell viability assay. The luminescent signal was measured by a microplate reader (Model: ETM-MU//SC-10-115/1, SpectraMax M_3) with the SoftMax Pro 5.4 software. The % relative of cell viability was then evaluated.

2.5   Characterization Techniques

The UV–visible (UV–vis) absorption analysis was recorded by an UV-2550 spec-trophotometer (Model: ESTM-TX-02-184; Software: UV-Probe [version-2.61]). It showed that AuNPs provided its maximum absorption peak at 522 nm. The mor-phology of AuNPs was examined using TEM (Model: FEI Tecnai F20 S/TEM). The synthesized AuNPs were centrifuged for 10 min at 10,000 rpm and 25 °C. A small droplet of AuNPs was dropped on the Para film and the copper grid coated with form var film was made into contacting on the AuNP drop for 5 min. The copper grid was dried inside a silica gel box over night. Later the sample was examined under TEM. The images were analyzed to determine the average particle size and morphology of synthesized AuNPs. Various images of the sample were captured and investigated. Finally, the data of average size was shown in mean ± standard deviation.

3   Results and Discussion

3.1   Characterization of AuNPs

The spectrum of AuNPs obtained is shown in Fig. 3. The maximum absorption peak was at ~522 nm. This indicates the characteristics of surface plasmon resonance of spherical AuNPs. The narrow absorption peak significantly implies a good stability of AuNPs. The spherical shape of AuNPs was observed using TEM as shown in Fig. 4. The average particle size of the AuNPs was ~35 ± 5 nm.
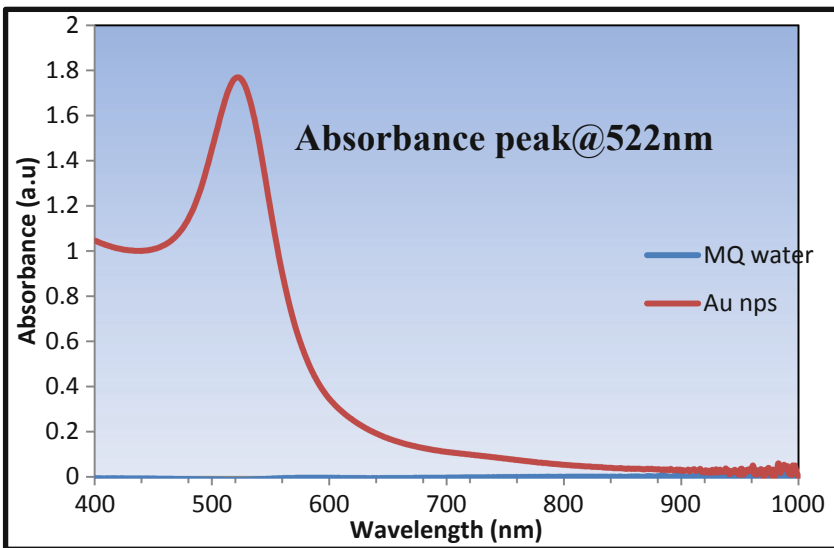
Fig. 3.   The absorption spectrum of AuNPs.
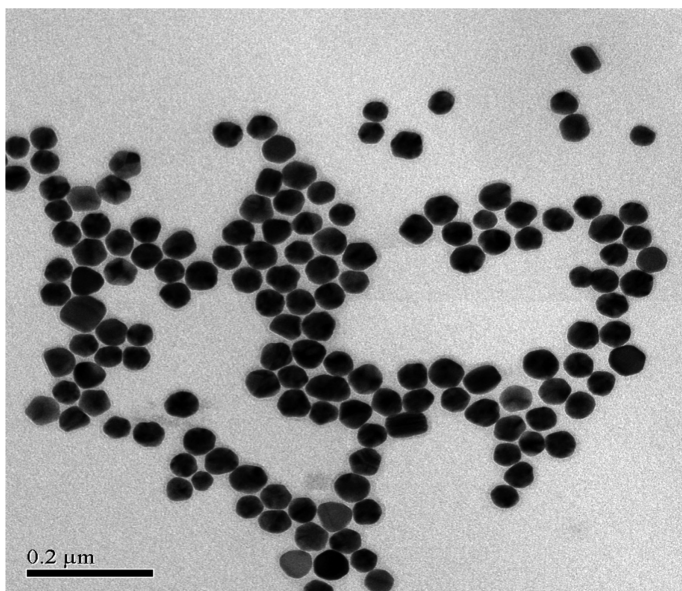
Fig. 4. The image of spherical AuNPs with a size $\sim 35 \pm 5$ nm

3.2 Cell Viability Test After Treating with AuNPs and Exposing to a LED Irradiation

The graph of cell viability of MCF-7 cells treated with AuNPs plus a LED irradiation shows in Fig. 5. From the results, the MCF-7 cells treated with LED alone had no change in cell viability which means that the LED treatment did not have any effect on cell death induction. However, when MCF-7 cells were treated with 0.5 µg/ml AuNPs plus a LED irradiation, a slight reduction of cell viability was found. Another treatment, MCF-7 cells were treated with 0.1 µg/ml AuNPs and then irradiated with a LED reduced more cell viability than that of 0.5 µg/ml AuNPs treatment. This implies that the more number of AuNPs interacting with cells might lead to more aggregation resulting in the change of surface plasmon resonance of AuNPs. This change could impact on the heat generation of AuNPs. The further investigation of this issue could be done in the future work.
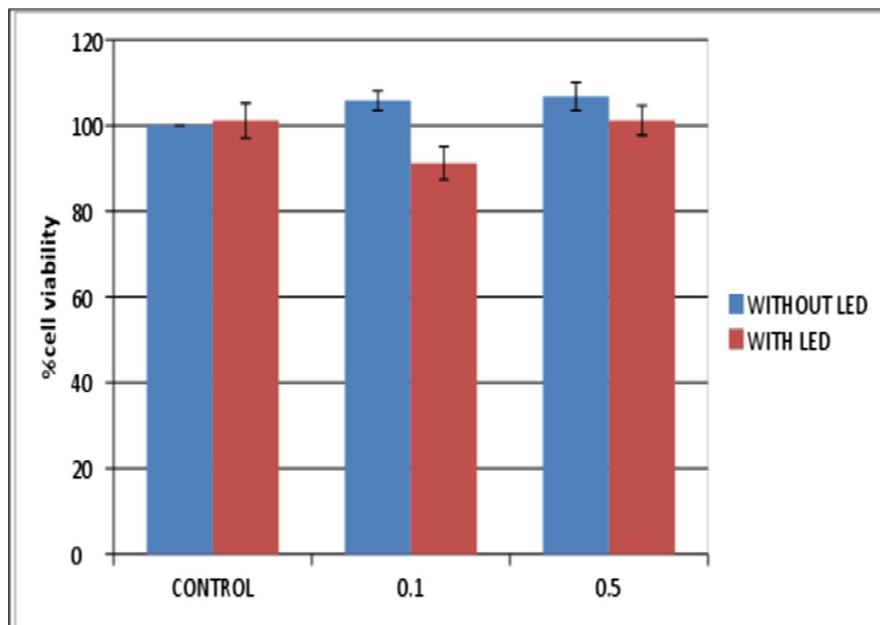
Fig. 5. Cell viability of MCF-7 cells treated with 0.1 µg/ml and 0.5 µg/ml AuNPs with and without LED irradiation. Non-treated cells were prepared as a control cell.

4   Conclusion

In this study, we applied AuNPs to MCF-7 cells in combination with a LED irradiation. The photothermal effect produced from AuNPs and low energy treatment (using LED) was detected. This data provide promising information of using low energy irradiation and AuNPs for cancer destruction. The proposed low energy would help reduce side effects that might occur from high energy irradiation. However, the relationship between the concentration of AuNPs and the aggregation rate of AuNPs should be concerned to reach high efficiency of PPT induction.

References

1. Rosli, N.S, Rahman, A.A., Aziz, A.A., Shamsuddin, S.: Enhancement of radiation cytotoxicity by gold nanoparticles in MCF-7 breast cancer cell lines. In: AIP Conference Proceedings, vol. 1657, p. 060007 (2015)
2. Priya, M.R.K., Iyer, P.R.: Anticancer studies of the synthesized gold nanoparticles against MCF 7 breast cancer cell lines. Appl. Nanosci. **5**(4), 443–448 (2015)
3. Cai, W., Gao, T., Hong, H., Sun, J.: Application of gold nanoparticles in cancer nanotechnology. Nanotechnool. Sci. Appl. **1**, 17–32 (2008)

4. Hussein, E.A., Zagho, M.M., Nasrallah, G.K., Elzatahry, A.A.: Recent advances in functional nanostructures as cancer photothermal therapy. Int. J. Nanomed. **13**, 2897–2906 (2018)
5. Xu, L., Du, J., Wan, C., Zhang, Y., Xie, S., Li, H., Yang, H., Li, F.: Ultrasound molecular imaging of breast cancer in MCF-7 orthotopic mice using gold nanoshelled poly (lactic-co-glycolic acid) nanocapsules: a novel dual-targeted ultrasound contrast agent. Int. J. Nanomed. **13**, 1791–1807 (2018)
6. Cao, Y., Li, S., Chen, C., Wang, D., Wu, T., Dong, H., Zhang, X.: Rattle-type Au@Cu2–xS hollow mesoporous nanocrystals with enhanced photothermal efficiency for intracellular oncogenic microRNA detection and chemophoto thermal therapy. Biomaterials **158**, 23–33 (2018)
7. Melancon, M.P., Zhou, M., Li, C.: Cancer theranostics with near-infrared light-activatable multimodal nanoparticles. Acc. Chem. Res. **44**(10), 947–956 (2018)
8. Vasimalai, N.: NIR Light-sensitive plasmonic gold nanomaterials for cancer photothermal and chemotherapy applications. In: Metal Nanoparticles and Clusters. Springer, United States (2018
9. Feng, J., Chen, L., Xia, Y., Xing, J., Li, Z., Qian, Q., Wang, Y., Wu, A., Zengand, L., Zhou, Y.: Bioconjugation of gold nanobipyramids for SERS detection and targeted photothermal therapy in breast cancer. ACS Biomater. Sci. Eng. **3**(4), 608–618 (2017)
10. Zou, L., Wang, H., He, B., Zeng, L., Tan, T., Cao, H.: Current approaches of photothermal therapy in treating cancer metastasis with nanotherapeutics. Theranostics **6**(6), 762–772 (2016)

Green Synthesis of Silver Nanoparticles from De-oiled Rhizomes of *Curcuma longa* L. and Its Biomedical Potential

Sinthia Ganesan[1], Palanichamy Mehalingam[2(✉)], and Govindan Sadasivam Selvam[3]

[1] Department of Biotechnology, V.V. Vanniaperumal College for Women (Autonomous), Virudhunagar, India
[2] Research Department of Botany, V.H.N. Senthikumara Nadar College (Autonomous), Virudhunagar, India
`mehalingamp@yahoo.co.in`
[3] Department of Biochemistry, School of Biological Sciences, Madurai Kamaraj University, Madurai, India

Abstract. The present study deals with the synthesis of silver nanoparticles using de-oiled rhizomes of Curcuma longa aqueous extracts and its biomedical potential. Tumeric is the rhizome of Curcuma longa (Zingiberaceae) and Curcumin is extracted from it. Curcumin finds extensive use in the pharmaceutical industry. Synthesis of silver nanoparticles from 1 mM silver nitrate solution using the extract of turmeric spent was done. The colour changed from pale yellow to dark brown indicating the synthesis of silver nanoparticles. The synthesized silver nanoparticles were characterized by UV visible spectroscopy, XRD, FTIR and Zeta potential. These green synthesised silver nanoparticles were tested for antimicrobial activity by agar well diffusion method against seven human pathogenic strains such as Bacillus subtilis, Staphylococcus aureus, Streptococcus faecalis, Klebsiella pneumoniae, Pseudomonas aeruginosa, E.coli and Candida albicans. The zone of inhibition increased with increase in the concentration of silver nanoparticles in well diffusion method. Anticancer activity of silver nanoparticles was tested on breast cancer cell line, MCF-7. Cytotoxic effect was observed in tested sample concentrations after 48 h treatment. It also revealed that increase in concentration of drug showed increased cytotoxicity over the MCF-7 cell line. This efficient biomedical potential of the synthesized silver nanoparticles paves the way for its application in the area of nano-medicine.

Keywords: Anticancer activity · Antimicrobial activity · Tumeric spent · MCF-7

1 Introduction

Nanotechnology, a young science based on ancient methods is emerging as a new trend in research. Nanoparticles due to their small size have very high surface area/volume and hence more drugs can be loaded to treat several diseases, especially microbial ones.

Metal nanoparticles made of gold, silver, iron,etc. show good biomedical potential. Particularly, silver nanoparticles have been studied widely and show promise as good antimicrobial agents which can aid pharmacology [1]. The reduced size of the particles alters their physical and chemical properties drastically paving the way to newer uses in every field of science. Nanoparticles are being used in every field including optics, paint industry, environmental protection, water purifiers and electronic industry [2]. Silver nanoparticles have excellent antimicrobial activity, thermoplasmonic capabilities, and superior surface Raman properties.

Tumeric (*Curcuma longa L.*) (Fig. 1) a monocot, is a well-known anti-bacterial and anti-cancer agent belonging to the *Zingiberaceae* family. It has been used in ayurvedic medicines since time immemorial. Turmeric is extensively used as a spice, food preservative and colouring material in India, China and South East Asia. It has been used in traditional medicine as a household remedy for various diseases, including the common cold, biliary disorders, anorexia, cough, diabetic wounds, hepatic disorders, rheumatism, sinusitis and as a antibiotic.

Fig. 1. *Curcuma longa* L.

Curcumin (diferuloylmethane), the main yellow bioactive component of turmeric, has been shown to have a wide range of biological actions which include its antiinflammatory, antioxidant, anticarcinogenic, antimutagenic, anticoagulant, antifertility, antidiabetic, antimicrobial, antifibrotic, antivenom, antiulcer and antifat activities. Its anticancer effect is mainly mediated through induction of cell death or apoptosis. Its antiinflammatory, anticancer and antioxidant roles have been used by many to control rheumatism, carcinogenesis and oxidative stress-related problems. Curcumin has already been used clinically to reduce post-operative inflammation [3].

There are many methods used for the production of silver nanoparticles (AgNPs) which include chemical [4], electrochemical [5], radiation [6], photochemical methods [7], Langmuir-Blodgett [8, 9] and biological techniques [10]. Biological synthesis is far superior as it offers several advantages which include rapid synthesis, high yields and more importantly, the lack of costly downstream processing required to produce the particles [11–13]. Biological methods include the use of plants or microbes as reducing agents. Of these, green synthesis of silver nanoparticle using plants is considered best

for the rapid production of large quantities of silver nanoparticles to successfully meet the growing needs and current market demand and simultaneously maintain a cleaner and safer environment for humans [14]. The biological route using plants is very fast, cost effective, environment friendly and non-toxic. Plants can function as both reducing and stabilizing agents and surpass microbial methods by bypassing the complicated process of maintaining cultures. Large scale production of commercial and economic nanoparticles is feasible by using easily available plant extracts. There are several studies that report on the use of plant extracts in nanoparticle synthesis [15].

For the last few decades, extensive work has been done to establish the biological activities and pharmacological actions of turmeric and its extracts. The essential oil, Curcumin, is extracted from turmeric and has high medicinal value. The de-oiled turmeric is an industrial waste and adulterant. The present study is directed towards the efficient synthesis and characterization of silver nanoparticles using aqueous extracts of de-oiled *Curcuma longa* and the study of its biomedical potential as an antimicrobial and anticancer drug.

2 Materials and Methods

2.1 Materials

De-oiled *Curcuma longa* (Fig. 2) was supplied by **Synthite,** the world's largest producer of value added spice extracts and natural spice powder. All the reagents purchased were of analytical grade and used without any further purification. Silver nitrate (AgNO$_3$) was purchased from Sigma-Aldrich from India. The bacterial strains were purchased from Gandhigram Rural Institute - Deemed University, Gandhigram. Mueller–Hinton broth and agar were purchased from Hi-Media, Mumbai, India. Double distilled water was used throughout the experiments.

Fig. 2. De-oiled *Curcuma longa* L.

2.2 Preparation of Extracts

The de-oiled turmeric sample was air dried and stored in the refrigerator. About 10 g of sample material was mixed with 100 ml of deionised water and added into a 500 ml beaker. The mixture was heated at 60 °C for 15 min. After that the solution was filtered with the help of Whatman No. 1 filter paper. Then the de-oiled turmeric aqueous extract (Fig. 3) was kept in refrigerator at 4 °C for future experiments.

Fig. 3. De-oiled *Curcuma longa* extract

2.3 Synthesis of AgNPs

For the reduction of silver ions, 90 ml of 1 mM AgNO3 aqueous solution of silver nitrate was taken in Erlenmeyer flask, and 10 ml of de-oiled turmeric sample extract was added to it separately at room temperature. After 30 min the solution turned pale yellow to dark brown indicating the formation of silver nanoparticles.

3 Characterization of AgNPs

The optical properties of the synthesized silver nanoparticles were studied using UV–vis spectroscopy (UV-1800v, Shimadzu, Japan). The surface morphology and size of the synthesized silver nanoparticles was analysed by using particle size analyser. The FTIR spectrum of synthesized silver nanoparticles was analysed with a Thermo Scientific Nicolet 380 FT-IR Spectrometer by KBr pellet method. The percentage presence of silver ions from the synthesized silver nanoparticles was done by using energy dispersive X-ray spectrum (EDX). The synthesized metallic nanoparticles was analysed by using X-ray diffractometer model (Shimadzu, Japan) with 40 kV, 30 mA with Cu k a radiation at 2θ angle.

4   Antimicrobial Activity

The antimicrobial activity was done using human pathogenic bacteria (*Bacillus subtilis*, *Staphylococcus aureus*, *Streptococcus faecalis*, *Klebsiella pneumoniae*, *Pseudomonas aeruginosa*, *E.coli*, *Candida albicans*) by agar well diffusion method. Muller Hinton agar medium was used to sub culture bacteria which were incubated at 37 °C for 24 h. Then the overnight inoculated cultures were taken and spread on the Muller Hinton agar plates. Wells were formed by using a cork borer of 6 mm diameter. Plant extract, silver nitrate and different concentration of AgNPs (100 μg/ml, 150 μg/ml, 200 μg/ml) were poured into each well. The streptomycin (20 μg/ml) was used as a control. The antimicrobial activity of AgNPs was determined by measuring the zone of inhibition around the well diameter (in mm) with the help of scale and the results were tabulated.

5   Anticancer Study

5.1   Preparation of Cell Suspension

For this study, the MCF-7cell lines were procured from National Centre for Cell Science (NCCS), Pune, India. A subculture of MCF 7 cells in Dulbecco's Modified Eagle's Medium (DMEM) was trypsinized separately. After discarding the culture medium, to the disaggregated cells in the flask, 25 ml of DMEM with 10% FCS was added. The cells were suspended in the medium by gentle passage with a pipette and the cells were homogenized.

5.2   Seeding of Cells

One ml of the homogenized cell suspension was added to each well of a 24 well culture plate along with different concentration of samples (3.12 to 400 μg/ml) and incubated at 37 °C in a humidified CO_2 incubator with 5% CO_2. After 48 h incubation the cells were observed under an inverted tissue culture microscope. With 80% confluence of cells, cytotoxicity assay was carried out.

5.3   Cytotoxicity Assay

The assay was carried out using (3- (4, 5- dimethyl thiazol-2yl)- 2, 5- diphenyltetrazolium bromide (MTT). MTT is cleaved by mitochondrial Succinate dehydrogenase and reductase of viable cells, yielding a measurable purple product formazan. This formazan production is directly proportional to the viable cell number and inversely proportional to the degree of cytotoxicity. After 48 h incubation, the wells were treated with MTT and left for 3 h at room temperature. The content of all the wells was removed using micropipette and 100 μl SDS in DMSO was added to dissolve the formazan crystals. Absorbance's were read using Read Well Touch micro plate reader at 570 nm [16].

6 Results and Discussion

On addition of de-oiled turmeric water extract to silver nitrate solution, a pale yellow solution was formed. The colour of the solution changed gradually from pale yellow to dark brown (Fig. 4) indicating the formation of silver nanoparticles. The colour change was immediate when exposed to sunlight and slow when kept in the dark indicating the catalytic role of sunlight which assists the formation of silver nanoparticles.
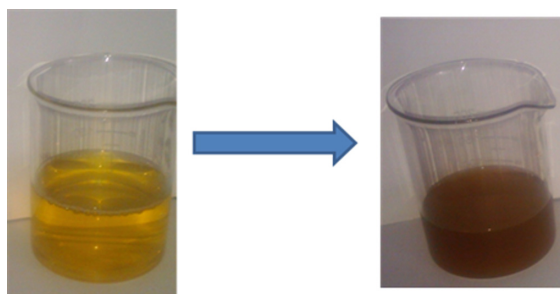
Fig. 4. Colour changes from yellow to brown on adding silver nitrate

6.1 Characterisation of Silver Nanoparticles

Optical Properties: The synthesized silver nanoparticles were characterized by **UV visible spectroscopy** to confirm the synthesis of silver nanoparticles. Due to surface Plasmon resonance of silver nanoparticles, a peak at 400–420 nm confirms the presence of silver. Two peaks were formed, one at 697 nm (1 in Fig. 5) and another at 417.5 nm (2 in Fig. 5). The peak at 417.5 nm corresponds to silver nanoparticles.
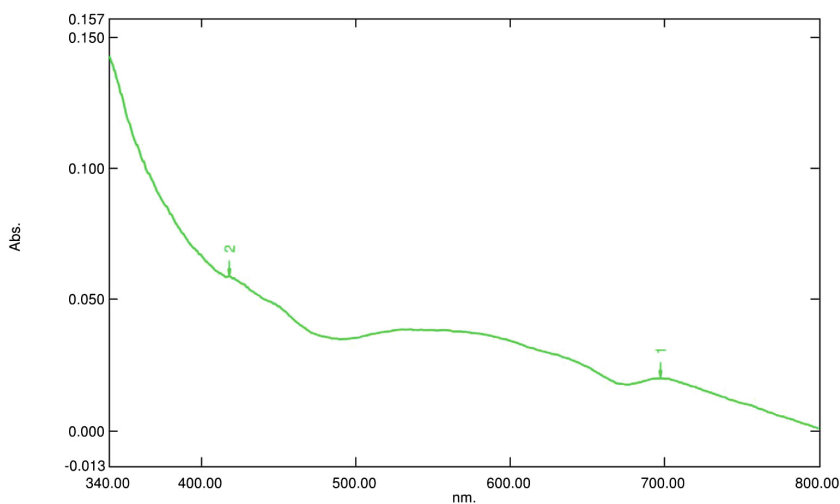
Fig. 5. UV spectra- peak 2 at 417.5 nm indicates AgNPs

FTIR Analysis: Fourier Transform Infra Red Spectroscopy was carried out to identify the groups responsible for reduction and stabilization of the synthesized silver nanoparticles. The FTIR spectrum (Fig. 6) showed four strong peaks at 3443.66 cm^{-1}, 1604.66 cm^{-1}, 1379.97 cm^{-1} and 1076.21 cm^{-1} and several smaller peaks at 775.33 cm^{-1}, 1745.46 cm^{-1}, 2926.78 cm^{-1}, 2313.46 cm^{-1}, 1311.50 cm^{-1}, 1229.54 cm^{-1}, 825.48 cm^{-1}, 775.33 cm^{-1} and 518.82 cm^{-1}. The highest absorbance at 3443.66 cm^{-1} corresponds to O-H stretch of carboxylic acids, phenols and alcohols; the second peak at 2926.78 cm^{-1} is assigned to the C-H stretch of alkanes; The peak at 1745.46 cm^{-1} indicates C = O stretch of aldehydes; 1604.66 cm^{-1} peak shows the presence of amides (N-H bend); The second highest peak at 1379.97 is for alkanes; 1311.50 cm^{-1} shows N-O stretch of nitro compounds; 1229.54 cm^{-1} corresponds to ethers(C-O-C); 1076.21 cm^{-1} to C-N stretch of aliphatic amines; peaks 825.48 cm^{-1} and 775.33 cm^{-1} correspond to aromatic p- and m- disubstituted compounds and 518.82 cm^{-1} corresponds to alkyl halides (C-Br stretch).
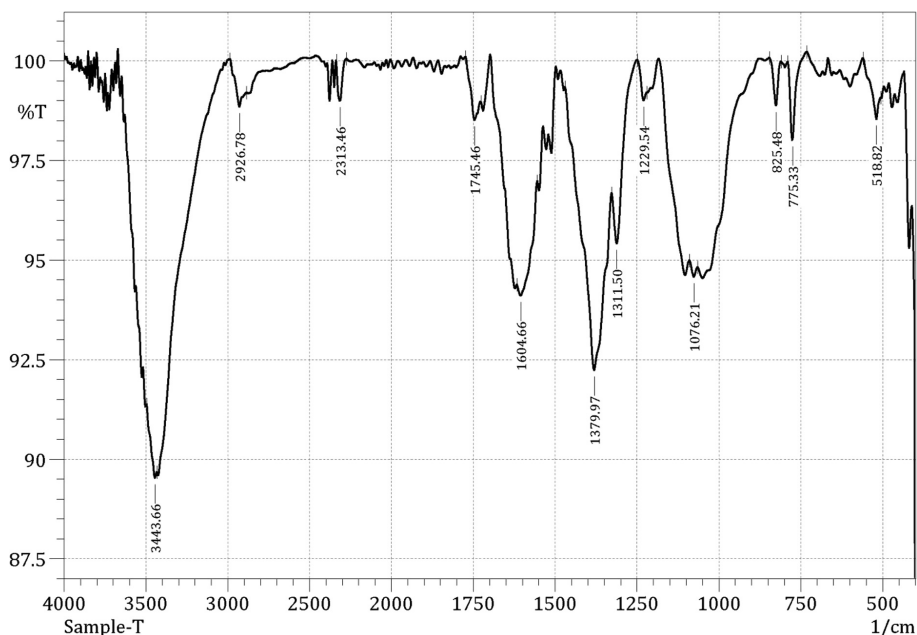

Fig. 6. FTIR spectra indicates presence of phenols

XRD Studies: X-Ray Diffraction studies were carried out with the synthesized silver nanoparticles to elucidate their crystalline structure. Crystal size was calculated using Debye-Scherrer equation. The equation can be written as:

$$\tau = K\lambda / \beta \cos \theta$$

where:

- τ is the mean size of the ordered (crystalline) domains, which may be smaller or equal to the grain size
- K is a dimensionless **shape factor**, with a value close to unity. The shape factor has a typical value of about 0.9, but varies with the actual shape of the crystallite
- λ is the X-ray wavelength
- β is the line broadening at half the maximum intensity (FWHM), after subtracting the instrumental line broadening, in radians. This quantity is also sometimes denoted as 2θ
- θ is the Bragg angle.

The average crystal size was calculated, using Scherrer-Debye's equation for FWHM and 2 theta values (Table 1), as **19.8 nm**.

Table 1. XRD analysis 2 theta values

Pos. [°2Th.]	Height [cts]	FWHM left [°2Th.]	d-spacing [Å]	Rel. Int. [%]
27.9692	48.66	0.2952	3.19016	51.33
32.3391	94.80	0.2460	2.76837	100.00
46.3627	65.06	0.3936	1.95847	68.63
54.8643	23.68	0.3936	1.67341	24.98
57.6923	16.87	0.5904	1.59793	17.80
67.5890	8.13	1.1808	1.38604	8.58
76.8832	15.86	1.1808	1.24001	16.73

The XRD graph (Fig. 7) shows major peaks at 2 theta values of 32.34, 46.36 and 76.88. The crystal structure was determined by comparing d-spacing values with standard data using JCPDF software. The crystal structure matched PDF #411402 for silver showing Hexagonal structure at planes 1.386 (112) and 1.2400 (201).
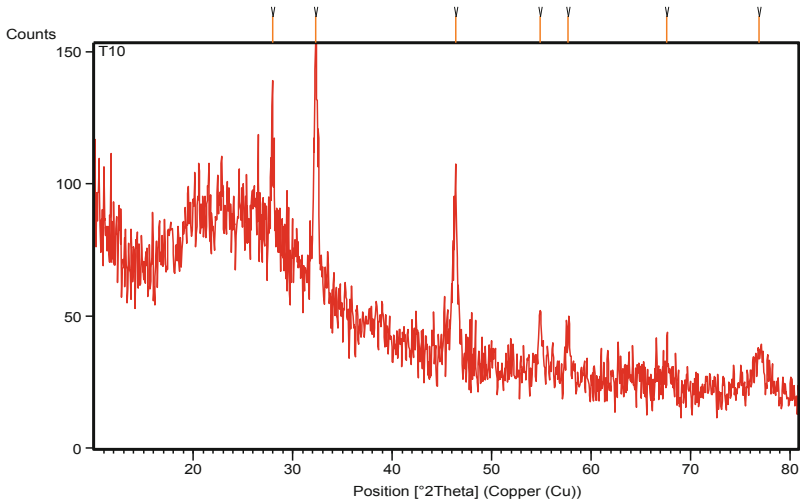
Fig. 7. XRD graph revealed hexagonal structure

Particle Size Analysis: The size of the synthesised nanoparticles was +measured using a Flow cell (Shimadzu SALD-2300). The size of the particles varies from 25 nm-75 nm with an average size of around 50 nm (Fig. 8).
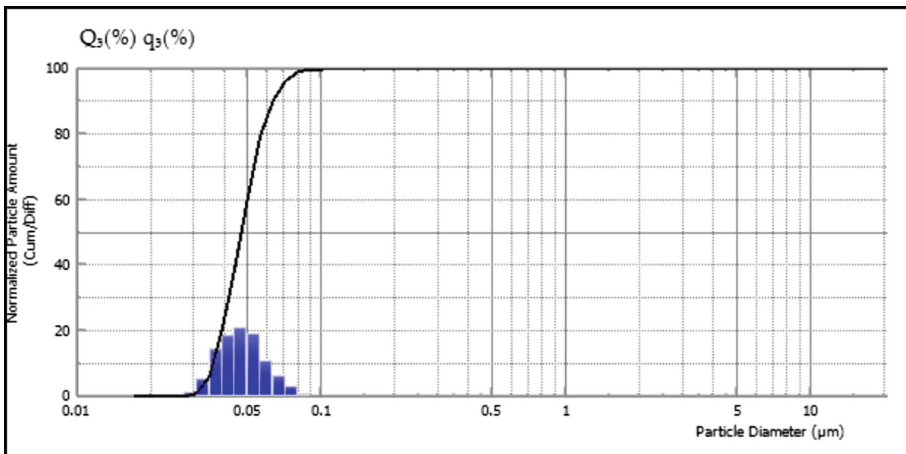
Fig. 8. Particle size analysis

6.2   Biomedical Potential

Antimicrobial Activity. The antimicrobial activity of silver nanoparticles against human pathogenic bacteria is mostly used in the medical field to hasten wound healing and also in water purification. The synthesized AgNPs were treated against seven bacterial strains: Gram positive bacteria such as *Bacillus subtilis*, *Staphylococcus*

aureus, *Streptococcus faecalis* and Gram negative bacteria *Klebsiella pneumoniae*, *Pseudomonas aeruginosa, E.coli* and a fungus *Candida albicans*. Agar well diffusion method was used (Fig. 9).

Gram positive bacteria
Bacillus subtilis
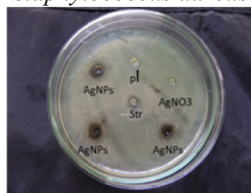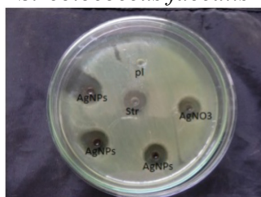
Gram negative bacteria
Klebsiella pneumonia

Fungi
Candida albicans

Staphylococcus aureus

Psuedomonas aeroginosa

Streotococcus faecalis
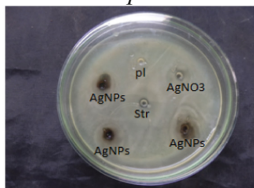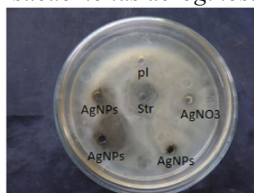
Escherichia coli

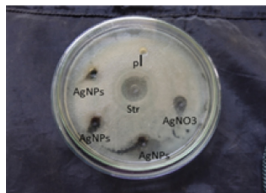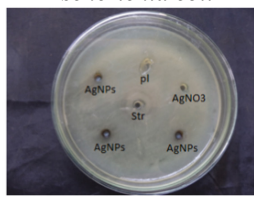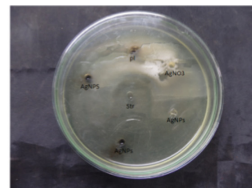**Fig. 9.** Antimicrobial activity by well diffusion method

The zones of inhibition (Table 2) illustrated that the maximum zone of inhibition was against (*Bacillus subtilis* 13 mm) and (*Pseudomonas aeruginosa 13* mm) respectively. The ZOI increased with increase in concentration of AgNPs. The

Table 2. Zone of inhibition (ZOI) in mm

S. No	Cultures	Plant extract	AgNO3 (100 µl)	AgNPs (100 µl)	AgNPs (200 µl)	AgNPs (300 µl)	Streptomycin
1	*Bacillus subtilis*	10	25	12	13	15	30
2	*Staphylococcus aureus*	12	22	13	17	19	25
3	*Streptococcus faecalis*	10	27	25	28	29	30
4	*Klebsiella pneumoniae*	10	30	15	18	20	31
5	*Pseudomonas aeruginosa*	12	35	22	23	24	20
6	*Escherichia coli*	10	27	16	18	19	32
7	*Candida albicans*	11	35	12	13	18	45

remaining bacterial strains were only fairly susceptible. The synthesized AgNPs exhibited significant antimicrobial activity against human pathogenic bacteria.

Cytotoxicity. The in-vitro cytotoxicity activity studies proved that MCF 7 cells were reduced significantly with increase in AgNPs concentration (Table 3). In the cell line, cytotoxic effect was observed in turmeric spent AgNPs concentration after 48 h treatment. It also revealed that increased concentration of AgNPs shown increased cytotoxicity over the MCF 7 cell line.

Table 3. MTTP assay for cytotoxicity

Conc of AgNPs	OD	OD (after 48 h)	Cell viablity
0	1.325	1.325	100.00
3.12	1.175	1.325	88.68
6.25	0.963	1.325	72.68
12.5	0.914	1.325	68.98
25	0.867	1.325	65.43
50	0.754	1.325	56.91
100	0.675	1.325	50.94
200	0.641	1.325	48.38

From the graph (Fig. 10) the IC 50 value was calculated as 1.84 showing that the nanoparticles showed good efficacy in destroying cancer cells.
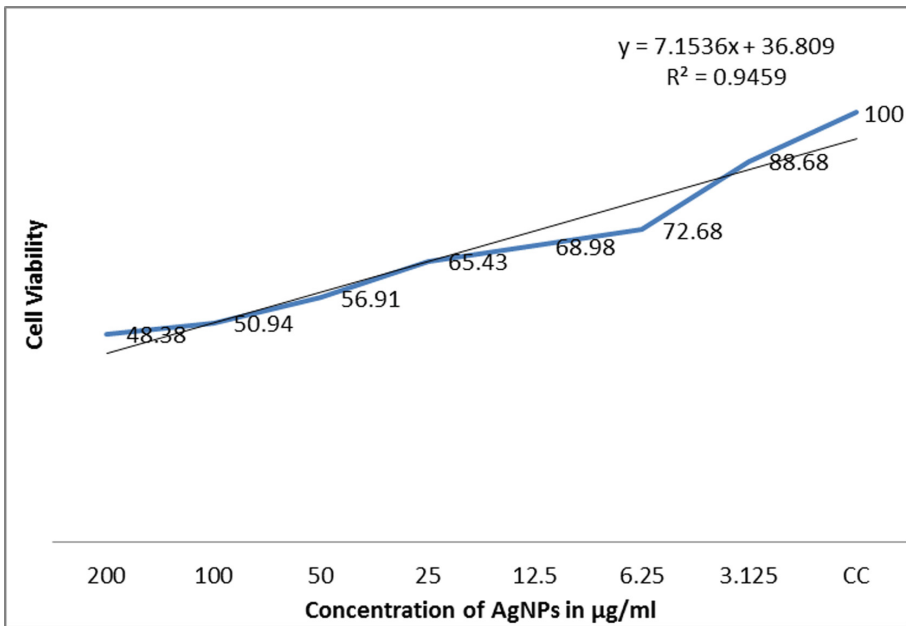
Fig. 10. MTTP assay for cytotoxicity

The cells were observed under an inverted tissue culture microscope (Fig. 11). The increase in concentration of AgNPs resulted in increase in cytotoxicity.

Control   100µg/ml   200µg/ml
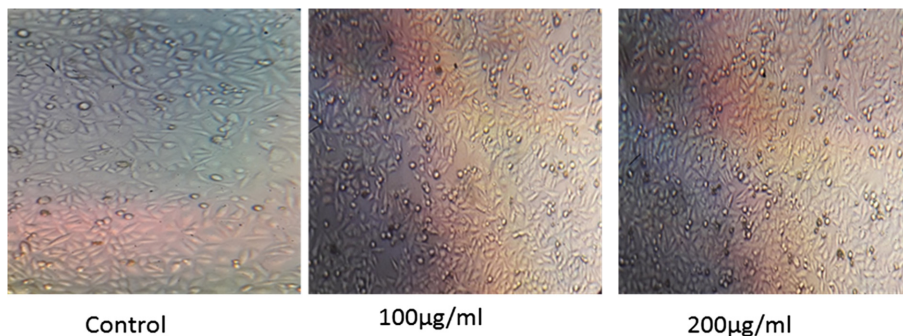
Fig. 11. MCF-7 treated with de-oiled turmeric AgNPs

7   Conclusion

The active ingredients in turmeric like curcumin and turmerone are not the only contents in turmeric that have medicinal value. Even the de-oiled turmeric devoid of turmerone and curcumin shows biomedical potential.

Silver nanoparticles were produced using de-oiled tumeric as reducing and capping agent in the presence of sunlight. They were characterised by UV-vis, FTIR, XRD and particle size analyser. Hexagonal silver nanoparticles of size around 40 nm, stabilized by phenol groups were obtained. The silver nanoparticles showed good antimicrobial activity against selected bacteria and fungi. The activity increased with increase in concentration of nanoparticles. Excellent activity against *Streptococcus faecalis* was seen comparable to Streptomycin. Cytotoxic effect was observed in tested sample concentrations after 48 h treatment. It also revealed that increase in concentration of drug showed increased cytotoxicity over the MCF-7 cell line with an effective IC 50 value of 1.84. This efficient biomedical potential of the synthesized silver nanoparticles paves the way for its application in the area of nano-medicine.

References

1. Rai, M., et al.: Synergistic antimicrobial potential of essential oils in combination with nanoparticles: emerging trends and future perspectives. Int. J. Pharm. **519**, 67–78 (2017)
2. Azizinezhad, F., et al.: Synthesis of the silver nanoparticles with the using of camomile plant. Eur. J. Exp. Bio. **4**(2), 124–127 (2014)
3. Chattopadhyay, I., Biswas, K., Bandyopadhyay, U., Banerjee, R.K.: Turmeric and curcumin: biological actions and medicinal applications. Curr. Sci. **87**(1), 46 (2004)

4. Sun, Y., Yin, Y., Mayers, B.T., Herricks, T., Xia, Y.: Uniform form silver nanowires synthesis by reducing AgNO$_3$ with ethylene glycol in presence of seeds and polyvinyl pyrrolidone. Chem. Mater. **14**, 4736–4745 (2002)
5. Yin, B., Ma, H., Wang, S., Chen, S.: Electrochemical synthesis of silver nanoparticles under protection of poly N-vinyl pyrrolidone. J. Phys. Chem. B **107**, 8898–8904 (2003)
6. Dimitrijevic, N.M., Bartels, D.M., Jonah, C.D., Takahashi, K., Rajh, T.: Radiolytically induced formation and optical absorption spectra of colloidal silver nanoparticles in supercritical ethane. J. Phys. Chem. B **105**, 954–959 (2001)
7. Callegari, A., Tonti, D., Chergui, M.: Photochemically grown silver nanoparticles with wavelength-controlled size and shape. Nano Lett. **3**, 1565–1568 (2003)
8. Zhang, L., Shen, Y.H., Xie, A.J., Li, S.K., Jin, B.K., Zhang, Q.F.: One-step synthesis of monodisperse silver nanoparticles beneath vitamin E Langmuir monolayers. J. Phys. Chem. B **110**, 6615–6620 (2006)
9. Swami, A., Selvakannan, P.R., Pasricha, R., Sastry, M.: One-step synthesis of ordered two dimensional assemblies of silver nanoparticles by the spontaneous reduction of silver ions by pentadecylphenol Langmuir monolayers. J. Phys. Chem. B **108**, 19269 (2004)
10. Naik, R.R., Stringer, S.J., Agarwal, G., Jones, S., Stone, M.O.: Biomimetic synthesis and patterning of silver nanoparticles. Nat. Mater. **1**, 169–172 (2002)
11. Gannimani, R., Perumal, A., Krishna, S., Sershen, M., Mishra, A., Govender, P.: Dig. J. Nanomater. Biostruct. **9**, 1669 (2014)
12. Das, V.L., Thomas, R., Varghese, R.T., Soniya, E., Mathew, J., Radhakrishnan, E.: 3 Biotech. **4**, 121 (2014)
13. Liu, B., Xie, J., Lee, J., Ting, Y., Chen, J.P.: Green synthesis of silver nanoparticles from Moringa oleifera leaf extracts and its antimicrobial potential. J. Phys. Chem. B **109**, 15256 (2005)
14. Banerjee, P., Satapathy, M., Mukhopahayay, A., Das, P.: Leaf extract mediated green synthesis of silver nanoparticles from widely available Indian plants: synthesis, characterization, antimicrobial property and toxicity analysis. Bioresour. Bioprocess. **1**, 3 (2014)
15. Moodley, J.S., Krishna, S.B.N., Pillay, K., Sershen, M., Govender, P.: School Advances in natural sciences: nanoscience and nanotechnology, vol. 9, p. 015011 (9pp) (2018)
16. Mosman, T.: Rapid colorimetric assay for cellular growth and survival, application to proliferation and cytotoxicity assays. J. Immunol. Methods **65**, 55–63 (1983)

In-Vitro Wound Healing and Release Kinetics of β-Cyclodextrin Encapsulated Curcumin Loaded Carrageenan Hydrogel Film: An Efficient Wound Dressing Material

Aswni Sundara Rajan, Kerensa Miriam Sheen, Balaji Sadhasivam, and Nachimuthu Saraswathy[(✉)]

Department of Biotechnology, Kumaraguru College of Technology, Chinnavedampatti, Coimbatore 641049, Tamilnadu, India
{aswni.l5bt,kerensa.l5bt,balaji.l7phd, saraswathy.n.bt}@kct.ac.in

Abstract. Curcumin has the potential as a therapeutic drug having wider pharmacological application. But due to its lipophilicity, it exhibits a deprived serum level absorption rate, resulting in rapid systemic elimination. Conjugation of curcumin in a polymeric micelle increase the bioavailability of curcumin as a drug delivery system. β-Cyclodextrins, being circular oligosaccharides with an α (1–4) linked α-D-glucopyranose structure, along with a lipophilic center and hydrophilic outer surface, entraps the curcumin in the central cavity. In this present work, encapsulated curcumin was prepared and characterized using FTIR, PSA, Zeta potential, EDAX and TEM. Carrageenan based hydrogel films loaded with β-CD/Curcumin were synthesized as a wound dressing material. Further, to understand release kinetics of encapsulated curcumin in hydrogel film, release behaviour of curcumin was carried out and the data was fitted in different models. Free radical scavenging activity studies showed the potency of β-CD/Curcumin loaded carrageenan hydrogel as a wound dressing material.

Keywords: Curcumin · Release kinetics · Encapsulation · B-cyclodextrin

1 Introduction

A wound is defined as a disruption in the epithelial lining of the skin or mucosal membrane as a result of either physical or thermal processes [1]. These disruptions in the skin membrane are a major risk for re-injury and the more severe reinfection, which is why wound healing is very important. Wound healing is a complex and dynamic process [2] that involves three major phases: the initial inflammatory phase the second proliferative phase and the final maturation phase [3, 4].

An ideal dressing material must be sterile, non-toxic and non-allergic, while also promoting angiogenesis and connective tissue synthesis [5]. Based on their function in the wound, they can be classifying as debridement, anti-bacterial, occlusive, absorbent and adhesive [6]; in case of the type of the material used to make the dressing, they are

classified as hydrocolloid, alginate and collagen [7] based on the physical form of the wound, they are classified as ointment, film, foam and gel [8].

Traditional wound dressings, such as gauze and cotton become too moist due to excessive wound drainage, adhering itself to the wound and making it difficult and painful to remove. Another disadvantage of gauze dressing is that they provide little occlusion which reduces moisture content, leading to a dehydrated wound bed, causing more injury to tissue [9]. Therefore, wound dressing materials are to be developed that are non-adhesive, more occlusive and more absorbent while also maintaining a good safety profile.

Modern wound dressing materials, like hydrocolloid, alginate and hydrogel-based materials are now more used than traditional dressing materials, because of their ability to create and more importantly, retain a moist environment around the wound, providing better and faster wound healing. But there is a lot of potential in hydrogel-based dressing materials, as they most resemble living tissues than other synthetically-derived systems, especially in their high moisture retentivity [10]. Other advantages in the use of hydrogels are elasticity and their ability to be adapted for the delivery of any drug molecule, regardless of size Hydrogels have also been deemed as "smart materials", because they are able to respond and adapt to changing stimuli in a living system, thus being able to release a drug in the body in a controlled manner [11]. Therefore, it is observed that hydrogels seem to obey all the characteristics of an ideal wound dressing, and because of their high moisture content, they also provide a cool feeling to the wound, enhancing the healing process while also giving comfort to the patient. In our study we have used carrageenan, a set of natural polysaccharides derived from the red seaweed class Rhodophyta [12], with 15 to 40% of ester-sulfate content and an average relative molecular mass well above 100 kDa, are finding novel applications in wound care and drug delivery. Carrageenans are now preferred for use because of their good pharmacokinetic properties, specifically its good biocompatibility, which is being used by researchers to improve drug formulation and prolong drug release for over 24 h [13] to 3 weeks [14]. Besides this, they also possess medicinal properties such as anti-bacterial, immuno-modulatory, and even anti-viral activity [15, 16], against Hepatitis A virus. Carrageenan is one of the most preferred natural polymers for formation of hydrogels and for encapsulation of pharmaceutical compounds because of its gelling properties. κ-carrageenans are the most commonly used class to be used for manufacturing hydrogels.

Curcumin has the potential as a therapeutic drug having wider pharmacological application. But due to its lipophilicity, it exhibits a deprived serum level absorption rate, resulting in rapid systemic elimination. Curcumin has been shown to possess significant anti-inflammatory, anti-oxidant, anti-carcinogenic, anti-mutagenic, anti-coagulant and anti-infective effects. Due to these properties and many more it has good wound healing properties. While curcumin has medicinal benefits that make it suitable for wound healing, it faces one major drawback. Being hydrophobic in nature, it cannot be administered orally as the metabolites it forms in the body are not stable and get easily excreted. For it to be suitable as part of a wound dressing material, it must have the ability to prolong its release into the body. In our study we look at encapsulation of curcumin molecules in suitable drug carriers like β-cyclodextrin (BCD) as a suitable method for prolonging the drug release.

Although curcumin has many medicinal benefits, a great limitation of its use in drug delivery applications is its poor bioavailability. Aggarwal and Sung [17] reviewed studies performed in both humans and animals and observed that curcumin when administered orally was very poorly bioavailable with little to no levels of curcumin metabolites present in serum tissue. These metabolites have a very short release time and are quickly eliminated from the body. Curcumin's low bioavailability is due to its hydrophobic nature, so it cannot be taken orally without some modifications to its structure to make it more hydrophilic. Many approaches are available to increase curcumin's bioavailability in aqueous solutions. Chemically modified structures of curcumin have also been developed. Many studies have been performed to demonstrate the different types of modifications that can be made to the structure of curcumin, as Vyas et al. [18] illustrated in the following Fig. 1:
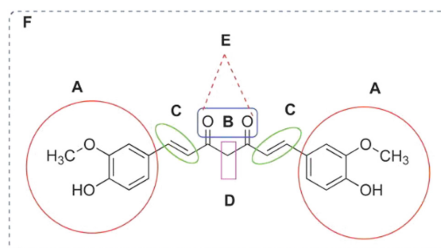
Fig. 1. Structural modification approaches to chemically modify curcumin.

Reviewing studies on chemical modifications of curcumin, there are five approaches that can be taken:

i. Modifying the aryl side chains on either side of the curcumin structure (A);
ii. Modifying the di-keto functionality (B);
iii. Modifying the double bonds (C);
iv. Modifying the active methylene functionality (D);
v. Modifying the complexing activity of curcumin by binding it to metal complexes (E).

All these approaches lead to structural analogues of curcumin, that have better bioavailability when compared to free curcumin.

Micelles are aqueous dispersions of self-assembled aggregates of surfactant or block co-polymers in the size range of 5–100 nm [19], making it suitable for oral administration of hydrophobic drugs such as curcumin in the body. They can be manufactured easily using various simple techniques such as dissolution, dialysis, and oil-in-water emulsions. This method is quite useful for curcumin to increase its bioavailability in the body [20]. The nano-micellar approach of increasing the bioavailability o can be considered as a better and more cost-economical approach as compared to the structural analogue approach explained previously. Nano-particle formulations (NP) can offer more effective drug delivery mechanisms than conventional drug delivery systems [21].

β-Cyclodextrins, are circular oligosaccharides with an α (1-4) linked α-D-glucopyranose structure, with a lipophilic center and hydrophilic outer surface, hence β-Cyclodextrins can form inclusion complexes with a wide variety of hydrophobic molecules. [22] For β-cyclodextrin (BCD), there has been much work on its encapsulation with curcumin being used to check its anti-cancer activity. Compatibility studies show that the self-assembly of BCD and free curcumin (BCD-Cur) shows great biocompatibility in aqueous solutions, with an uptake in cells being more than 0.6 mg/ml. This is because the self-assemblies are stable when produced in a solvent evaporation technique. In prostate cancer cell lines, a formulation of β-cyclodextrin encapsulated curcumin showed great promise, with cellular uptake of BCD-Cur being significantly more than free curcumin [23].

2 Materials

Curcumin was purchased from Sigma-Aldrich, Beta Cyclodextrin and L-Carrageenan purchased from HiMedia labs. LR grade Carbinol, Tween®20 and Glycerol purchased from HiMedia. All tests were performed using autoclaved distilled water.

3 Methods

3.1 Preparation and Optimization of Gel Films

2% w/v and 1% w/v L-Carrageenan gels were prepared by sol-gel method. Stock solutions of 2% w/v and 1% w/v L-Carrageenan were first prepared in distilled water and heated till clear solution was obtained. One set of gels were prepared with 0.5% w/v glycerol solution and one set was prepared without glycerol. These solutions were then cast and left to set overnight. After the gels were set, they were left to dry in the hot air oven for 6 h. The dried films were then observed for differences in texture.

3.2 Encapsulation/Preparation of β-Cyclodextrin Curcumin Nano Micelle

The ratio for β-cyclodextrin (BCD) and Methanolic Curcumin (MC) was optimized to be 11.3:0.36 mg/ml. The first stock solution of 11.3 mg/ml BCD was prepared in distilled water for 50 ml, next stock solution of 0.36 mg/ml MC was prepared for 50 ml. The stock solution was transferred to a brown bottle and prepared to be mounted on magnetic stirrer. The MC solution was added dropwise whilst continuous stirring, after which 20 μl of Tween20 was added, and the bottle was recapped. The stirring continued for 24 h. After 24 h a colloidal solution appeared. This solution was centrifuged at 5000 rpm for 15 min, and the pellet was left to dry in hot air oven at 55 °C till it became dry. The pellet NMC was scraped out and stored in dry conditions.

3.3   Preparation of NMC-Hydrogels

2%w/v L-Carrageenan gels were prepared by sol-gel method. A stock solution of 2% w/v L-Carrageenan were first prepared in distilled water and heated till clear solution was obtained. 1 mg/ml β-cyclodextrin encapsulated curcumin (BCD-Cur) was suspended in distilled water. These suspensions were mixed with their respective gel solutions before casting. The castings were left to set overnight.

3.4   Encapsulation Efficiency

1 mg/ml stock solution of the NMC procured was prepared in methanol and OD checked at 420 nm in a UV-Visible spectrophotometer. The solution was serially diluted till an accepted OD value was reached. The following formula was used to calculate the encapsulation efficiency of βcyclodextrin,

$$Drug\ encapsulation\% = \left[\frac{Amount\ of\ curcu\min\ encapsulated}{Amount\ of\ curcu\min\ used}\right] X\ 100$$

3.5   Particle Size Analysis and Zeta Potential

The particle size and zeta potential of the NMC was evaluated by using Malvern® Mastersizer 2000-Particle Size Analyser and Nano-range Zetasizer.

3.6   Release Studies

The films were cut into 2×2 cm squares. Each square was suspended into 5 ml of distilled water. Samples of 1 ml were drawn every hour and the solutions were replenished with 1 ml of fresh distilled water. The samples were taken, and absorbance was measured via UV-visible spectrophotometer at 420 nm. This process was repeated until the gel lost its integrity. The release kinetics was studied by using the open-access software KinetDS3.

3.7   Swelling Studies

The films were cut into 2×2 cm squares. Each square was suspended into 5 ml of distilled water. Once every hour the gel was taken out of the solution, blotted dry and weighed. The gels were then immersed in fresh distilled water. This process was repeated until the gel lost its integrity.

3.8   Free Radical Scavenging Activity

Curcumin is a good anti-oxidant and will reduce 1,1-Diphenyl-2-picrylhydrazil (DPPH), hence it is a good free radical scavenger. Scavenging activity was found for both the compound as well as the film. Stock of 1 mg/ml of the compound was prepared in methanol. Different concentrations (20 μl–100 μl) were then pippeted into test tubes, 3 ml methanolic DPPH was added into each test tubes and incubated in dark

for 30 min. OD of each concentration were taken at 520 nm. The films were immersed in 3 ml of methanolic DPPH and OD were taken every 10 min for 1 h at 520 nm. The ant-oxidant activity of the NMC was calculated by using the formula,

$$Scavenging\ Activity = \left[\left(\frac{OD_{control} - OD_{sample}}{OD_{control}}\right) - 1\right]$$

4   Results and Discussion

4.1   FT-IR

Fourier Transform-Infra-Red (FT-IR) spectroscopy measures a sample's absorbance of infra-red light at various wavelength to determine the material's composition and structure.

The FT-IR spectrum of methanolic curcumin showed a broad peak at 3319.49 cm^{-1}, indicating the phenolic OH stretch long; broad peak at 1450.47 cm^{-1} indicates the C-O stretch in the aromatic ring. The FT-IR showed signature peak at 3280.92 cm^{-1} indicating the OH stretch an arrow peak at 2108.20 cm^{-1} and a broad peak at 1645.28 cm^{-1} representing the C-C stretch in the aromatic ring. All peaks of the β-cyclodextrin-curcumin coincide the peaks of β-cyclodextrin. Peak at 1014.56 cm^{-1} and 112.43 cm^{-1} coincide with the peaks of curcumin. There is modification at peaks 3319.49 cm^{-1}, 2831.50 cm^{-1}, 114.86 cm^{-1} and 1024.20 cm^{-1} of curcumin in the encapsulated curcumin FT-IR spectrum, indicating the bonding of β-cyclodextrin and curcumin (Fig. 2).
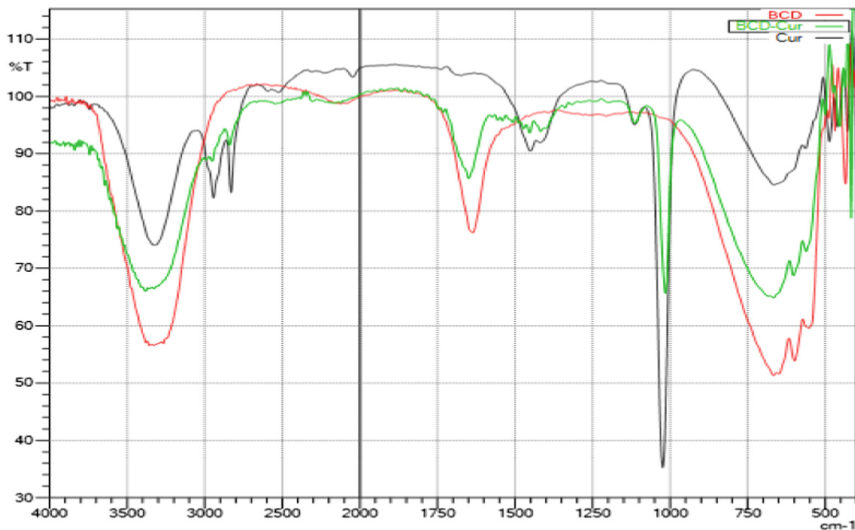

Fig. 2. FT-IR spectrum of β-cyclodextrin-curcumin

4.2   Texture Studies

After the gels were set, they were left to dry in the hot air oven for 6 h. The dried films were then observed for differences in texture (Table 1).

Table 1. Texture Studies of the prepared gel films

Hydrogel film	Observation
1% carrageenan	Brittle, may crack on touch, feels light, is not elastic, very thin, clear, smooth
1.5% carrageenan	Brittle, is not cracked when touched, is slightly elastic, thin, clear, smooth
2% carrageenan	Slightly brittle, slightly elastic, clear, smooth
1% carrageenan + 0.5% glycerol	Flexible, does not crack when touched, crease formation when bent, elastic, clear, smooth
1.5% carrageenan + 0.5% glycerol	Flexible, more elastic than previous, elastic, clear, smooth
2% carrageenan + 0.5% glycerol	Most flexible, thicker than all, most elastic, clear, smooth

4.3   Film Formation

The hydrogel prepared from L-carrageenan and encapsulated curcumin, was left to dry for 6 h in a hot air oven at 55 °C (Fig. 3).

(i)   (ii)
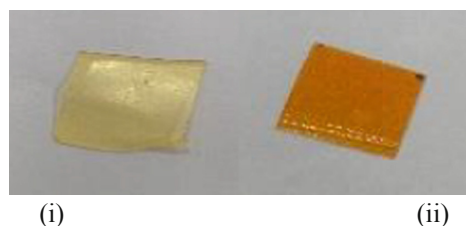
Fig. 3. 2% Carrageenan hydrogel films incorporated with encapsulated curcumin. (i) β-cyclodextrin encapsulated curcumin (ii) free curcumin.

4.4   Drug Encapsulation Efficiency

The main motive behind encapsulation of curcumin was to increase its hydrophilicity. β-cyclodextrin has a hydrophilic exterior and a polar cavity that is slightly hydrophobic. The curcumin is hypothesised to interact with the β-cyclodextrin molecule inside its cavity. The molecular weight of β-cyclodextrin is 1134.9 g/mol and the diameter of the inner cavity is approximately 60 nm [22]. For a working volume 50 ml each of the compound and the drug the encapsulation efficiency was calculated using the above-mentioned formula, equalled to 88.76% for β-cyclodextrin-curcumin.

4.5   Particle Size

The smaller size of a particle higher the surface area for reaction. The particle size of the NMC was identified using Malvern® 2000- Particle Size Analyser. The range of particle size of β-cyclodextrin encapsulated curcumin is 110–800 nm in diameter, with one peak observed at 311.5 nm, and the average particle size is 345.2 nm in diameter (Fig. 4).
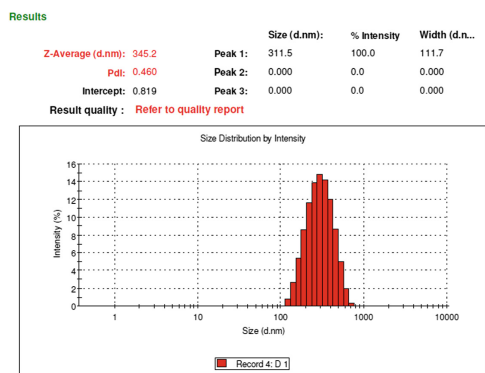
Fig. 4. Report of particle size of β-cyclodextrin-curcumin

4.6   Zeta Potential

Zeta potential indicates the electrostatic interactions of the particles in a fluid environment. This term is used to for determining the surface charge of nanoparticles. The zeta potential of the NMC was identified using Malvern® Nano-range Zetasizer. The zeta potential for β-cyclodextrin encapsulated curcumin was found to be −24.9 mV. The negative charge indicates that at the surface of the molecule, aligning of the amphilic β-cyclodextrin are such that the un-substituted −OH groups are pointing upwards towards the aqueous surrounding, rendering a potential surface hydrophobicity (Fig. 5).
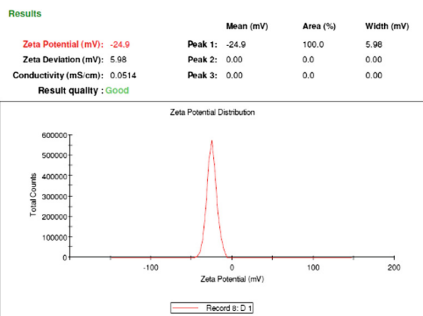
Fig. 5. Report of zeta potential of β-cyclodextrin- curcumin

4.7   Release Kinetics

As mentioned in the methodology the release kinetics for both the films were recorded and plotted to find the trend, the data were then put into the open-access software KinetDS3 to identify the model of release. Michaelis Menten (refer Fig. 7) was the best fit for the release of encapsulated curcumin from film. The dissolution rate for β-cyclodextrin-curcumin is slow and sustained (Fig. 6).
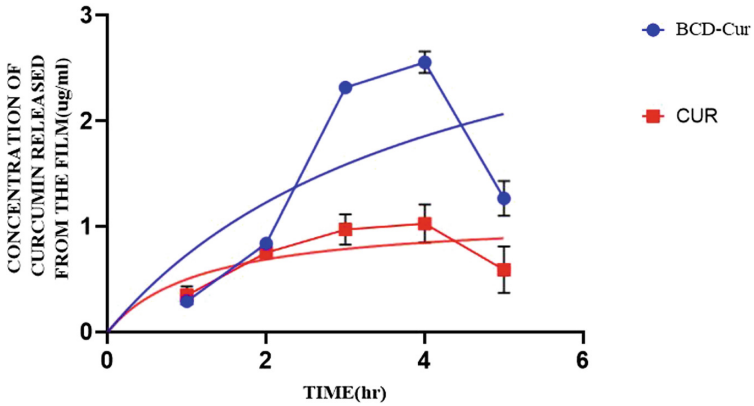
Fig. 6. Graph showing the trends in release kinetics of β-cyclodextrin encapsulated curcumin and free curcumin incorporated in 2% carrageenan hydrogel film
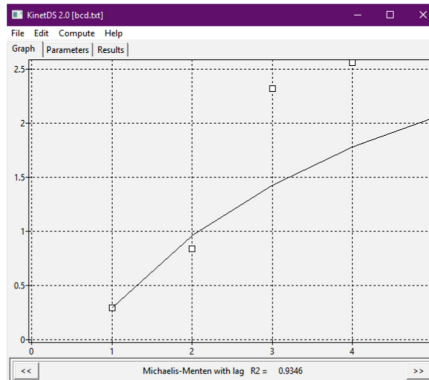
Fig. 7. Output of the KinetDS3 for β-cyclodextrin encapsulated curcumin

The equation governing the rate of dissolution is y = ymax*(x-lag)/(Km + x-lag).

4.8   Swelling Studies

Hydrogels have the excellent ability to retain high amount of water into them. Swelling of the hydrogel films were carried out as mentioned in the methodology. There was 6 h stability for a 2×2 cm film. Carrageenan hydrogel are composed of polymer chains containing charged groups, mainly sulfate groups [24]. The sulfate groups are ionizable and take up negative charge. The same negative charges repel each other and increase the distance between the chains and thereby increasing the network of the gel to take in more water. The hydrogel attained its equilibrium at the third hour and lost its integrity at the sixth hour. The β-cyclodextrin encapsulated curcumin film follows a stable swelling rate with a peak at the 3rd hour, unlike free curcumin incorporated film which sharply declines as the gel integrity is lost (refer Fig. 8).
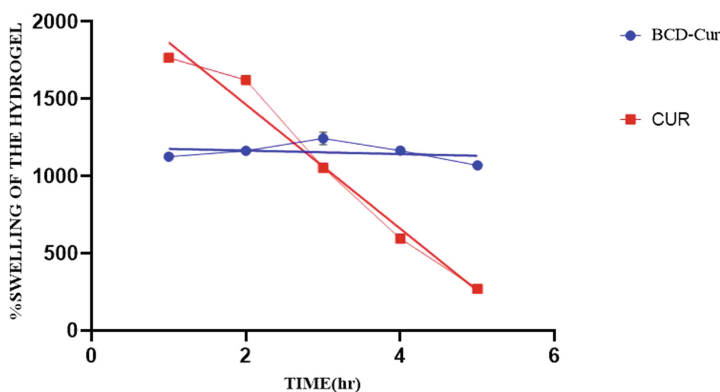
Fig. 8. Graph showing the trend of the swelling studies of β-cyclodextrin-cyclodextrin curcumin and free curcumin compounds.

4.9   Free Radical Scavenging Activity

1,1-Diphenyl-2-picrylhydrazil (DPPH) is a stable free radical that accepts an electron or hydrogen radical to become a stable dimanetic molecule. Decolorization of stable 1,1-diphenyl-2-picryl hydrazyl radical (DPPH) in the presence of anti-oxidant was noted to evaluate the radical scavenging activity of the test compounds. Curcumin exhibits ant-inflammatory activity by generating reactive oxygen species. This property of curcumin is due to the presence of functional groups like two each of hydroxyl, methoxy and phenyl groups. β-cyclodextrin-curcumin has a lowered anti-oxidant activity compared to curcumin ($p < 0.005$) (Figs. 9 and 10).
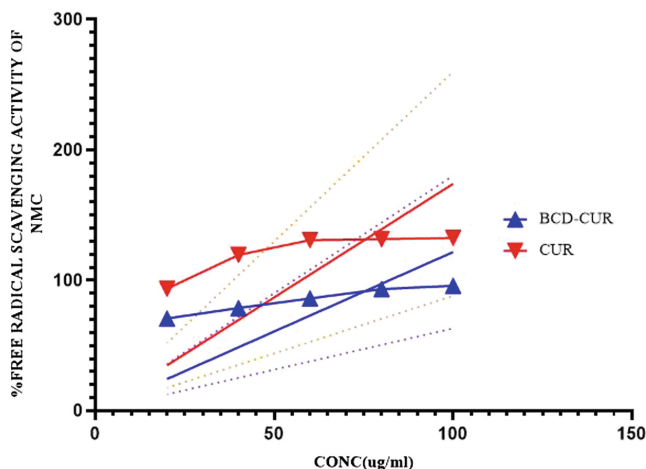
Fig. 9. Graph showing the trend in anti-oxidant activity for β-cyclodextrin and free curcumin compounds. *CONC (μg/ml)—Concentration of test compounds in μg/ml
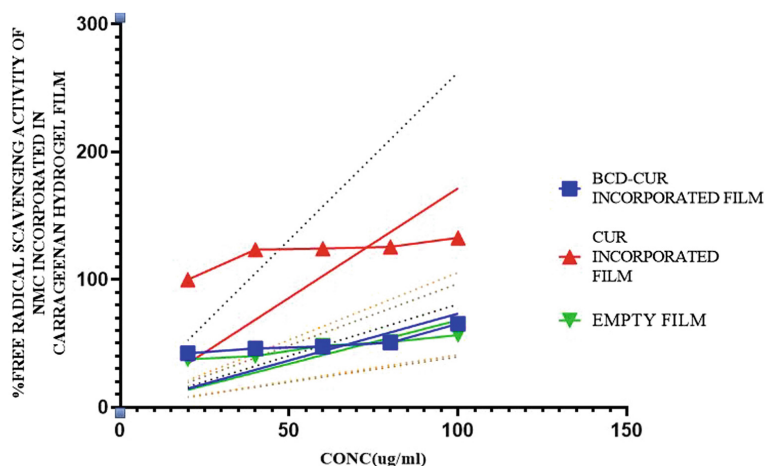
Fig. 10. Graph showing the trend in anti-oxidant activity for β-cyclodextrin and free curcumin when incorporated in carrageenan hydrogel film. *CONC (μg/ml)—Concentration of test compounds in μg/ml

5 Conclusion

The main motive of this research was to increase the hydrophilicity of curcumin. Previous researches have shown that hydrophilicity can be increased by either chemical modification, encapsulation or nano micelle formation. Curcumin is a novel drug which has wide therapeutic uses, the only drawback being less bio-available and hydrophobic. The need for the hour would be to overcome these problems in a cost effective and

efficient manner. β-cyclodextrin is a seven membered glucopyranose, toroidal shaped molecule with hydrophobic interior and hydrophilic exterior. It is a natural product derived from the enzymatic conversion of starch. It is assumed that the curcumin is encapsulated inside the cavity of the β-cyclodextrin. It showed impressive encapsulation of the curcumin, 88.76% with a yield of 16.42 mg/ml for a working volume of 50 ml. The particle size is the significant factor when it comes to nano micelle, it was reported good quality, within 500 nm, also the stability of the NMC is good with negative surface charge (within −30 mV). The chemical reaction between the two compounds and curcumin were analysed from the FT-IR spectrum. β-cyclodextrin-curcumin incorporated carrageenan hydrogel film showed slow and sustained release but there was not much effect in the swelling of hydrogel.

References

1. Robson, M.C., Steed, D.L., Franz, M.G.: Wound healing: biologic features and approaches to maximize healing trajectories. Curr. Probl. Surg. **2**, 72–140 (2001)
2. Shankar, M., Ramesh, B., Kumar, D.R., Babu, M.N.: Wound healing and it's important—a review. Der Pharmacol. Sinica **1**, 24–30 (2014)
3. Vanwijck, R.: Surgical biology of wound healing. Bull. Mem. l'Acad. Med. Belgique **156**, 175–184 (2001)
4. Tarnuzzer, R.W., Schultz, G.S.: Biochemical analysis of acute and chronic wound environments. Wound Repair Regener. **4**, 321–325 (1996)
5. Dhivya, S., Padma, V.V., Santhini, E.: Wound dressings–a review. BioMedicine **5** (2015)
6. Purna, S.K., Babu, M.: Collagen based dressings–a review. Burns: J. Int. Soc. Burn Injur. **26**, 54 (2000)
7. Queen, D., Orsted, H., Sanada, H., Sussman, G.A.: Dressing history. Int. Wound J. **1**, 59–77 (2004)
8. Falabella, A.F.: Debridement and wound bed preparation. Dermatolog. Ther. **19**, 317–325 (2006)
9. Boateng, J.S., Matthews, K.H., Stevens, H.N., Eccleston, G.M.: Wound healing dressings and drug delivery systems: a review. J. Pharmac. Sci. **97**, 2892–2923 (2008)
10. Gupta, P., Vermani, K., Garg, S.: Hydrogels: from controlled release to pH-responsive drug delivery. Drug Discov. Today **7**, 569–579 (2002)
11. Traitel, T., Goldbart, R., Kost, J.: Smart polymers for responsive drug-delivery systems. J. Biomater. Sci. Polym. Ed. **19**, 755–767 (2008)
12. Liu, J., Zhan, X., Wan, J., Wang, Y., Wang, C.: Review for carrageenan-based pharmaceutical biomaterials: favourable physical features versus adverse biological effects. Carbohyd. Polym. **121**, 27–36 (2015)
13. Pavli, M., Vrečer, F., Baumgartner, S.: Matrix tablets based on carrageenans with dual controlled release of doxazosin mesylate. Int. J. Pharmac. **400**, 15–23 (2010)
14. Grenha, A., Gomes, M.E., Rodrigues, M., Santo, V.E., Mano, J.F., Neves, N.M., Reis, R.L.: Development of new chitosan/carrageenan nanoparticles for drug delivery applications. J. Biomed. Mater. Res. Part A: Off. J. Soc. Biomater. Jpn. Soc. Biomater. Aust. Soc. Biomater. Korean Soc. Biomater. **92**, 1265–1272 (2010)

15. Mert, T., Sahin, M., Sahin, E., Yaman, S.: Anti-inflammatory properties of Liposome-encapsulated clodronate or Anti-Ly6G can be modulated by peripheral or central inflammatory markers in carrageenan-induced inflammation model. Inflammopharmacology 1–10 (2019)
16. Koenighofer, M., Lion, T., Bodenteich, A., Prieschl-Grassauer, E., Grassauer, A., Unger, H., Fazekas, T.: Carrageenan nasal spray in virus confirmed common cold: individual patient data analysis of two randomized controlled trials. Multidisc. Respirat. Med. **9**, 57 (2014)
17. Aggarwal, B.B., Sung, B.: Pharmacological basis for the role of curcumin in chronic diseases: an age-old spice with modern targets. Trends Pharmacol. Sci. **30**, 85–94 (2009)
18. Vyas, Alok: Perspectives on new synthetic curcumin analogs and their potential anticancer properties. Curr. Pharm. Des. **19**, 2047–2069 (2013)
19. Lu, Y., Park, K.: Polymeric micelles and alternative nanonized delivery vehicles for poorly soluble drugs. Int. J. Pharm. **453**, 198–214 (2013)
20. Ipar, V.S., Dsouza, A., Devarajan, P.V.: Enhancing Curcumin Oral Bioavailability ThroughNanoformulations. Eur. J. Drug Metabol. Pharmacokinet. 1–22 (2019)
21. Yadav, P., Bandyopadhyay, A., Chakraborty, A., Sarkar, K.: Enhancement of anticancer activity and drug delivery of chitosan-curcumin nanoparticle via molecular docking and simulation analysis. Carbohydr. Polym. **182**, 188–198 (2018)
22. Rachmawati, H., Edityaningrum, C.A., Mauludin, R.: Molecular inclusion complex of curcumin–β-cyclodextrin nanoparticle to enhance curcumin skin permeability from hydrophilic matrix gel. AapsPharmscitech **14**, 1303–1312 (2013)
23. Yallapu, M.M., Jaggi, M., Chauhan, S.C.: β-cyclodextrin-curcumin self-assembly enhances curcumin delivery in prostate cancer cells. Colloids Surf. B: Biointerfaces **79**, 113–125 (2010)
24. Distantina, S., Fadilah, F., Kaavessina, M.: Swelling behaviour of kappa carrageenan hydrogel in neutral salt solution. World Acad. Sci. Eng. Technol. Int. J. Chem. Mol. Nuclear Mater. Metall. Eng. **10**, 998–1001 (2016)
25. Irie, T., Otagiri, M., Sunada, M., Uekama, K., Ohtani, Y., Yamada, Y., Sugiyama, Y.: Cyclodextrin-induced hemolysis and shape changes of human erythrocytes in vitro. J. Pharmac.-Dyn. **5**, 741–744 (1982)

Phytosynthesis of Silver Nanoparticles Using *Rhynchosia heynei* Wight & Arn Leaf Extract: Characterization and *in Vitro* Assessment of Antimicrobial, Antioxidant and Anticancer Activities

S. Soneya[1], N. Vasudeva Reddy[1], K. V. Saritha[1(✉)],
Venkata Subbaiah Kotakadi[2], and T. Vijaya[3]

[1] Department of Biotechnology, Sri Venkateswara University,
Tirupati, A.P., India
kvsarithasvu@gmail.com
[2] DST-PURSE Centre, Sri Venkateswara University, Tirupati, A.P., India
[3] Department of Botany, Sri Venkateswara University, Tirupati, A.P., India

Abstract. In the present investigation, here we first report the phytosynthesis of silver nanoparticles (AgNPs) using shade dried aqueous leaf extract of *Rhynchosia heynei* Wight & Arn is a crop wild relatives (CWR) of pigeon peas (*Cajanus*), beans (*Phaseolus*) and grams (*Vigna*). *R. heynei* is a rare, an endemic and vulnerable category as an according to the IUCN Red list of threatened species (ver.2012.2), a global database of Plant species to track at risk species, it is herbaceous under shrub, an important, indigenous, threatened forestry species of traditional shrub of tribal medicinal plant species belonging to family *Fabacaea* and it is classified in Tribe *phaceoleae* and sub-tribe *Cajaninae* and sub-family *papilionoideae* and it is found in the forests of seshachalam biosphere reserve in Tirumala hills, Chittoor district, Rayalaseema region, Andhra Pradesh state, Eastern Ghats of India. The shade dried aqueous leaf extract of *R. heynei* acts as reducing and capping agent that mediates the synthesis and stabilization of RH-AgNPs (*R. heynei* leaf synthesized AgNPs). Phytosynthesized RH-AgNPs were 5–20 nm in size, face centered cubic crystalline in nature, spherical in shape, and possesses zeta potential value of −31.4 mV. UV-Vis spectroscopy analysis confirmed the formation of silver nanoparticles. FTIR analysis demonstrated that polyhydroxy compounds and proteins respectively involved the bioreduction and capping processes of the particles that prevents agglomeration which in turn gives stability. The stability of RH-AgNPs will be further confirmed through zeta potential measurement by dynamic light scattering (DLS) analysis technique. Both X-ray Diffraction (XRD) and SAED results emphasized that the phytosynthesized RH-AgNPs were crystal particles in nature. Particle size distribution showed that RH-AgNPs were 5–20 nm in size with hydrodynamic radius of 11.2 nm. In addition to silvernano particles energy - dispersive X-ray analysis (EDX) analysis of the RH-AgNPs showed the elemental composition of colloidal solution of RH-AgNPs. The EDX spectrum of RH-AgNPs exhibit strong signal of silver (Ag) element. The elemental composition of the colloidal solution of RH-AgNPs. Transmission electron microscope (TEM) micrographs showed that the RH-AgNPs formed were polydispersed in

nature without agglomeration. Phytosynthesized RH-AgNPs exhibited excellent bactericidal activity against different human pathogens including *Klebsiella pneumoniae*, *Escherichia coli* (Gram-ve), *Bacillus subtilis* and *Staphylococcus aureus* (Gram +ve). RH-AgNPs exhibited effective antioxidant property by scavenging DPPH and H_2O_2 radicals with the IC_{50} values of 77.7 and 88.6 µg/mL respectively. Further RH-AgNPs exhibited dose-dependent anti-cancer activity with maximum inhibition of 85% and 72% respectively against different cancer cell lines of human colon carcinoma (COLO205) and lung adenocarcinoma (A549). Application of silver nanoparticles (AgNPs) have revolutionized the medicinal industry. Due to their distinctive properties small size (1–100 nm), shape and electrical properties these nanoparticles are able to cross cell and nuclear membrane and induce cyto/genotoxicity. Phytosynthesized (plant based) AgNPs have targeting biological pathways has become tremendously prominent due to the higher efficiency and fewer side effects as compared to other commercial cancer drugs and have emerged as alternative antimicrobial agent to chemically synthesiszed nanoparticles assume their methods of synthesis is a simple, rapid and single-step bioreduction method which is environment friendly and non toxic and cost effective.

1   Introduction

Nanotechnology is one of the most promising and emerging areas of science that intertwines various diverse scientific disciplines such as material science, physics, chemistry, biomedicine and biotechnology [1]. Metal nanoparticles engrossed attention of researchers due to large surface area to volume ratio, spatial confinement (≤ 100 nm) and surface energy [2]. The applications of metal nanoparticles, particularly AgNPs have broadened due to their characteristic optical, electronic, mechanical, thermal and magnetic properties [2, 3]. Due to these diverse physicochemical properties, AgNPs have been widely employed in the manufacturing of optical receptors [4], intercalation materials for electrical batteries [5], sensors [6], catalysts in biochemical and chemical reactions [7], signal enhancers in SERS based enzyme Immunoassay [8], bio-analyzers [9], drug delivery [10], bio-imaging [11], silver-embedded fabrics in sporting equipment [12], cytotoxic, antioxidant, and antimicrobial agents [13–16].

The diverse physicochemical properties of AgNPs are generally determined by their size, shape, crystalinity and stability. Hence the AgNPs synthesis with controlled size and definite shape has been a challenge that has been significantly addressed in recent times. Various physical and chemical approaches including laser ablation [17], thermal decomposition [18], γ-radiation assisted [19], lithographic [20] photochemical [21], electrochemical [22], polyol [23] and polyaniline [24] processes have been

reported. But these are not ecofriendly due to involvement of toxic radiations and hazardous chemicals. Hazardous chemicals like sodium borohydride, hydroxylamine, poly-N-vinyl pyrrolidone, polyvinyl alcohol and tetrahydroxy methyl phosphochloride that pose health and environmental risks [22–24]. The application of such hazardous materials is still the subject of supreme concern because toxic chemicals on the nanomaterials could limit applications of nanomaterials in biomedical field. Biological methods are very rapid, simple and cost-effective and do not involve any toxic chemicals. Hence the biosynthesis of non-toxic, clean, biocompatible and eco-friendly NPs produced deserves merit. Different plant extracts including *Helecteris isora* [13], *Pueraria tuberosa* [14], *Phoenix dactylifera* [15], *Bergenia ciliata* [16], *Achyranthes aspera* [25], *Ocimum sanctum* [26], *Petroselinum crispum* [27], *Ailanthus excelsa* [28], *Capsicum annum* [29], and *Rhynchosia suaveolens* [30] have been reported for the application of silver nanoparticles (AgNPs) have revolutionized the medicinal industry. Due to their distinctive properties small size (1–100 nm), shape and electrical properties these nanoparticles are able to cross cell and nuclear membrane and induce cyto/genotoxicity. Phytosynthesized (plant based) AgNPs have targeting biological pathways has become tremendously prominent due to the higher efficiency and fewer side effects as compared to other commercial cancer drugs and have emerged as alternative antimicrobial agent to chemically synthesiszed nanoparticles assume their methods of synthesis is a simple, rapid and single-step bioreduction method which is environment friendly and non toxic and cost effective.

Rhynchosia heynei Wight & Arn is a crop wild relatives (CWR) of pigeon peas (*Cajanus*), beans (*Phaseolus*) and grams (*Vigna*). *R. heynei* is a rare, an endemic and vulnerable category as an according to the IUCN Red list of threatened species, (ver.2012.2), a global database of Plant species to track at risk species, it is herbaceous under shrub, an important, indigenous, threatened traditional and tribal medicinal plant species belonging to family *Fabacaea*, and it is classified in Tribe *phaceoleae* and sub-tribe *Cajaninae* and subfamily *papilionoideae* and the vernacular name of *R. heynei* is Adavi vuluva. It is found in the forests of Tirumala hills, native to Seshachalam biosphere reserve, Chittoor district, Rayalaseema region, Andhra Pradesh state, Eastern Ghats of India. The synonym of *R. heynei* is as *Rhynchosia coodoorensis*. The leaves of *R. heynei* have been widely used for antimicrobial agents, rheumatic pains, arthritis and skin diseases by Adivasi tribal people (chenchu, Lambada) inhabiting the hill ranges of Eastern Ghats [31, 46]. The genus *Rhynchosia*, usually known as snout bean. Phytochemical analysis of *R. heynei* was not yet reported. Biological properties of the plant were also not yet explored. In the present study we report the phytochemical analysis, total phenolic and flavonoid contents of the plant *R. heynei* for the first time. In the present study, we report the successful synthesis of AgNPs using aqueous leaf extract of *R. heynei*. The phytosynthesized RH-AgNPs were characterized by using various physico-chemical techniques like UV-Vis analysis, Fourier transform infrared (FTIR), Transmission electron microscopy (TEM), X-ray diffraction (XRD), and Dynamic light scattering (DLS). The phytosynthesized RH-AgNPs were assessed for different biological activities including antimicrobial, free radical scavenging and anticancer activities.

2   Materials and Methods

2.1   Chemicals

Silver nitrate ($AgNO_3$) was purchased from Sigma Aldrich, USA. 1 mM of $AgNO_3$ solution was prepared by adding 169.8 mg of $AgNO_3$into 1L of sterile double distilled water. a broad-spectrum antibiotic drug of streptomycin, RPMI-1640 medium (PC3) or Dulbecco's Modified Eagle's (DME) medium (COLO205 and MCF-7) supplemented with 10% (v/v) heat-inactivated fetal bovine serum, 2 mM glutamine,1 mM NaHCO3,100 μg/mL streptomycin and 100 units/mL penicillin. MTT [3-(4, 5-dimethylthiazol-2-yl)-2, 5-diphenyl tetrazolium bromide], phosphate buffer saline (PBS) pH-7.4, 100 μL of DMSO, hydrogen peroxide (H_2O_2) radical scavenging assay, 40 mM phosphate buffer, Ascorbic acid, by DPPH (1,1-diphenyl-2-picrylhydrazyl), 100 mL of methanol, Nutrient agar (NA), $AlCl_3$, Folin-Ciocalteu's phenol reagent, Standards of phenolic acids (gallic acid), for flavonoids (quercetin).

2.2   Collection of Plant Material

The plant *R. heynei* was collected from seshachalam biosphere reserve, near Ramakrishna Teertham which is located in the Tirumala hills of Chittoor district, Rayalaseema region, Andhra Pradesh state, Eastern Ghats of India (see Fig. 1). The plant was authenticated by taxonomist Dr. K. Madhava Chetty, Associate Professor, Department of Botany and the voucher specimens (SVUTY-RH01-05) were stored in the herbarium of Sri Venkateswara University, Tirupati, Andhra Pradesh, India.

Fig. 1. Plant image of *R. heynei* Wt. & Arn. showing leaves and Note an erect shrub growth
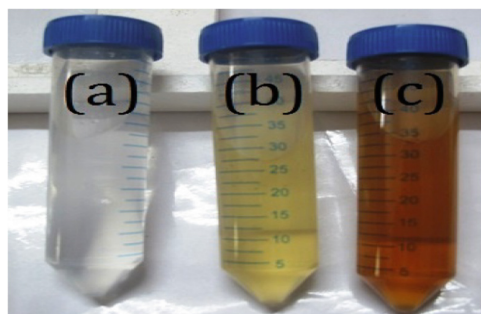
Fig. 2. A Schematic representation of visual colour change of the phytosynthesis of RH-AgNPs. a. 1 mM of AgNO3 solution b. Reaction mixture containing shade dried leaf aqueous extract of *R. heynei* and AgNO3 solution c. Dark brown solution indicates the formation of phytosynthesis of RH-AgNPs.

2.3 Phytochemical Screening, Estimation of Total Phenolic and Flavonoid Contents from Aqueous Leaf Extract of *R. heynei* (RHLE)

The phytochemical screening was carried out to reveal the presence of major plant metabolites including proteins, carbohydrates, triterpenoids, phenolic compounds, flavonoids and alkaloids. The results were expressed as present (+), or absent (−). The total phenolic content (TPC) of the *R. heynei* aqueous leaf extract was determined by using Folin-Ciocalteu's spectrometric method and the total flavonoid content (TFC) of the *R. heynei* extract was estimated by aluminium chloride (AlCl$_3$) colorimetric method [32].

2.4 Preparation of Plant Extract of RHLE and Phytosynthesis of RH-AgNPs

The healthy and fresh leaves were washed with tap water and then rinsed with double distilled water (DDW) for 3 times. The leaves were shade dried completely for about 5 days and then ground into a fine leaf powder. Ten grams of fine grounded RH leaf powder was taken and added into 100 mL of sterile DDW, mixed well and then boiled at 50–60 °C in a micro oven for about 30 min and then cooled and kept incubation at room temperature (RT) for 1 h. After 1 h of incubation, filtration was carried out, the obtained aqueous shade dried leaf extract of *R. heynei* was collected and used for the phytosynthesis of AgNPs.RH Leaf synthesized aquous extract (RHLE) of 10 mL was taken and added into 90 mL of 1 mM AgNO$_3$ solution, which was heated for 15 min at 50 °C and then the experimental solution incubated in the dark at RT for 4 h. After incubation, initially the reduction of silver (Ag$^+$) ions into AgNPs by the *R. heynei* leaf extract was visually detected by observing the change in color was observed from greenish yellow to dark brown, which indicates the phytosynthesis (*R. heynei* leaf synthesized AgNPs) of RH-AgNPs (Fig. 2).

2.5   Characterization of RH-AgNPs

UV-Vis (PerkinElmer UV-Vis spectrometer) analysis was done to authenticate the production of RH-AgNPs. FTIR (Alpha interferometer, Bruken, Switzerland) analysis of RH-AgNPs was carried out to determine the functional groups that take part in biosynthesis and coating of RH-AgNPs. Crystal structure of RH-AgNPs was determined by XRD analysis (Ultima IV X-ray powder diffractometer, Rigaku Ltd, Tokyo, Japan). The sizes and shapes of the phytosynthesized RH-AgNPs were determined by TEM analysis (FEI Tecnai F12, Philips Optics Ltd, Holland) Energy dispersive X-ray (EDX) spectrum and selected area electron diffraction (SAED) pattern was also recorded for the phytosynthesized RH-AgNPs. Zeta potential measurement, Particle size distribution and hydrodynamic radius (average particle diameter) were determined using DLS (HORIBA Nanopartica analyzer).

2.6   *In Vitro* Biological Effects

2.6.1   *In Vitro* Assessment of Antimicrobial Property of RH-AgNPs

Antimicrobial property of RH-AgNPs was checked by employing disc diffusion method [33] against different human pathogenic bacteria including *E. coli*, *K. pneumoniae*, *B. subtilis* and *S. aureus*. Five sterile paper discs were placed on each petriplate containing nutrient agar (NA) media inoculated with 200 μL of microbial inoculum. One disc contains standard antibiotic ampicillin. Second disc contains 25 μL of RH-AgNPs. Third disc contains 25 μL of RHLE. Fourth disc contains 25 μL of 1 mM $AgNO_3$ and final disc contains no test sample. The test plates were placed in the BOD chamber for 24 h at 37 °C. After incubation, growth inhibition of bacteria was observed and measured the diameter of inhibition zone (mm).

2.6.2   *In Vitro* Assessment of Antioxidant Property Assay of RH-AgNPs

Antioxidant property of RH-AgNPs was proved by DPPH and H_2O_2 radical scavenging assays [34]. In this two assays, ascorbic acid was used as standard antioxidant.

2.6.3   DPPH Radical Scavenging Assay

In vitro anti oxidant activity of the RH-AgNPs was carried out by 2,2′-diphenyl-1-picrylhydrazyl (DPPH) free radical scavenging assay [45]. Prepared the stock solution of DPPH by dissolving 4 mg of DPPH in 100 mL of methanol and stored at 5 °C. Different concentrations (25, 50, 75 and 100 μg/mL) of test samples (RHLE, RH-AgNPs and ascorbic acid) were dissolved separately in methanol. 1 mL of methanolic solution containing different test samples was added to 2 mL of of DPPH stock solution (1 mM/L). This reaction solution was incubated in the dark for 45 min at room temperature and then after incubation, the absorbance was recorded at 517 nm. The percentage of DPPH radical scavenging activity was measured by taking the absorbance at 517 nm using the following equation.

$$\% \, Radical \, scavenging \, activity \, (RSA) = [(Absorbance \, of \, control - Absorbance \, of \, test \, sample)/Absorbance \, of \, control] \times 100$$

2.6.4   H₂O₂ Radical Scavenging Assay

In vitro anti oxidant activity of the RH-AgNPs was further confirmed by hydrogen peroxide (H_2O_2) radical scavenging assay. The capability of RH-AgNPs to scavenging H_2O_2 radical was assessed by the method of Patel et al. [45]. 1 mL of different concentrations of test samples (25, 50, 75 and 100 µg/mL) were added to 2 mL of H_2O_2 solution prepared in 40 mM phosphate buffer (pH 7.4) and then incubated for 15 min. After incubation, the absorbance was measured at 230 nm for each sample against a blank containing phosphate buffer without H_2O_2. Ascorbic acid was used as standard antioxidant. The percentage of Radical scavenging activity (RSA) was calculated using % RSA = [(Ac − As)/Ac] × 100. Where Ac is the absorbance of the control and As is the absorbance of the sample. Different concentrations (25, 50, 75 and 100 µg/mL) of test samples were equally and separately added to H_2O_2 solution (prepared in 40 mM phosphate buffer), incubated for 15 min and then optical density (OD) values were recorded at 230 nm for each sample. The percentage of inhibition or scavenging was calculated using the formula.

$$\% \, \text{Scavenging} \, = \, [(\text{OD of control} \, - \, \text{OD of test sample}) \, / \, \text{OD of control}] \, \times \, 100$$

2.6.5   *In Vitro* Assessment of Anticancer Activity Assay of RH-AgNPs

The cancer cell lines A549 (human lung adenocarcinoma) and COLO205 (human colon cancer) were obtained from National Centre for Cellular Sciences (NCCS), Pune, India. Cells were cultured either in RPMI-1640 (COLO205) or DMEM (A549) supplemented with 2 mM–glutamine, 10% (v/v) heat-inactivated fetal bovine serum), 1 mM NaHCO3, 100 units/ml penicillin and 100 µg/ml streptomycin. The cell lines were maintained in CO2 incubator at 37 °C. 3-(4,5-dimethyl thiazol-2-yl)-2,5-diphenyl tetrazolium bromide (MTT) assay was employed [35] to determine the cytotoxic activity of RH-AgNPs against human cancer cell lines including COLO205 and A549. Briefly, the cells were seeded in 96 well plates at a concentration of 5×10^3 cells/100 µL, incubated at 37 °C in 5% CO_2 chamber for overnight. After incubation, the cells were treated with different concentrations of RH-AgNPs. After 24 h, 10 µL of MTT (5 mg/mL in PBS pH-7.4) was mixed and incubated again for 3 h. Then discarded the medium and dissolved the formazan crystals in 100 µL of DMSO and the absorbance were measured at 570 nm (Spectra MAX plus; SOFTmax PRO-5.4). Decrease in the cell viability percentage was determined and the IC_{50} values were calculated.

3   Results and Discussion

Phytochemical profiling of *R. heynei* leaf extract (RHLE) showed the presence of proteins, carbohydrates, phenolic compounds, flavonoids, triterpenoids and alkaloids (Table 1). The TPC of the RHLE was found to be 267.3 ± 5.06 µg/g GAE and the TFC of the RHLE *was* found to be 102.53 ± 4.1 µg/g QE.

Table 1. Phytochemical profiling of leaf extracts of *R. heynei*

S. no.	Plant compounds	±
1	Proteins	+
2	Carbohydrates	+
3	Phenolic compounds	+
4	Flavonoids	+
5	Alkaloids	+
6	Triterpenoids	+

3.1 Phytosynthesis of RH-AgNPs

In this study RHLE acts as bioreduction agent which converts the silver (Ag^+) ions AgNPs *i.e.,* RH-AgNPs (RHLE mediated synthesis of AgNPs). Color change of the experimental solution from light greenish yellow color to dark brown indicates the synthesis of RH-AgNPs. Phytosynthesis of RH-AgNPs was further authenticated by taking UV-Vis spectrum between 200–800 nm. UV-Vis spectrum (see Fig. 3) of dark brown color colloidal solution showed the peak at 440 nm which indicated the presence of phytosynthesized RH-AgNPs. This peak is characteristic feature of AgNPs, due to localized SPR (surface plasmon resonance) phenomena excited in the visible range [1–4]. The clear SPR peak indicates that phytosynthesized RH-AgNPs are small in size without any agglomeration.
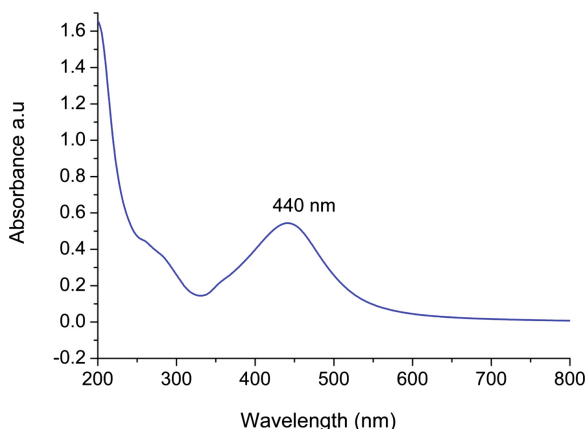
Fig. 3. UV-Vis spectrum of phytosynthesized RH-AgNPs.

3.2 FTIR Analysis of RH-AgNPs

FTIR spectrum exhibited different peaks at 625, 691, 820, 1055, 1330,1605, 1715, 2348, 2885, 2979, 3234 and 3744 cm^{-1} (see Fig. 4). The narrow and small peaks at 625, 691 and 820 cm^{-1} responsible for aliphatic C-H stretching vibrations. A sharp

peak at 1055 cm^{-1} might be due to C-N (primary amine) functional group of proteins [36]. A clear peak at 1330 cm^{-1} is responsible for C-O group of carboxylic compounds [37]. A sharp peak at 1605 cm^{-1} could be due to amide linkage of proteins [38]. A peak at 1715 cm^{-1} is responsible for aromatic C-H stretching. The clear peak at 2348 cm^{-1} is due to C–O/N–H group of proteins [39]. The peaks at 2885 and 2979 cm^{-1} are the characteristic peaks of stretching vibrations of C = C linkage. The peaks 3234 and 3744 cm^{-1} are responsible for O-H group of polyols such as phenols, flavonoids and tannins etc. [40]. FTIR spectrum revealed that polyphenols played a major role in the phytosynthesis of RH-AgNPs. Further it is revealed that proteins possibly involved in the capping of the particles that prevents agglomeration which in turn gives stability [30]. The stability of RH-AgNPs will be further confirmed through zeta potential measurement by DLS analysis.
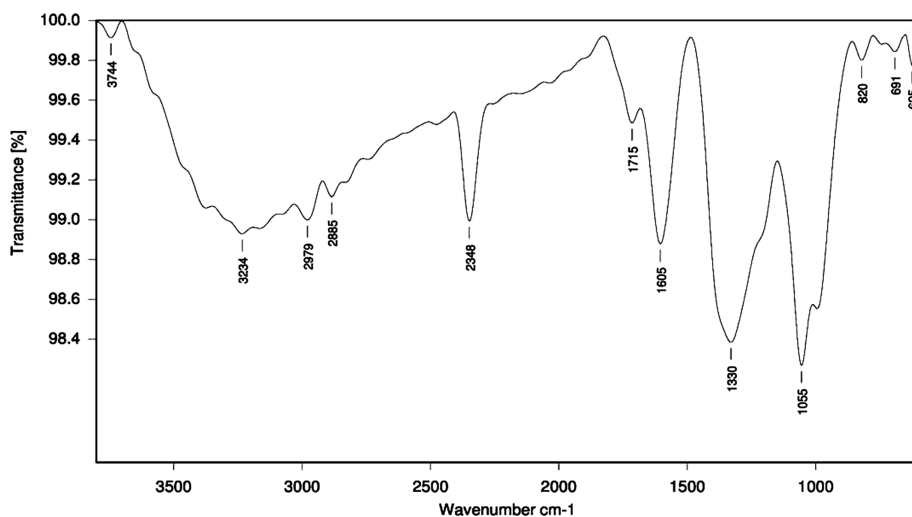
Fig. 4. FTIR pattern of phytosynthesized RH-AgNPs.

3.3   XRD and EDX Analysis of RH-AgNPs

Crystal structure of phytosynthesized RH-AgNPs was determined by XRD analysis (see Fig. 5a). XRD pattern showed four diffraction peaks at 38.46°, 44.75°, 64.79° and 77.56° corresponding to (111) (200) (220) and (300) planes respectively, which indicates the crystalline nature of RH-AgNPs with face centered cubic (FCC) structure (JCPDS No. 89-3722). EDX analysis of the RH-AgNPs showed the elemental composition of colloidal solution of RH-AgNPs (Fig. 5b). The EDX spectrum of RH-AgNPs exhibit strong signal of silver (Ag) element. The elemental composition of the colloidal solution of RH-AgNPs was given in the Table 2.

Fig. 5. (a) XRD pattern and (b) EDX spectrum of RH-AgNPs.

Table 2. EDX spectrum of RH-AgNPs.

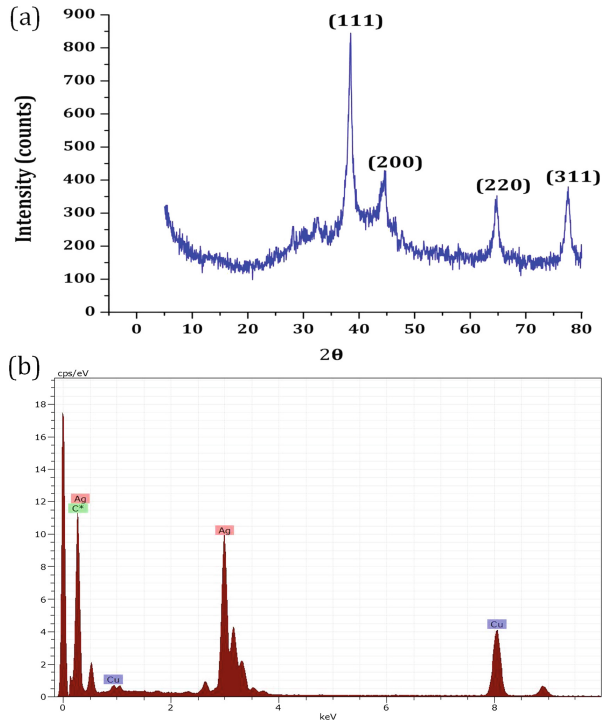| Element	Series	Net unn. C	norm. C	Atom. C	C. Error (3 Sigma)
		[wt.%]	[wt.%]	[at.%]	[wt.%]
Silver	K-series 7901	25.46	25.46	4.03	2.55
Carbon	K-series 30619	65.83	65.83	93.63	6.11
Copper	K-series 31775	8.70	8.70	2.34	0.87
Total		100.00	100.00	100.00	

3.4   TEM Study and SAED Pattern of RH-AgNPs

TEM study was carried out to reveal the size and shape of phytosynthesized RH-AgNPs. The TEM micrographs at different magnifications from 200 nm to 10 nm were represented in (see Fig. 6). TEM micrographs showed that the RH-AgNPs are poly-dispersed in nature without agglomeration. The synthesized RH-AgNPs are in different shapes such as spherical, rhombic, cubic and small nanorods. But majority of RH-AgNPs were spherical shaped. The phytosynthesized RH-AgNPs were 5–20 nm in size. The size of the RH-AgNPs was further determined by particle size analysis using

DLS. Crystal analysis of RH-AgNPs at 10 nm resolution showed crystal lattice fringes with d spacing value of 0.222 nm (see Fig. 7a). Further SAED pattern (see Fig. 7b) clearly showed the Debye-Scherer rings of the planes of the face cubic crystal structure. Both XRD and SAED results emphasized that the phytosynthesized RH-AgNPs were crystal particles.
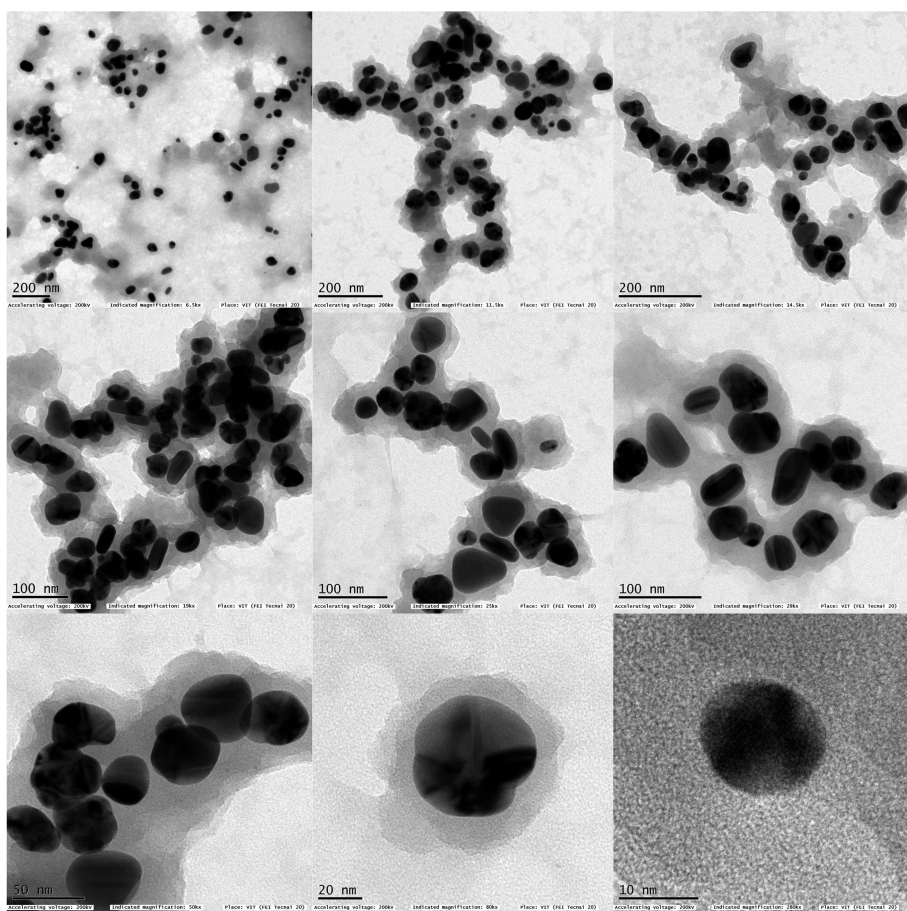

Fig. 6. TEM study of RH-AgNPs. TEM pictures at different scales with different magnifications including 200 nm with 6.5 kx, 200 nm with 11.5 kx, 200 nm with 14.5 kx; 100 nm with 19 kx, 100 nm with 25 kx, 100 nm with 29 kx; 50 nm with 50 kx, 20 nm with 80 kx, and 10 nm with 280 kx magnification.
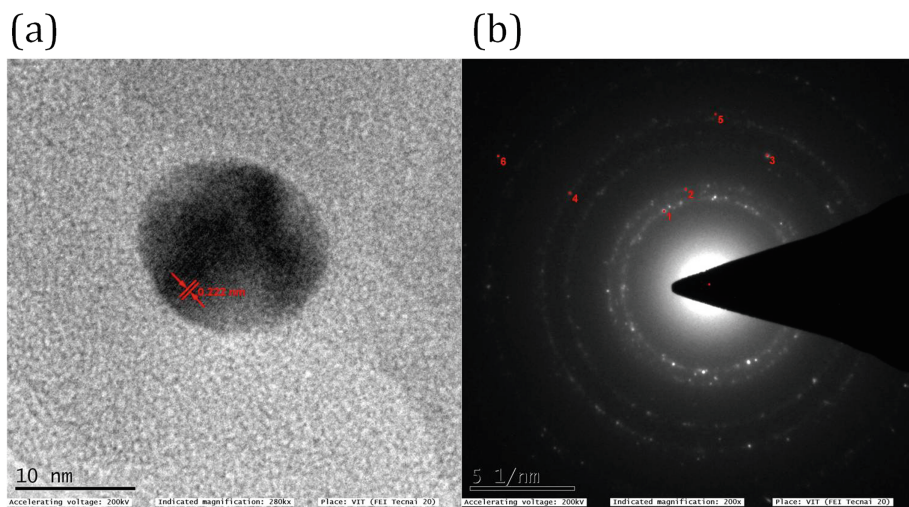
Fig. 7. (a) Crystal analysis of RH-AgNPs showing lattice fringes with 'd' space value of 0.222 nm and (b) SAED pattern of RH-AgNPs crystal at 200x magnification.

3.5 DLS Analysis of RH-AgNPs

Particle size distribution showed that RH-AgNPs were 5–20 nm in size with hydrodynamic radius of 11.2 nm (see Fig. 8a). The distribution form of RH-AgNPs was monodispersed and the particle size distribution was agreed with TEM results. RH-AgNPs showed poly dispersity index value of 0.433 and Z-average value of 4880.1 nm. Zeta potential value of RH-AgNPs was determined as –31.4 mV (see Fig. 8b). Zeta potential is an important measurement which determines the stability of phytosynthesized RH-AgNPs. This higher negative value of zeta potential indicates the long term stability of RH-AgNPs without agglomeration. The non-agglomeration of RH-AgNPs could be due to the coating or capping by plant proteins. The presence of plant proteins in the colloidal solution of RH-AgNPs was determined by FTIR analysis. Nanoparticles' stability is crucial for their application in biomedicine/clinical fields. RH-AgNPs showed poly dispersity index value of 0.433 and Z-average value of 4880.1 nm. Zeta potential value of RH-AgNPs was determined as –31.4 mV.

3.6 *In Vitro* Biological Effects

3.6.1 *In Vitro* Assessment of Antimicrobial Activity Assay of RH-AgNPs

In this study, RH-AgNPs showed effective antimicrobial activity against both Gram −ve (*K. pneumoniae* and *E. coli*) Gram +ve (*B. subtilis* and *S. aureus*) human pathogens (see Fig. 7a–d). RHLE showed growth inhibitory zones of 3.7, 5.4, 4.8 and 6.5 mm respectively against *K. pneumonia*, *E. coli*, *B. subtilis* and *S. aureus*. While RH-AgNPs showed the growth inhibitory zones of 13.5, 10.6, 10.4 and 12.8vmm

(a) Calculation Results

Peak No.	S.P.Area Ratio	Mean	S. D.	Mode
1	1.00	11.2 nm	2.7 nm	11.0 nm
2	---	--- nm	--- nm	--- nm
3	---	--- nm	--- nm	--- nm
Total	1.00	11.2 nm	2.7 nm	11.0 nm

Cumulant Operations
Z-Average   : 4880.1 nm
PI   : 0.433
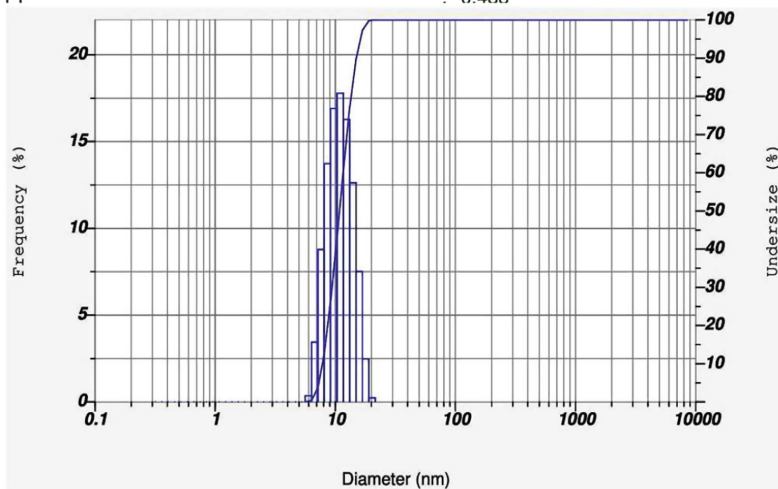
(b) Calculation Results

Peak No.	Zeta Potential	Electrophoretic Mobility
1	-31.4 mV	-0.000244 cm2/Vs
2	--- mV	--- cm2/Vs
3	--- mV	--- cm2/Vs

Zeta Potential (Mean)   : -31.4 mV
Electrophoretic Mobility Mean   : -0.000244 cm2/Vs

Fig. 8. (a) Particle size distribution and (b) Zeta potential measurement of RH-AgNPs.

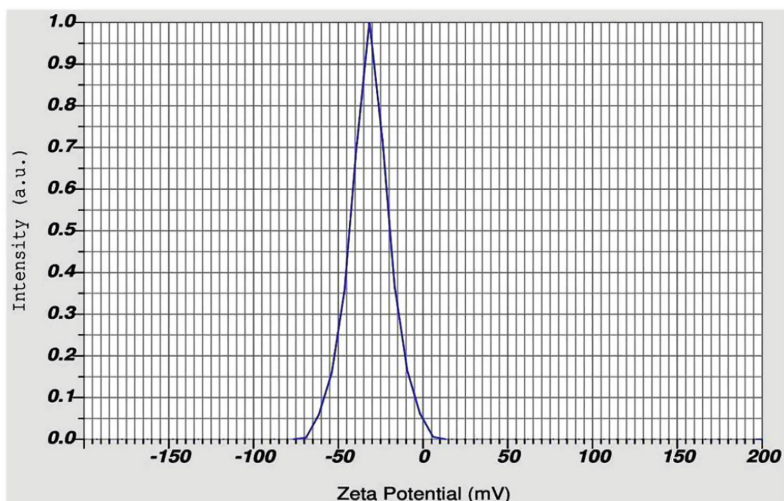respectively against *K. pneumonia*, *E. coli*, *B. subtilis*, and *S. aureus*. The results clearly depicted that both RHLE and RH-AgNPs significantly affected the bacterial growth. RH-AgNPs were two times effective compared to RHLE. The reason could be explained by three ways viz., general antibacterial nature of silver, small size of NPs, polyphenols, flavonoids and plant proteins around the surfaces of NPs. The diameter of inhibition zones (mm) produced by RHLE, RH-AgNPs, $AgNO_3$ and a broad-spectrum standard antibiotic drug of ampicillin were compared (see Figs. 9 and 10). RH-AgNPs produced the growth inhibitory zones between 10–14 mm. RHLE produced the growth inhibitory zones between 3.5–6.5 mm only and 1 mM $AgNO_3$ produced growth inhibitory zones between 2–5 mm. The results clearly depicted that RH-AgNPs (1 mM $AgNO_3$ + RHLE) exhibited 2–4 fold effective antimicrobial activity compared $AgNO_3$ and RHLE alone. This might be due to synergistic effect of $AgNO_3$, phytochemicals of RHLE and further the small size of NPs. In this study, RH-AgNPs were ultra sized (5–20 nm). The ultra sized NPs easily percolate the bacterial membrane and cause the cell death by bacterial DNA fragmentation. The ultra sized NPs easily enter inside the bacterial cell and bind with catalytic site of metabolically important enzymes. As a result, growth of the bacteria or cell division was arrested, consequently cell death occurs [41, 42]. Antimicrobial property of AgNPs is an important application, widely employed in the preparation of hospital gloves, dressing materials, implants, medical kits, glass vials, injectables, devices, and polymer products used in hospitals.
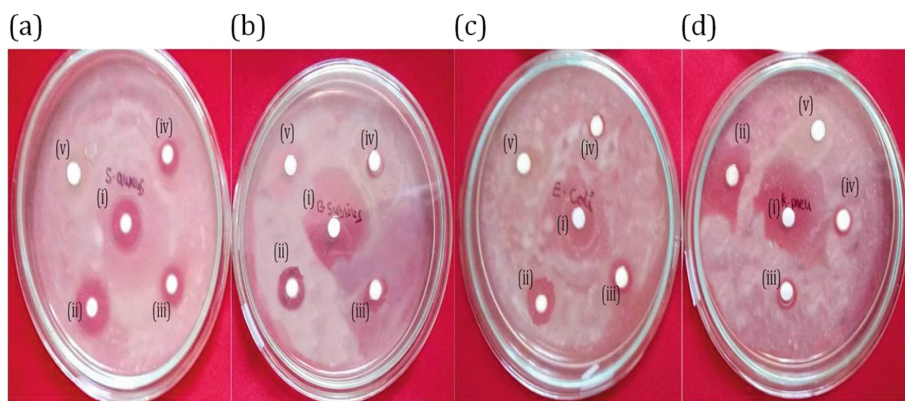
Fig. 9. *In vitro* Antimicrobial property of RH-AgNPs against both different bacterial organisams of Gram +ve and Gram –ve. (a) *S. aureus*, (b) *B. subtilis*, (c) *E. coli*, and (d) *K. pneumonia*. (i) Growth inhibitory zone produced by a standard broad-spectrum antibiotic drug of ampicillin, (ii) Growth inhibitory zone produced by RH-AgNPs, (iii) Growth inhibitory zone produced by RHLE, (iv) Growth inhibitory zone produced by 1 mM $AgNO_3$ and (v) No inhibition zone.
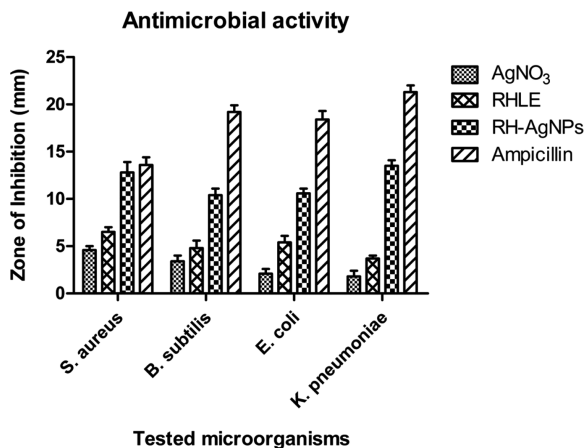
Fig. 10. Comparison of antimicrobial activity of AgNO$_3$, RHLE, RH-AgNPs and a standard broad-spectrum antibiotic drug of Ampicillin.

3.6.2 *In Vitro* Assessment of Antioxidant Activity Assay of RH-AgNPs

In this study, phytosynthesized RH-AgNPs showed concentration dependant inhibition against both DPPH (see Fig. 11a) and H$_2$O$_2$ free radicals (see Fig. 11b). Results showed that percentage of scavenging activity is increased with increase in concentration of RH-AgNPs. RHLE and RH-AgNPs showed the maximum inhibition of 52% and 57% respectively against DPPH radicals. IC$_{50}$ values of RHLE and RH-AgNPs were determined as 91.5 and 77.7 μg/mL respectively. RHLE and RH-AgNPs also showed excellent scavenging capability against H$_2$O$_2$. RHLE and RH-AgNPs exhibited maximum scavenging activity of 41% and 52% respectively against H$_2$O$_2$ radicals. IC$_{50}$ values of RHLE and RH-AgNPs against H$_2$O$_2$ radicals were determined as 122.7 and 88.6 μg/mL respectively. The significant free radical quenching capacity of RH-AgNPs could be due to the phenols, flavonoids and proteins. Phenols and flavonoids especially involved in the bioreduction process. While, proteins could be involved in the capping of RH-AgNPs [30]. Different reactive oxygen species (hydroxy, epoxy, superoxide, peroxides, singlet oxygen species, and peroxylnitrile) causes oxidative stress in the different human disorders like atherosclerosis, inflammation, cancer, ageing and neurodegenerative disorders. Antioxidants are the compounds of synthetic or natural origin that inhibits the cell damage caused by oxidative stress. Due to side effects caused by synthetic antioxidants, scientists focused on the use of bioactive compounds and their derivatives as natural antioxidant systems to protect against the oxidative stress caused by reactive oxygen species in the different human disorders [30, 41].
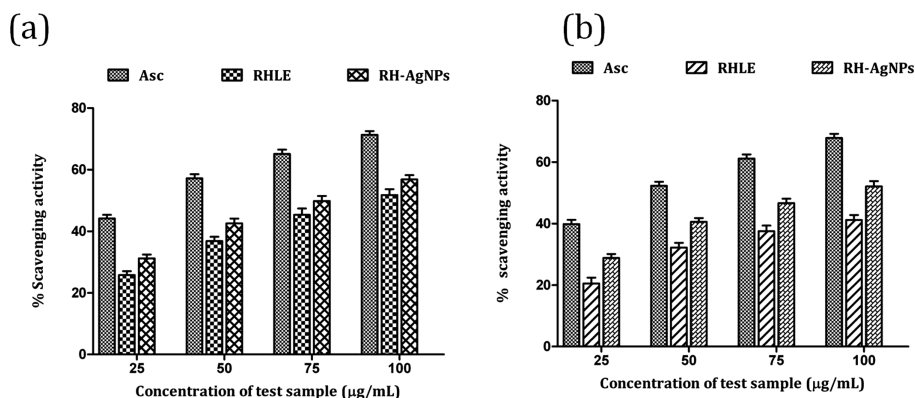
Fig. 11. *In vitro* Antioxidant activity of various concentrations of ascorbic acid, RHLE and RH-AgNPs were used for radical scavenging activity (a) DPPH scavenging activity (b) H_2O_2 scavenging activity

3.6.3 *In Vitro* Assessment of Anticancer Activity Assay of RH-AgNPs

In this study, RH-AgNPs were tested against human cancer cell lines including COLO205 and A549 by employing MTT assay. RH-AgNPs showed concentration dependant cytotoxicity against both COLO205 and A549 cells (see Fig. 12). Percentage of cell viability (or live cells) decreases with the increase in RH-AgNPs concentration. RH-AgNPs showed maximum inhibition of 85% and 72% respectively against COLO205 and A549 cells. IC_{50} values of RH-AgNPs were determined as 38.14 and 86.8 µg/mL against COLO205 and A549 cells respectively. Thus the RH-AgNPs were found to possess effective cytotoxicity against cancer cells. The results of in this study are in consonant with previous reports. Phytosynthesized AgNPs using *Rhynchosia suaveolens* [30], *Origanum vulgare* [42], *Rosa damascene* [43] showed effective cytotoxicity against A549 cells with IC_{50} values of 30, 80, 100 and 24.7 µg/mL respectively. Phytosynthesized AgNPs using *Ficus religiosa* [44] showed significant cytotoxicity against COLO205 cells.

The capability of NPs to penetrate into cells is mainly depend upon the physical properties including surface charge, size and morphology. In this study phytosynthesized RH-AgNPs are ultra sized (5–20 nm with average diameter of 11.2 nm). This ultra sized NPs possess the advantage of high permeability and retention property over the large sized NPs (>30 nm). Cells can easily take up these NPs through different endocytosis mechanisms. Ultra sized NPs can enhance the therapeutic efficacy of drugs due to three main reasons including effectual diffusion, profound penetration and enhanced accumulation in the tumor matrix. As a result, tumorogenic cells can be eradicated completely [30, 41]. Where as NPs with 30–100 nm size could not penetrate profoundly into and reach only superior layers of tumor matrix. Consequently, tumorogenic cells cannot be eradicated. Hence the phytosynthesized ultra sized RH-AgNPs can be developed as future therapeutic agents for cancer treatment and drug delivery.
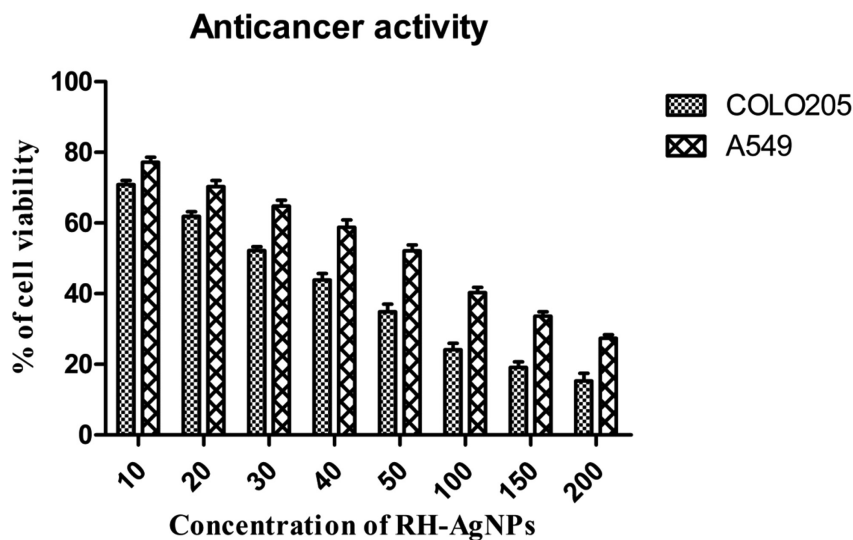
Fig. 12. *In vitro* Anticancer activity of various concentrations of RH-AgNPs against human cell lines of COLO205 and A549 by employing MTT assay.

4 Conclusion

In this study, we first reported the simple, rapid, robust and eco-friendly method of phytosynthesis of RH-AgNPs using shade dried aqueous leaf extract of *R. heynei* (RHLE) as a reducing agent. This study also reports the phytochemical profiling, total phenolic and flavonoid contents of *R. heynei* leaf extract and revealed that polyphenolic compounds and proteins involved in the biosynthesis and capping processes. Phytosynthesized RH-AgNPs were stable, ultra sized and spherical shaped crystals. Moreover RH-AgNPs proved their potent biomedical importance by exhibiting and effective antibacterial, antioxidant and anticancer activities against human cell lines of COLO205 and A549 by employing MTT assay, when compared with standard drugs suitable for the formulation of new type of antimicrobial material for reducing infective potential of the tested bacterial species and cytotoxicity against human cancer cell lines. Thus, the RH-AgNPs proved their biopharmaceutical importance.

Compliance with Ethical Standards. Conflict of Interest: The authors confirmed that there is no conflict of interest.

References

1. Narayanan, K.B., Sakthivel, N.: Green synthesis of biogenic metal nanoparticles by terrestrial and aquatic phototrophic and heterotrophic eukaryotes and biocompatible agents. Adv. Colloids Interface Sci. **169**, 59–79 (2011). https://doi.org/10.1016/J.CIS.2010.02.001
2. Adekoya, J.A., Ogunniran, K.O., Siyanbola, T.O., Dare, E.O., Revaprasadu, N.: Band structure, morphology, functionality, and size-dependent properties of metal nanoparticles. In: Noble and Precious Metals-Properties, Nanoscale Effects and Applications. IntechOpen (2018). https://dx.doi.org/10.5772/intechopen.72761
3. Coronado, E.A., Encina, E.R., Stefani, F.D.: Optical properties of metallic nanoparticles: manipulating light, heat and forces at the nanoscales. Nanoscale **3**, 4042–4059 (2011). https://doi.org/10.1039/c1nr10788g
4. Zhang, Y., Huang, R., Zhu, X., Wang, L., Wu, C.: Synthesis, properties, and optical applications of noble metal nanoparticle-biomolecule conjugates. Chin. Sci. Bull. **57**(2–3), 238–246 (2012). https://doi.org/10.1007/s11434-011-4747-x
5. Wang, T., Kaempgen, M., Nopphawan, P., Wee, G., Mhaisalkar, S., Srinivasan, M.: Silver nanoparticle-decorated carbon nanotubes as bifunctional gas-diffusion electrodes for zinc–air batteries. J. Power Sourc. **195**(13), 4350–4355 (2010). https://doi.org/10.1016/j.powsour.2009.12.137
6. Lee, K.S., El-Sayed, M.A.: Gold and silver nanoparticles in sensing and imaging: sensitivity of plasmon response to size, shape, and metal composition. J. Phys. Chem. B **110**(39), 19220–19225 (2006). https://doi.org/10.1021/jp062536y
7. Xu, R., Wang, D., Zhang, J., Li, Y.: Shape-dependent catalytic activity of silver nanoparticles for the oxidation of styrene. Chem. Asian J. **1**(6), 888–893 (2006). https://doi.org/10.1002/asia.200600260
8. Choo, J.: Simultaneous detection of multiple biomarkers using SERS based immuno analysis. Rapid Commun. Photosci. **1**, 49 (2012)
9. Penn, S.G., He, L., Natan, M.J.: Nanoparticles for bioanalysis. Curr. Opin. Chem. Biol. **7**(5), 609–615 (2003). https://doi.org/10.1016/j.cbpa.2003.08.13
10. De Jong, W.H., Borm, P.J.: Drug delivery and nanoparticles: applications and hazards. Int. J. Nanomed. **3**(2), 133–149 (2008)
11. Sharma, P., Brown, S., Walter, G., Santra, S., Moudgil, B.: Nanoparticles for bioimaging. Adv. Coll. Interface. Sci. **123**, 471–485 (2006). https://doi.org/10.1016/j.cis.2006.05.026
12. Klaus, T., Joerger, R., Olsson, E., Granqvist, C.G.: Silver-based crystalline nanoparticles, microbially fabricated. Proc. Natl. Acad. Sci. **96**(24), 13611–13614 (1999). https://doi.org/10.1073/pnas.96.24.13611
13. Bhakya, S., Muthukrishnan, S., Sukumaran, M., Grijalva, M., Cumbal, L., Benjamin, J.F., Rao, M.V.: Antimicrobial, antioxidant and anticancer activity of biogenic silver nanoparticles–an experimental report. RSC Adv. **6**(84), 81436–81446 (2016). https://doi.org/10.1039/C6RA17569D
14. Satpathy, S., Patra, A., Ahirwar, B., Delwar Hussain, M.: Antioxidant and anticancer activities of green synthesized silver nanoparticles using aqueous extract of tubers of *Pueraria tuberosa*. Artif. Cells Nanomed. Biotechnol. **46**, 1–15 (2018). https://doi.org/10.1080/21691401.2018.1489265

15. Oves, M., Aslam, M., Rauf, M.A., Qayyum, S., Qari, H.A., Khan, M.S., Ismail, I.M.: Antimicrobial and anticancer activities of silver nanoparticles synthesized from the root hair extract of *Phoenix dactylifera*. Mater. Sci. Eng. C **89**, 429–443 (2018). https://doi.org/10.1016/j.msec.2018.03.035

16. Phull, A.R., Abbas, Q., Ali, A., Raza, H., Zia, M., Haq, I.U.: Antioxidant, cytotoxic and antimicrobial activities of green synthesized silver nanoparticles from crude extract of *Bergenia ciliata*. Future J. Pharmac. Sci. **2**(1), 31–36 (2016). https://doi.org/10.1016/j.fjps.2016.03.001

17. Tsuji, T., Iryo, K., Watanabe, N., Tsuji, M.: Preparation of silver nanoparticles by laser ablation in solution: influence of laser wavelength on particle size. Appl. Surf. Sci. **202**(1–2), 80–85 (2002)

18. Navaladian, S., Viswanathan, B., Viswanath, R.P., Varadarajan, T.K.: Thermal decomposition as route for silver nanoparticles. Nanoscale Res. Lett. **2**(1), 44–48 (2007). https://doi.org/10.1007/s11671-006-9028-2

19. Chen, P., Song, L., Liu, Y., Fang, Y.E.: Synthesis of silver nanoparticles by γ-ray irradiation in acetic water solution containing chitosan. Radiat. Phys. Chem. **76**(7), 1165–1168 (2007). https://doi.org/10.1016/j.radphyschem.2006.11.012

20. Hulteen, J.C., Treichel, D.A., Smith, M.T., Duval, M.L., Jensen, T.R., Van Duyne, R.P.: Nanosphere lithography: size-tunable silver nanoparticle and surface cluster arrays. J. Phys. Chem. B **103**(19), 3854–3863 (1999). https://doi.org/10.1021/jp9904771

21. Maretti, L., Billone, P.S., Liu, Y., Scaiano, J.C.: Facile photochemical synthesis and characterization of highly fluorescent silver nanoparticles. J. Am. Chem. Soc. **131**(39), 13972–13980 (2009)

22. Yin, B., Ma, H., Wang, S., Chen, S.: Electrochemical synthesis of silver nanoparticles under protection of poly (N-vinylpyrrolidone). J. Phys. Chem. B **107**(34), 8898–8904 (2003). https://doi.org/10.1021/jp0349031

23. Wiley, B., Herricks, T., Sun, Y., Xia, Y.: Polyol synthesis of silver nanoparticles: use of chloride and oxygen to promote the formation of single-crystal, truncated cubes and tetrahedrons. Nano Lett. **4**(9), 1733–1739 (2004). https://doi.org/10.1021/nl048912c

24. Jing, S., Xing, S., Yu, L., Wu, Y., Zhao, C.: Synthesis and characterization of Ag/polyaniline core–shell nanocomposites based on silver nanoparticles colloid. Mater. Lett. **61**(13), 2794–2797 (2007). https://doi.org/10.1016/j.matlet.2006.10.032

25. Elumalai, D., Kaleena, P.K., Ashok, K., Suresh, A., Hemavathi, M.: Green synthesis of silver nanoparticle using *Achyranthes aspera* and its larvicidal activity against three major mosquito vectors. Eng. Agric. Environ. Food **9**(1), 1–8 (2016). https://doi.org/10.1016/j.eaef.2015.08.002

26. Singhal, G., Bhavesh, R., Kasariya, K., Sharma, A.R., Singh, R.P.: Biosynthesis of silver nanoparticles using *Ocimum sanctum* (Tulsi) leaf extract and screening its antimicrobial activity. J. Nanopart. Res. **13**(7), 2981–2988 (2011). https://doi.org/10.1007/s11051-010-0193-y

27. Roy, K., Sarkar, C.K., Ghosh, C.K.: Plant-mediated synthesis of silver nanoparticles using parsley (*Petroselinum crispum*) leaf extract: spectral analysis of the particles and antibacterial study. Appl. Nanosci. **5**(8), 945–951 (2015). https://doi.org/10.1007/s13204-014-0393-3

28. Vinmathi, V., Jacob, S.J.P.: A green and facile approach for the synthesis of silver nanoparticles using aqueous extract of *Ailanthus excelsa* leaves, evaluation of its antibacterial and anticancer efficacy. Bull. Mater. Sci. **38**(3), 625–628 (2015). https://doi.org/10.1007/s12034-015-0916-x

29. Li, S., Shen, Y., Xie, A., Yu, X., Qiu, L., Zhang, L., Zhang, Q.: Green synthesis of silver nanoparticles using *Capsicum annuum* L. extract. Green Chem. **9**(8), 852–858 (2007). https://doi.org/10.1039/B615357G

30. Bethu, M.S., Netala, V.R., Domdi, L., Tartte, V., Janapala, V.R.: Potential anticancer activity of biogenic silver nanoparticles using leaf extract of *Rhynchosia suaveolens*: an insight into the mechanism. Artif. Cells Nanomed. Biotechnol. **46**(sup1), 104–114 (2018). https://doi.org/10.1080/21691401.2017.1414824

31. Chadburn, H.: *Rhynchosia heynei*. The IUCN Red List of Threatened Species 2012: e. T19892259A20134626. http://dx.doi.org/10.2305

32. Raaman, N.: Phytochemical Techniques (2006). ISBN 81-89422-30-8

33. Cruickshank, R.: Medical Microbiology: A Guide to Diagnosis and Control of Infection. E&S Livingston Ltd., Edinburgh (1968)

34. Rammohan, A., Gunasekar, D., Reddy, N. V., Vijaya, T., Devillee, A., Bodo, B.: Structure elucidation and antioxidant activity of the phenolic compounds from *Rhynchosia suaveolens*. Nat. Prod. Comm. **1**0, 609–611 (2015). https://www.ncbi.nim.nih.gov/m/pubmed/25973488

35. Mosmann, T.: Rapid Colorimetric assay for cellular growth and survival: application to and cytotoxicity assays. J. Immunol. Methods **65**, 55–63 (1983). https://doi.org/10.1016/0022-1759(83)90303-4

36. Fayaz, A.M., Balaji, K., Kalaichelvan, P.T., Venkateshan, R.: Fungal based synthesis of silver nanoparticles—an effect of temperature on the size of particles. Coll Surf B: Biointerfaces **74**, 123–126 (2009). https://doi.org/10.1016/j.colsurfb.2009.07.002

37. Arunachalam, K.D., Arun, L.B., Annamalai, S.K., Arunachalam, A.M.: Potential anticancer properties of bioactive compounds of *Gymnema sylvestre* and its biofunctionalized silver nanoparticles. Int. J. Nanomed. **10**, 31–41 (2015)

38. Juibari, M.M., Abbasalizadeh, S., Jouzani, G.S., Noruzi, M.: Intensified biosynthesis of silver nanoparticles using a native extremophilic *Ureibacillus thermosphaericus* strain. Mater. Lett. **65**(6), 1014–1017 (2011). https://doi.org/10.1007/s12668-015-0185-6

39. Netala, V.R., Kotakadi, V.S., Nagam, V., Bobbu, P., Ghosh, S.B., Tartte, V.: First report of biomimetic synthesis of silver nanoparticles using aqueous callus extract of Centella asiatica and their antimicrobial activity. Appl. Nanosci. **5**(7), 801–807 (2015). https://doi.org/10.1007/s13204-014-0374-6

40. Baker, S., Kumar, K.M., Santosh, P., Rakshith, D., Satish, S.: Extracellular synthesis of silver nanoparticles by novel Pseudomonas veronii AS41G inhabiting *Annona squamosa* L. and their bactericidal activity. Spectrochim. Acta Part A Mol. Biomol. Spectrosc. **136**, 1434–1440 (2015)

41. Netala, V.R., Bukke, S., Domdi, L., Soneya, S., Reddy, S.G., Bethu, M.S., Tartte, V.: Biogenesis of silver nanoparticles using leaf extract of *Indigofera hirsuta* L. and their potential biomedical applications (3-in-1 system). Artif. Cells Nanomed. Biotechnol. **46** (sup1), 1138–1148 (2018). https://doi.org/10.1080/21691401.2018.1446967

42. Sankar, R., Karthik, A., Prabu, A., Karthik, S., Shivashangari, K.S., Ravikumar, V.: *Origanum vulgare* mediated biosynthesis of silver nanoparticles for its antibacterial and anticancer activity. Colloids Surf. B **108**, 80–84 (2013). https://doi.org/10.1016/j.colsurfb.2013.02.033

43. Venkatesan, B., Subramanian, V., Tumala, A., Vellaichamy, E.: Rapid synthesis of biocompatible silver nanoparticles using aqueous extract of *Rosa damascena* petals and evaluation of their anticancer activity. Asian Pac. J.Trop. Med. **7**, S294–S300 (2014). https://doi.org/10.1016/S1995-7645(14)60249-2

44. Nakkala, J.R., Rani, M., Sadras, S.R.: Green synthesized nano silver: Synthesis, physicochemical profiling, antibacterial, anticancer activities and biological *in vivo* toxicity. J. Col. Interface Sci. **499**, 33–45 (2017). https://doi.org/10.1016/j.jcis.2017.03.090

45. Patel, A., Patel, A., Patel, N.M.: Determination of polyphenols and free radical scavenging activity of Tephrosia purpurea linn leaves (Leguminosae). Pharmacogn. Res. **2**, 152–158 (2010). https://doi.org/10.4103/0974-8490.65509
46. Bhakshu, L.M., Raju, R.R.V.: Chemical composition and in vitro antimicrobial activitiy of essential oil of Rhynchosia heynei, an endemic medicinal plant from Eastern Ghats of India. Pharm. Biol **47**(11), 1067–1070 (2009). https://doi.org/10.3109/13880200902991573

Acoustical and Excess Properties on Ternary Liquid Mixtures of Ortho Methoxy Phenol, 1 Butanol and n-Hexane at Different Temperatures

P. S. Syed Ibrahim[1(✉)], S. Chidambaravinayagam[2],
J. Senthil Murugan[3], and J. Edward Jeyeakumar[2]

[1] Department of Chemistry, Sriram Engineering College, Perumalpattu,
Thiruvallur District, Tamil Nadu, India
syedibuji@gmail.com
[2] PG and Research Department of Chemistry, Presidency College,
Chennai, India
[3] Department of Chemistry, SIVET College, Gowrivakkam, Chennai, India

Abstract. The Ultrasonic velocity (U), density (ρ), and viscosity (η) have been measured experimentally for the ternary liquid mixtures of ortho methoxy phenol (omp), 1 butanol and n hexane at various temperatures viz., 303 K, 308 K and 313 K at constant frequency 2 MHz. for different concentrations ranges from 0.001 M to 0.01 M. The thermodynamic and acoustical parameters such as adiabatic compressibility (β), Rao constant (R), absorption coefficient (α/f^2), internal pressure (π_i), cohesive energy (CE), free volume (Vf), free length (Lf), acoustic impedance (z), available volume (Va), viscous relaxation time and Lenard Jones potential were calculated from the experimental data. The various excess properties including excess Ultrasonic velocity, excess acoustic impedance, excess free length, excess adiabatic compressibility, excess free volume and excess internal pressure were also computed. These parameters in accordance with their ultrasonic velocities corresponding to different concentrations of the mixture have been discussed. The molecular interactions were predicted based on the results obtained for ultrasonic velocities of different concentrations of the ternary mixtures at different temperatures.

Keywords: Molecular interactions · Ultrasonic velocity · Ternary liquid mixture · Excess adiabatic compressibility · Internal pressure · Excess acoustic impedance

1 Introduction

The ultrasonic study is one of the most important studies in diagnosing the interactions of the molecules [1]. In particular, the ultrasonic waves when it hits the system which is under investigation causes the interaction because of which there is the change with respect to structure, forces of attraction and thermochemical aspects in between the constituent molecules [2, 3]. The previous studies such as NMR, IR and UV by which the structural changes or nature of bonding can be enunciated for even small chemical

reactions occurred but this ultrasonic study may be substantiated even for extremely less concentrated solutions (in order 10^{-4} M) since the ultrasonic waves are highly sensitive [4–6]. Also the special characters possessed by the donor which is ortho methoxy phenol in this ternary system of OMP+1 butanol+n hexane belongs to a derivative of phenolic ether whose chemical, physical properties and its applications stimulate the authors to probe the present study.

OMP used in many organic reactions including electrophilic aromatic substitution reaction, regioselective (hydroxy methylation) reactions etc., This compound provides best smell to whisky and other substances due to which it finds applications in perfumery industries and in the preparation of vanillin. The synthesis of vanillin involves unwanted inorganic by products and more cost, this prompted the author to carry out the present study.

Hydrogen bonding plays the most important role in molecular interactions. Eventually, the ternary system which is under investigations containing 1 butanol possess hydrogen bonding along with OMP (donor) wherein the ethereal oxygen has enough tendency to form hydrogen bonding that makes the interactions, strong.

Although a large number of investigations are carried in liquid mixtures having cyclo hexane (or) benzene as one of the components, it is found that no work has been made so for to measure the ultrasonic velocity of the ternary mixtures of ortho methoxy phenol, 1 butanol and n hexane. Furthermore, for many practical purposes it is necessary to predict the excess properties of a multi component liquid mixture from the properties of the pure components rather than the normal acoustical properties.

Therefore, the present study has been undertaken by the authors to provide useful information regarding the molecular interactions possessed by the system of ortho methoxy phenol, 1 Butanol and n- hexane at different temperatures.

2 Materials and Methods

The mixtures (OMP+1 butanol+n hexane) of various concentrations in mole fraction were prepared by taking analytical reagent grade and spectroscopic reagent grade chemicals with minimum assay of 99.9% and obtained from E Merck Ltd (India). All the component liquids were purified by the standard methods [7]. The density, viscosity, and ultrasonic velocity were measured for various concentrations viz., 0.001–0.01 M at different temperatures viz. 303 K, 308 K, and 313 K keeping constant frequency of 2 MHz. Ultrasonic velocity measurements were made using an ultrasonic interferometer (Model F-81, supplied by M/S Mittal Enterprises, New Delhi) with the accuracy of ± 0.1 m·s^{-1}. Water at desired temperature is circulated through the outer jacket of the double-walled measuring cell containing the experimental liquid. The densities of the mixture were measured using a 10-ml specific gravity bottle by relative measurement method with an accuracy of $\pm$ 0.01 kg·m^{-3}. An Oswald viscometer (10 ml) with an accuracy of ± 0.001 Ns·m^{-2} was used for the viscosity measurement. The flow time was determined using a digital racer stopwatch with an accuracy of ± 0.1 s.

2.1 Theory and Calculations

Intermolecular free length (Lf), is calculated using the standard expression

$$L_f = K\beta^{1/2} \tag{1}$$

Where K is a temperature dependent constant known as Jacobson constant and β is the adiabatic compressibility that can be calculated from the speed of sound (U) and the density of the medium (ρ) as

$$\beta = \left(u^2\rho\right)^{-1} \tag{2}$$

The relation for free volume in terms of ultrasonic velocity and the viscosity (η) of liquid as

$$V_f = \left(M_{eff}U/\ k\eta\right)^{1/2} \tag{3}$$

Expression for the determination of internal pressure π_i by the use of free volume as

$$\pi_i = bRT(K\eta/U)^{1/2}\left(\rho^{2/3}/M_{eff}^{7/6}\right) \tag{4}$$

Where b stands for cubic packing which is assumed to be 2 for liquids and K is a dimensionless constant independent of temperature and nature of liquids and its value is 4.281×109, T is the absolute temperature and Meff is the effective molecular weight. The viscous relaxation time was obtained using the relation

$$\tau = (4/3)\beta\,\eta \tag{5}$$

Gibbs free energy is calculated from the relation

$$\Delta G = KT\ \ln(KT\tau/h) \tag{6}$$

Where τ is the viscous relaxation time, K the Boltzman's constant, T, the absolute temperature and h is the Planck's constant.

The acoustic impendance is given by,

$$Z = U\rho \tag{7}$$

Where U and ρ are the velocity and density of liquid, respectively.

In order to study the non-ideality of the liquid mixtures, namely excess parameters (AE) of all the acoustic parameter were computed by

$$AE = Aexp - Aideal \tag{8}$$

Where Aid = $\sum nAiXi$, Ai is any acoustical parameters and Xi the mole fraction of the liquid components of I.

3   Results and Discussions

The experimentally measured values of density, viscosity and ultrasonic velocity for the mixtures at 303 K 308 K and 313 K are presented in Table 1. Table 2 represents the excess values of acoustic impedance and ultrasonic velocity. The excess adiabatic compressibility and excess free length are depicted in Table 3. Excess values of free volume and internal pressure for the mixture are presented in Table 4.

From the Table 1, it was observed that the ultrasonic velocity of the ternary liquid mixtures increases with increasing concentration of the mixture at 303 K which suggests that weak interactions due to dipole-dipole nature of the OMP and 1 butanol but at 308 K and 313 K an uneven trend is observed due to dipole-induced dipole nature of system while the viscosity and density is found to be decreases/increases with increasing concentration at all the working temperatures. But it is noted that when the temperature increases for a particular concentration of the mixture, the ultrasonic velocity decreases due to thermal agitation.

In order to understand more about the interaction between the components of liquid mixtures, it is necessary to discuss the same in terms of excess parameters [8] rather than the calculated values of normal acoustic properties like adiabatic compressibility, free length, free volume, internal pressure and acoustic impedance whose values were tabulated from Tables 5, 6, 7, 8 and 9 respectively for which no discussions were provided in this study. The Table 10 revealed Experimental values of Density, Viscosity and Ultrasonic velocity for each pure component present in the ternary mixture and those values are found to be in good agreement with the theoretical values. The excess properties can yield an idea about the linearity or non- linearity of the system as association or other type of interactions. It can be seen from Tables 2, 3 and 4.

Table 2, the acoustic impedance increases with increasing concentration of the mixture at irrespective of the temperatures. The negative values show the strong interactions present between the component molecules. The corresponding plot is given in Fig. 1.

Table 2, it is noticed that the values of excess velocity increases with increase in concentration at all the temperatures under which investigation is done. Further the negative values predict the linear behavior of the system and weak to moderate interactions exhibits by the system. The corresponding plot is given in Fig. 2.

Table 3, the adiabatic compressibility is the decrease in volume per unit increase in pressure when no heat flows in or vice versa. It is indirectly proportional to the square of the density and ultrasonic velocity. But with respect to excess properties the values obtained are negative. This negative values strongly support the nature of the interactions which is found to be strong that attributed to the closed packed nature of the molecules. Similar conclusions were also arrived by Islam and Quadri [9]. In our present investigation the excess adiabatic values (magnitude alone) increase while the concentration increases at irrespective of the working temperatures under the influence of ultrasonic sound. The corresponding plot is given in Fig. 3.

Table 3, the Excess free length decreases with increase of concentration which predicts the presence of specific molecular interaction between the molecules of the liquid mixture. The adiabatic compressibility and free length are the deciding factors of the ultrasonic velocity in liquid systems. The values of excess inter molecular free length follows the same trend as that of β^E (adiabatic compressibility). The values of excess inter molecular free length (L_f^E) are negative. The negative deviation of excess free length is an indication of the existence of strong interaction between the components. This is due to dipole – dipole, dipole-induced dipole and charge transfer complex formation owing to hydrogen bonding. The corresponding plot is given in Fig. 4.

Table 4, Free volume is the space available in the system when the constituent molecules come closure for interaction. In the present study the values of excess free volume show an uneven trend when the concentration of the mixture increases at irrespective of temperatures. But along the temperature at 308 K the values show higher than at 303 K and lower than at 313 K for all the concentration (except 0.001 M). This clearly indicated that there is a stronger interactions experienced by the molecules at 303 and 313 K rather than at 308 K for which weaker interactions are predicted. The corresponding plot is given in Fig. 6.

Table 4, the internal pressure is important factor in deciding the thermodynamic properties of liquids [10]. The internal pressure is the cohesive force, which is a resultant of force of attraction and force of repulsion between the molecules. Internal pressure also gives an idea of the solubility characteristics. In the present study the negative excess internal pressure π_i^E over the entire range of the concentration of the system also supports the presence of interaction. The corresponding plot is given in Fig. 5.

Table 1. Experimental values of velocity, viscosity and density of OMP+1-butanol+n hexane

Sl. no.	Con. (M) $\times 10^{-3}$	Velocity (U) ms^{-1} at			Viscosity (η) Nsm^{-2} $\times 10^{-4}$ at			Density (ρ) Kgm^{-3} at		
		303 K	308 K	313 K	303 K	308 K	313 K	303 K	308 K	313 K
1	1	1062.22	1028.02	1018.13	5.346	5.709	5.235	797.2	789.0	786.8
2	2	1065.12	1032.22	1018.96	5.391	5.880	5.248	792.0	788.4	786.2
3	3	1064.78	1030.56	1020.54	5.347	5.755	5.301	797.7	795.8	787.4
4	4	1080.05	1033.25	1018.27	5.252	5.745	5.218	791.2	789.0	785.7
5	5	1063.22	1029.47	1019.69	5.231	5.718	5.119	790.3	795.8	786.2
6	6	1070.00	1035.35	1018.58	5.361	5.630	5.221	797.2	790.7	786.2
7	7	1075.22	1029.61	1020.40	5.388	5.506	5.163	797.2	789.5	784.5
8	8	1068.45	1040.00	1020.56	5.248	5.478	5.242	792.3	790.7	787.4
9	9	1067.51	1034.84	1018.55	5.260	5.532	5.126	789.2	788.4	787.9
10	10	1081.10	1030.98	1019.12	5.241	5.744	5.097	791.2	790.7	785.7

Table 2. Computed values of excess acoustic impedance and excess ultrasonic velocity of OMP +1-butanol+n hexane

Sl. no.	Con. (M) × 10^{-3}	Excess acoustic impedence (Z_E) Kgms^{-1}			Excess ultrasonic velocity (U_E) (m/s)		
		Temperature (K)			Temperature (K)		
		303	308	313	303	308	313
1	1	−51249	−38885	−64409	−61.536	−68.281	−28.988
2	2	−38506	−39164	−14981	−102.26	−102.43	−47.312
3	3	−113212	−107630	−53303	−142.67	−139.33	−69.666
4	4	−180697	−181282	−110591	−164.35	−169.13	−86.06
5	5	−263661	−240777	−157877	−215.35	−202.95	−107.48
6	6	−313704	−299674	−204593	−240.27	−224.94	−117.97
7	7	−368341	−360455	−247115	−264.54	−256.61	−138.93
8	8	−433018	−402537	−283765	−298.80	−270.39	−142.74
9	9	−489125	−456283	−321826	−325.43	−298.14	−161.17
10	10	−523999	−502009	−358542	−335.92	−323.17	−177.46

Table 3. Computed values of excess adiabatic compressibility and excess free length of OMP +1-butanol+n hexane

Sl. no.	Con. (M) × 10^{-3}	Excess adiabatic compressibility (β^E) × 10^{-10} N^{-1}m^2			Excess free length (L_f^E) (m) × 10^{-10}		
		Temperature (K)			Temperature (K)		
		303	308	313	303	308	313
1	1	−2.851	−0.946	−4.338	−6.35	−6.18	−6.71
2	2	−4.115	−2.519	−7.466	−6.02	−5.87	−6.44
3	3	−5.410	−4.146	−10.659	−5.71	−5.57	−6.18
4	4	−7.136	−5.925	−14.045	−5.42	−5.29	−5.93
5	5	−8.295	−7.878	−17.981	−5.13	−5.02	−5.70
6	6	−10.215	−10.032	−22.206	−4.86	−4.76	−5.47
7	7	−12.221	−12.418	−26.888	−4.60	−4.51	−5.25
8	8	−14.145	−15.077	−32.006	−4.34	−4.27	−5.04
9	9	−16.527	−18.060	−37.957	−4.10	−4.04	−4.84
10	10	−19.516	−21.427	−44.564	−3.87	−6.18	−4.64

Table 4. Computed values of excess internal pressure and excess free volume of OMP+1-butanol+n hexane

Sl. no.	Con. (M) $\times 10^{-3}$	Excess internal pressure $(Nm^{-2}) \times 10^{+8}$			Excess free volume $(V_f^E) \times 10^{-7}$ (m³)		
		Temperature (K)			Temperature (K)		
		303	308	313	303	308	313
1	1	−0.21	−0.08	−1.89	0.19	2.11	2.37
2	2	−0.47	−2.60	−4.43	0.40	2.03	2.36
3	3	−0.77	−5.79	−7.33	0.39	2.09	2.33
4	4	−1.13	−8.92	−1.04	0.52	2.11	2.38
5	5	−1.37	−1.13	−1.34	0.48	2.11	2.45
6	6	−1.56	−1.43	−1.54	0.38	2.18	2.38
7	7	−1.78	−1.69	−1.79	0.44	2.23	2.42
8	8	−2.04	−1.93	−1.97	0.54	2.28	2.37
9	9	−2.24	−2.11	−2.21	0.46	2.23	2.44
10	10	−2.45	−2.21	−2.40	0.52	2.10	2.47
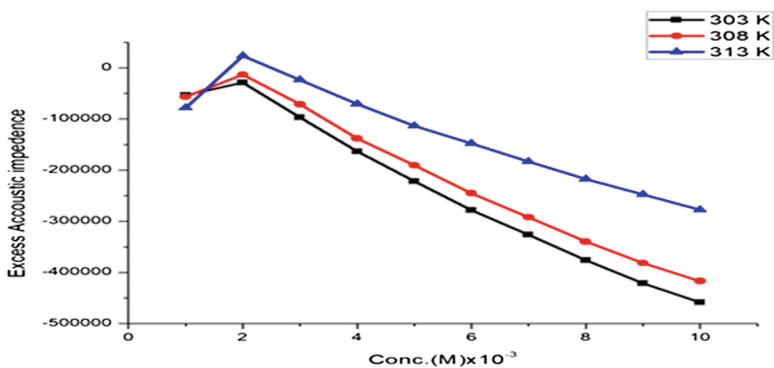
Fig. 1. Plot between concentration (M) $\times 10^{-3}$ vs acoustic impedance
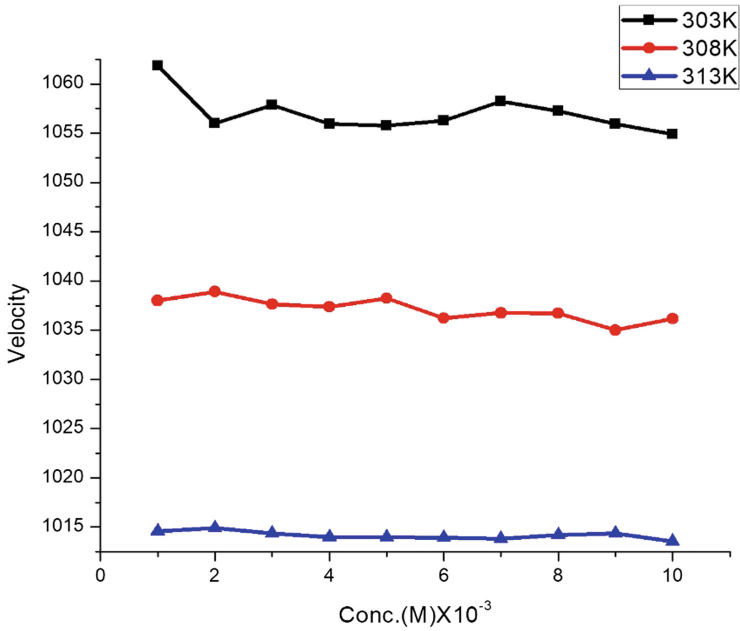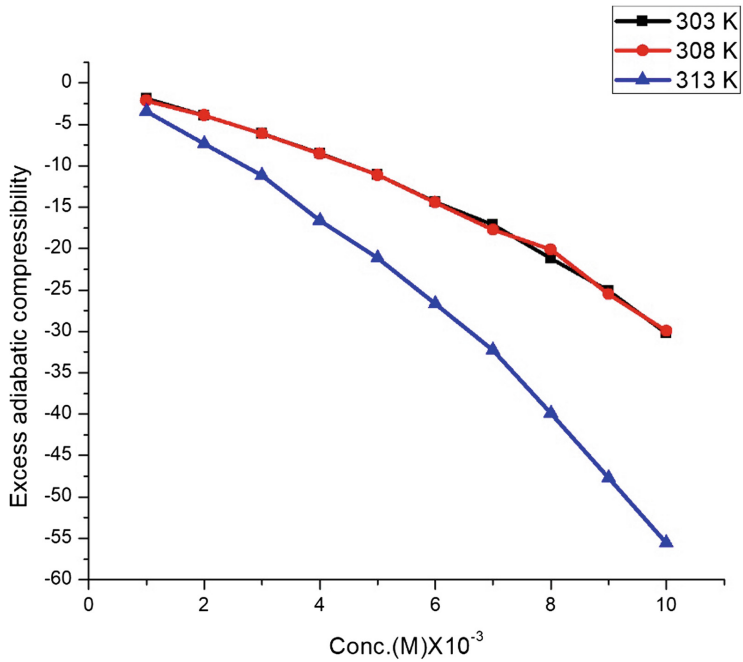
Fig. 2. Plot between concentration (M) $\times$ 10^{-3} vs ultrasonic velocity

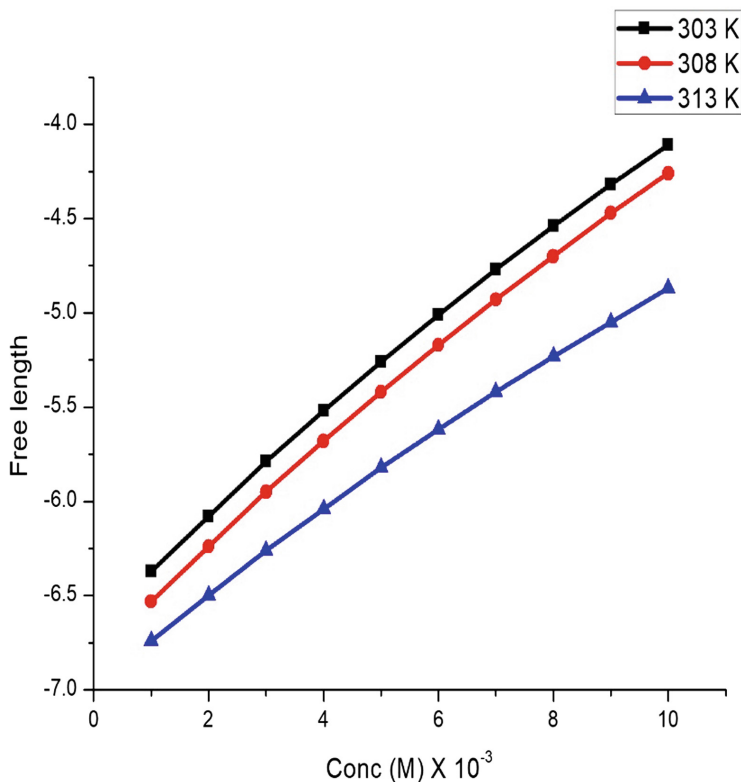**Fig. 3.** Plot between concentration (M) $\times$ 10^{-3} vs adiabatic compressibility

Fig. 4. Plot between concentrations (M) $\times$ 10^{-3} vs excess free length

Table 5. The calculated values of adiabatic compressibilities of ortho methoxy phenol (OMP) +1 butanol+n hexane at different temperatures

S. no.		1	2	3	4	5	6	7	8	9	10
Conc. (M) $\times$ 10^{-3}		1	2	3	4	5	6	7	8	9	10
(β) $N^1m^2 \times 10^{-9}$	303 K	1.11	1.11	1.11	1.08	1.12	1.1	1.09	1.11	1.11	1.108
	308 K	1.21	1.19	1.18	1.19	1.19	1.18	1.19	1.17	1.18	1.190
	313 K	1.23	1.23	1.22	1.23	1.22	1.23	1.22	1.22	1.22	1.230
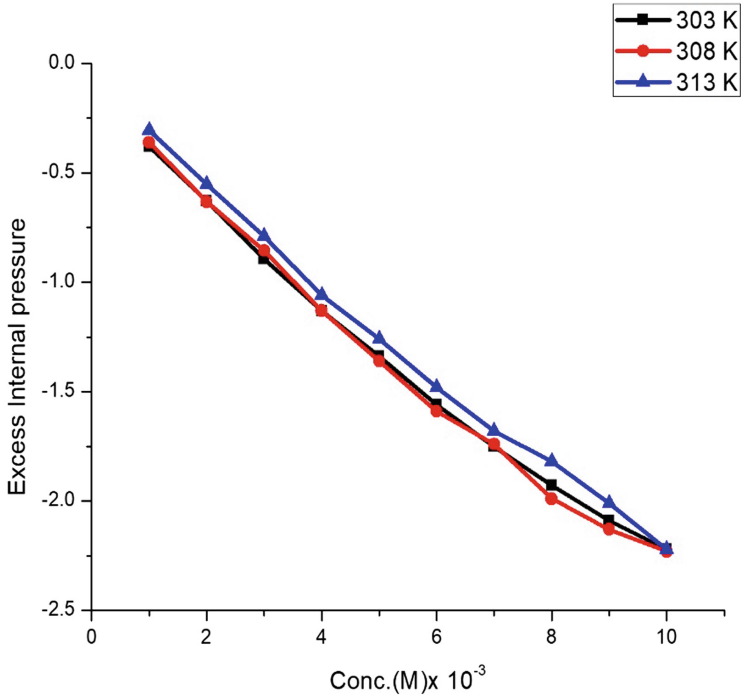
Fig. 5. Plot between concentrations (M) $\times 10^{-3}$ vs internal pressure
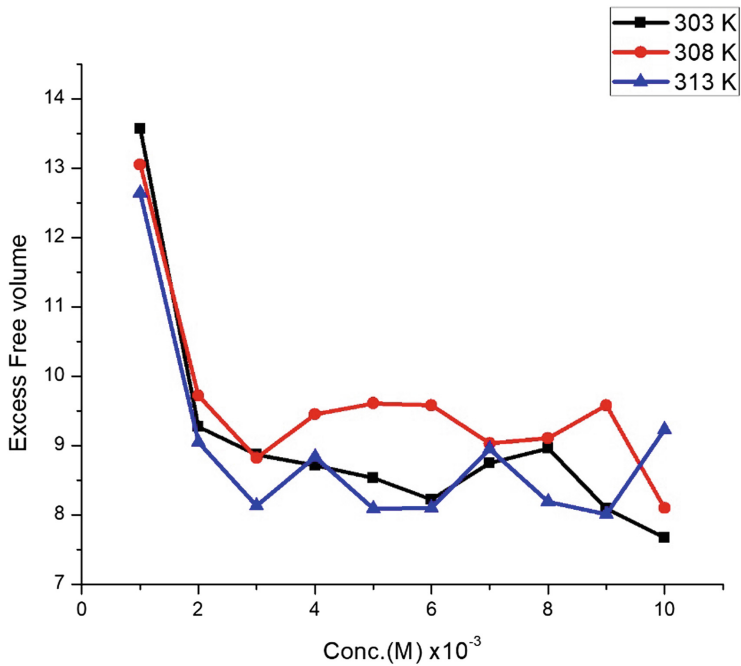

Fig. 6. Plot between concentrations (M) $\times 10^{-3}$ vs free volume

Table 6. The calculated values of free length of ortho methoxy phenol (OMP)+1 butanol+n hexane at different temperatures

S. no.		1	2	3	4	5	6	7	8	9	10
Conc. (M) $\times$ 10^{-3}		1	2	3	4	5	6	7	8	9	10
L_f (m) $\times$ 10^{-11}	303 K	6.62	6.56	6.54	6.48	6.58	6.51	6.48	6.54	6.56	6.47
	308 K	6.87	6.79	6.77	6.78	6.77	6.76	6.8	6.73	6.77	6.79
	313 K	6.95	6.89	6.87	6.89	6.88	6.89	6.88	6.87	6.88	6.89

Table 7. The calculated values of free volume of ortho methoxy phenol (OMP)+1 butanol+n hexane at different temperatures (K)

S. no.		1	2	3	4	5	6	7	8	9	10
Conc. (M) $\times$ 10^{-3}		1	2	3	4	5	6	7	8	9	10
L_f (m) $\times$ 10^{-11}	303 K	2.444	2.423	2.452	2.573	2.528	2.461	2.461	2.535	2.523	2.585
	308 K	2.108	2.030	2.091	2.105	2.108	2.176	2.231	2.283	2.232	2.098
	313 K	2.367	2.361	2.331	2.379	2.453	2.378	2.424	2.370	2.444	2.467

Table 8. The calculated values of internal pressure of ortho methoxy phenol (OMP)+1 butanol +n hexane at different temperatures

S. no.		1	2	3	4	5	6	7	8	9	10
Conc. (M) $\times$ 10^{-3}		1	2	3	4	5	6	7	8	9	10
Internal pressure (Nm^2) $\times$ 10^{+8}	303 K	2.91	3.62	3.62	3.54	3.56	3.61	3.61	3.56	3.56	3.54
	308 K	3.02	3.82	3.81	3.78	3.8	3.74	3.71	3.69	3.7	3.79
	313 K	2.91	3.62	3.62	3.54	3.56	3.61	3.61	3.56	3.56	3.54

Table 9. The calculated values of acoustic impedance of ortho methoxy phenol (OMP)+1 butanol+n hexane at different temperatures

S. no.		1	2	3	4	5	6	7	8	9	10
Conc. (M) $\times$ 10^{-3}		1	2	3	4	5	6	7	8	9	10
Acoustic impedence ($\times 10^{+5}$)	303 K	8.47	8.44	8.49	8.55	8.40	8.53	8.57	8.47	8.42	8.55
	308 K	8.11	8.14	8.20	8.15	8.19	8.19	8.13	8.22	8.16	8.15
	313 K	8.01	8.01	8.04	8.00	8.02	8.01	8.01	8.04	8.03	8.01

Table 10. Experimental values of density, viscosity and ultrasonic velocity for each component present in the ternary mixture

Sl. no.	Name of the component in the mixture	Experimental value		
		Density Kgm^{-3}	Viscosity Nsm^{-2}	Ultrasonic velocity ms^{-1}
1	OMP	1.080	0.388	1683.2
2	1 Butanol	0.877	0.131	1240.1
3	n hexane	0.651	0.243	1076.1

4   Conclusions

The strong molecular association arises due to dipole-dipole interaction and the polar/non polar nature of different molecular entities in the mixture. The values of excess parameters support the existence of interactions due to hydrogen bonding and –I effect of –OCH3 group and the formation of charge transfer complex. In this present study it is observed that the chemical reaction will be allowed due to dipole-diplole interactions and dipole – induced dipole interactions between OMP and 1 - butanol in n hexane.

References

1. Arul, G., Palaniappan, L.: Ultrasonic study of 1-butanol in pyridine with benzene. Ind. J. Pure. Apple Phys. **43**, 755–758 (2005)
2. Kannappan, V., Jaya Shanthi, R.: Ultrasonic studies of induced dipole-dipole interactions in binary liquids mixtures. Ind. J. Pure. Appl. Phys. **43**, 750–754 (2005)
3. Kannappan, A.N., Rajendran, V.: Acoustic parameters of some ternary liquid mixtures. Ind. J. Pure. Appl. Phys. **30**, 240–242 (1992)
4. Ali, A., Nain, A.A.K., Hyder, S.: Molecular interactions in formamide+isomeric butanols: an ultrasonic and volumetric study. J. Solution Chem. **32**(10), 865–877 (2003)
5. Aralaguppi, M.I., Barragi, J.C.: Physicochemical and excess properties of the binary mixtures of methylcyclohexane + ethanol + propan-1-ol + propan-2-ol, + butan-1-ol, + 2-methyl-1-propanol or 3-methyl-1-butanol at T = 298.15, 303.15 and 308.15 K. J. Chem. Therm. **38**, 434–442 (2006)
6. Niham, P.S., Kapade, V.M., Hasan, M.: Molecular interactions in binary mixtures of bromobenzene with normal alkanols C1-C4: an ultrasonic study. Ind. J. Pure Appl. Phys. **38**, 170–173 (2000)
7. Furniss, B.S., Hannaford, A.J., Smith, P.W.G., Tatchell, A.R.: Vogel's Text book of Practical Organic Chemistry, 5th edn. Longman Scientific & Technical, New York (1989)
8. Sridevi, U., Samatha, K., Viswanatha, Sarma A.: Excess thermodymamic properties in binary liquids. J. pure Appl. Ultrason. **26**, 1–11 (2004)
9. Islam, M.R.: Quadri, ultrasonic velocity and viscosity of binary liquid mixtures. Thermo. Chim. Acta. **115**, 335–340 (1987)
10. Rajendran, V., Marikani, A.: Investigation of thermodynamic properties of amine-alcohol mixtures at 303.15 K. Acoustics Lett. **18**, 90–94 (1994)

A Facile Route for the Fabrication of Nanocompositie by Effective Impregnation Through the Biopolymer Matrix and Its Characterisation

T. Uma Rajalakshmi[1,2(✉)] and G. Alagumuthu[2]

[1] Department of Chemistry, Rani Anna Govt. College for Women
(Affiliated to Manonmaniam Sundarnar University), Tirunelveli, TN, India
umarajalakshmi2@gmail.com
[2] Department of Chemistry, Sri Paramakalyani College
(Affiliated to Manonmaniam Sundarnar University), Alwarkurichi, TN, India

Abstract. Nanoscience and nanotechnology primarily deal with the synthesis characterization exploration and exploitation of nanostructural materials. Polymer nanocomposite materials have lately received great attention in both academia and industry. Small additions of inorganic usually surface-treated nanoparticles have a very positive effect on the electrical properties of insulating polymers. Biopolymers are polymers produced by living organisms in other words they are polymeric biopolymers. Cyclodextrins are a group of naturally occurring cyclic oligosaccharides, with six, seven, or eight glucose subunits linked by α-(1, 4) glycosidic bonds in a torus shaped structure and are denominated as α-, β-, and γ-CD respectively. In the present study, zincoxide/biopolymer nanocompositie was successfully fabricated by a simple and cost effective method. The possible nanomaterial zincoxide was successfully synthesized by simple precipitation technique and then effectivcly impregenated through the β-cyclodextrin matrix. The morphology of the synthesized nanocompositie was investigated using scanning electron microscopy and transmission electron microscopy. The crystalline nature of the nanocomposite was studied using an X-ray diffractometer. XRD analysis revealed the spherical shape allignment of zincoxide with hexagonal wurtzite structure. UV-Vis, FTIR spectral analysis and AFM studies where also performed for the synthesized nano compositie.

Keywords: Zincoxide · Biopolymer · Scanning electron microscopy (SEM)

1 Introduction

Nanotechnology deals with the science of production, manipulation and use of materials at subatomic level to produce novel products. It has tremendous applications in diagnostic devices, drug delivery, tissue engineering, environmental chemistry, water filtration etc. Nano-sized metal particles have great attention due to its unique optical, electrical and magnetic properties [1]. The two approaches followed for the synthesis of nanomaterials are (i) top down and (ii) bottom up approaches. Top down approach

involves synthesis of nanomaterials from bulk, materials through size reduction using mechanical methods such as mechanical milling [2, 3]. Bottom up approach involves synthesis of nanomaterials from the self-assembly of their constituent atoms into larger, organized systems using chemical or vapour methods. Bottom up approaches have been widely used by the researchers due to advantages like reproducibility, relative case of scale up and high degree of control on morphology. zincoxide nanoparticles become one of the most important functional materials due to its unique optical, electronic properties such as near-UV emission, catalytic, optical transparency, electric conductivity, piezoelectricity etc. It has superior durability, greater selectivity and heat resistance than organic and inorganic materials [4].

Recently, zincoxide nanomaterials have been observed to have important application in improved photocatalytic degradation of dyes. Many researchers have reported their achievements in preparing zincoxide nanomaterials and its composites through different methods and their improved application in photocatalytic degradation of organic dyes have been extensively studied [5]. Different methods like simple precipitation method, hydrothermal method, aerosol, micro-emulsion, ultrasonic, sol–gel method, evaporation of solution and suspensions, evaporative decomposition of solution (EDS), solid state reaction, conventional ceramic fabrication, wet chemical synthesis, spray pyrolysis method [6–11] etc. have been adopted by researchers for the synthesis of nanosized ZnO. Among these synthetic routes, simple precipitation technique compared with other traditional methods provides a facile route for low cost and large-scale production, which does not need expensive raw materials and complicated equipments [7, 12]. The preparation of zincoxide nanostructures by the simple precipitation technique from zinc salt solutions, such as $Zn(NO_3)_2$, $Zn(CH_3COO)_2 \cdot 2H_2O$, $ZnSO_4$, with alkali solutions containing LiOH, NH_4OH, NaOH, etc. have been investingated [7].

Cyclodextrins (CDs) are a group of naturally occurring cyclic oligosaccharides, with six, seven, or groups makes the upper and lower eight glucose subunits linked by α-(1, 4) glycosidic bonds in a torus shaped structure and are denominated as α-, β- and γ-CD respectively. These are biopolymers which contain primary and secondary hydroxyl groups at the 2, 3 and the 6 positions, respectively [13]. They form a rigid structure because of the formation of a belt of intermolecular hydrogen bonds between hydroxyl groups at the 2 and 3 positions of adjacent glucose units. The rotation of the primary hydroxyl groups is possible, thus reducing the effective diameter of the cavity on the primary side of the molecule thereby the upper and lower end of the molecule is rendered hydrophilic. The cavity of the cyclodextrins is rendered hydrophobic because of the presence of glycosidic oxygens and C–H units. Greater attention has recently been focused on cyclodextrin based polymers in a wide variety of applications because of their unique sorption properties. Recently, a number of insoluble cyclodextrin polymers have been widely used for various applications such as contaminants removal from wastewater, protein refolding, drug delivery etc. In the present work zincoxide/β-cyclodextrin nanocompositie was successfully synthesized by a facile route and characterized by XRD, SEM, TEM, FTIR, UV-VIS absorption spectra, AFM etc.

2   Materials and Methods

Zincnitrate, ammoniumcarbonate, β-cyclodextrin and ethanol were purchased from Merck, India Pvt.Ltd. Deionised water was used throughout the reaction process. All the reagents used in this study were of analytical grade. The synthetic procedures for the zincoxide particles by direct precipitation method is described below. The Zn $(NO_3)_2$ solutions (1.5 mol/L) was slowly dropped into the $(NH_4)_2CO_3$ solution a (2.25 mol/L) with vigorous stirring. And then, the precipitate derived from the above reaction was collected by filtration and rinsed three times with high-purity water followed by ethanol. Subsequently the washed precipitate was dried at 80 °C to form the precursor zincoxide. Finally, the precursors was calcined at a temperature of 550 °C for 2 h in the muffle furance [14] to obtain the nanosized zincoxide particles. The precursor zincoxide nanoparticles is mixed with 50 ml of a solution containning biopolymer β-cyclodextrin under proper proportions and stirred uniformly for about 8 h. The resulting mixture is poured in an autoclave coated with teflon lining maintained at 160 °C for 12 h, filtered washed with ethanol and water and dried at 60 °C for 2 h. The synthesized nanocimposite was characterised by XRD, SEM, TEM, FTIR, UV-VIS absorption spectra, AFM etc.

3   Results and Discussion

3.1   XRD

X-ray diffraction paterrn is used to confirm the purity, phase, average particle size and over all synthesized nanocomposites. From Fig. 1, the peaks at 2θ = 31°, 34°, 36°, 47°, 56°, 62°, 67° and 69° of zincoxide/β-cyclodextrin nanocomposites are corresponding to (100), (002), (101), (102), (110), (103), (112) and (201) in the JCPDS data card 89-0510. Hexagonal structure of zincoxide was confirmed by the (1 0 1) crystalline peak and the average crystal size of synthesized zincoxide nanoparticle is found to be 39 nm.

The presence of β-cyclodextrin as well as zincoxide characteristic reflections indicated the maintenance of the β-cyclodextrin and ZnO nanoparticles in crystallographic organization of the nanocomposite. The presence of high and narrow shaped peaks highlight that zincoxide nanoparticles possess high crystallinity and low surface defects [15] and were of ultrapure phase.

3.2   SEM

Figure 2 depicts the uniform distribution of granular zincoxide into the polymer matrix. It is observed that zincoxide nanoparticles are almost spherical in shape and are effectively impregnated through the biopolymer matrix & hence it appears as agglomerated macromolecules.
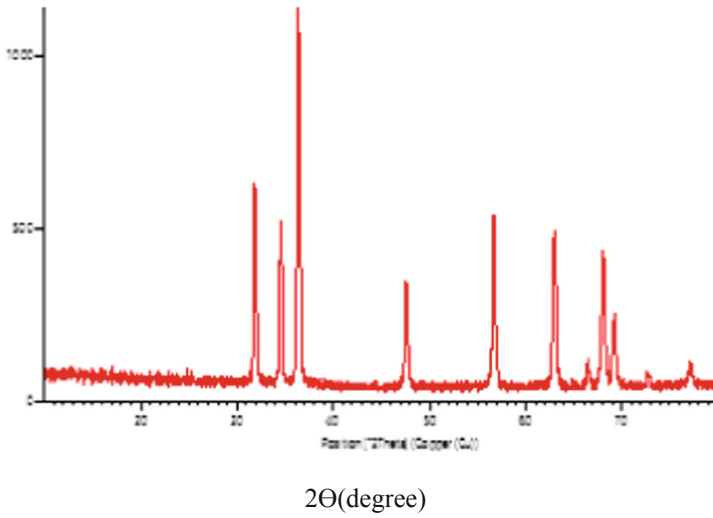
2Θ(degree)

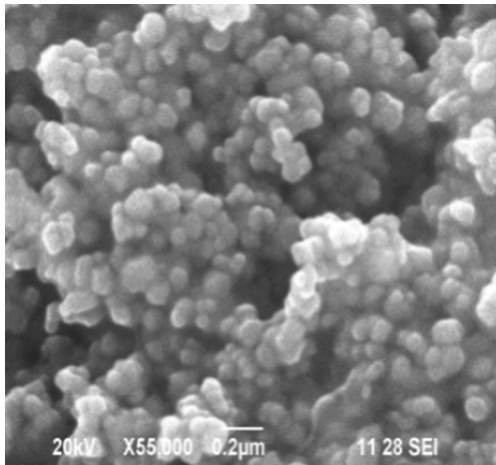**Fig. 1.** XRD pattern of ZnO β-cyclodextrin nanocomposite

Fig. 2. SEM image of the prepared Zincoxide/β-cyclodextrin nanocomposite

3.3 TEM

Figure 3 shows the TEM image of the prepared zincoxide/β-cyclodextrin nanocomposite. The size of the particle observed is in the range of 40 nm which is in good agreement with Debye–Scherer formula using XRD. After composite formation, zincoxide nanoparticles were found to be entrapped in the bio polymer matrix.
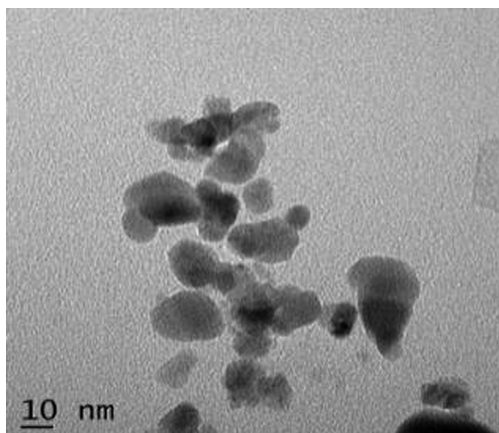
Fig. 3. TEM image of the prepared zincoxide/β-cyclodextrin nanocomposite

3.4   FTIR

Fourier transform infrared spectroscopy (FTIR) data of the zincoxide/β-cyclodextrin nanocomposite is represented in the Fig. 4. The absorption band characteristic of Cyclodextrin was observed at 3448 cm^{-1} corresponding to OH group and the peaks near 1637 cm^{-1} 1543 cm^{-1} and 1460 cm^{-1} are assigned to symmetric and asymmetric stretching vibration of COO^{-} groups [16]. The band around 1100 cm^{-1} (C-O-C) stretching were attributed to saccharide structure [17]. The absorption band around 2922 cm^{-1} may be due to the C-H stretching of the CH$_2$ group. The peak around 450 cm^{-1} is the characteristic absorption of Zn-O bond.
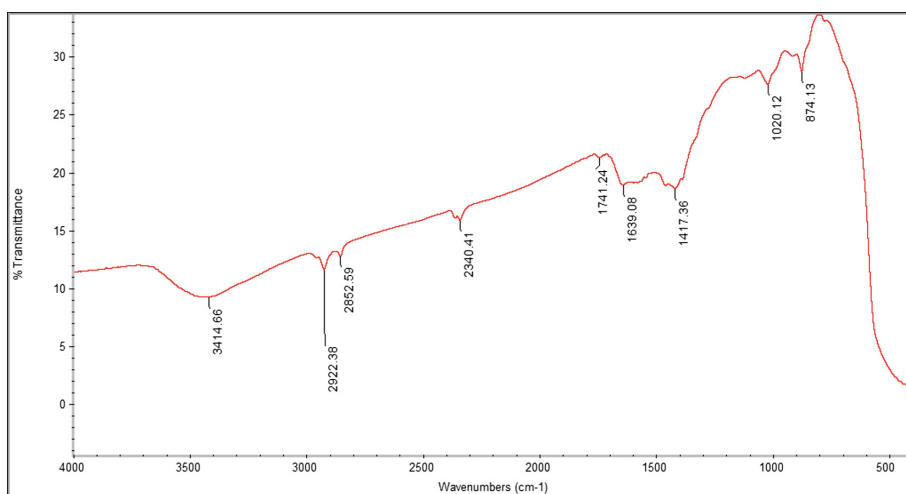
Fig. 4. FTIR spectra of the ZnO/β-cyclodextrin nanocomposite

3.5   UV-Vis

The UV-vis absorption spectra of the synthesised nanocomposite is shown in Fig. 5. A broad absorption peak was observed around 360–380 nm which is characteristic band for the pure ZnO [18]. A red shift in the absorption edge may be due to the changes in the morphologies, particle size and surface microstructures [19] which may be due to the presence of the biopolymer β-CD. It is known that the ZnO nanoparticles with absorption at higher wavelength in the UV-visible spectrum have higher particles size [18]. The band gap energy can be determined by substituting the value of the absorption peak at a given wavelength in the following equation [20].

$$Eg = h\upsilon g = hc/\lambda g \tag{1}$$

where h = 4.14 × 10^{-15} eVs, c = 2.99 × 10^{8} m/s, λg = wavelength and Eg is the band gap energy.
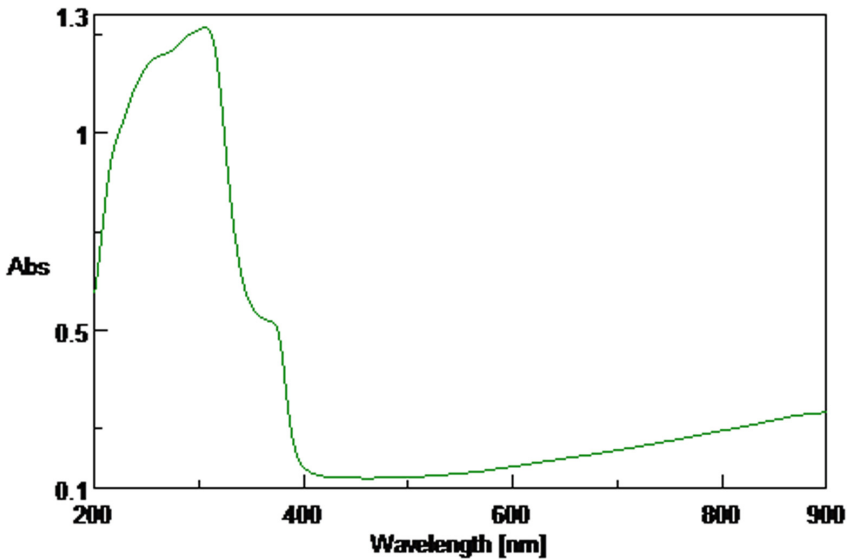
Fig. 5. UV-vis spectra of the ZnO/β-cyclodextrin nanocomposite

    The band gap energy is caluculated according to Eq. (1) and it is shown in the Fig. 6. From the figure the Eg value is caluculated to be around 3.02 eV. Figure 6 shows the band gap energy of the ZnO/β-cyclodextrin nanocomposite.

3.6   AFM

Surface topology of the synthesized zincoxide nanoparticles was studied by Atomic Force microscope (AFM) analysis as shown in Fig. 7(a and b). The results showed a uniform surface and indicated that the particles have uniform dimensions.
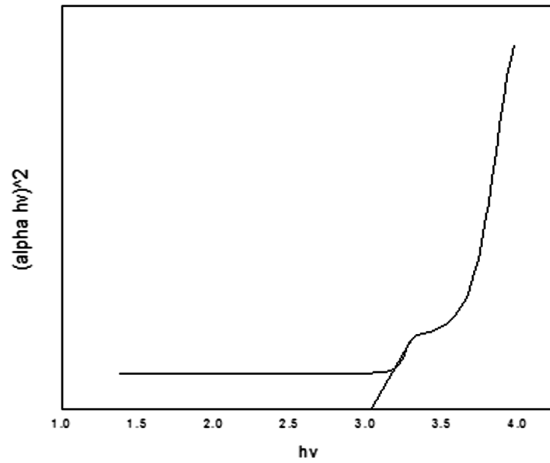
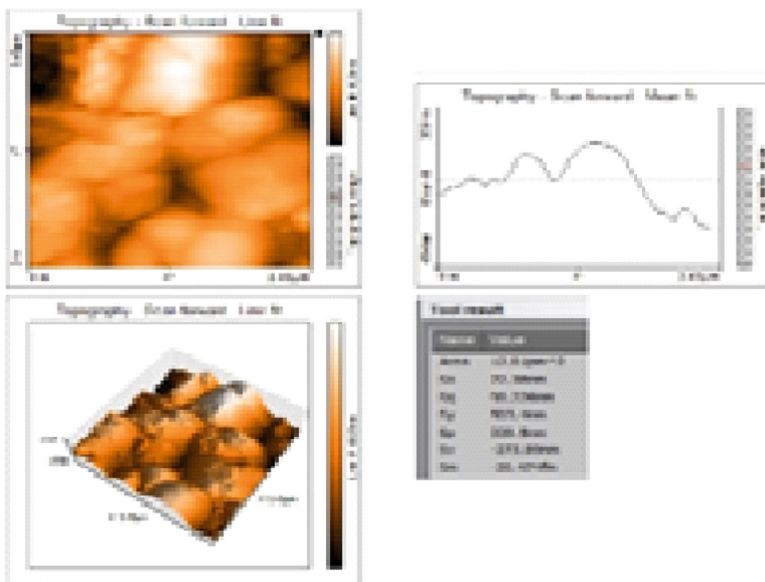**Fig. 6.** Band gap energy of the ZnO/β-cyclodextrin nanocomposite

Fig. 7. AFM image of the prepared Zincoxide/β-cyclodextrin nanocomposite

4   Conclusion

The zincoxide/β-cyclodextrin nanocomposite was prepared by a facile process. The XRD pattern of the synthesized nanocomposite shows that the particle size was 39 nm. From SEM analysis, it is found that the particles are almost spherical in shape in which the zincoxide nanoparticles were effectively impregnated through the

biopolymer matrix. The band gap energy of the ZnO/β-cyclodextrin nanocomposite is caluculated to be around 3.02 eV. TEM results confirm that the zincoxide nanoparticles (with a mean diameter of 40 nm) were encapsulated by the biopolymer. The FTIR spectra confirms the functional groups of β-cyclodextrin and zinxoxide. The AFM results showed a uniform surface and indicated that the particles have uniform dimensions.

References

1. Yong, N.L., et al.: Synthesis and characterization of silver oxide nanoparticles by a novel method. Int. J. Sci. Eng. Res. **4**, 155–158 (2013)
2. Manikandan, S., Karthikeyan, N., Silambarasan, M., Rajan, K.S.: Sub-micron dispersions of sand in water prepared by stirred bead milling and ultrasonication: a potential coolant. Appl. Therm. Eng. **44**, 1–10 (2012)
3. Silambarasan, M., Manikandan, S., Rajan, K.S.: Viscosity and thermal conductivity of dispersions of sub-micron TiO_2 particles in water prepared by stirred bead milling and ultrasonication. Int. J. Heat Mass Transf. **55**, 7991–8003 (2012)
4. Chitra, K., Annadurai, G.: Antimicrobial activity of wet chemically engineered spherical shaped ZnO nanoparticles on food borne pathogen. Int. Food Res. J. **20**(1), 59–64 (2013). [6]. R. Mohamed, I. Mkhalid, E. Baeissa, M. Al-Rayyani
5. Goh, H.S.: ZnO nanoflake arrays prepared via anodization and their performance in the photodegradation of methyl orange. Turk. J. Chem. **1**(35), 375–391 (2011)
6. Kanade, K.G.: Effect of solvents on the synthesis of nano-size zinc oxide and its properties. Mater. Res. Bull. **41**, 590–600 (2006)
7. Darezereshki, E., et al.: A novel thermal decomposition method for the synthesis of ZnO nanoparticles from low concentration ZnSO4 solutions. Appl Clay Sci. **54**, 107–111 (2011)
8. Kołodziejczak-Radzimska, A., Jesionowski, T.: Zinc oxide-from synthesis to application: a review. Materials **7**, 2833–2881 (2014)
9. Nagaraju, G.: Surfactant free hydrothermally derived ZnO nanowires, nanorods, microrods and their characterization. Mater. Sci. Semicond. Process. **13**, 21–28 (2010)
10. Zareie, M.: A simple method for preparation of micro-sized ZnO flakes. Mater. Lett. **91**, 255–257 (2013)
11. Kale, R.B.: Morphological evolution of hydrothermally derived ZnO nano and microstructures. Opt.-Int. J. Light Electron. Opt. **127**, 4621–4624 (2016)
12. Chen, C.: Synthesis and characterization of nano-sized ZnO powders by direct precipitation method. Chem. Eng. J. **144**, 509–513 (2008)
13. Zhao, D., Zhao, L., Zhu, C.S., Huang, W.Q., Hu, J.L.: Water insoluble ß-cyclodextrin polymer crosslinked by citric acid synthesis and adsorption properties toward phenol and methylene blue. J. Inclus. Phenom. Macrocycl. Chem. **63**, 195–201 (2009)
14. Chen*, C., Liu, P., Lu, C.: Synthesis and characterisation of nano-size ZnO powders by direct precipitation method, July 2008
15. Lupan, O., Emelchenko, G.A., Ursaki, V.V., Chai, G., Redkin, A.N., Gruzintsev, A.N., Tiginyanu, I.M., Chow, L., Ono, L.K., Roldan Cuenya, B., Heinrich, H., Yakimov, E.E.: Synthesis and characterization of ZnO nanowires for nanosensor applications. Mater. Res. Bull. **45**, 1026–1032 (2010)

16. Dang, D.K., Sundaram, C., Ngo, Y.L.T., Chung, J.S., Kim, E.J., Hur, S.H.: One pot solid-state synthesis of highly fluorescent N and S co-doped carbon dots and its use as fluorescent probe for Ag+ detection in aqueous solution. Sens. Actuators B **255**, 3284–3291 (2018)
17. Zhang, C.L., Liu, J.C., Yang, W.B., Chen, D.L., Jiao, Z.G.: Experimental and molecular docking investigations on the inclusion mechanism of the complex of phloridzin and hydroxypropyl β – cyclodextrin. Food Chem. **215**, 124–128 (2017)
18. Chieng, B.W., Loo, Y.Y.: Synthesis of ZnO nanoparticles by modified polyol method. Mater. Lett. **73**, 78–82 (2012)
19. Zak, A.K., Abrishami, M.E., Majid, W.H.A., Yousef, R., Hosseini, S.M.: Effect of annealing temperature on some structural and optical properties of ZnO nanoparticles prepared by a modified sol-gel combustion method. Ceram. Int. **37**, 393–398 (2011)
20. Sharma, D., Sharma, S., Kaith, B.S., Rajput, J., Kaur, M.: Synthesis of ZnO nanoparticles using surfactant free in-air and microwave method. Appl. Surf. Sci. **257**, 9661–9672 (2011)

Author Index